



HAL
open science

Closed-loop control separated flows using real-time PIV

Eliott Varon

► **To cite this version:**

Eliott Varon. Closed-loop control separated flows using real-time PIV. Mechanics [physics.med-ph]. Université Paris sciences et lettres, 2017. English. NNT : 2017PSLET008 . tel-01865213

HAL Id: tel-01865213

<https://pastel.hal.science/tel-01865213>

Submitted on 31 Aug 2018

HAL is a multi-disciplinary open access archive for the deposit and dissemination of scientific research documents, whether they are published or not. The documents may come from teaching and research institutions in France or abroad, or from public or private research centers.

L'archive ouverte pluridisciplinaire **HAL**, est destinée au dépôt et à la diffusion de documents scientifiques de niveau recherche, publiés ou non, émanant des établissements d'enseignement et de recherche français ou étrangers, des laboratoires publics ou privés.

THÈSE DE DOCTORAT

de l'Université de recherche Paris Sciences et Lettres
PSL Research University

Préparée à l'École supérieure de Physique et de Chimie
Industrielles de la ville de Paris

Closed-loop control of separated flows using real-time PIV

École doctorale n°391

SCIENCES MÉCANIQUES, ACOUSTIQUE, ÉLECTRONIQUE ET ROBOTIQUE DE PARIS

Spécialité FLUID MECHANICS

Soutenue par **Eliott VARON**
le 13 octobre 2017

Dirigée par **Jean-Luc AIDER**

COMPOSITION DU JURY :

M Jean-Luc AIDER
PMMH-ESPCI-UPMC
Directeur de thèse

M Jacques BORÉE
PPRIME-ISAE-ENSMA
Rapporteur

M Olivier CADOT
University of Liverpool
Examineur

Mme Valérie FERRAND
ISAE-SUPAERO
Examinatrice

M Philippe GILOTTE
Plastic Omnium Auto Exterior
Invité

M Philippe GUIBERT
Institut Jean Le Rond d'Alembert-UPMC
Président

M David LO JACONO
IMFT-Université Paul Sabatier
Rapporteur

M Denis SIPP
ONERA-DAAA
Examineur

À ma famille.

À Arthur, Bethy et Jackie.

Remerciements

Je réalise à quel point je fus chanceux, pour ne pas dire privilégié, d'avoir eu un tel environnement comme cadre pour ma thèse. Je tiens en effet à saluer Jean-Luc pour ses précieux conseils, sa confiance répétée et son utile insistance à m'envoyer confronter nos idées dans de nombreuses conférences et réunions. Merci pour avoir grandement contribué à la naissance et à l'aboutissement de ces travaux. J'ai aussi eu l'opportunité de collaborer avec des personnes venant de divers horizons - Philippe G., Yoann et Stéphanie (Plastic Omnium) ; Pierric et Stéphane (PRISME) ; Denis, Peter et Juan (ONERA et Imperial College) - qui m'ont tous considérablement apporté sur les plans scientifique et technique comme humain. Je leur en suis extrêmement reconnaissant. Je n'oublie pas non plus d'y inclure Nicolas pour m'avoir lancé dans ce grand bain il y a trois ans. La version définitive du présent manuscrit n'aurait finalement pu exister sans la lecture minutieuse et critique des rapporteurs, qu'ils en soient sincèrement remerciés, ainsi que l'ensemble du jury pour tous nos échanges constructifs.

Malgré l'isolement apparent du sujet de cette thèse, au regard du reste des thématiques traitées au PMMH, l'ensemble du laboratoire a également apporté sa pierre à l'édifice. Effectivement, du fait même de cette singularité qui consiste à réunir sous un même toit des sujets aussi riches et variés, j'y ai largement trouvé de quoi satisfaire ma soif de connaissances. Notamment en cogitant sur des problèmes de physique, d'informatique ou de plans d'expériences - Laurette, Thierry, Sylvain, Xavier-Benoît, Tahar, Olivier, Alain, Amaury, Justine et Antonios. Mais c'est aussi en discutant de tous les sujets qui nous passaient logiquement par la tête - Vincent, Clothilde, Hugo, Lukasz, Yacine, Charly, Thibault, Hadrien, Marion, Adrien, Ashraf, Matthiew, Florence, Thomas, Lucie, Marine, Jean, Gaspard, Benoît, Ali, Gab, Alex, Ludovic... (dans un ordre purement arbitraire) -, que ce soit autour d'un billard, d'un tennis de table ou d'un rock band, que j'ai définitivement apprécié de me rendre tous les jours au laboratoire. Cette ambiance agréable est en grande partie due à l'organisation humaine qui y prévaut et pour laquelle je tiens à exprimer chaleureusement ma gratitude envers Claudette, Frédérique et Philippe. Je remercie enfin tou-te-s les technicien-ne-s, malheureusement trop anonymes, qui facilitent tant le quotidien au laboratoire.

Pour finir, si j'ai pu être tant heureux pendant ces trois années intenses, je le dois aussi à mes proches. J'exprime donc ma plus grande affection à Juliette qui aura quotidiennement et inlassablement eu foi en moi. Pour m'avoir indéfiniment supporté et offert l'opportunité de si longues études malgré ma difficulté à leur en rendre clair le contenu, mon indéfectible reconnaissance va à mes parents, ma sœur, mes grands-parents, mes oncles et tantes, ainsi que leurs enfants. Mes pensées vont de même à Hélène, Laurent et Élisabeth. Bien entendu, et pour conclure, mes amis ont aussi énormément compté dans cette aventure par leur désir d'en savoir toujours plus sur mes avancées ("Alors, ça trouve?") et leurs nombreuses invitations à des voyages et week-ends loin du laboratoire (bien trop déclinées hélas). Merci donc à Charles, Thomas A., Émilie, Julien L., Thomas L., Marion, Sophie, Matthieu B., Quentin, Julie, Claire M., Simon, Armand, Justine, Delphine, Flo, Jérémie, Lorelei, Manon, Lucien, Raphaël, Elsa, Roman, Arthur, Adrien, Charlotte H., Greg, Pauline, Théo, Claire R., Crevette, Rémi B., Hélène, Marco, Charlotte R., Matthieu

R., Giulia, Rémi J., Julien B., Zelda, Félix, Gilles, Charlotte V., Laurie...

Contents

0.1	Résumé détaillé	1
0.2	Thesis abstract	2
0.3	Communications	2
1	Introduction to flow control	5
1.1	Context	5
1.1.1	State of the world	5
1.1.2	Research at PMMH	9
1.2	Separated flows	9
1.2.1	Triggering a flow separation	9
1.2.2	Dynamics generated by the separation	10
1.3	Flow control	11
1.3.1	Passive control	11
1.3.2	Active control	12
1.4	Conclusion and discussion	14
2	Real-time PIV using optical flow	21
2.1	Introduction	22
2.1.1	Velocimetry techniques	22
2.1.2	Optical flow for PIV: the origin of good	24
2.2	Functioning	25
2.2.1	FOLKI method	25
2.2.2	Real-time computation	30
2.3	Optimal parameters	35
2.3.1	BFS in the hydrodynamic channel	35
2.3.2	Influence of optical flow parameters	38
2.4	Conclusions and perspectives	43
2.4.1	Future improvements	44
3	Velocity fields analysis for real-time PIV	53
3.1	Velocity fields	53
3.1.1	Time-averaged velocity	53
3.1.2	Velocity fluctuations	54
3.2	Vortex detection	55
3.2.1	Swirling strength criterion	55
3.2.2	Q -criterion	56
3.3	Separated flow activity	57

3.4	Conclusions and perspectives	59
4	The dynamic observer	63
4.1	Introduction	64
4.1.1	Reduced-order model	64
4.1.2	Dynamic observer principle	65
4.2	Experimental application	67
4.2.1	The boundary layer over a flat plate	67
4.2.2	Experimental setup	70
4.2.3	Flow characterization	72
4.2.4	Experimental dynamic observer	75
4.3	Conclusions and perspectives	81
4.3.1	Discussion	82
4.3.2	Perspectives	82
5	Turbulent square-back bluff body wake	87
5.1	Introduction	88
5.1.1	A model to rule them all...	88
5.1.2	The slanted rear configuration	89
5.1.3	The square-back Ahmed body	91
5.2	Experimental setup	93
5.2.1	Bluff body	93
5.2.2	Wind tunnel	93
5.2.3	Measurements and the Holy Grail: No intrusion	94
5.3	Time-averaged characteristics of the unforced wake	98
5.3.1	Incoming flow	98
5.3.2	Mean wake topology	99
5.3.3	Global aerodynamic indicators	101
5.4	Unsteady characteristics and large-scale dynamics	102
5.4.1	Unsteady characteristics	103
5.4.2	Bimodality and more	104
5.4.3	Coherent structures	118
5.5	Conclusions	120
6	Turbulent wake as a dynamical system	127
6.1	Quasi strange attractor dynamics	127
6.1.1	Clues to weak chaos	129
6.1.2	A chaos portrait	132
6.2	Conclusions and discussion	137

7 Control of the chaotic dynamics of a turbulent wake	143
7.1 Introduction	143
7.1.1 Turbulent wake control	143
7.1.2 Micro-jets system	145
7.2 Open-loop forcing of the wake	147
7.2.1 Continuous blowing in different regions	147
7.2.2 Pulsed blowing in different regions	149
7.3 Closed-loop control of the wake dynamics	153
7.3.1 Principle of the closed-loop experiments	153
7.3.2 Stabilization of the wake	154
7.3.3 Creation of a multimodal state	157
7.4 Conclusions and issues raised	160
7.4.1 Perspectives	162
8 Conclusions and perspectives	167
8.1 Concluding remarks	167
8.2 Perspectives	168
8.2.1 Real-time PIV anywhere	169
8.2.2 The transition from laminar to turbulent has been delayed	169

0.1 Résumé détaillé

Le travail réalisé pendant ces trois années au laboratoire de physique et mécanique des milieux hétérogènes (PMMH) dans l'École supérieure de physique et de chimie industrielles de la ville de Paris (ESPCI) peut se décomposer en trois parties. La première consiste en l'amélioration continue d'un outil de mesure vélocimétrique développé récemment au PMMH. La seconde partie est un exemple d'application de cet outil pour un écoulement dans un canal hydraulique. Finalement des essais réalisés en collaboration avec Plastic Omnium à la soufflerie Malavard du laboratoire PRISME à Orléans constitue le dernier volet.

Tout d'abord, le **chapitre 1** présente le contexte dans lequel s'inscrit cette thèse. Le phénomène d'écoulements décollés y est introduit en soulignant son omniprésence dans la nature comme dans les écoulements industriels (aérodynamique externe des véhicules, des bâtiments, écoulements autour d'aubes de turbines, aérodynamique interne dans des tuyaux...). Comme de tels écoulements sont soit nuisibles (sources de vibrations et de bruit aéroacoustique, augmentation de la traînée, réduction de la portance), soit avantageux (efficacité des mélanges), les enjeux associés à leur compréhension et à leur maîtrise sont rappelés.

Le **chapitre 2** explique le principe de fonctionnement d'un capteur visuel mesurant *en temps réel* (~ 10 ms) des champs denses de vitesse des écoulements. Appartenant aux techniques de vélocimétrie laser par image de particules (PIV), cette méthode expérimentale est basée sur un algorithme de flot optique issu du domaine de la vision par ordinateur. Les améliorations qui y ont été successivement apportées sont exposées, avec notamment la mise en place d'un dispositif pouvant mesurer des vitesses rencontrées en soufflerie industrielle. Les paramètres de l'algorithme sont finalement testés afin d'établir un ajustement correct entre précision des résultats et rapidité d'exécution. Pour caractériser finement les écoulements, des grandeurs sont également dérivées des champs de vitesse. Leurs calculs sont détaillés dans le **chapitre 3**.

Une première application de la PIV par flot optique est illustrée par le **chapitre 4** dans le cadre de l'identification de système. Un algorithme d'apprentissage récemment conçu pour construire un modèle réduit d'une simulation de couche limite sur plaque plane est en effet mise en œuvre expérimentalement. Les mesures sont réalisées dans un canal hydrodynamique au PMMH et laissent une grande liberté dans le choix des données d'entrée du système. Les données de sortie sont calculées par décomposition en modes propres orthogonaux (POD) des champs de vitesses. Le modèle retenu *in fine* permet bien de prédire la dynamique de la transition de la couche limite laminaire vers la turbulence.

Enfin, le **chapitre 5** donne les caractéristiques moyennes et instationnaires d'un sillage pleinement turbulent derrière le corps de Ahmed, une géométrie modélisant une voiture très simplifiée. La pression au culot, les vitesses de l'écoulement et les forces aérodynamiques agissant sur le corps sont mesurées. Un comportement bimodal latéral apparaît clairement pour différentes grandeurs : pression à la paroi, vitesse dans la zone de recirculation, forces de dérive. Une étude du sillage avec des outils issus de la théorie des systèmes dynamiques est proposée dans le **chapitre 6**. Des indices de l'existence d'un attracteur étrange faiblement chaotique dans la dynamique du sillage sont exposés, tout en soulignant le caractère stochastique de cette dernière. Ce travail est conclu

dans le **chapitre 7** par de nombreux essais de contrôle de l'écoulement à l'aide de micro-jets discontinus installés sur le bord supérieur du culot. La symétrisation du sillage est atteinte pour un soufflage pulsant à la fréquence correspondant au lâché tourbillonnaire. Une loi de contrôle réactif consistant à suivre et forcer la recirculation grâce à la PIV temps réel est exécutée avec succès.

0.2 Thesis abstract

The **chapter 1** introduces the separated flows, ubiquitous processes in nature and industrial systems, such as diffusers, airfoils, air conditioning plants and moving vehicles. As the separation can strongly influence the performances of such devices, investigating their dynamics and their possible control is of great interest.

The **chapter 2** presents a new velocimetry method developed in the laboratory PMMH for five years. After explaining its algorithm functioning, the hardware and the software used are detailed. The different parameters to obtain proper velocity fields are investigated for a well known flow: the backward-facing step (BFS). Quantities which can be extracted in *real-time* (RT) from the velocity fields are discussed in **chapter 3**. These calculations are fundamental to use the camera as a visual sensor in a closed-loop experiment. Some of these quantities are related to specific flow like the recirculation area, characteristic of the wakes. Other are intended to detect structures like the Q -criterion. All these tools are implemented on the GPU and are illustrated via measurements in the BFS flow.

In **chapter 4**, a reduced-order model method well suitable for amplifier flows, the dynamic observer, is presented. After applying to the boundary layer over a flat plate, a closed-loop control based on the flow reconstruction is investigated.

In **chapter 5**, we will first summarize the cutting-edge knowledge about the flow around a simple car model. After introducing the experimental setup, the natural flow is studied. In **chapter 6**, the 3D full turbulent wake dynamics can be characterized by the single trajectory of its projected barycenter. After recovering a classic chaotic pattern, its inner characteristics are analyzed more thoroughly, by evaluating, in particular, the family of random process to which it belongs, the largest Lyapunov exponent of the system and the correlation dimension. The **chapter 7** presents a closed-loop control of the turbulent wake behind the square-back Ahmed body described in **chapter 5** and in **chapter 6**. After introducing the micro-jets system, different control strategies are tested.

0.3 Communications

Most of the findings obtained during the thesis have been presented at various international conferences and national meetings:

- 10th Pacific Symposium on Flow Visualization and Image Processing June 15-18

2015, Napoli, Italy ([chapter 2](#) and [chapter 4](#)).

- **Bifurcations and Instabilities in Fluid Dynamics** July 15-17 2015, Paris, France ([chapter 4](#)).
- **15th European Turbulence Conference** August 25-28 2015, Delft, the Netherlands ([chapter 4](#)).
- **Aerovehicles 2** June 21-23 2016, Gothenburg, Sweden ([chapter 7](#)).
- **11th European Fluid Mechanics Conference** September 12-16 2016, Sevilla, Spain ([chapter 7](#)).
- **52nd 3AF International Conference on Applied Aerodynamics** March 27-29 2017, Lyon, France ([chapter 6](#) and [chapter 7](#)).
- **16th European Turbulence Conference** August 21-24 2017, Stockholm, Sweden ([chapter 6](#) and [chapter 7](#)).
- **Congrès Français de Mécanique** August 28 - September 1st 2017, Lille, France ([chapter 2](#), [chapter 6](#) and [chapter 7](#)).

Some of the results presented have been published or are currently considered for publications:

- Chaotic dynamics of large-scale structures in a turbulent wake. (2017) Eliott Varon, Yoann Eulalie, Stephie Edwige, Philippe Gilotte, and Jean-Luc Aider. *Phys. Rev. Fluids* **2**, 034604.
- Control of the chaotic dynamics of a turbulent 3D wake. Eliott Varon, Yoann Eulalie, Stephie Edwige, Philippe Gilotte, and Jean-Luc Aider. [Submitted in *Phys. Rev. Fluids*]
- Experimental application of the dynamic observer to capture forced transient boundary layer dynamics. Eliott Varon, Juan Guzmán Iñigo, Denis Sipp, Peter J. Schmid, and Jean-Luc Aider. [Under consideration for *Journal of Fluid Mechanics*]

If the reader has any questions about the content of the thesis, the author can be reached at eliott.varon@zaclys.net.

Introduction to flow control

The global context of the thesis is briefly presented. After introducing the separated flows, different methods to control them are exposed. It shall be mentioned that most of the previous works on the subjects studied during this thesis are reviewed in the introduction of each other chapter.

1.1 Context	5
1.1.1 State of the world	5
1.1.2 Research at PMMH	9
1.2 Separated flows	9
1.2.1 Triggering a flow separation	9
1.2.2 Dynamics generated by the separation	10
1.3 Flow control	11
1.3.1 Passive control	11
1.3.2 Active control	12
1.4 Conclusion and discussion	14

1.1 Context

1.1.1 State of the world

The long-lived greenhouse gases in the atmosphere followed a cyclic evolution over long periods of several thousands years as displayed in Figure 1.1(a) (Barnola *et al.*, 2003; Ruddiman & Raymo, 2003; Schilt *et al.*, 2010). However, since the Industrial Revolution, their concentration has exponentially increased until reaching new maxima as shown in Figure 1.1(b) (MacFarling Meure *et al.*, 2006). Such a rupture in the natural cycle of greenhouse gases has led to the current rapid climate change and has anthropic origins. Indeed, with other indicators (geochemical signatures, extinction rates...), it constitutes pieces of evidence of the long-time impacts of the human activities on Earth's ecosystems, geology and climate (Waters *et al.*, 2016), to the point where the today's epoch is now called Anthropocene (Monastersky, 2015). This is the reason why it is interesting to analysis the main causes of greenhouse gases emissions in order to prioritize future efforts to reduce them.

The transport sector contributes currently to a quarter of the global CO₂ emissions, which amounts to 32.3 Gt, as displayed in Figure 1.2(a). Road vehicles are the most responsive to

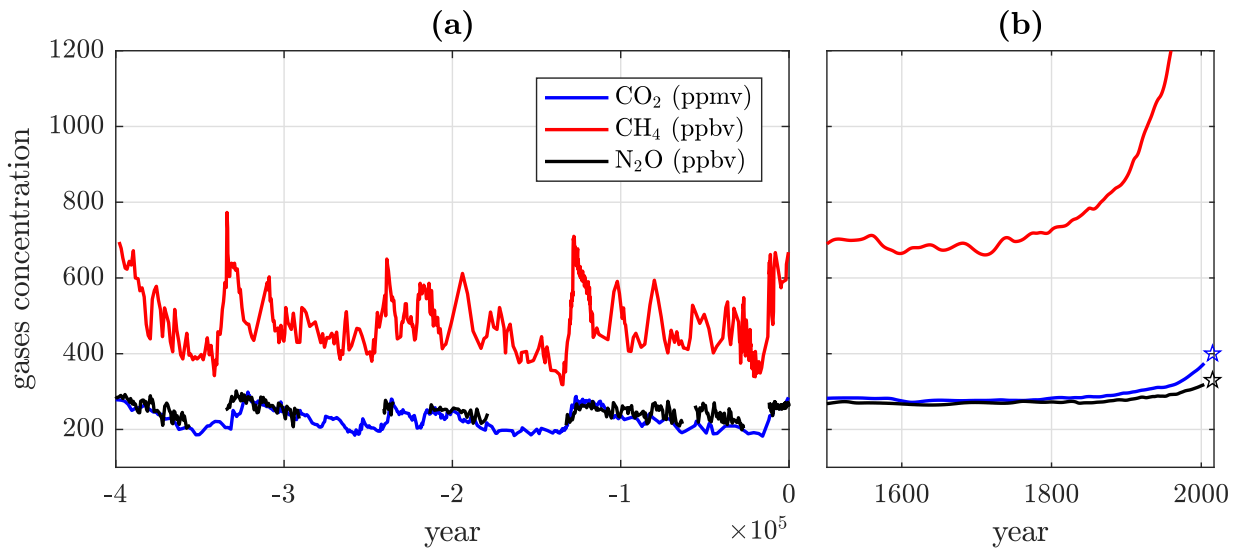


Figure 1.1 – Concentration of carbon dioxide (CO₂), methane (CH₄) and nitrous oxide (N₂O) in the atmosphere (a) from the year -400,000 to 0 (ice cores) and (b) from the year 1500 to 2017 (ice cores and direct air measurements). *ppmv* and *ppbv* stand for *parts per million by volume* and *parts per billion by volume* respectively.

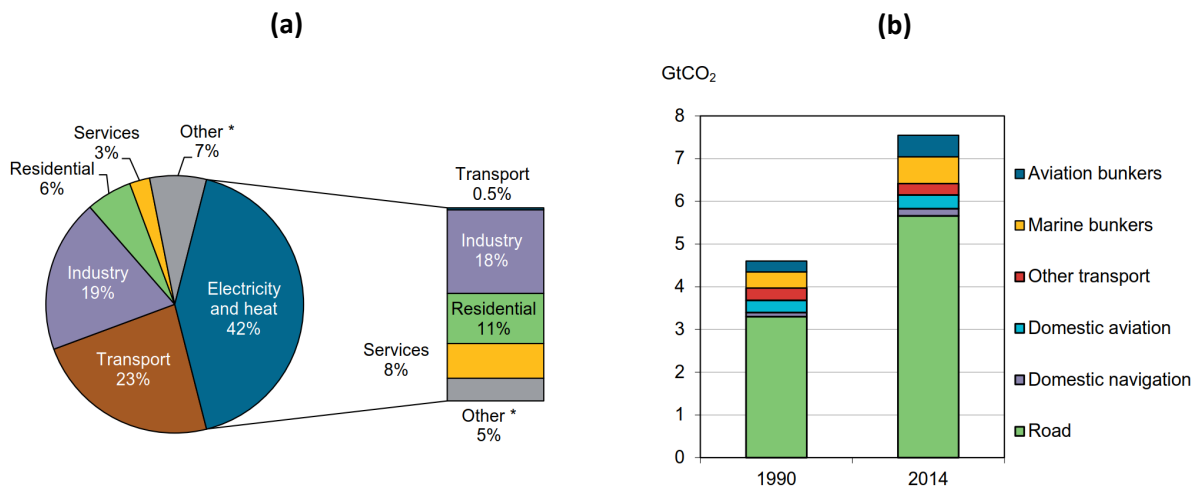


Figure 1.2 – World CO₂ emissions (a) by sector and (b) from transport in 2014, estimated by International Energy Agency (2016). The total emissions are 32.3 GtCO₂.

these emissions according to Figure 1.2(b) and especially light-duty vehicles which contributes finally to 9% all in all (The International Council on Clean Transportation, 2015). These emissions as well as the air pollutant ones are due to the combustion process transforming the chemical energy contained in petroleum or in alternative fuels into heat, which is used to obtain the propulsion of the vehicle (kinetic energy). The emissions of a vehicle are therefore related to the oil consumption: used units are either gCO₂/km or L/100km.

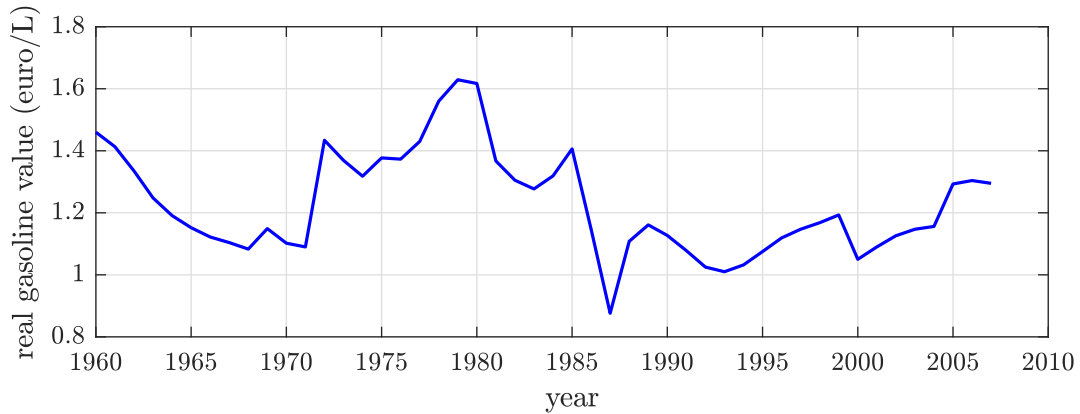


Figure 1.3 – Mean real gasoline value in France based on year 2007 (according to *Annuaire statistique de la France*).

The main other reason to reduce the fuel consumption of a vehicle is economic. Most of the clients take indeed into account the fuel cost when buying a car and they will consequently look rather for efficient vehicles. This pushed car manufacturers to define their own standards like the Corporate average fuel economy (CAFE) to face the oil crisis in the seventies (see Figure 1.3).

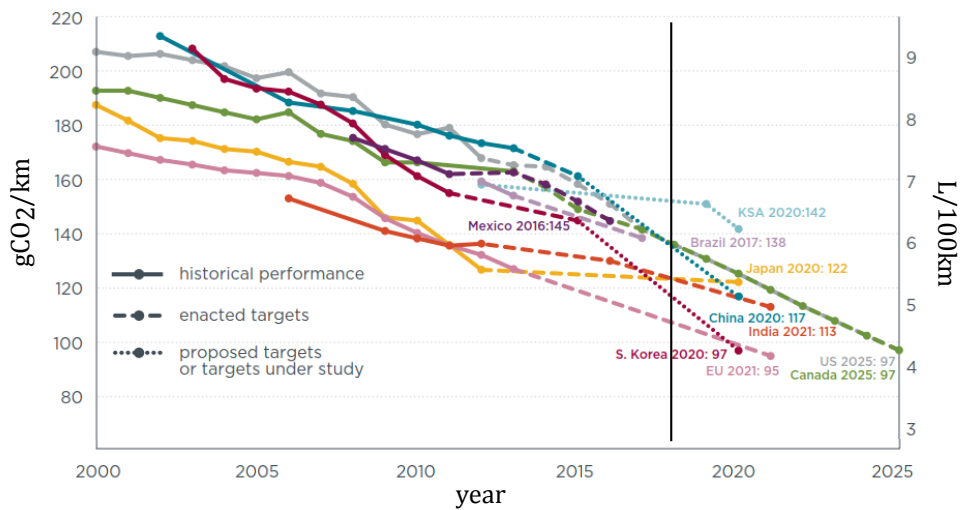


Figure 1.4 – Light-duty vehicle efficiency standards by The International Council on Clean Transportation (2015). Vertical grey line is year 2017.

Modern standards are finally created by states as summarized in Figure 1.4 to limit the CO₂ emissions, which are verified through official tests like the Worldwide Harmonized Vehicles Test Procedure (WLTP). To comply with these regulations the manufacturers have to improve the vehicle engine efficiency which is estimated at 40% for conventional gasoline cars (Carpenter *et al.*, 2008; Roura & Oliu, 2012). Developing kinetic energy recovery system and lightweighting the vehicle are complementary ways to increase the fuel economy.

Another solution involves improving the car aerodynamic efficiency. At a constant speed on a

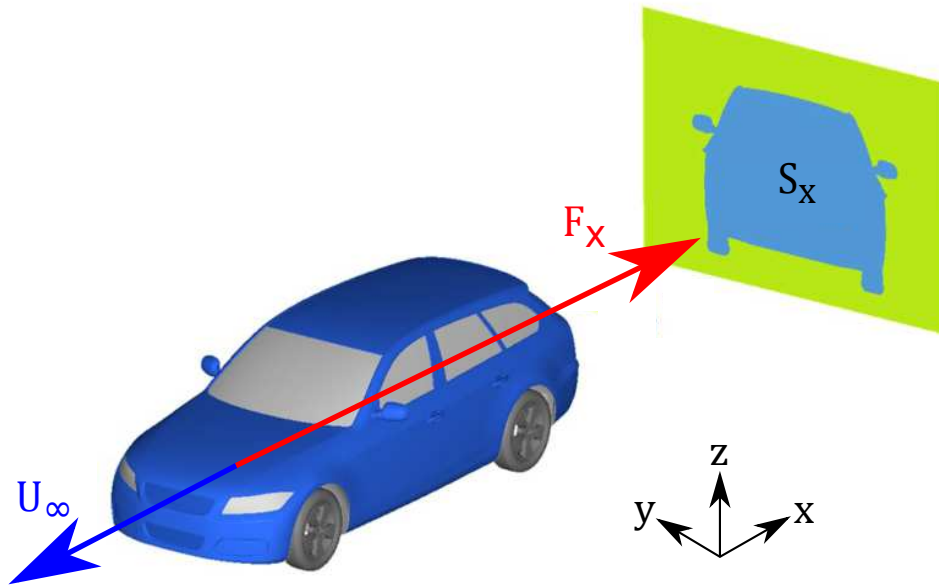


Figure 1.5 – Sketch of the drag force F_x , inspired by Eulalie (2014).

highway, denoted U_∞ and called the free stream velocity - around 110 km/h - a car is indeed essentially subjected to the aerodynamic drag F_x drawn in Figure 1.5, the rolling resistance being most important at lower speeds. This force is characterized through the aerodynamic coefficient C_x , defined by

$$C_x = \frac{F_x}{\frac{1}{2}\rho U_\infty^2 S_x}, \quad (1.1)$$

where S_x is the frontal area. Thus, reducing the car C_x leads to save fuel consumption. Two other aerodynamic forces are evaluated: the lift F_z and the derive F_y .

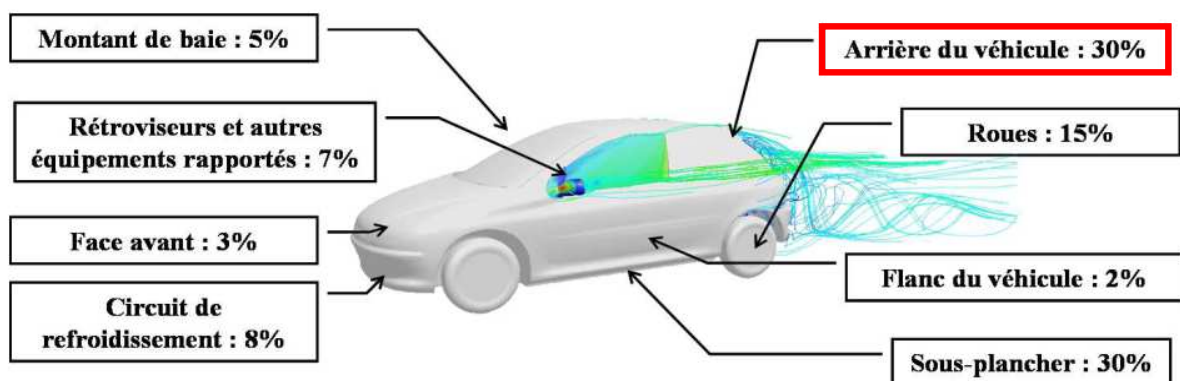


Figure 1.6 – Drag contribution on a personal car according to PSA (Jermann, 2016).

The parts of a vehicle contributes differently to the total aerodynamic drag as summarized in Figure 1.6. The present thesis focuses on the rear part where separation of the flow occurs, which will be detailed further.

1.1.2 Research at PMMH

Consequently, transport domain is more than ever an important subject of research. The field in fluid dynamics which especially aims at reducing the energy consumption or improving the energy transformation is the flow control. This is the reason why Plastic Omnium Auto Exterior (PO), worldwide supplier of several car manufacturers, and the laboratory Physique et Mécanique des Milieux Hétérogènes (PMMH) have decided to collaborate. PO can indeed produce small devices, like micro jets embedded in personal cars, modifying the wake behind it, while PMMH develops a visual sensor, allowing the capture in real time of the flow around various geometries.

The present thesis is part of this collaboration as a continuation of the previous works of [Gautier \(2014\)](#) who developed a real time PIV setup for a water channel. By adapting this setup to a wind tunnel facility, the purpose is to obtain a reactive control based on PIV measurements to manipulate a three-dimensional (3D) fully turbulent wake. This work benefits from a continuous 17-years study on flow control done at the PMMH laboratory as well as from recent experiments made by PO. The successive PhD students contributors over the years to this research are:

2001-2004 J. F. Beaudouin, supervised by J.-L. Aider (PSA Peugeot-Citroën) and J. E. Wesfreid (PMMH),

2002-2005 B. Thiria, supervised by J. E. Wesfreid (PMMH), on the dynamic and stability properties of forced open flows ([Thiria, 2005](#));

2006-2009 T. Duriez, supervised by J. E. Wesfreid (PMMH) and J.-L. Aider (PMMH), on the control of flow over a ramp via vortex generator devices ([Duriez, 2009](#));

2009-2012 P. Joseph, supervised by J.-L. Aider (PMMH) and X. Amandolese (IAT), within the CARAVAJE project, on control of the external aerodynamic of automotive vehicles by pulsed jets ([Joseph, 2012](#));

2008-2012 T. Cambonie, supervised by J.-L. Aider (PMMH), on the interactions between one or many jets with a boundary layer (Jets in Cross Flow) ([Cambonie, 2012](#));

2011-2014 N. Gautier, supervised by J.-L. Aider (PMMH), on closed-loop controls based on real-time PIV ([Gautier, 2014](#));

2011-2014 Y. Eulalie, supervised by I. Mortazavi (CNAM) and P. Gilotte (PO), on the effects of micro-jets on the wake behind a simple car model ([Eulalie, 2014](#)).

1.2 Separated flows

1.2.1 Triggering a flow separation

By introducing the boundary layer concept, [Prandtl \(1904\)](#) enabled to better understand how a flow interacts with a solid, as well recalled by [Anderson Jr. \(2005\)](#). This layer makes indeed the link between the free stream, far from the solid influence, and the flow at the solid surface. Developing over the body, this region of the flow is submitted to the viscous effects due to

the presence of the body, creating strong velocity gradients. Depending on the shape and the orientation of the body, the flow will accelerate and decelerate, producing pressure gradients.

If the boundary layer encounters an adverse pressure gradient (the pressure increases along the body surface), the flow momentum inside the boundary layer decreases until the velocity near the wall cancels. The flow separation occurs, producing a recirculation bubble from the location where the velocity is negative as displayed in Figure 1.7. Downstream of the recirculation bubble, the flow will reattach where the adverse pressure gradient is not strong enough to maintain the separation. The bubble is thus delimited by the separatrix surface, joining the lines of separation and of reattachment. The bubble exists to balance the kinetic energy from the free stream into the boundary layer.

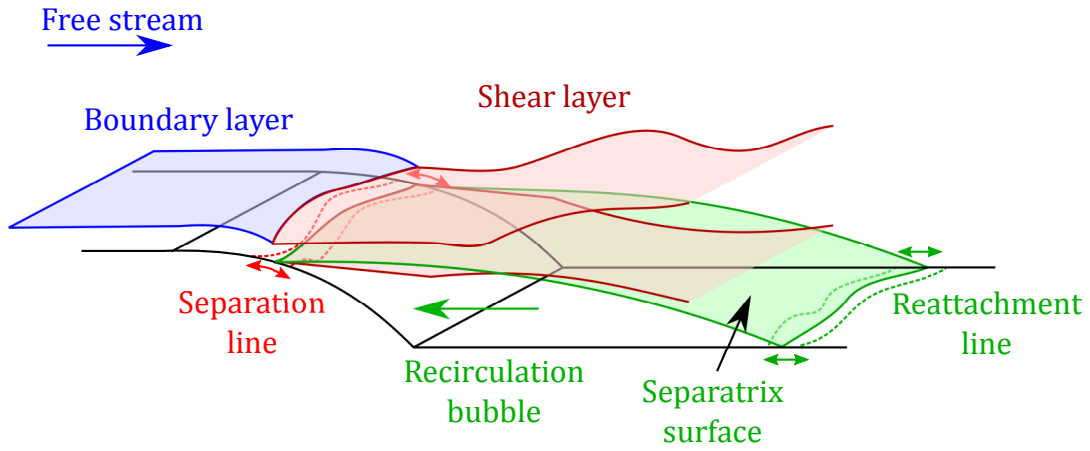


Figure 1.7 – Sketch of a *time-averaged* flow separation for a rounded backward-facing ramp. Dashed lines are the limits of the fluctuations of the separation (red) and the reattachment (green) lines.

Even if the topology of a separated flow highly depends on the body geometry, two categories can be distinguished. The first one contains the flow along a solid, concerned in chapter 2, chapter 3 (backward-facing step) and chapter 4 (flat plate). The second kind of separation implies two interacting shear layers produced by a bluff body, which chapter 5, chapter 6 and chapter 7 deal with. For a given body shape, the separation triggering is also determined by the state of the flow via the Reynolds number

$$Re_L = \frac{L \times U_\infty}{\nu}, \quad (1.2)$$

where L is a characteristic length of the {flow,body} system and ν the kinematic viscosity of the fluid. The Reynolds number represents the ratio between inertial forces and viscous forces. For instance $Re_L \sim 10^6$ for a car on a highway.

1.2.2 Dynamics generated by the separation

The lines of separation and of reattachment fluctuate around mean positions, except when the separation line is forced by geometry discontinuities (straight edge). This unsteady behavior is

due to different instabilities interacting with each other, like the Kelvin-Helmholtz one and the vortex shedding one. In the last part of [chapter 2](#) and in [chapter 3](#), most of these instabilities are detailed and discussed through the backward-facing step flow, a benchmark for the study of separated flows ([Aider & Danet, 2006](#)).

The dynamics differ strongly from an instability to another. To make comparisons between them, each dynamic is associated to a dimensionless frequency (or range of frequencies) called the Strouhal number,

$$St_L = \frac{L \times f}{U_\infty}, \quad (1.3)$$

where f is the characteristic frequency of the unsteady behavior. It allows for instance to experimentally locate their complex spatial structure by analysing the power spectrum of the velocity measured at different positions in the flow.

1.3 Flow control

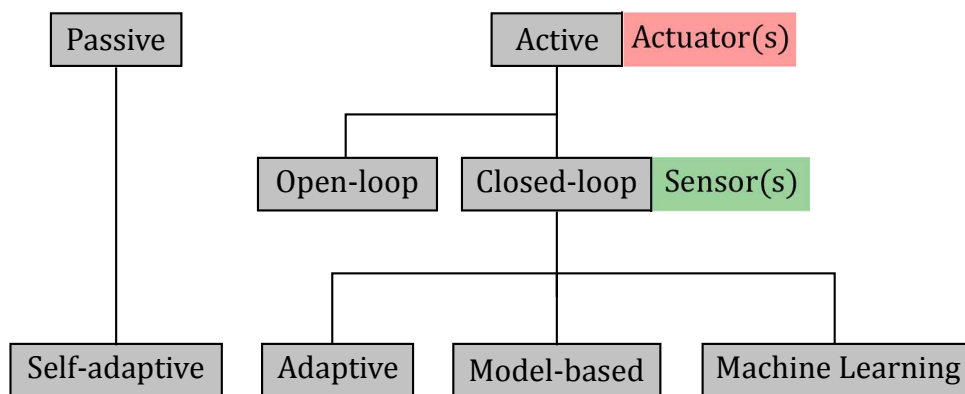


Figure 1.8 – Summary of the flow control categories.

Flow separation strongly affects the aerodynamic in ground vehicles applications (cars, trucks, trains), as well as wind turbines, air vehicles (airplanes, helicopters, launchers) and turbomachineries. For example, this phenomenon is responsible for most of the drag experienced by ground vehicles and for the loss of lift of an airplane (stall). Nonetheless, it may greatly improve the mixing efficiency between fluids ([Ottino, 1990](#)), like air and fuel in a combustion engine. It is thereby of interest to properly modify the flow behavior regarding the desired effect. As depicted in [Figure 1.8](#), control methods are classically classified into two groups ([Gad-el Hak, 1989](#); [Choi et al., 2008](#)): passive control and active control. A few examples will be given here as illustrations but more are available in [chapter 7](#).

1.3.1 Passive control

The idea behind passive control is to optimize the shape of a body to increase aerodynamic performance. [Beaudoin & Aider \(2008\)](#) tested different configurations of flaps added to the rear

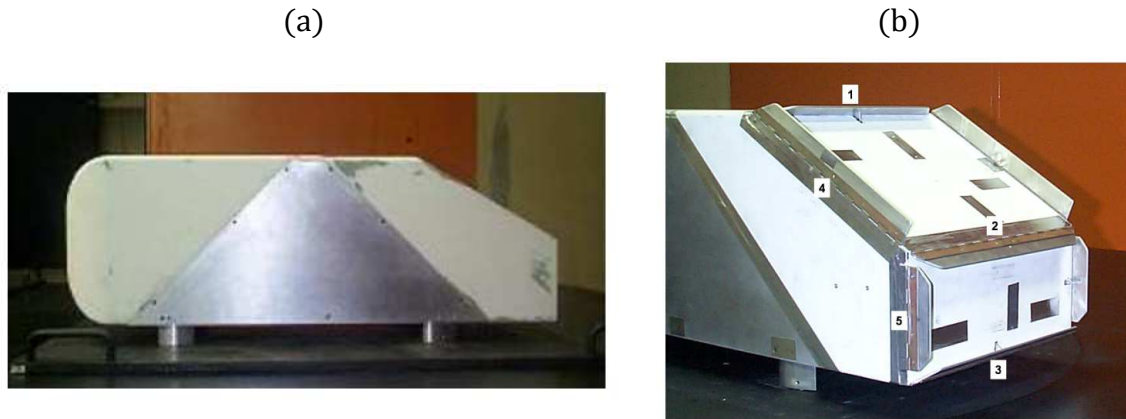


Figure 1.9 – (a) Side view of the simplified car model. (b) Model equipped with the different flaps on all the rear edges. Courtesy of J.L. Aider.

edges of a simplified car model and Aider *et al.* (2010) used vortex generators to reduce the circulation of trailing vortices behind another bluff body, leading to drag reduction.

A passive control strategy is usually defined for a specific flow configuration and is often associated to the idea that it cannot adapt to possible changes in the flow state. Nonetheless, the self-adaptive method, based on biomimetics (Bhushan, 2009), seems to allow a kind of *natural* reactive control for passive approach. For instance, replacing the rigid blades of a small wind turbine by well designed elastic ones greatly improves its energy conversion (Cognet *et al.*, 2017). The blades will indeed deform with respect to the incoming wind.

1.3.2 Active control

Active control consists in adding momentum into the flow to modify its characteristics by bringing energy through a device called actuator. Cattafesta III & Sheplak (2011) reviewed the variety of these devices used in active flow control like the fluidic, the moving surface and the plasma actuators. The actuator activity consequently requires extra costs in energy which have to be lower than the energy saved thanks to the control (Seifert, 2007).

The control law driving the actuator(s) is defined according to two approaches: the open-loop control and the closed-loop control. The former determines an offline control law. For example, by putting a cylinder into rotation, its mean wake is modified in comparison to the immobile configuration (Tokumaru & Dimotakis, 1991; Protas & Wesfreid, 2002; Thiria *et al.*, 2006). This can improve the aerodynamic performances, depending on the rotation frequency.

Taking into account the state of the flow by measuring some of its characteristics in real time via sensors enables to design closed-loop control laws. The actuator will consequently force the flow regarding any noticed change, ensuring better robustness and efficiency than the open-loop approach. This requires to have access to some values of the flow like the velocity or the pressure, and/or of forces acting on the body. This is the reason why, in a laboratory environment, a real

time PIV setup is of great interest.

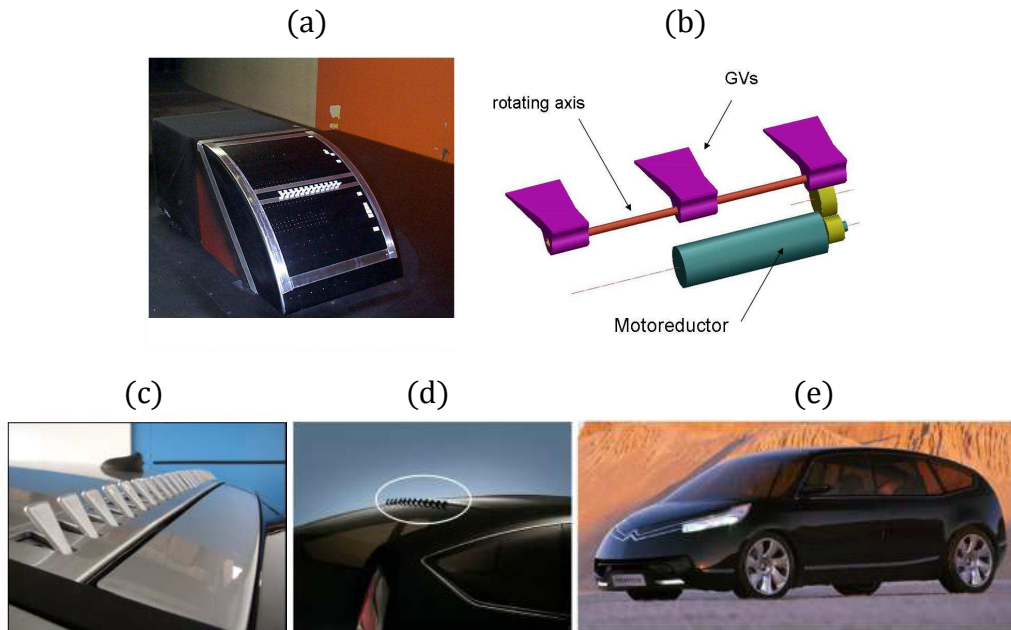


Figure 1.10 – Active vortex generators (a) on the simplified car model, (c) on a Citroën C4 (2004) and (d, e) on the concept-car Citroën C-Airlounge (2003). (b) Sketch of the active vortex generators system. Courtesy of J.L. Aider.

The first possibility of closed-loop approach is the adaptive control. It consists in putting the flow into the desired state regardless of exogenous events such as unwanted perturbations. For instance, [Beaudoin *et al.* \(2006\)](#) replaced the sharp edge of a backward-facing step by a cylinder, whose rotating velocity is driven either by a proportional integral correction or by an extremum seeking method, both using drag measurements. Based on the latter method, [Beaudoin *et al.* \(2008\)](#) used the above mentioned active vortex generators, whose angle with the free stream can be set as shown in [Figure 1.10\(b\)](#). These experimental devices have then been tested on a Citroën C4 [[Figure 1.10\(c\)](#)] and a concept-car [[Figure 1.10\(d\)](#) and (e)]¹.

The control law may be based on a model of the flow and of the forcing, called the plant and the compensator respectively ([Sipp & Schmid, 2013](#)). A direct approach consists in considering the full dynamics of the flow. As it implies a full knowledge of the flow, this restricts this method to the simplest flows. If the flow dynamics can be related to known physical systems, a physic-based model can be built.

A recent approach consists in obtaining model-free control laws through machine learning ([Duriez *et al.*, 2017](#)). A large variety of control laws are evaluated regarding the minimization of a cost function. The best laws are used to design new ones, tested again until converging to the best one. Even if this approach allows to get rid of the nonlinearity problem inherent to the flow dynamics, it does not ensure any stability robustness due to its functioning. [Gautier *et al.* \(2015\)](#) successfully implemented a genetic algorithm which created a control law reducing the

1. These experiments remain unpublished so far.

recirculation area behind a backward-facing step.

1.4 Conclusion and discussion

The context of the present work has been globally introduced. The freedom of movement is clearly internationally recognized by most of the countries since the article 13 of the Universal Declaration of Human Rights in 1948, the article 12 of the International Covenant on Civil and Political Rights in 1966 and the article 45 of the Charter of Fundamental Rights of the European Union proclaimed in 2000. Ensuring this right by developing travel means - bicycle, car, bus, metro, train, boat, plane... - contributes actually to improve the society by giving us the possibility of new encounters, cultural exchanges, world exploration and collaborative works. What the people produce is also part of the transport challenge through the design of specific vehicles for the transport of goods trade such as: trucks, container ships, freight trains and cargo planes.

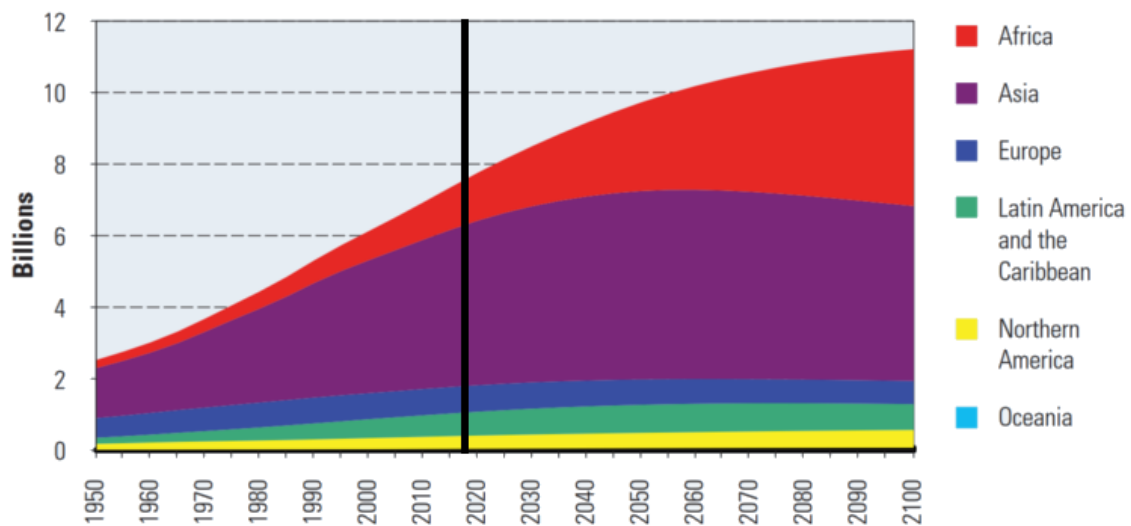


Figure 1.11 – History and projection of the total population by major area. (United Nations, 2015).

As the worldwide population exponentially grows for years, doubling in 50 years from mid-twentieth as shown by Figure 1.11, needs for transport also increase (as well as the expectations for better life quality). No radical change in this trend is expected for the next 80 years since the total population will still increase according to the predictions of United Nations (2015).

15 years ago, fuel economy for tractor-trailer trucks were already estimated between 6.5 and 16.5% thanks to simple passive devices (cross-flow vortex trap, vortex strake, under-body convergent duct) allocated in the regions responsible for the highest aerodynamic drag (Wood & Bauer, 2003). Despite of all these past discoveries, Figure 1.2(b) reveals that all possible drag reduction devices invented after years of research did not instantaneously change the rising CO₂ emission

due to transport. Therefore it shall be kept in mind that, even if flow control is a good option to optimize aerodynamics performances in the long run, firstly the application of a working device takes years after its discovery and secondly diminishing CO₂ concentration in the atmosphere does not depend only on it but also on political and societal decisions.

The PMMH laboratory develops a real time visual sensor for laboratory use, allowing new experimental strategies for closed-loop control in automobile applications via micro jets designed by PO. The visual sensor will be used for different kinds of separated flows.

Bibliography

- AIDER, J.L., BEAUDOIN, J.F. & WESFREID, J.E. (2010) Drag and lift reduction of a 3D bluff-body using active vortex generators. *Experiments in Fluids* **48** (5), pp. 771–789. doi:10.1007/s00348-009-0770-y. 12
- AIDER, J.L. & DANET, A. (2006) Large-eddy simulation study of upstream boundary conditions influence upon a backward-facing step flow. *Comptes Rendus Mécanique* **334** (7), pp. 447–453. doi:10.1016/j.crme.2006.05.004. 11
- ANDERSON JR., J.D. (2005) Ludwig Prandtl's boundary layer. *Physics Today* **58** (12), p. 42. doi:10.1063/1.2169443. 9
- BARNOLA, J.M., RAYNAUD, D., LORIUS, C. & BARKOV, N. (2003) Historical CO₂ record from the Vostok ice core. In *In Trends: A Compendium of Data on Global Change*. Carbon Dioxide Information Analysis Center, Oak Ridge National Laboratory, U.S. Department of Energy, Oak Ridge, Tenn., U.S.A. 5
- BEAUDOIN, J.F. & AIDER, J.L. (2008) Drag and lift reduction of a 3D bluff body using flaps. *Experiments in Fluids* **44** (4), p. 491. doi:10.1007/s00348-007-0392-1. 11
- BEAUDOIN, J.F., CADOT, O., AIDER, J.L. & WESFREID, J.E. (2006) Drag reduction of a bluff body using adaptive control methods. *Physics of Fluids* **18** (8), p. 085107. doi:10.1063/1.2236305. 13
- BEAUDOIN, J.F., CADOT, O., WESFREID, J.E. & AIDER, J.L. (2008) Feedback control using extremum seeking method for drag reduction of a 3D bluff body. In *IUTAM Symposium on Flow Control and MEMS: Proceedings of the IUTAM Symposium held at the Royal Geographical Society, 19–22 September 2006, hosted by Imperial College, London, England* (ed. J.F. Morrison, D.M. Birch & P. Lavoie), pp. 365–372. Dordrecht: Springer Netherlands. doi:10.1007/978-1-4020-6858-4_44. 13
- BHUSHAN, B. (2009) Biomimetics: lessons from nature—an overview. *Philosophical Transactions of the Royal Society of London A: Mathematical, Physical and Engineering Sciences* **367** (1893), pp. 1445–1486. doi:10.1098/rsta.2009.0011. 12
- CAMBONIE, T. (2012) Experimental study of a jet in crossflow at low velocity ratios using volumetric velocimetry. PhD thesis, Université Pierre et Marie Curie, Paris, France. 9
- CARPENTER, J.A., GIBBS, J., PESARAN, A.A., MARLINO, L.D. & KELLY, K. (2008) Road transportation vehicles. *MRS Bulletin* **33** (4), p. 439–444. doi:10.1557/mrs2008.86. 7
- CATTAFESTA III, L.N. & SHEPLAK, M. (2011) Actuators for active flow control. *Annual Review of Fluid Mechanics* **43** (1), pp. 247–272. doi:10.1146/annurev-fluid-122109-160634. 12

- CHOI, H., JEON, W.P. & KIM, J. (2008) Control of flow over a bluff body. *Annual Review of Fluid Mechanics* **40** (1), pp. 113–139. doi:10.1146/annurev.fluid.39.050905.110149. 11
- COGNET, V., COURRECH DU PONT, S., DOBREV, I., MASSOUH, F. & THIRIA, B. (2017) Bioinspired turbine blades offer new perspectives for wind energy. *Proceedings of the Royal Society of London A: Mathematical, Physical and Engineering Sciences* **473** (2198). doi:10.1098/rspa.2016.0726. 12
- DURIEZ, T. (2009) Vortex generators application to separated flows control. PhD thesis, Université Paris Diderot, Paris, France. 9
- DURIEZ, T., BRUNTON, S.L. & NOACK, B.R. (2017) *Machine Learning Control - Taming Nonlinear Dynamics and Turbulence*. Springer. doi:10.1007/978-3-319-40624-4. 13
- EULALIE, Y. (2014) Aerodynamic analysis and drag reduction around an Ahmed bluff body. PhD thesis, Université de Bordeaux, Bordeaux, France. 8, 9
- GAUTIER, N. (2014) Flow control using optical sensors. PhD thesis, PMMH, EPSCI, France. 9
- GAUTIER, N., AIDER, J.L., DURIEZ, T., NOACK, B.R., SEGOND, M. & ABEL, M. (2015) Closed-loop separation control using machine learning. *Journal of Fluid Mechanics* **770**, pp. 442–457. doi:10.1017/jfm.2015.95. 13
- GAD-EL HAK, M. (1989) The art and science of flow control. In *Frontiers in Experimental Fluid Mechanics* (ed. M. Gad-el Hak), pp. 211–290. Berlin, Heidelberg: Springer Berlin Heidelberg. doi:10.1007/978-3-642-83831-6_5. 11
- INTERNATIONAL ENERGY AGENCY (2016) *CO₂ Emissions from Fuel Combustion. Tech. Rep.* OECD/IEA. 6
- JERMANN, C. (2016) Eclatement tourbillonnaire dans le sillage turbulent d’un véhicule générique. PhD thesis, Université Aix Marseille, Marseille, France. 8
- JOSEPH, P. (2012) Application of control by pulsed jets on a bluff body. PhD thesis, Université Pierre et Marie Curie, Paris, France. 9
- MACFARLING MEURE, C., ETHERIDGE, D., TRUDINGER, C., STEELE, P., LANGENFELDS, R., VAN OMMEN, T., SMITH, A. & ELKINS, J. (2006) Law Dome CO₂, CH₄ and N₂O ice core records extended to 2000 years BP. *Geophysical Research Letters* **33** (14). doi:10.1029/2006GL026152. 5
- MONASTERSKY, R. (2015) Anthropocene: The human age. *Nature* **519**, pp. 144–147. doi:10.1038/519144a. 5
- OTTINO, J.M. (1990) Mixing, chaotic advection, and turbulence. *Annual Review of Fluid Mechanics* **22** (1), pp. 207–254. doi:10.1146/annurev.fl.22.010190.001231. 11
- PRANDTL, L. (1904) Fluid motion with very small friction. In *3rd International Mathematics Congress, Heidelberg, Germany*, pp. 484–491. 9

- PROTAS, B. & WESFREID, J.E. (2002) Drag force in the open-loop control of the cylinder wake in the laminar regime. *Physics of Fluids* **14** (2), pp. 810–826. doi:10.1063/1.1432695. 12
- ROURA, P. & OLIU, D. (2012) How energy efficient is your car? *American Journal of Physics* **80** (7), pp. 588–593. doi:10.1119/1.4704821. 7
- RUDDIMAN, W.F. & RAYMO, M.E. (2003) A methane-based time scale for Vostok ice. *Quaternary Science Reviews* **22** (2), pp. 141 – 155. doi:10.1016/S0277-3791(02)00082-3. 5
- SCHILT, A., BAUMGARTNER, M., BLUNIER, T., SCHWANDER, J., SPAHNI, R., FISCHER, H. & STOCKER, T.F. (2010) Glacial–interglacial and millennial-scale variations in the atmospheric nitrous oxide concentration during the last 800,000 years. *Quaternary Science Reviews* **29** (1), pp. 182 – 192. doi:10.1016/j.quascirev.2009.03.011. 5
- SEIFERT, A. (2007) Closed-loop active flow control systems: actuators. In *Active Flow Control: Papers contributed to the Conference “Active Flow Control 2006”, Berlin, Germany, September 27 to 29, 2006* (ed. R. King), pp. 85–102. Berlin, Heidelberg: Springer Berlin Heidelberg. doi:10.1007/978-3-540-71439-2_6. 12
- SIPP, D. & SCHMID, P. (2013) Closed-loop control of fluid flow: a review of linear approaches and tools for the stabilization of transitional flows. *Journal Aerospace Lab* **7** (6). 13
- THE INTERNATIONAL COUNCIL ON CLEAN TRANSPORTATION (2015) Policies to reduce fuel consumption, air pollution, and carbon emissions from vehicles in G20 nations. *Tech. Rep.. ICCT*. 6, 7
- THIRIA, B. (2005) Dynamic and stability properties of forced open flows. PhD thesis, Université Pierre et Marie Curie, Paris, France. 9
- THIRIA, B., GOUJON-DURAND, S. & WESFREID, J.E. (2006) The wake of a cylinder performing rotary oscillations. *Journal of Fluid Mechanics* **560**, p. 123–147. doi:10.1017/S0022112006000656. 12
- TOKUMARU, P.T. & DIMOTAKIS, P.E. (1991) Rotary oscillation control of a cylinder wake. *Journal of Fluid Mechanics* **224**, p. 77–90. doi:10.1017/S0022112091001659. 12
- UNITED NATIONS (2015) World Population Prospects: The 2015 Revision, World Population 2015 Wallchart. ST/ESA/SER.A/378. *Tech. Rep..* Department of Economic and Social Affairs, Population Division. 14
- WATERS, C.N., ZALASIEWICZ, J., SUMMERHAYES, C., BARNOSKY, A.D., POIRIER, C., GALUSZKA, A., CEARRETA, A., EDGEWORTH, M., ELLIS, E.C., ELLIS, M., JEANDEL, C., LEINFELDER, R., MCNEILL, J.R., RICHTER, D.D., STEFFEN, W., SYVITSKI, J., VIDAS, D., WAGREICH, M., WILLIAMS, M., ZHISHENG, A., GRINEVALD, J., ODADA, E., ORESKES, N. & WOLFE, A.P. (2016) The Anthropocene is functionally and stratigraphically distinct from the Holocene. *Science* **351** (6269). doi:10.1126/science.aad2622. 5
- WOOD, R.M. & BAUER, S.X.S. (2003) Simple and low-cost aerodynamic drag reduction devices for tractor-trailer trucks. In *SAE Technical Paper*. SAE International. doi:10.4271/2003-01-3377. 14

Real-time PIV using optical flow

This chapter introduces an original velocimetry method developed in the laboratory PMMH for five years. After detailing its algorithm functioning, the hardware and the software used are presented, especially their critical role in the frequency of the real-time measurements. The influence of different experimental and computational parameters on the quality of the instantaneous velocity fields is then investigated, using a backward-facing step flow as a benchmark.

2.1	Introduction	22
2.1.1	Velocimetry techniques	22
2.1.1.1	FFT-PIV and derivatives	22
2.1.1.2	PTV	23
2.1.2	Optical flow for PIV: the origin of good	24
2.2	Functioning	25
2.2.1	FOLKI method	25
2.2.1.1	Forward additive method	26
2.2.1.2	Inverse additive method	28
2.2.1.3	Symmetric additive method	28
2.2.1.4	Gaussian pyramid	29
2.2.2	Real-time computation	30
2.2.2.1	Camera-laser association	30
2.2.2.2	Graphic Processor Unit	33
2.2.2.3	LabVIEW program	33
2.3	Optimal parameters	35
2.3.1	BFS in the hydrodynamic channel	35
2.3.1.1	The separated shear layer and the reattachment region	36
2.3.1.2	The recirculation bubble	38
2.3.2	Influence of optical flow parameters	38
2.3.2.1	Interrogation window radius and particles density	39
2.3.2.2	The classic accuracy-speed compromise	40
2.4	Conclusions and perspectives	43
2.4.1	Future improvements	44

2.1 Introduction

2.1.1 Velocimetry techniques

Only optical techniques measuring a velocity field will be discussed in the present section. Even if local sensors like laser Doppler velocimetry or hot-wire have often better temporal resolution and enables to store less data, the different studies during this thesis require quantitative information on spatial structure only given by velocity fields. For each of the presented method in this section, the flow is seeded by small particles acting like tracers of the fluid movements.

2.1.1.1 FFT-PIV and derivates

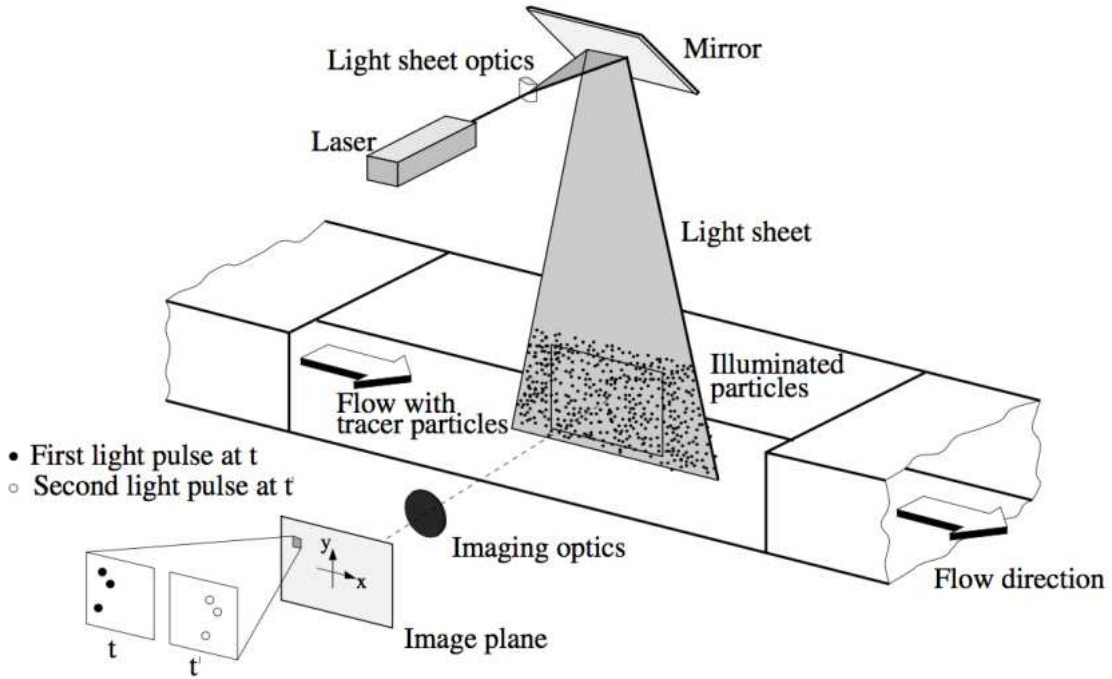


Figure 2.1 – Classic 2D-2C PIV setup and process (Raffel *et al.*, 2007).

Two-dimensional two-components (2D-2C) velocity fields have been commonly computed via the particle image velocimetry (PIV) technique for more than 30 years (Meynart, 1982). This technique is reviewed by Adrian (2005) and completely detailed by Raffel *et al.* (2007). Briefly, the principle consists in illuminating a plane with a laser sheet generated by a laser beam passing through a cylindrical lens to highlight only the particles, as shown in Figure 2.1. Two successive snapshots are recorded by a camera at time t and $t' = t + dt$. Each snapshot is then divided into sub-windows capturing an ensemble of particles. Each sub-window of the snapshot t is cross correlated with corresponding sub-windows of the snapshot t' . The resulting maximum peak in the correlation should correspond to the displacement (amplitude and direction) of the followed

group of particles.

Measurements accuracy requires optimized experimental conditions such as the optical devices (Kähler *et al.*, 2012), the size and the density of the particles (Keane & Adrian, 1990), and the interrogation window size (Foucaut *et al.*, 2004). The accuracy may be improved via advanced methods like the multiple pass interrogation combined with grid refining schemes (Scarano & Riethmuller, 1999), which shift the sub-windows and iteratively decrease their size. Even so, the accuracy is limited when dealing with flows including strong gradients and vorticities, especially turbulent flows. A solution consists in iteratively deforming the sub-windows using initial displacement estimations (Scarano, 2002), improving the cross correlation results by better following the particles.

To save post-processing time, the cross correlation is computed using a fast Fourier transform (FFT). Some advanced methods previously mentioned may even save more time for time-resolved images data set (Shi *et al.*, 2013). Depending on the sub-window definition and the snapshot size, computing one velocity field may take indeed from several seconds to a few minutes. When there are thousands images to process, this may result in days of calculation, depending on the computing power. When dealing with a few days experimental campaign, it becomes necessary to use large computing facilities.

More components and dimensions can be reach through derived PIV techniques. For example, for stereo-PIV it is necessary to add a second camera or even more (Fouras *et al.*, 2008) recording the same PIV plane at a different angle to compute the third component of the velocity field (2D-3C) via geometric reconstruction (Arroyo & Greated, 1991). Continuous improvements are applied to this method to compensate the various distortions introduced by the extra optical devices (Soloff *et al.*, 1997; Wieneke, 2005; Fouras *et al.*, 2007). Illuminating and recording a volume rather than a plane enables to reach the third spatial dimension of the velocity fields by decomposing the cross correlation function at different depths (Fouras *et al.*, 2009). The volumetric correlation PIV designation has been consequently given to this technique. Finally, 3D-3C velocity fields are computed either through holographic PIV (Barnhart *et al.*, 1994; Hinsch, 2002), or through volumetric three-component velocimetry (Pereira *et al.*, 2000, 2006), or through volumetric reconstruction of the particles distribution in tomographic PIV (tomoPIV) (Elsinga *et al.*, 2006).

2.1.1.2 PTV

Unlike the Eulerian approach of the PIV, particle tracking velocimetry (PTV) consists in tracking single particles between two or more successive images as illustrated by Figure 2.2. This Lagrangian technique requires low-seeding densities to distinguish each particle trajectory. Resulting in sparse estimation of flow displacements, the tracking can be realized either in 2D or in 3D (Dracos, 1996). The latter, similar to the tomoPIV technique, is limited in resolution by the low tracers density requirement (Maas *et al.*, 2009) but recent improvements have enhanced the 3D reconstructing particles Cornic *et al.* (2015).

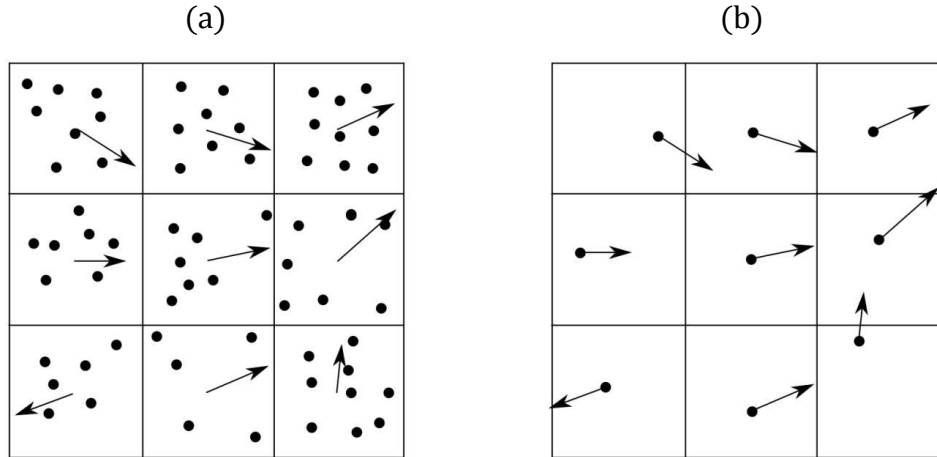


Figure 2.2 – Difference in particle density between (a) PIV and (b) PTV, from [Gautier \(2014\)](#).

2.1.2 Optical flow for PIV: the origin of good

Optical flow algorithms have been first introduced by [Horn & Schunck \(1981\)](#) in the computer science community for the challenging machine vision problem ([Fennema & Thompson, 1979](#)). The objective is to measure the visual displacement field by analysing any video sequence, which has been successfully achieved first by [Horn & Schunck \(1981\)](#) for synthetic images, and by [Fitzpatrick \(1988\)](#) for experimental snapshots. [Jara-Wilde *et al.* \(2015\)](#) recently reviewed the three existing optical flow approaches: the global one assuming that images have time-invariant total intensity ([Horn & Schunck, 1981](#)), the local one assuming a constant flow within a user-defined neighbourhood ([Lucas & Kanade, 1981](#)), and the last one combining the two previous methods ([Bruhn *et al.*, 2002](#)).

As an alternative to the FFT-PIV, a first optical flow algorithm has been specifically designed at the LIMSI¹ to process images intended for PIV ([Quénot *et al.*, 1998](#)) and even for sPIV recently ([Faure *et al.*, 2010](#); [Douay *et al.*, 2013](#)). Based on dynamic programming, this method computes iteratively the flow displacement over strips of the snapshots. At each iteration, the strips become thinner and switch between vertical and horizontal alignments. Another optical flow algorithm has also been optimized for PIV at the IRISA/INRIA² ([Corpetti *et al.*, 2006](#)). This one derives from the continuity equation and a second-order regularizer ([Corpetti *et al.*, 2002](#)). Even if both algorithms give dense velocity fields (one vector per pixel), it seems that their spatial resolution is not better than advanced FFT-PIV ([Stanislas *et al.*, 2008](#)) and their computation time is at least of the same order as standard FFT-PIV.

Following improvements in the displacement estimations of the local approach ([Le Besnerais & Champagnat, 2005](#)), [Champagnat *et al.* \(2011\)](#) proposed a fast optical flow algorithm dedicated to PIV application and detailed below. [Davoust *et al.* \(2012\)](#) and [Sartor *et al.* \(2012\)](#) used

1. Laboratoire d'informatique pour la mécanique et les sciences de l'ingénieur at Orsay (France).

2. Institut de recherche en informatique et systèmes aléatoires and Institut national de recherche en informatique et en automatique, both at Rennes (France).

this algorithm to fast post-process their snapshots for a turbulence jet flow study and for an investigation of the interaction between a shock wave and a turbulent boundary layer respectively. It shall be mentioned that optical flow applications in velocimetry via the local approach concerns also PTV, enabling a better accuracy in the near-wall measurements when properly tuning the algorithm settings (Miozzi, 2004; Miozzi *et al.*, 2008).

2.2 Functioning

The method used to compute the velocity fields in the following experiments is based on the Lukas-Kanade optical flow algorithm called FOLKI-GPU, implemented first at ONERA on a graphic processor unit (GPU) by Champagnat *et al.* (2011). The original code has been improved at the PMMH laboratory by Gautier (2014) and during the present thesis to satisfy experimental constraints due to the material (camera, laser) and the environment (water, air).

2.2.1 FOLKI method

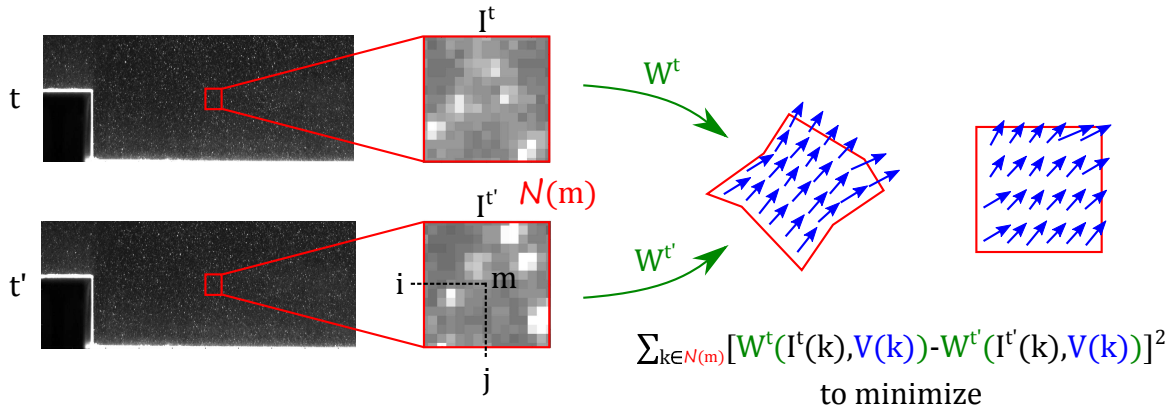


Figure 2.3 – Principle of the optical flow algorithm based on the local approach.

Feature	Optical flow	FFT-PIV
Matching criteria	minimize SSD	maximize cross correlation
Matching method	Gauss-Newton method	direct searching
Calculation mode	parallel matrixwise	sequential pointwise
Dense fields output	yes (1 vector/px)	no
Sub-pixel interpolation	at each pass	at final pass

Table 2.1 – Comparisons of the major features between optical flow and FFT-PIV, from Pan *et al.* (2015).

The FOLKI algorithm consists in estimating at each pixel m the intensity displacement which minimizes the sum of square differences (SSD) between the intensity over a warped interrogation

window (IW) centred in m at time t and the intensity over the warped IW at time $t' = t + dt$ as shown in [Figure 2.3](#). The iterative least-square Gauss-Newton method is particularly well suited to solve this minimization problem on condition of initializing the computation with a zero displacement. As real displacements are far from zero, the images resolution is deliberately degraded via a Gaussian pyramid reduction (see [Figure 2.6](#) later). This creates several copies of the original images with lower space resolutions, making the intensity displacements consequently reduced, close to zero. The iterative calculation is thus applied to the most reduced images (top of the pyramid) first. The resulting displacement is then used as the initial estimate at the higher resolution in the pyramid (lower level). The process is repeated until recovering the initial image resolution (base of the pyramid), giving thus the final displacement. [Table 2.1](#) compares the major features between this optical flow algorithm and FFT-PIV.

Like for PIV-FFT, a common pre-processing of the raw snapshots is required before applying the optical flow algorithm to eliminate the influence of illumination inhomogeneities ([Gautier & Aider, 2015](#)). The standard local equalization of the image intensity \tilde{I} is thereby obtained in each pixel $m(i, j)$ from the zero normalized sum of square differences (ZNSSD)

$$\tilde{I}(m) = \frac{I(m) - \bar{I}(m)}{\sqrt{\bar{I}^2(m) - \bar{I}^2(m)}}, \quad (2.1)$$

where $\bar{I}(m)$ is a local mean for a chosen radius of 5 pixels around m .

[Baker & Matthews \(2004\)](#) give a large summary of the different approaches used in optical flow to solve the displacement computation: the *compositional* and the *additive* algorithms. As the *additive* ones only are implemented in the present code, only these methods are described here.

2.2.1.1 Forward additive method

According to [Lucas & Kanade \(1981\)](#), the most direct method consists in, for each pixel m , looking for the best displacement $\mathbf{V}(m)$ minimizing the SSD between the intensity field around m taken at time t , denoted I^t , and the second one taken at time $t' = t + dt$, denoted $I^{t'}$, and shifted over $\mathbf{V}(m)$

$$\sum_{k \in \mathcal{N}(m)} (I^t(k) - I^{t'}(k + \mathbf{V}(m)))^2, \quad (2.2)$$

where $\mathcal{N}(m)$ is a square IW centred in pixel m and of side $2R_{IW} + 1$.

The Gauss-Newton iterative descent is typically designed to solve [Equation 2.2](#), $I^t(k) - I^{t'}(k + \mathbf{V}(m))$ being the residual. The estimated displacement at the iteration step i , $\mathbf{V}_i(m)$, is thus calculated such as $\mathbf{V}_i(m) \sim \mathbf{V}(m)$. [Le Besnerais & Champagnat \(2005\)](#) explain that $\mathbf{V}(m) \sim \mathbf{V}(k)$ can be assumed at each pixel k in the IW to ensure fast convergence. Referred as the constant constraint, this assumption leads to

$$\sum_{k \in \mathcal{N}(m)} (I^t(k) - I^{t'}(k + \mathbf{V}_i(k) + \mathbf{V}(m) - \mathbf{V}_i(k)))^2, \quad (2.3)$$

which enables a first-order expansion of Equation 2.3 around $k + \mathbf{V}_i(k)$, denoting $\Delta\mathbf{V}(k) = \mathbf{V}(m) - \mathbf{V}_i(k)$,

$$\sum_{k \in \mathcal{N}(m)} (I^t(k) - I^{t'}(k + \mathbf{V}_i(k)) - \nabla I^{t'}(k + \mathbf{V}_i(k))^T \Delta\mathbf{V}(k))^2. \quad (2.4)$$

As minimizing Equation 2.4 amounts to its partial derivative cancellation with respect to $\Delta\mathbf{V}(k)$, the equation to solve becomes

$$\sum_{k \in \mathcal{N}(m)} \nabla I^{t'}(k + \mathbf{V}_i) \cdot \nabla I^{t'}(k + \mathbf{V}_i)^T \Delta\mathbf{V} - \nabla I^{t'}(k + \mathbf{V}_i)(I^t(k) - I^{t'}(k + \mathbf{V}_i)) = \mathbf{0}, \quad (2.5)$$

where the k precision is dropped for $\mathbf{V}_i(k)$ and $\Delta\mathbf{V}(k)$ for convenience. The operator $\mathbf{H} = \sum_{k \in \mathcal{N}(m)} \nabla I^{t'}(k + \mathbf{V}_i) \cdot \nabla I^{t'}(k + \mathbf{V}_i)^T$ is defined as the Gauss-Newton approximation to the Hessian. Finally $\mathbf{V}(m)$ is recovered by replacing $\Delta\mathbf{V}$ in Equation 2.5

$$\mathbf{V}(m) = \mathbf{H}^{-1} \sum_{k \in \mathcal{N}(m)} \nabla I^{t'}(k + \mathbf{V}_i)(I^t(k) - I^{t'}(k + \mathbf{V}_i)) + \nabla I^{t'}(k + \mathbf{V}_i)^T \mathbf{V}_i. \quad (2.6)$$

The computed displacement $\mathbf{V}(m)$ will then be used as a better estimation $\mathbf{V}_{i+1}(m)$ at the next iteration until converging.

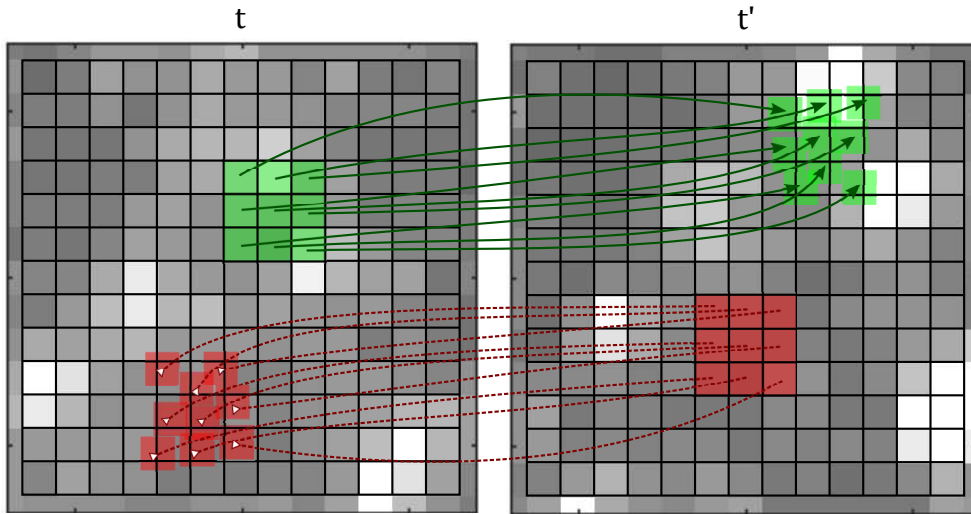


Figure 2.4 – Forward (green, solid, top) and inverse (red, dashed, bottom) additive warping illustrations for $R_{IW} = 1$.

The dependency of \mathbf{V}_i on k and not on m is crucial to replace the integration over the IW, $\sum_{k \in \mathcal{N}(m)}$, by a convolution over the entire snapshot, implying that the IW is warped instead of being shifted. Each warping value changes at each iteration until converging, avoiding especially image interpolations per pixel. Concretely it means that parallel computing is well suited to solve this minimization problem since each step of the iteration is simultaneously done for each pixel m . Figure 2.4 shows how pixels of the green IW are modified in the first snapshot t to match the second snapshot t' intensity at the best.

2.2.1.2 Inverse additive method

As H and $\nabla I^{t'}(k + \mathbf{V}_i)$ depend on \mathbf{V}_i in Equation 2.6, their values have to be computed at each iteration of the Gauss-Newton descent. In order to save computation time Baker & Matthews (2004) give another approach based on the works of Hager & Belhumeur (1998) and Bouguet (2001), consisting in warping the first snapshot I^t over $\Delta \mathbf{V}$ and the second one over \mathbf{V}_i

$$\sum_{k \in \mathcal{N}(m)} (I^t(k - \Delta \mathbf{V}) - I^{t'}(k + \mathbf{V}_i))^2. \quad (2.7)$$

Following the same steps as in the forward additive method and still assuming $\mathbf{V}(m) \sim \mathbf{V}_i(k)$ for $k \in \mathcal{N}(m)$, we finally obtain

$$\mathbf{V}(m) = \mathbf{H}^{-1} \sum_{k \in \mathcal{N}(m)} \nabla I^t(k) (I^t(k) - I^{t'}(k + \mathbf{V}_i) + \nabla I^t(k)^T \mathbf{V}_i), \quad (2.8)$$

where the Hessian is $\mathbf{H} = \sum_{k \in \mathcal{N}(m)} \nabla I^t(k) \cdot \nabla I^t(k)^T$. Now \mathbf{H} and $\nabla I^t(k)$ need to be computed only once. Compared to the previous method, the gradient of image at t' , $\nabla I^{t'}(k + \mathbf{V}_i)$, is here replaced by the gradient of image at time t , $\nabla I^t(k)$. With this method, the pixels in the IW of the second snapshot are warped to match the correct intensity of the first snapshots as illustrated in Figure 2.4 through the bottom red IW.

2.2.1.3 Symmetric additive method

Zhao & Sawhney (2002) and Averbuch & Keller (2004) propose the symmetric approach consisting of moving both IW by $\mathbf{V}(m)/2$. In this case the problem amounts to the minimization of

$$\sum_{k \in \mathcal{N}(m)} (I^t(k - \frac{\mathbf{V}(m)}{2}) - I^{t'}(k + \frac{\mathbf{V}(m)}{2}))^2. \quad (2.9)$$

Following the same steps as in the previous methods and denoting the average of the spatial intensity gradient between both snapshots as $\nabla \bar{I}(k) = \frac{1}{2}(\nabla I^t(k - \frac{\mathbf{V}_0}{2}) + \nabla I^{t'}(k + \frac{\mathbf{V}_0}{2}))$,

$$\mathbf{V}(m) = \mathbf{H}^{-1} \sum_{k \in \mathcal{N}(m)} \nabla \bar{I}(k) (I^t(k - \frac{\mathbf{V}_0}{2}) - I^{t'}(k + \frac{\mathbf{V}_0}{2}) + \nabla \bar{I}(k)^T \mathbf{V}_0). \quad (2.10)$$

The Hessian is $\mathbf{H} = \sum_{k \in \mathcal{N}(m)} \nabla \bar{I}(k) \cdot \nabla \bar{I}(k)^T$ and has to be computed at each iteration. An intermediate snapshot is obtained by warping snapshots t and t' .

Despite this supplementary computation, this is the chosen additive method for the present optical flow algorithm. It indeed gives the best accuracy while keeping acceptable time calculations as explained by Champagnat *et al.* (2011); Pan *et al.* (2015) and illustrated in Figure 2.5.

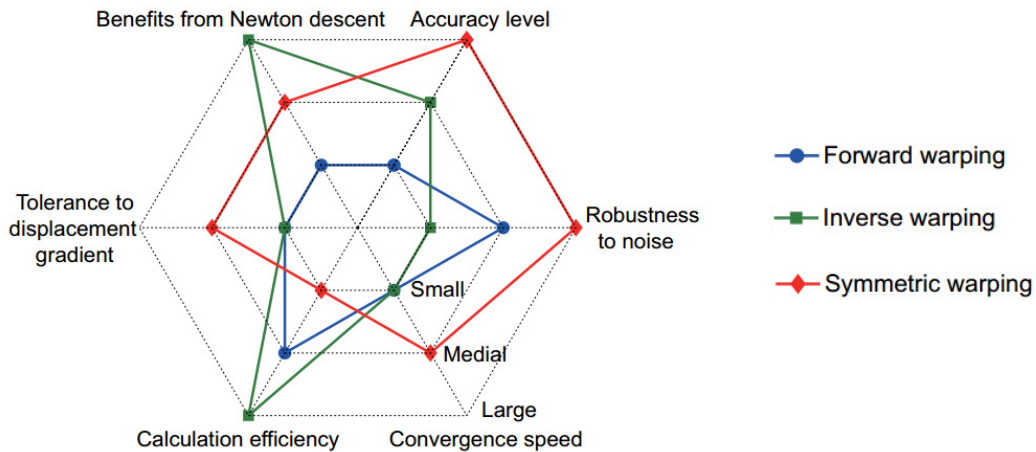


Figure 2.5 – Additive methods comparison from Pan *et al.* (2015).

2.2.1.4 Gaussian pyramid

Solving Equation 2.10 implies to properly initiate the iteration (step $i = 0$) and ensuring small displacement increment to validate the first-order expansion giving Equation 2.5. In order to enable the convenient estimation $\mathbf{V}_0 = \mathbf{0}$, the displacement inside the IW has to be as small as possible. Thus, before computing \mathbf{V} , a reduction of the snapshot is performed in the algorithm through a Gaussian pyramid reduction, the details of which are given by Burt & Adelson (1983).

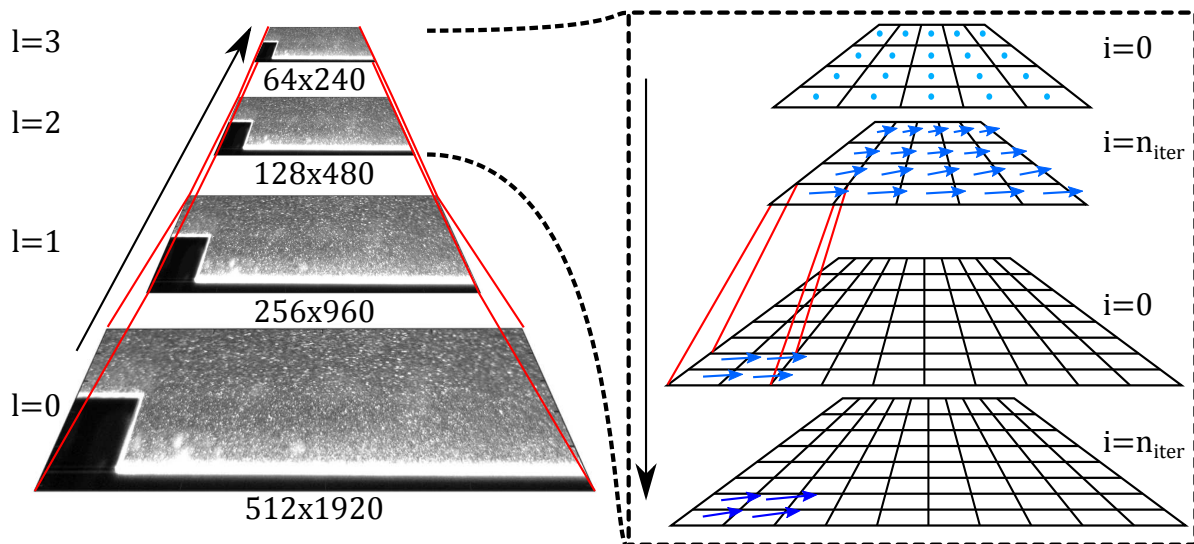


Figure 2.6 – Gaussian pyramid applied to a 1920×512 snapshot with $n_{level} = 3$ (left) and iterative computation of the displacement field for the two highest pyramid levels (right).

Introduced in the optical flow framework by Enkelmann (1988) and completely implemented by Bouguet (2001), this technique degrades the space resolution of a picture to reduce its dimension. It consists in locally smoothing distinct squares of four pixels into one pixel, which divides the

size of the entire snapshot by four. The process can be repeated to make far particles artificially close. This creates the successive levels l of a pyramid with the original snapshot as its base ($l = 0$) and the last transformed image as its top ($l = n_{level}$), as illustrated in Figure 2.6.

At each increase in the pyramid, the displacement at the level l becomes

$$\mathbf{V}^l = \mathbf{V}/2^l, \quad (2.11)$$

where \mathbf{V} is the original displacement. At each level l , the Gauss-Newton iteration starts from the displacement resulting from the previous level $\mathbf{V}_0^l = \mathbf{V}^{l+1}$. It then converges to the resulting displacement \mathbf{V}^l , which is subsequently used as the first guess of the lower level $l-1$: $\mathbf{V}^l = \mathbf{V}_0^{l-1}$. The last level $l = n_{level}$ has to be chosen such as $\max(\mathbf{V}^{n_{level}}) \sim 1 - 2$ px in order to obtain the proper initialization of the whole algorithm with $\mathbf{V}_0^{n_{level}} = \mathbf{0}$. The algorithm goes on until reaching the first level $j = 0$.

2.2.2 Real-time computation

As previously mentioned, FOLKI-GPU has been improved by Gautier & Aider (2015) to obtain *real-time*, meaning high frequency, computation of instantaneous experimental velocity fields. The interests of online computation are multiple:

1. Fast post-processing,
2. Parametric studies achievable,
3. Possibility to avoid storing large data sets of images,
4. Camera used as a non-intrusive sensor in a close-loop application.

The present thesis focuses mainly on the last point for its application on fully turbulent flows (chapter 7). Real-time PIV has already been reported for FFT-PIV by reducing the processed images (Siegel *et al.*, 2003; Willert *et al.*, 2010) or using Field-Programmable Gate Arrays (FPGA) (Yu *et al.*, 2006; Munoz *et al.*, 2009), up to 15 fps at $Re = 1.5 \times 10^4$. Nonetheless, these methods seem unable to provide dense data fields at higher Reynolds numbers.

The global data flow of the optical flow algorithm is summarized in Figure 2.7. It starts with the images readout: the camera sends the snapshots to the frame-grabber. These images are then stored in the random-access memory (RAM) before being copied in the GPU memory. The resulting velocity fields are finally delivered into the RAM. Outside the GPU, data are handled by the central processing unit (CPU). Images can be written from the RAM on a solid-state drive. This optional step is critical when dealing with large images. The camera and the GPU used in the different setups are detailed below. The management of the devices together with the optical flow algorithm is made possible through a LabVIEW program explained hereafter.

2.2.2.1 Camera-laser association

To reach high-speed computation of the instantaneous velocity fields, the camera must stream snapshots of intensity fields at high frequency to the RAM. Unfortunately, most of the cameras

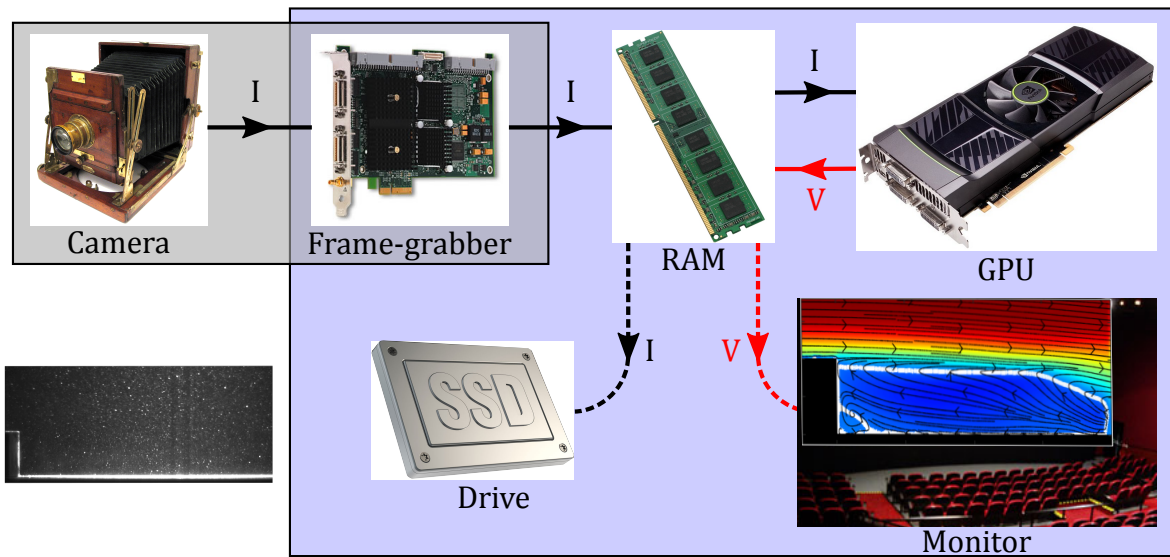


Figure 2.7 – Sketch of the data flow: I and V stand for Images and Velocity fields respectively. Dashed lines are optional data transfer.

made for PIV (inter-frame time, spatial resolution, sensitivity...) store the entire set of acquired images in an internal buffer before transferring them to the computer in one go. Capturing rapid flow dynamics requires indeed to quickly free the camera sensor and this is well done by adding directly rapid memory into the camera. Nevertheless, some cameras dedicated to velocimetry are able to stream and two configurations have been designed according to the facility where the flow is studied: a hydrodynamic channel or a wind tunnel.

Hydraulic configuration Regarding the velocities encountered in a water channel ($\sim 10 \text{ cm}\cdot\text{s}^{-1}$), the time exposure of the camera sensor is of the order of magnitude $\sim 1 \text{ ms}$. The plane to study is illuminated by a laser sheet created by the 8 W continuous laser *Genesis MX-6185* (Coherent, USA) operating at the wavelength 532 nm. The camera *acA 2000-340km* (Basler, Germany) records pictures of the illuminated particles [Figure 2.8(a)]. The sampling rate is thus related to the frame rate of the camera. An optical filter selecting only the laser frequency is mounted on the objective to reduce the light noise.

Aero configuration In wind tunnel facilities a common PIV setup is composed of a pulsed laser and a double-frame camera, both triggered by a synchronizer. Due to the higher velocities inside a wind tunnel ($\sim 10 \text{ m}\cdot\text{s}^{-1}$), the capture duration has to be shorter ($\sim 10 \text{ ns}$) to avoid the spread of the particles position. This requires to illuminate the particles with high energy laser pulses ($\sim 100 \text{ mJ}$) at two consecutive close moments separated by $\sim 10 \mu\text{s}$. Double-frame cameras are specifically manufactured to record two images so close in time, by working synchronously with the pulsed laser, as illustrated by Figure 2.8(b). For other cameras, the frame straddling method enables also to capture two snapshots in a similar way but this requires a very high frame rate capability. Already available, the double-frame camera *PowerView Plus 4MP* (TSI, USA) has

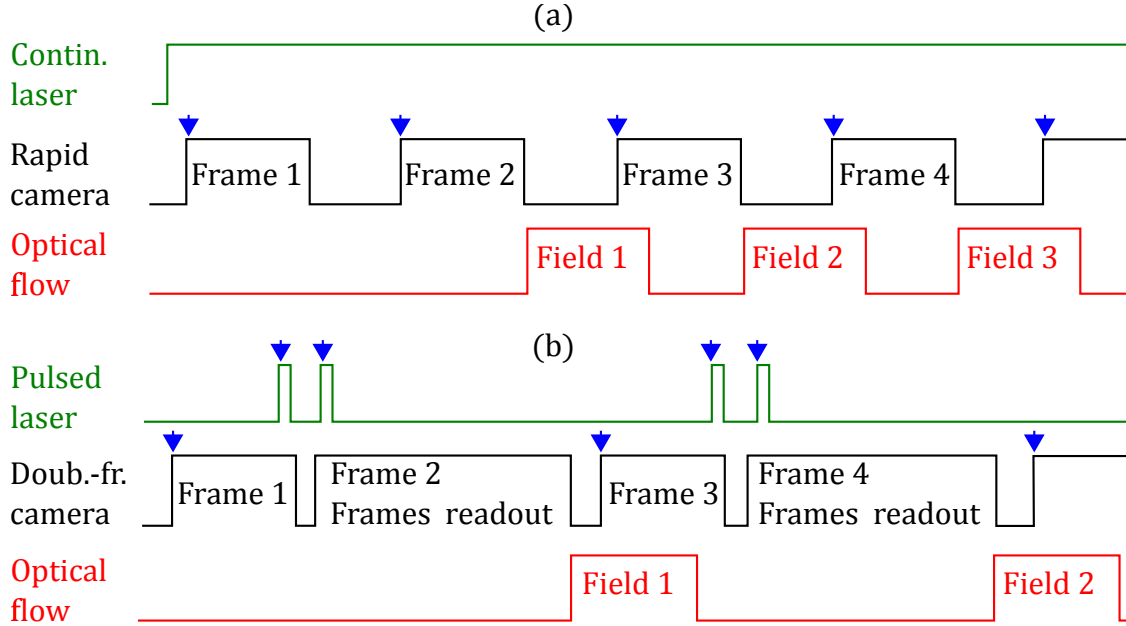


Figure 2.8 – Standard sequence diagrams for (a) the hydro configuration and (b) the aero configuration. Blue arrows shows the triggered processes.

been synchronized to the 200 mJ double-cavity pulsed (15 Hz) YaG laser *Twins BSL* (Quantel, France & USA) by programming a *NI-9402* digital module (National Instruments, USA) linked to both devices via Bayonet Neill–Concelman (BNC) connectors. In this configuration, the sampling rate is consequently defined by setting the laser pulses frequency.

The main advantage of the hydraulic setup is the possibility to process successive images one by one, leading to a computing speed equal to the snapshots acquisition frequency. In contrast, the velocity fields computation for the aero configuration is limited to half of the double-frame camera speed. The characteristics of the used cameras and the sizes of the recorded snapshots are summarized in [Table 2.2](#). The dimensions and the bit precision determine the size of the images. In the present case the TSI camera generates heavy data comparing to the Basler one³. For both configurations, images are then transferred to the frame-grabber device *NI PCIe-1433* (National Instruments, USA) through Camera Link (CL) cables (510 to 600 Mb.s⁻¹).

Cameras	Resolution ($W(\text{px}) \times H(\text{px})$)	Frame rate (Hz)	Size (Mb)
acA2000-340km (Basler)	1920 × 512	340	7.7 (8-bit PNG)
PowerPlus 4MP (TSI)	2048 × 2048	15	65.7 (16-bit PNG)

Table 2.2 – Cameras characteristics.

3. It was impossible to modify the bit depth of the TSI camera via LabVIEW due to an unresolved miscommunication between the device and the software despite the help of Illunis and National Instruments engineers as explained hereafter.

2.2.2.2 Graphic Processor Unit

Optical flow algorithms are particularly well suited to be implemented on a GPU due to their highly parallel computation as demonstrated by Marzat *et al.* (2009). They indeed computed $640 \text{ px} \times 480 \text{ px}$ intensity displacement fields at 15 Hz by coding an algorithm as the one presented hereinbefore. The emergence of accessible programming-language dedicated to the GPU, such as the Compute Unified Device Architecture (CUDA) from NVIDIA corporation (NVIDIA, 2017) and OpenCL, was a crucial step to improve and facilitate parallel and, consequently, real-time computation.

The first operating real-time PIV setup in the laboratory has been installed by Gautier (2014). Using CUDA language, the optical flow and the ZNSSD pre-processing have been implemented on the GPU of a *GeForce GTX 580* (NVIDIA, USA), a simple precision graphics card with 520 processing cores clocked at 800 Mhz (NVIDIA, 2010). The graphic card has been upgraded into a *GeForce GTX 1070* (1920 cores at 1683 Hz) for the most recent experiments (see the perspectives of the chapter 7).

2.2.2.3 LabVIEW program

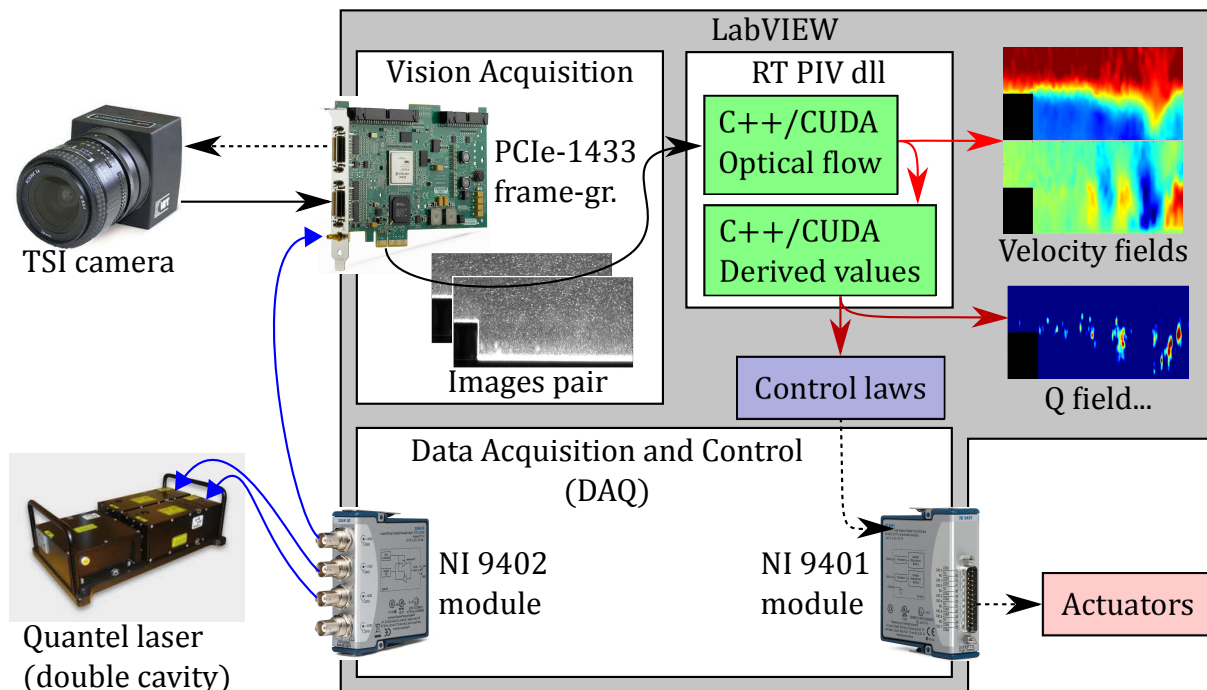


Figure 2.9 – Sketch of the LabVIEW program organization regarding the different devices related to in the aero configuration. Blue arrows are trig (TTL) signals, dashed black arrows are command signals, solid black arrows are images data, light red arrows are velocity fields and dark red arrow is the set of values derived from the velocity (introduced in the next chapter, a Q-criterion is given as an example).

A homemade LabVIEW (National Instruments, USA) interface has been continuously developed since 2012 to properly manage the hardware, together with the optical flow algorithm, as sketched in Figure 2.9. Choosing to write a LabVIEW software comes from the facility to set the cameras via the NI frame-grabber, to implement user C++ dynamic-link libraries (dll), and to drive various actuators (chapter 4 and chapter 7) via NI modules.

In addition to a software development kit, most of the camera manufacturers, especially Basler here, provide a peculiar file for LabVIEW programming (.icd extension) including serial commands and timing control specific to their cameras. This allows to directly command the camera through LabVIEW language. For instance, it has been possible to set the frame rate by triggering the camera via the *NI-9402* digital module. Unfortunately, this file did not exist for the TSI camera, which turned out to be in fact the *RMV4022* model formerly manufactured by Illunis (USA). The serial commands list available in the user manual and exchanges with Illunis engineers enabled finally to write the missing .icd file. It is noteworthy that only the last version of this camera model (post-2014) can correctly interpret the serial commands.

The program has been consequently adapted to the aero configuration by activating the double-frame mode and by sending TTL signals from the digital module to the frame-grabber device and to the double cavity laser [Figure 2.8(b)]. The frame-grabber transmits the trig signal to the camera. The only required setting regarding the camera is the exposure time of the first frame since the second frame is exposed during the entire readout step. One TTL signal corresponds thus to a images pair. Two other successive TTL signals are separately sent to each head laser to trig the pulses, such as the first pulse occurs just before the end of the first exposure and the second pulse occurs at the beginning of the second exposure. The delay between the two pulses is therefore the main setting concerning the laser, the duration of a pulse being ~ 10 ns.

The first version of the optical flow algorithm had been briefly provided by A. Plyer⁴. Improved by N. Gautier, the entire code is included in a C++ dll file, called RT PIV in Figure 2.9, composed of CUDA v5 and C++ functions. C++ functions concern the CPU activity, while the CUDA ones concern the GPU. In the LabVIEW program the snapshots are easily managed to feed these functions by pair to obtain velocity fields as well as their derived values (chapter 3). These values are used in control laws to command actuators through the *NI-9401* digital module. During the present thesis the code has been updated, taking partly advantage of the new CUDA v8 functions and libraries. The management of data transfer between the CPU memory and the GPU memory benefits particularly from this update, using the *cuBLAS* library, well designed for matrices manipulations, and the *Thrust* library for integral computation. A new instantaneous value detailed in the next chapter is even monitored thanks to the *cuFFT* library, dedicated to the fast Fourier transform computations.

4. Former PhD student (2008-2012) and research engineer since 2012 at ONERA.

2.3 Optimal parameters

As rigorously demonstrated by [Champagnat *et al.* \(2011\)](#); [Gautier & Aider \(2015\)](#) and [Pan *et al.* \(2015\)](#) for different flow configurations, the optical flow algorithm is efficient to compute accurate velocity fields if its parameters like the IW radius R_{IW} , the pyramid level n_{level} and the number of iteration n_{iter} are well tuned. The particle density has also to be properly determined as it will be explained. To determine these settings, we investigated (A. Giannopoulos' internship) a well known geometry: the backward-facing step (BFS). It is noteworthy that comparing optical flow PIV to the FFT-PIV through synthetic ([Pan *et al.*, 2015](#)) and experimental ([Champagnat *et al.*, 2011](#)) data processing has already given recipes to obtain high accuracy. The purpose here is to well calibrate the images processing for a real-time application.

2.3.1 BFS in the hydrodynamic channel

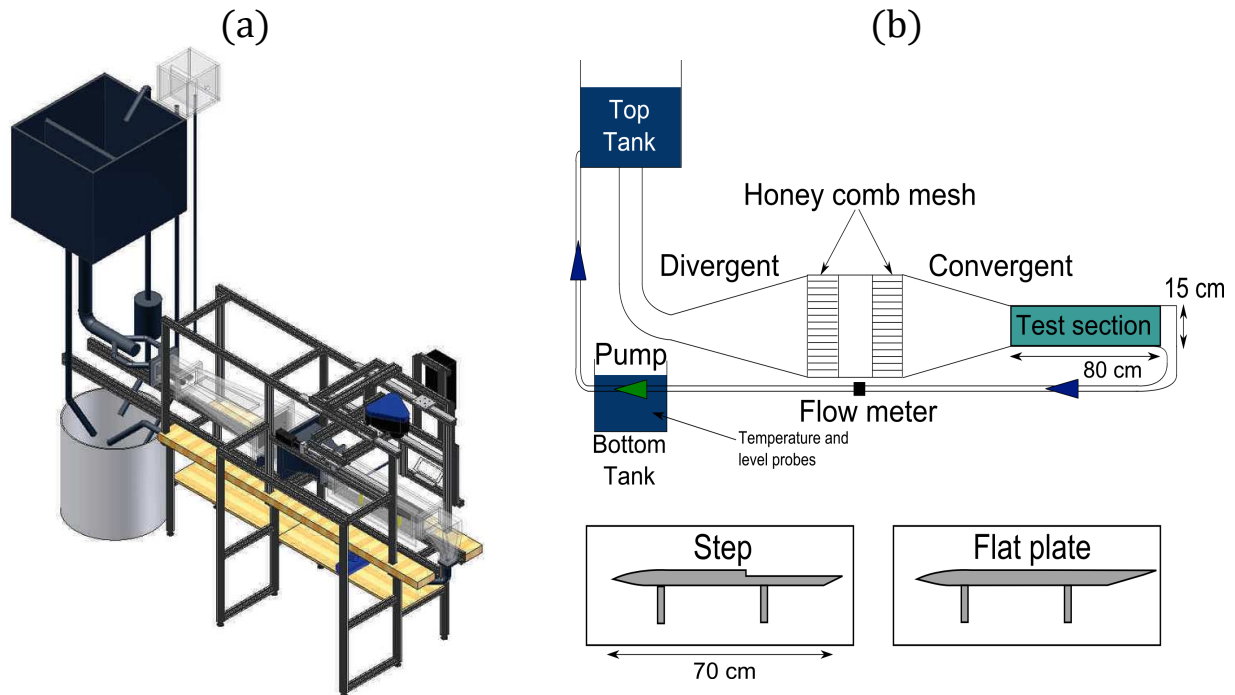


Figure 2.10 – (a) CAD sketch and (b) diagram of the hydrodynamic channel at the PMMH laboratory, from [Cambonie \(2012\)](#) and [Gautier \(2014\)](#) respectively.

Experiments takes place at PMMH in the closed hydraulic channel detailed in [Figure 2.10](#). The flow is driven by gravity and the water is continuously pumped from a bottom tank to a top one. A divergent and a convergent sections, separated by honeycombs, stabilize the flow in the test section in order to ensure laminar profile and avoid undesired disturbances upstream. The test section is 80 cm long and 15 cm wide. A NACA 00020 profile is used to smoothly start the boundary layer, growing along a flat-plate before reaching the BFS 33.5 cm downstream of the leading edge.

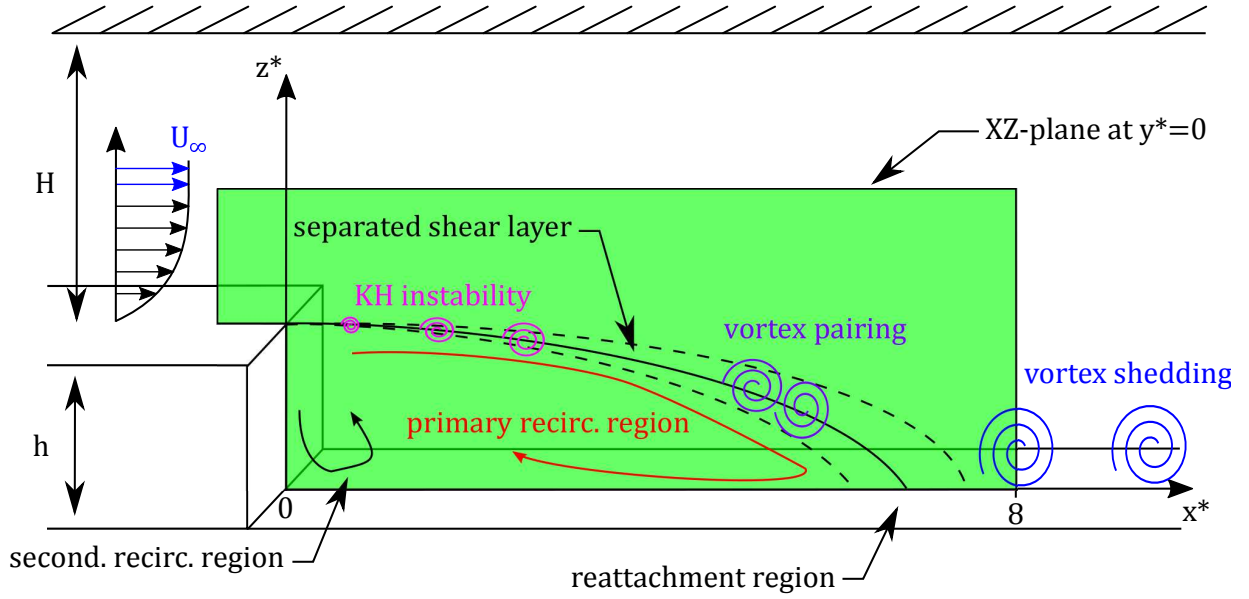


Figure 2.11 – BFS flow sketch and PIV plane, inspired from Spazzini *et al.* (2001).

The BFS is a simple 2D geometry to study the complexity of the separated flows (Armaly *et al.*, 1983) since it has a fixed separation point and the generated disturbances do not perturb its wake. The main characteristic of a step is naturally its height h , defining the expansion ratio

$$E = \frac{H}{H + h}, \quad (2.12)$$

where H is the channel height upstream of the BFS. In the presented experiments, $H = 7$ cm and $h = 1.5$ cm, giving $E = 0.82$. The Reynolds number is classically based on the BFS height

$$Re_h = \frac{U_\infty h}{\nu}, \quad (2.13)$$

where the free stream velocity U_∞ goes from 1.4 to 22 $\text{cm}\cdot\text{s}^{-1}$. The maximum turbulence intensity measured for the presented runs at the step before the separation is $T_u = 1.2\%$. Nondimensionalization is applied to the spatial variables such as $x^* = x/h$ and $z^* = z/h$.

The vertical symmetry XZ-plane is investigated as illustrated in Figure 2.11. A very thin layer of the fluorescent paint *FP Rhodamine 6G* has been applied on the surfaces illuminated by the laser sheet to reduce the reflections and thus to avoid near-wall miscalculations. Following experimental fields obtained via optical flow will be compared to visualizations made at the PMMH laboratory in 2010, shown in Figure 2.12. Three main interdependent regions can be defined: the shear layer, the recirculation bubble and the reattachment region.

2.3.1.1 The separated shear layer and the reattachment region

Because of the geometry, the primary separation point is located at the top of the step edge, introducing a local discontinuity of the velocity. As the velocity has to be continuous downstream

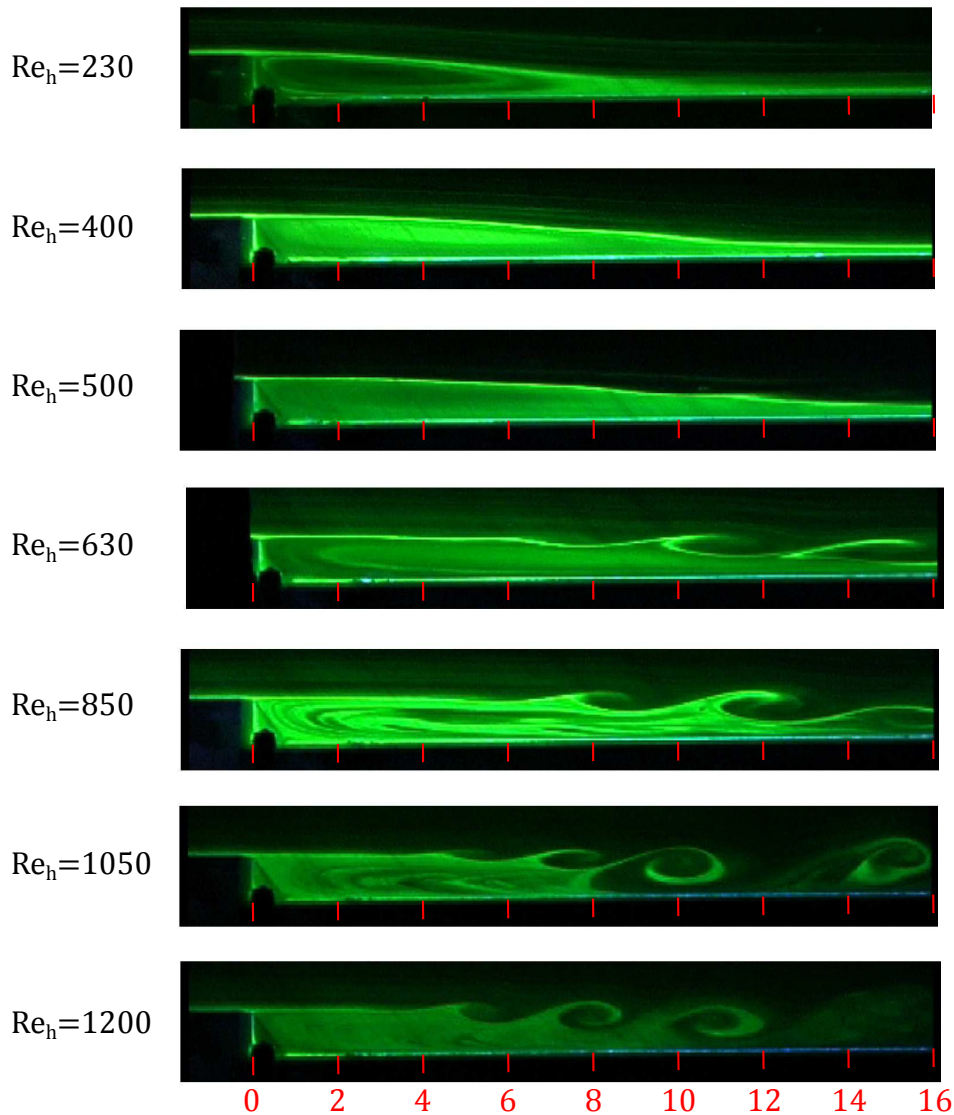


Figure 2.12 – BFS flow visualized with fluorescent dye at different Reynolds numbers: $230 \leq Re_h \leq 1200$.

of this point, a necessary strong vorticity sheet exists between the free stream above and the recirculation regions below. It is called the free shear layer and develops coherent structures - the shedding vortices - which are the results of two processes: the roll-up and the vortices pairing (Winant & Browand, 1974).

The roll-up process explains how vortices appear. Along the shear layer, the strong vorticity increases certain small wavy perturbations which becomes vortices. Thanks to the linearized stability theory applied to a hyperbolic-tangent velocity profile representing the shear layer, Michalke (1964) demonstrates that the disturbances having their wave length higher than the shear layer size are amplified. This unsteady phenomenon is known as the Kelvin-Helmholtz (KH) instability and it is sensitive to the upstream condition (Aider *et al.*, 2007). According to Troutt

et al. (1984), the growth rate of the shear layer depends directly on the vortex pairing process, which gives birth to larger vortices shed downstream of the region where the flow reattaches. These structures make the shear layer transit from 2D to 3D dynamics, whereas the not paired part of the small-scale structures feed the recirculation bubble (Bradshaw & Wong, 1972).

For low expansion ratio and $Re_h < 200$, an instability above the reattachment point has been numerically highlighted by Beaudoin *et al.* (2004) as the origin of stationary large-scale streamwise longitudinal vortices which are experimentally observed downstream of the BFS. They demonstrate that the radius of the local streamlines curvature (Sipp & Jacquin, 2000) can actually makes the pressure across the boundary layer varying, triggering this so-called Görtler (or centrifugal) instability. This kind of structures is typically observed for boundary layer on concave walls.

2.3.1.2 The recirculation bubble

The entire separated region forms the recirculation bubble downward of the BFS. The mean recirculation area (Gautier & Aider, 2013), as well as the mean recirculation length (Thangam & Knight, 1989), is related to the Reynolds number. They both increase until a maximum at $Re_h \simeq 600$ and then decrease before reaching a quasi-plateau from $Re_h \simeq 2100$.

The recirculation bubble is also subject to the flapping motion, an instability whose frequency is one order of magnitude lower than the shedding frequency. A secondary recirculation region takes place downstream of the step edge and upstream of a secondary separation point. Its dynamics are highly detailed by Spazzini *et al.* (2001), explaining that this region is the seat of quasi-periodic events of intense activity whose frequency corresponds to the flapping one. A typical cyclic activity is the growth of the secondary recirculation bubble until its size reaches the same order of magnitude of the step height and then collapses. The flapping motion together with the Kelvin-Helmholtz instability produce the oscillation of the reattachment line (Dejoan & Leschziner, 2004).

2.3.2 Influence of optical flow parameters

First, the particles density and the IW radius are investigated together since their are related to each other regarding the displacement accuracy. Then, the number of iterations and the pyramid level are chosen as a compromise between accuracy performance and computation time. For each experiment, the flow is seeded with 20 μm neutrally buoyant polyamid particles (Dantec Dynamics, Denmark). The different parameters have been set for various Reynolds numbers. When instantaneous fields are used, the presented observations are based on several of these fields, even if only one is displayed for succinctness reason.

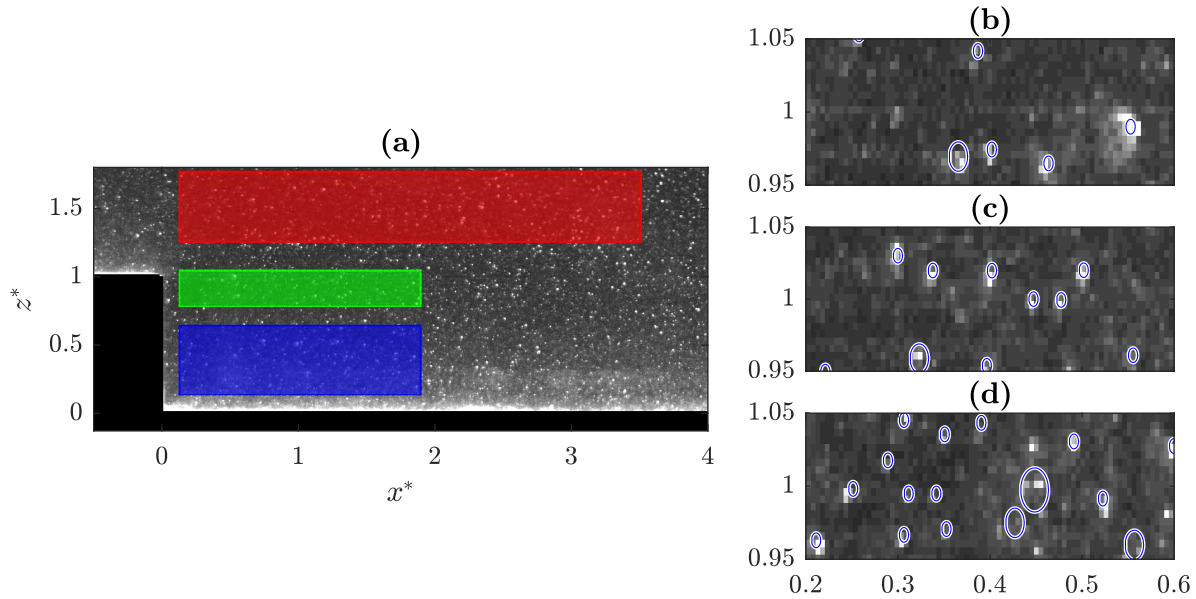


Figure 2.13 – (a) Positions of the different ROIs in the PIV window for the particles detection: the free stream (red rectangle), the shear layer (green rectangle) and the recirculation area (blue rectangle). Detection of the particles in an enlarged region inside the shear layer for different particles concentrations ($\times 10^{-2}$ ppp): (b) 1.1, (c) 1.7 and (d) 2.2.

2.3.2.1 Interrogation window radius and particles density

According to Pan *et al.* (2015) three factors must be taken into account to properly set the IW radius R_{IW} : the number of particles inside the IW d_p , the spatial averaging effect and the constant constraint. To estimate the particles density, the MATLAB *imfindcircles* function based on the circular Hough transform is used to identify the particles. Six different concentrations are studied at $Re_h = 820$. For each one, the averaged number of particles per pixel (ppp) is estimated by counting them in 600 snapshots. The calculation is done in the entire PIV window, as well as in three different regions of interest (ROIs) represented in Figure 2.13(a): the free stream, the shear layer and the recirculation area. The detection algorithm is illustrated in Figure 2.13(b-d) for increasing concentrations. Even if the algorithm seems to miss few particles due to the noise in all cases, particles in the laser sheet are globally well detected. The estimated values will consequently slightly underestimate the real number of particles.

Entire PIV window	1.1	1.4	1.7	1.9	2.1	2.2
Free stream ROI	1.0	1.3	1.6	1.7	1.9	2.1
Shear layer ROI	1.2	1.4	1.7	1.8	2.0	2.1
Recirculation ROI	1.6	2.0	2.5	2.7	3.0	3.4

Table 2.3 – Concentration of particles ($\times 10^{-2}$ ppp) in different ROIs of the PIV window.

Table 2.3 summarizes the results with a low dispersion ($\sim 0.05 \times 10^{-2}$ ppp). As expected the

recirculation area concentrates more particles than the shear layer, having itself more tracers than the free stream. The large difference between the concentration in the recirculation ROI and the other ones is also due to the noise, which is more important near the wall. The values for the entire PIV window will be considered for the next calculations.

The IW setting is evaluated for the fifth data set at $Re_h = 820$ by regarding the optical density d_p , the number of particles inside an IW. The IW radius is investigated for $R_{IW} \in \{7, 11, 15, 19, 23, 27\}$, the other optical flow parameters being fixed at $n_{iter} = 5$ and $n_{level} = 3$, following previous recommendations (Champagnat *et al.*, 2011; Gautier, 2014). These IW settings correspond to $d_p \in \{4.6, 11, 20, 31, 45, 62\}$ respectively. The resulting instantaneous and time-averaged fields are compared to the flow observed for close Reynolds numbers in Figure 2.12). The mean profiles converge past 300 velocity fields and are computed for 600 ones.

Figure 2.14 display one instantaneous and the time-averaged velocity fields. It is stressed that the instantaneous fields are computed from the same snapshots pairs. The recirculation length and vortex shedding are expected to be around $L_{rec}^* \simeq 7$ for this Reynolds number. The former is only obtained for $d_p = \{11, 20\}$ [Figure 2.14(c-f)], while the latter is visible for $d_p = \{4.6, 11, 20, 31\}$ [Figure 2.14(a,c,e,g)]. It clearly appears that increasing the IW radius smooth the fields. This effect is amplified in the recirculation area since the particles concentration is here the most important. It may lead to make the constraint displacement assumption wrong near the reattachment region [Figure 2.14(g-l)]. Due to the simultaneous computation of the displacement in each pixel, such errors are propagated far from their origin. In the shear layer, this even suppresses a real vortex [Figure 2.14(i) and (k)]. For too low radius, the SSD minimization score seems to be insufficient to compute the free stream velocities [Figure 2.14(a) and (b)].

For the zone including low velocity gradient, the more the particles are inside the IW the more accurately \mathbf{V} can be computed, avoiding bias induced by noise. Nevertheless there is a saturation effect which makes number of particles larger than a threshold no more efficient. If R_{IW} is even too large, the spatial averaging effect misrepresents the regions of strong vorticity as seen previously. This is due to the validity of the constant constraint assumption made to get Equation 2.4, according to Pan *et al.* (2015) who state that this assumption holds only if $\max(\nabla \mathbf{V}) < 1$ (in px/px), limiting the size of the IW. The IW radius and the density are fixed to $R_{IW} \simeq 10$ px and $d_p \sim 15$ in the next measurements made during the thesis. These settings are in good agreement with Champagnat *et al.* (2011).

2.3.2.2 The classic accuracy-speed compromise

Using the previously determined IW radius and particles density, the minimum number of iterations n_{iter} is now investigated for the BFS flow, fixing $n_{level} = 3$. Figure 2.15 shows that the instantaneous velocity fields are not converged yet for $n_{iter} < 5$ even though the global flow seems to correspond to the visualization in Figure 2.12. Figure 2.15(a) shows that the displacements near the wall and the borders are more difficult to compute accurately. Only small differences appear between the computed fields for $n_{iter} \geq 5$. To avoid useless computations and loss in calculation efficiency, the number of iterations will be therefore fixed to $n_{iter} = 5$ for the following

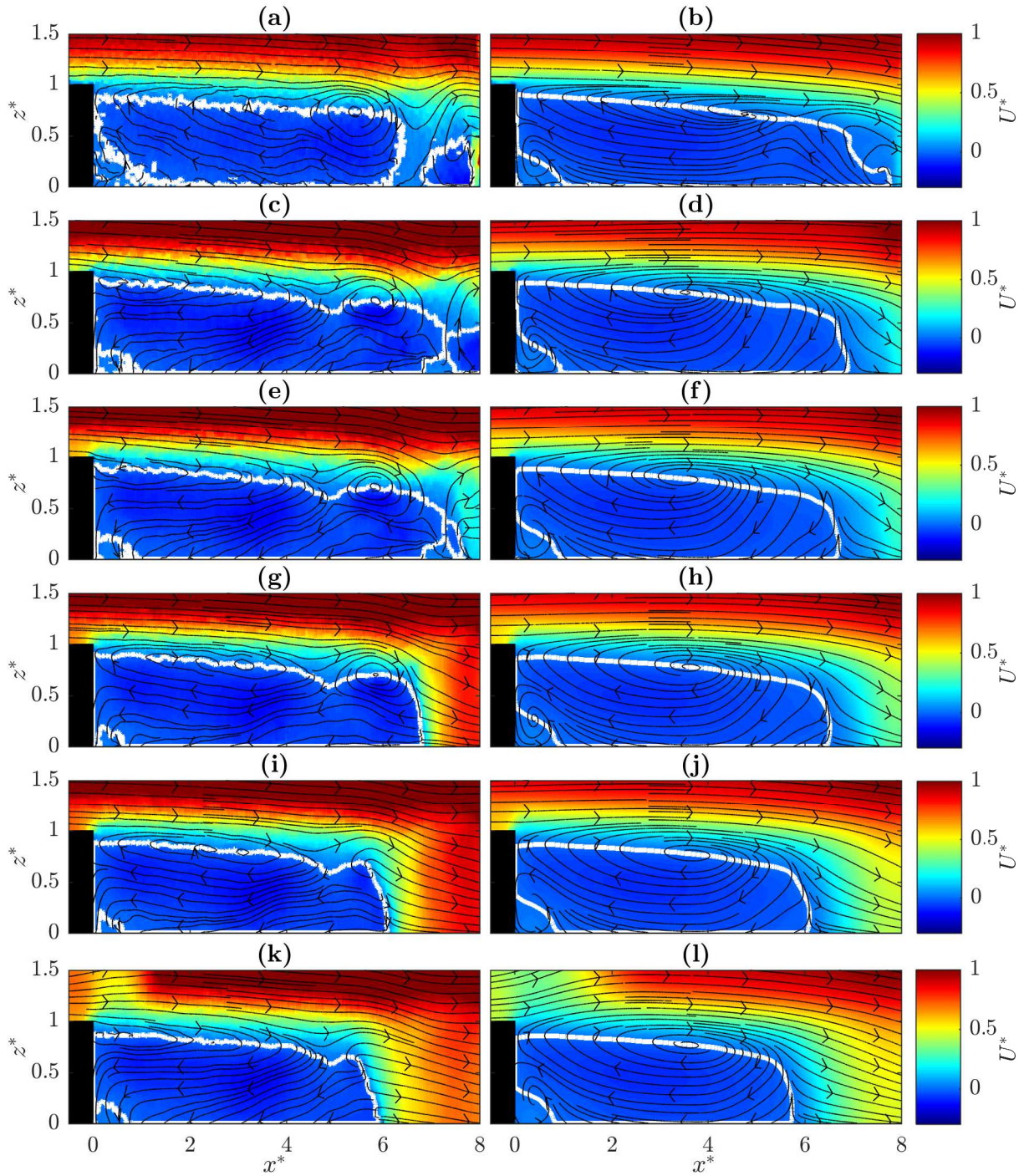


Figure 2.14 – Instantaneous (left) and mean (right) streamwise component of the velocity at $Re_h = 820$, together with the separatrix (white), computed with (a,b) $R_{IW} = 7$ px, (c,d) $R_{IW} = 11$ px, (e-f) $R_{IW} = 15$ px, (g,h) $R_{IW} = 19$ px, (i,j) $R_{IW} = 23$ px, and (k,l) $R_{IW} = 27$ px.

experiments.

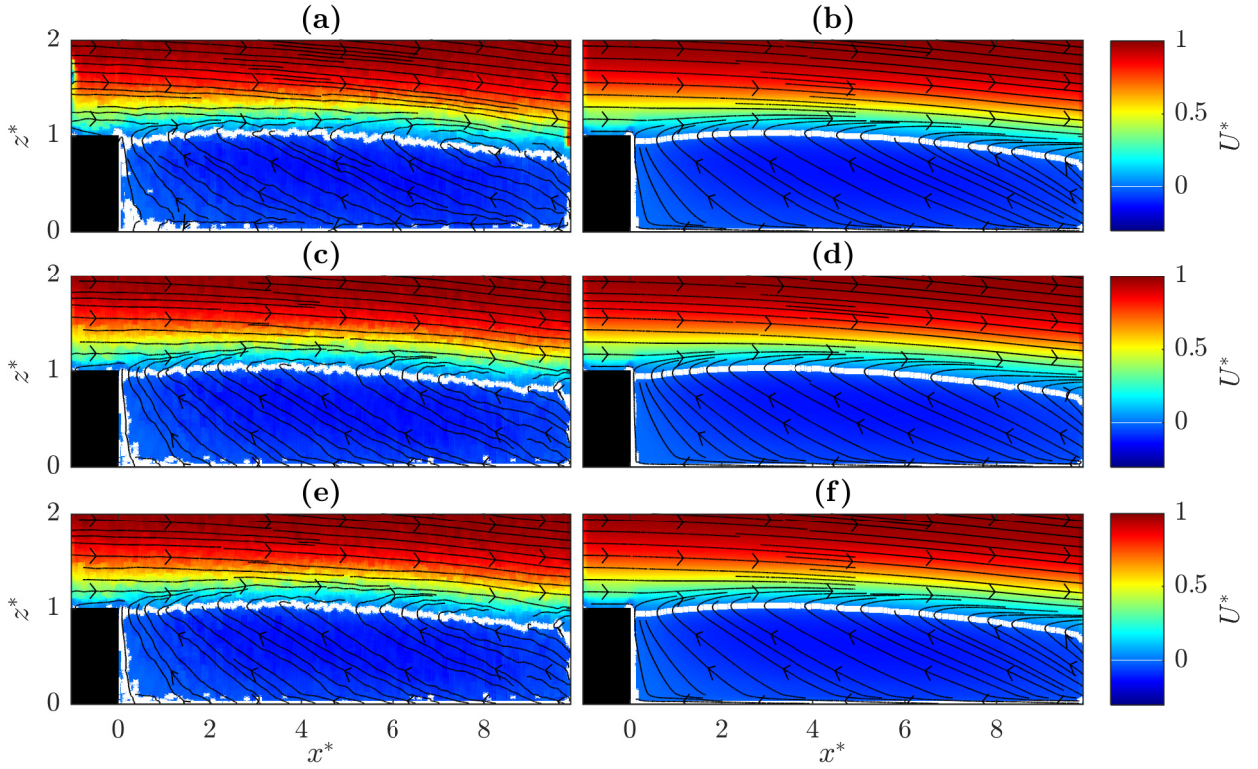


Figure 2.15 – Instantaneous (left) and mean (right) streamwise component of the velocity at $Re_h = 360$, together with the separatrix (white), computed with (a,b) $n_{iter} = 3$, (c,d) $n_{iter} = 5$, and (e-f) $n_{iter} = 7$.

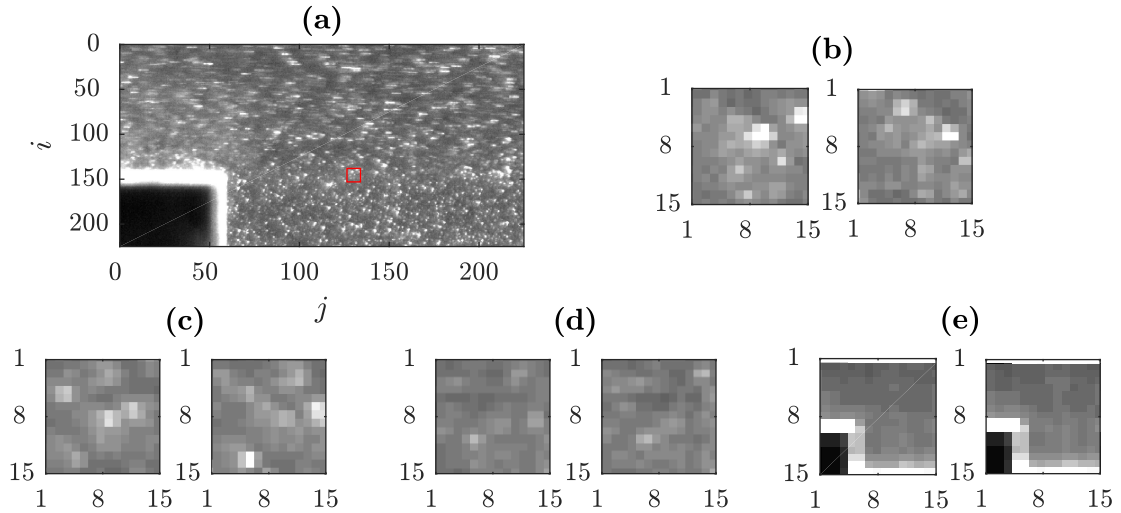


Figure 2.16 – (a) Instantaneous snapshot at $Re_h = 981$, together with an IW (red square) and its corresponding contents at time (b) t and $t + dt$. Contents for the same IW after (c) $n_{level} = 1$, (d) $n_{level} = 3$ and (e) $n_{level} = 5$.

As explained previously, the level of the image reduction pyramid n_{level} is crucial for the gradient

descent computation since it determines the initial guess $\mathbf{V}_0 = \mathbf{0}$. An original displacement \mathbf{V} is reduced to $\mathbf{V}/2^{n_{level}}$ after n_{level} . Figure 2.16(c-e) display the resulting IWs of two successive snapshots located in Figure 2.16(a) for different levels compared to the original ones [Figure 2.16(b)]. For $n_{level} = 1$, the intensity differences between the two IWs are still too important, whereas they enable to obtain $\mathbf{V}_0 = \mathbf{0}$ from $n_{level} = 3$. Beyond this level the reduction in size of the snapshot is too important and the real displacements are completely lost. The pyramid level has thus to be chosen regarding the sensor size as well as the free stream. As 8-10 px is often the aimed maximal displacement between two successive snapshots in PIV by setting the proper time delay between the two laser pulses (aero) or the camera frequency acquisition (hydro), $n_{level} = 3$ is particularly recommended (Champagnat *et al.*, 2011; Gautier & Aider, 2015).

n_{iter}	1	2	3	4	5	6	7	8
n_{level}								
2	32.3	50.0	45.5	45.5	43.5	37.0	34.5	25.0
3	31.3	31.3	30.3	41.7	38.5	34.5	32.3	23.4
4	52.6	50.0	43.5	40.0	37.0	34.5	32.3	29.4

Table 2.4 – Averaged fields per second (FPS) reached to compute 1920×512 velocity fields *offline*.

The performances of the optical flow algorithm are evaluated for different combinations of the optical flow parameters, the IW radius being still fixed, by computing 1000 velocity fields offline from $1920 \text{ px} \times 512 \text{ px}$ 8-bit PNG written on an internal solid-state drive, operating a $4 \times Xeon E5-1607 3.00 \text{ GHz}$ (Intel, USA) and the *GeForce GTX 1070*. The maximal displacements between the successive snapshots constituting the data set are around 8.5 px. The results are summarized in Table 2.4. Only the velocity fields obtained for $[n_{iter} = 1, n_{level} = 2]$ seem incorrectly computed, giving maximal displacements lower than 5.5 px. It appears that 50 velocity fields per second (FPS) can be accurately processed offline. Similar calculations have been done for $2048 \text{ px} \times 2048 \text{ px}$ 16-bit PNG, leading to 7.5 FPS. This rate is also obtained in real-time (chapter 5 and chapter 7). Relating to Table 2.2, this reveals that the optimum FPS is reached for the aero configuration. These speeds represent $0.02 \mu\text{s}/\text{vector}$ and $0.03 \mu\text{s}/\text{vector}$ respectively, which is in good agreement with previous measurements made for *online* computation of smaller 8-bit snapshots (Gautier & Aider, 2015). It shall be mention that images are read from the drive through SATA III technology (4800 Mb.s^{-1} , 8 times faster than CL) for the offline evaluation.

2.4 Conclusions and perspectives

A new PIV method, based on an optical flow algorithm using a local approach, has been successfully implemented on different GPUs using CUDA language. This method allows rapid calculation of dense and accurate velocity fields from 4MP images. It is embedded in a homemade LabVIEW program which handles the devices involved in the PIV and in flow control. Extra CUDA functions allow also to very fast compute values derived from the velocity as detailed in chapter 3. This program is now operational for a hydrodynamic channel as well as for a large wind tunnel.

Regarding the material requirement, most of the set-up already installed for 2D-2C FFT-PIV in wind tunnel may be directly used with the LabVIEW program, making the optical flow technique affordable for research facilities. Nevertheless, the main current constraint for the hardware is related to the camera and the frame-grabber, which have to be compliant with the LabVIEW environment.

Even if the velocity fields obtained thanks to the optical flow algorithm have their spatial resolution tied to the size of the IW such as for advanced PIV algorithms, they are dense (one vector per pixel), giving not only better results in the vicinity of edges and obstacles but also smoother fields. To achieve such results, the algorithm parameters have to be properly set regarding the optical devices and the experimental conditions. The IW radius will thereby depend both on the tracers density and on the free stream velocity which is mainly fixed via the inter-frames time the camera can reach. The Gaussian pyramid level will depend on the free stream velocity only, being cautious regarding the obstacles position with respect to the sensor size. Finally the number of iterations can be estimated via trial and error, making a compromise between accuracy and computation speed, which is limited by

1. the LabVIEW program not enough optimized,
2. the data transfer rates (low/medium CL) and the bit depth,
3. the memory management (CPU-GPU).

2.4.1 Future improvements

The different elements slowing down the data flow and the code itself should be soon improved. The latter will be modified to include an adapting IW radius to deal with the different constraints imposed by the investigated flow. Such approach has been suggested and successfully tested in the last version of FOLKI, called e-FOLKI (Plyer *et al.*, 2016). Before, the code will completely benefit from the new CUDA libraries since its update is still in progress. This implies an upgrade of the 32-bit LabVIEW program to a 64-bit version (especially for the *cuFFT* library). Actually, this has been already done for the hydro configuration but requires a change in the camera for the aero configuration, due to an apparent incompatibility of the TSI camera with 64-bit program.

Saving the images processed in real-time, instead of just getting rid of them, decreases also the performances since it globally adds a step in the images management process. Grouping several solid-state drives into redundant array of independent disks (RAID 0) may considerably reduce the induced extra time. On the other hand, if only closed-loop control is of interest, the implementation of the optical flow code directly in the camera may be considered. This is the reason why writing a version of the algorithm for a FPGA configuration will also be investigated.

The LabVIEW program allows to target several ROIs to define multi input, either for closed-loop control laws (chapter 3) or for reduced-order models (chapter 4). For the moment the ROIs are created once the RAM receives the image. The time to obtain the aimed quantities may therefore be reduced by directly selecting the ROIs in the camera sensor to avoid useless data transfer. This is what is planned with a new fast camera, which benefits also from the CoaXPress high

speed interface technology (1.25 to 6.25 Gb.s⁻¹), which seems to stretch the transfer rate limit between the camera and the frame-grabber.

Bibliography

- ADRIAN, R.J. (2005) Twenty years of particle image velocimetry. *Experiments in Fluids* **32** (2), pp. 159–169. doi:[10.1007/s00348-005-0991-7](https://doi.org/10.1007/s00348-005-0991-7). 22
- AIDER, J.L., DANET, A. & LESIEUR, M. (2007) Large-eddy simulation applied to study the influence of upstream conditions on the time-dependant and averaged characteristics of a backward-facing step flow. *Journal of Turbulence* **8**, p. N51. doi:[10.1080/14685240701701000](https://doi.org/10.1080/14685240701701000). 37
- ARMALY, B.F., DURST, F., PEREIRA, J.C.F. & SCHÖNUNG, B. (1983) Experimental and theoretical investigation of backward-facing step flow. *Journal of Fluid Mechanics* **127**, p. 473–496. doi:[10.1017/S0022112083002839](https://doi.org/10.1017/S0022112083002839). 36
- ARROYO, M.P. & GREATED, C.A. (1991) Stereoscopic particle image velocimetry. *Measurement Science and Technology* **2** (12), p. 1181. doi:[10.1088/0957-0233/2/12/012](https://doi.org/10.1088/0957-0233/2/12/012). 23
- AVERBUCH, A. & KELLER, Y. (2004) Fast motion estimation using bidirectional gradient methods. *IEEE Transactions on Image Processing* **13**, pp. 1042–1054. doi:[10.1109/TIP.2004.823823](https://doi.org/10.1109/TIP.2004.823823). 28
- BAKER, S. & MATTHEWS, I. (2004) Lucas-Kanade 20 years on: A unifying framework. *International Journal of Computer Vision* **56** (3), pp. 221–255. doi:[10.1023/B:VISI.0000011205.11775.fd](https://doi.org/10.1023/B:VISI.0000011205.11775.fd). 26, 28
- BARNHART, D.H., ADRIAN, R.J. & PAPEN, G.C. (1994) Phase-conjugate holographic system for high-resolution particle-image velocimetry. *Applied Optics* **33** (30), pp. 7159–7170. doi:[10.1364/AO.33.007159](https://doi.org/10.1364/AO.33.007159). 23
- BEAUDOIN, J.F., CADOT, O., AIDER, J.L. & WESFREID, J.E. (2004) Three-dimensional stationary flow over a backward-facing step. *European Journal of Mechanics - B/Fluids* **23** (1), pp. 147 – 155. doi:[10.1016/j.euromechflu.2003.09.010](https://doi.org/10.1016/j.euromechflu.2003.09.010). 38
- BOUGUET, J. (2001) Pyramidal implementation of the Lucas-Kanade feature tracker: description of the algorithm. *Tech. Rep.*. Intel Corporation. 28, 29
- BRADSHAW, P. & WONG, F.Y.F. (1972) The reattachment and relaxation of a turbulent shear layer. *Journal of Fluid Mechanics* **52** (1), p. 113–135. doi:[10.1017/S002211207200299X](https://doi.org/10.1017/S002211207200299X). 38
- BRUHN, A., WEICKERT, J. & SCHNÖRR, C. (2002) Combining the advantages of local and global optic flow methods. In *Pattern Recognition: 24th DAGM Symposium Zurich, Switzerland, September 16–18, 2002 Proceedings* (ed. L. Van Gool), pp. 454–462. Berlin, Heidelberg: Springer Berlin Heidelberg. doi:[10.1007/3-540-45783-6_55](https://doi.org/10.1007/3-540-45783-6_55). 24
- BURT, P. & ADELSON, E. (1983) The Laplacian pyramid as a compact image code. *IEEE Transactions on Communications* **31** (4), pp. 532–540. doi:[10.1109/TCOM.1983.1095851](https://doi.org/10.1109/TCOM.1983.1095851). 29

- CAMBONIE, T. (2012) Experimental study of a jet in crossflow at low velocity ratios using volumetric velocimetry. PhD thesis, PMMH, EPSCI, France. 35
- CHAMPAGNAT, F., PLYER, A., LE BESNERAIS, G., LECLAIRE, B., DAVOUST, S. & LE SAINT, Y. (2011) Fast and accurate PIV computation using highly parallel iterative correlation maximization. *Experiments in Fluids* **50**, pp. 1169–1182. doi:10.1007/s00348-011-1054-x. 24, 25, 28, 35, 40, 43
- CORNIC, P., CHAMPAGNAT, F., CHEMINET, A., LECLAIRE, B. & LE BESNERAIS, G. (2015) Fast and efficient particle reconstruction on a 3D grid using sparsity. *Experiments in Fluids* **56** (3), p. 62. doi:10.1007/s00348-015-1933-7. 23
- CORPETTI, T., HEITZ, D., ARROYO, G., MÉMIN, E. & SANTA-CRUZ, A. (2006) Fluid experimental flow estimation based on an optical-flow scheme. *Experiments in Fluids* **40** (1), pp. 80–97. doi:10.1007/s00348-005-0048-y. 24
- CORPETTI, T., MÉMIN, E. & PEREZ, P. (2002) Dense estimation of fluid flows. *IEEE Transactions on Pattern Analysis and Machine Intelligence* **24** (3), pp. 365–380. doi:10.1109/34.990137. 24
- DAVOUST, S., JACQUIN, L. & LECLAIRE, B. (2012) Dynamics of $m=0$ and $m=1$ modes and of streamwise vortices in a turbulent axisymmetric mixing layer. *Journal of Fluid Mechanics* **709**, pp. 408–444. doi:10.1017/jfm.2012.342. 24
- DEJOAN, A. & LESCHZINER, M. (2004) Large eddy simulation of periodically perturbed separated flow over a backward-facing step. *International Journal of Heat and Fluid Flow* **25** (4), pp. 581–592. doi:10.1016/j.ijheatfluidflow.2004.03.004. 38
- DOUAY, C.L., FAURE, T.M. & LUSSEYRAN, F. (2013) Stereoscopic PIV using optical flow: application to a cavity recirculation. *Experiments in Fluids* **54** (8), p. 1579. doi:10.1007/s00348-013-1579-2. 24
- DRACOS, T. (1996) Particle tracking velocimetry (PTV). In *Three-Dimensional Velocity and Vorticity Measuring and Image Analysis Techniques: Lecture Notes from the Short Course held in Zürich, Switzerland, 3–6 September 1996* (ed. T. Dracos), pp. 155–160. Dordrecht: Springer Netherlands. doi:10.1007/978-94-015-8727-3_7. 23
- ELSINGA, G.E., SCARANO, F., WIENEKE, B. & VAN OUDHEUSDEN, B.W. (2006) Tomographic particle image velocimetry. *Experiments in Fluids* **41** (6), pp. 933–947. doi:10.1007/s00348-006-0212-z. 23
- ENKELMANN, W. (1988) Investigations of multigrid algorithms for the estimation of optical flow fields in image sequences. *Computer Vision, Graphics, and Image Processing* **43** (2), pp. 150–177. doi:10.1016/0734-189X(88)90059-X. 29
- FAURE, T.M., DOUAY, C.L., MOCHKI, S., LUSSEYRAND, F. & QUENOT, G. (2010) Stereoscopic PIV using optical flow: Investigation of a recirculating cavity flow. In *8th International ERCOFTAC Symposium on Engineering Turbulence Modeling and Measurements, Marseille : France*, , vol. 3, pp. 905–910. 24

- FENNEMA, C.L. & THOMPSON, W.B. (1979) Velocity determination in scenes containing several moving objects. *Computer Graphics and Image Processing* **9** (4), pp. 301 – 315. doi:10.1016/0146-664X(79)90097-2. 24
- FITZPATRICK, J.M. (1988) The existence of geometrical density-image transformations corresponding to object motion. *Computer Vision, Graphics, and Image Processing* **44** (2), pp. 155 – 174. doi:10.1016/S0734-189X(88)80003-3. 24
- FOUCAUT, J.M., CARLIER, J. & STANISLAS, M. (2004) PIV optimization for the study of turbulent flow using spectral analysis. *Measurement Science and Technology* **15** (6), p. 1046. doi:10.1088/0957-0233/15/6/003. 23
- FOURAS, A., DUSTING, J. & HOURIGAN, K. (2007) A simple calibration technique for stereoscopic particle image velocimetry. *Experiments in Fluids* **42** (5), pp. 799–810. doi:10.1007/s00348-007-0293-3. 23
- FOURAS, A., LO JACONO, D. & HOURIGAN, K. (2008) Target-free stereo PIV: a novel technique with inherent error estimation and improved accuracy. *Experiments in Fluids* **44** (2), pp. 317–329. doi:10.1007/s00348-007-0404-1. 23
- FOURAS, A., LO JACONO, D., NGUYEN, C.V. & HOURIGAN, K. (2009) Volumetric correlation PIV: A new technique for 3D velocity vector field measurement. *Experiments in Fluids* **47** (4), p. 569. doi:10.1007/s00348-009-0616-7. 23
- GAUTIER, N. (2014) Flow control using optical sensors. PhD thesis, PMMH, EPSCI, France. 24, 25, 33, 35, 40
- GAUTIER, N. & AIDER, J.L. (2013) Control of the separated flow downstream of a backward-facing step using visual feedback. *Proceedings of the Royal Society of London A: Mathematical, Physical and Engineering Sciences* **469** (2160). doi:10.1098/rspa.2013.0404. 38
- GAUTIER, N. & AIDER, J.L. (2015) Real-time planar flow velocity measurements using an optical flow algorithm implemented on GPU. *Journal of Visualization* **18** (2), pp. 277–286. doi:10.1007/s12650-014-0222-5. 26, 30, 35, 43
- HAGER, G. & BELHUMEUR, P. (1998) Efficient region tracking with parametric models of geometry and illumination. *IEEE Transactions on Pattern Analysis and Machine Intelligence* **20** (10), pp. 1025–1039. doi:10.1109/34.722606. 28
- HINSCH, K.D. (2002) Holographic particle image velocimetry. *Measurement Science and Technology* **13** (7), p. R61. doi:10.1088/0957-0233/13/7/201. 23
- HORN, B.K. & SCHUNCK, B.G. (1981) Determining optical flow. *Artificial Intelligence* **17** (1), pp. 185 – 203. doi:10.1016/0004-3702(81)90024-2. 24
- JARA-WILDE, J., CERDA, M., DELPIANO, J. & HÄRTEL, S. (2015) An implementation of combined local-global optical flow. *Image Processing On Line* **5**, pp. 139–158. doi:10.5201/ipol.2015.44. 24

- KÄHLER, C.J., SCHARNOWSKI, S. & CIERPKA, C. (2012) On the resolution limit of digital particle image velocimetry. *Experiments in Fluids* **52** (6), pp. 1629–1639. doi:10.1007/s00348-012-1280-x. 23
- KEANE, R.D. & ADRIAN, R.J. (1990) Optimization of particle image velocimeters. I. Double pulsed systems. *Measurement Science and Technology* **1** (11), p. 1202. doi:10.1088/0957-0233/1/11/013. 23
- LE BESNERAIS, G. & CHAMPAGNAT, F. (2005) Dense optical flow by iterative local window registration. In *Image Processing. ICIP. IEEE International Conference*, , vol. 1, pp. 137–140. IEEE. doi:10.1109/ICIP.2005.1529706. 24, 26
- LUCAS, B. & KANADE, T. (1981) An iterative image registration technique with an application to stereo vision. *Proceedings of the International Joint Conference on Artificial Intelligence* **81**, pp. 674–679. 24, 26
- MAAS, H.G., PUTZE, T. & WESTFELD, P. (2009) Recent developments in 3D-PTV and tomo-PIV. In *Imaging Measurement Methods for Flow Analysis: Results of the DFG Priority Programme 1147 "Imaging Measurement Methods for Flow Analysis" 2003-2009* (ed. W. Nitsche & C. Dobriloff), pp. 53–62. Berlin, Heidelberg: Springer Berlin Heidelberg. doi:10.1007/978-3-642-01106-1_6. 23
- MARZAT, J., DUMORTIER, Y. & DUCROT, A. (2009) Real-time dense and accurate parallel optical flow using CUDA. In *17th International Conference on Computer Graphics, Visualization and Computer Vision, Plzeň, Czech Republic*. 33
- MEYNART, R. (1982) Digital image processing for speckle flow velocimetry. *Review of Scientific Instruments* **53** (1), pp. 110–111. doi:10.1063/1.1136808. 22
- MICHALKE, A. (1964) On the inviscid instability of the hyperbolic tangent velocity profile. *Journal of Fluid Mechanics* **19** (04), pp. 543–556. doi:10.1017/S0022112064000908. 37
- MIOZZI, M. (2004) Particle image velocimetry using feature tracking and Delaunay tessellation. In *Proceedings of 12th international symposium on applied laser techniques to fluid mechanics, Lisbon, Portugal*. 25
- MIOZZI, M., JACOB, B. & OLIVIERI, A. (2008) Performances of feature tracking in turbulent boundary layer investigation. *Experiments in Fluids* **45** (4), p. 765. doi:10.1007/s00348-008-0531-3. 25
- MUNOZ, J.M.I., DELLAVALE, D., SONNAILLON, M.O. & BONETTO, F.J. (2009) Real-time particle image velocimetry based on FPGA technology. In *2009 5th Southern Conference on Programmable Logic (SPL)*, pp. 147–152. doi:10.1109/SPL.2009.4914899. 30
- NVIDIA (2010) *Whitepaper. NVIDIA's Next Generation CUDA Compute Architecture: Fermi*. 33
- NVIDIA (2017) *CUDA Toolkit Documentation v8.0*. 33

- PAN, C., XUE, D., XU, Y., WANG, J. & WEI, R. (2015) Evaluating the accuracy performance of Lucas-Kanade algorithm in the circumstance of PIV application. *Science China Physics, Mechanics and Astronomy* **58**, p. 104704. doi:10.1007/s11433-015-5719-y. 25, 28, 29, 35, 39, 40
- PEREIRA, F., GHARIB, M., DABIRI, D. & MODARRESS, D. (2000) Defocusing digital particle image velocimetry: a 3-component 3-dimensional DPIV measurement technique. Application to bubbly flows. *Experiments in Fluids* **29** (1), pp. S078–S084. doi:10.1007/s003480070010. 23
- PEREIRA, F., STÜER, H., GRAFF, E. & GHARIB, M. (2006) Two-frame 3D particle tracking. *Measurement Science and Technology* **17** (7), p. 1680. doi:10.1088/0957-0233/17/7/006. 23
- PLYER, A., LE BESNERAIS, G. & CHAMPAGNAT, F. (2016) Massively parallel Lucas Kanade optical flow for real-time video processing applications. *Journal of Real-Time Image Processing* **11** (4), pp. 713–730. doi:10.1007/s11554-014-0423-0. 44
- QUÉNOT, G.M., PAKLEZA, J. & KOWALEWSKI, T.A. (1998) Particle image velocimetry with optical flow. *Experiments in Fluids* **25** (3), pp. 177–189. doi:10.1007/s003480050222. 24
- RAFFEL, M., WILLERT, C.E., WERELEY, S.T. & KOMPENHANS, J. (2007) *Particle Image Velocimetry*. Springer. doi:10.1007/978-3-540-72308-0. 22
- SARTOR, F., LOSFELD, G. & BUR, R. (2012) PIV study on a shock-induced transition in transonic flow. *Experiments in Fluids* **53**, pp. 815–827. doi:10.1007/s00348-012-1330-4. 24
- SCARANO, F. (2002) Iterative image deformation methods in PIV. *Measurement Science and Technology* **13** (1). doi:10.1088/0957-0233/13/1/201. 23
- SCARANO, F. & RIETHMULLER, M.L. (1999) Iterative multigrid approach in PIV image processing with discrete window offset. *Experiments in Fluids* **26** (6), pp. 513–523. doi:10.1007/s003480050318. 23
- SHI, S., NEW, T. & LIU, Y. (2013) Improvements to time-series TR-PIV algorithms using historical displacement and displacement variation information. *Flow Measurement and Instrumentation* **29** (Supplement C), pp. 67 – 79. doi:10.1016/j.flowmeasinst.2012.10.011. 23
- SIEGEL, S., COHEN, K., MCLAUGHLIN, T. & MYATT, J. (2003) Real-time particle image velocimetry for closed-loop flow control studies. In *41st Aerospace Sciences Meeting and Exhibit, Aerospace Sciences Meetings, Reno, USA*. doi:10.2514/6.2003-920. 30
- SIPP, D. & JACQUIN, L. (2000) *A Criterion of Centrifugal Instabilities in Rotating Systems*, pp. 299–308. Berlin, Heidelberg: Springer Berlin Heidelberg. doi:10.1007/3-540-44535-8_21. 38
- SOLOFF, S.M., ADRIAN, R.J. & LIU, Z.C. (1997) Distortion compensation for generalized stereoscopic particle image velocimetry. *Measurement Science and Technology* **8** (12), p. 1441. doi:10.1088/0957-0233/8/12/008. 23
- SPAZZINI, P., IUSO, G., ONORATO, M., ZURLO, N. & CICCÀ, G.D. (2001) Unsteady behavior of back-facing step flow. *Experiments in Fluids* **30** (5), pp. 551–561. doi:10.1007/s003480000234. 36, 38

- STANISLAS, M., OKAMOTO, K., KÄHLER, C.J., WESTERWEEL, J. & SCARANO, F. (2008) Main results of the third international PIV Challenge. *Experiments in Fluids* **45** (1), pp. 27–71. doi:10.1007/s00348-008-0462-z. 24
- THANGAM, S. & KNIGHT, D.D. (1989) Effect of stepheight on the separated flow past a backward facing step. *Physics of Fluids A: Fluid Dynamics* **1** (3), pp. 604–606. doi:10.1063/1.857430. 38
- TROUTT, T.R., SCHEELKE, B. & NORMAN, T.R. (1984) Organized structures in a reattaching separated flow field. *Journal of Fluid Mechanics* **143**, pp. 413–427. doi:10.1017/S0022112084001415. 37
- WIENEKE, B. (2005) Stereo-PIV using self-calibration on particle images. *Experiments in Fluids* **39** (2), pp. 267–280. doi:10.1007/s00348-005-0962-z. 23
- WILLERT, C., MUNSON, M. & GHARIB, M. (2010) Real-time particle image velocimetry for closed-loop flow control applications. In *15th International Symposium on Applications of Laser Techniques to Fluid Mechanics, Lisbon, Portugal*. 30
- WINANT, C.D. & BROWAND, F.K. (1974) Vortex pairing: The mechanism of turbulent mixing-layer growth at moderate Reynolds number. *Journal of Fluid Mechanics* **63** (02), pp. 237–255. doi:10.1017/S0022112074001121. 37
- YU, H., LEESER, M., TADMOR, G. & SIEGEL, S. (2006) Real-time particle image velocimetry for feedback loops using FPGA implementation. *Journal of Aerospace Computing, Information, and Communication* **3** (2), pp. 55–62. doi:10.2514/1.18062. 30
- ZHAO, W. & SAWHNEY, H. (2002) Is super-resolution with optical flow feasible? In *ECCV '02 Proceedings of the 7th European Conference on Computer Vision - Part I*, pp. 599–613. Springer-Verlag London. doi:10.1007/3-540-47969-4_40. 28

Velocity fields analysis for real-time PIV

This short chapter details all the quantities which can be extracted in real-time (RT) from the velocity fields. This a fundamental step to be able to use the camera as a visual sensor in a closed-loop experiment. Some of these output are related to specific flow like the recirculation area for wakes. Other are intended to detect structures like the Q-criterion. All these tools are implemented on the GPU and will be illustrated via measurements in the previously seen BFS flow for $Re_H = 2 \times 10^3$ ($T_u = 1.2\%$).

3.1	Velocity fields	53
3.1.1	Time-averaged velocity	53
3.1.2	Velocity fluctuations	54
3.2	Vortex detection	55
3.2.1	Swirling strength criterion	55
3.2.2	Q-criterion	56
3.3	Separated flow activity	57
3.4	Conclusions and perspectives	59

3.1 Velocity fields

The Reynolds decomposition is used to have access to the turbulent part of the flow. Its application to the 2D-2C velocity fields $\mathbf{V} = (u, w)$ resulting from the optical flow is

$$\mathbf{V} = \bar{\mathbf{V}} + \mathbf{V}', \tag{3.1}$$

where $\bar{\mathbf{V}} = (U, W)$ and $\mathbf{V}' = (u', w')$ are the mean velocity and the fluctuations respectively. The former can be easily used to compute profiles free from noise, giving direct access to the general flow characteristics of the boundary layer (see [chapter 4](#)). The latter carry the flow dynamics.

3.1.1 Time-averaged velocity

By cumulating the instantaneous velocity fields $\mathbf{V}(n)$ in the same variable, the time-averaged velocity $\bar{\mathbf{V}}$ is straightforwardly obtained. This online post-process can adapt to the dynamics via

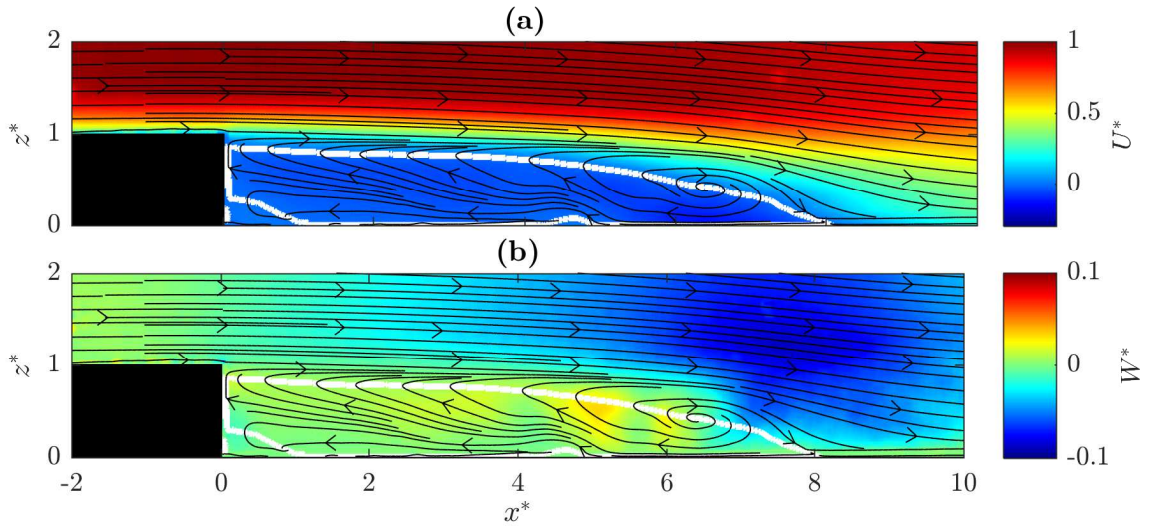


Figure 3.1 – Time-averaged (a) streamwise and (b) normal to the wall components of the velocity over 2000 fields, together with the mean separatrix (white line). $Re_H = 2 \times 10^3$.

optional moving-average window and user-defined conditions to only keep specific velocity fields. This way, the RT computed conditional-averaged fields are easily obtained without storing large amount of data, even if the time-resolution of the streamed images is inadequate to capture the main flow dynamics (see chapter 5).

3.1.2 Velocity fluctuations

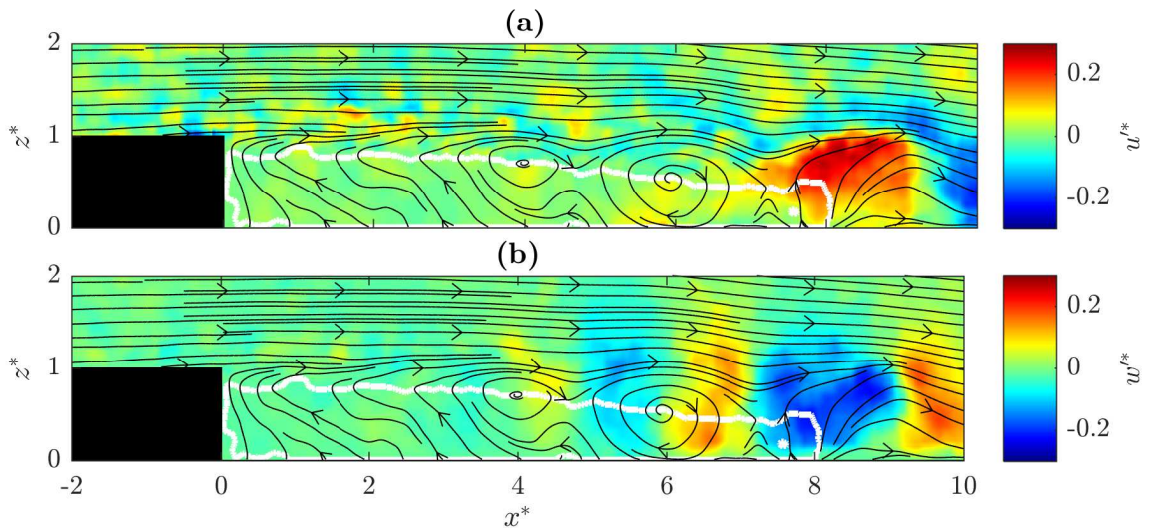


Figure 3.2 – Instantaneous fluctuations of (a) the streamwise and (b) the normal to the wall components of the velocity, together with the instantaneous separatrix (white line). $Re_H = 2 \times 10^3$.

Computing the mean velocity fields online enables overall to obtain directly the flow fluctuations $\mathbf{V}'(n)$, shown in Figure 3.2 for the BFS flow. The turbulence kinetic energy (TKE), defined as

$$k = \frac{1}{2} \|\mathbf{V}'\|^2, \quad (3.2)$$

is consequently obtained. It is an interesting value to monitor since it is produced by the flow fluctuations. For instance, Gautier & Aider (2014b) derived an auto-regressive moving-average exogenous (ARMAX) model (Hervé *et al.*, 2012) to minimize the TKE at $Re_h = 4 \times 10^2$.

3.2 Vortex detection

An objective when studying unsteady flows is to follow coherent structures, especially vortices, since they are peculiar patterns influencing and moving in the fluid (Jeong & Hussain, 1995). Detecting such structures enables to divide the flow in regions of different dynamics but distinguishing a large-scale vortex from the small-scale turbulent motion embedded inside remains a difficult task. How is mathematically defined a vortex? There is no absolute answer to this question, which is the reason why there are many criteria for vortex identification.

Two historic approaches have given birth to several detection tools: the Eulerian and the Lagrangian techniques. On one hand, Lagrangian techniques delimit regions of different dynamics from a finite set of successive velocity fields. For instance, in space oceanography, the finite-time Lyapunov exponent (FTLE) (Haller, 2002; Shadden *et al.*, 2005) is used to identify mixing regions and to predict oil slick extent from the geostrophic velocities (Mezić *et al.*, 2010). On the other hand, Eulerian methods detect regions of vortices, defined from the instantaneous velocity field and its gradients. The presented tools come from this side.

3.2.1 Swirling strength criterion

Chong *et al.* (1990) proposed to identify the 2D vortex core as a region where the velocity gradient has complex conjugate eigenvalues. They define thus the swirling strength criterion λ_{Ci} from the characteristic polynomial of $\nabla\mathbf{V}$ as

$$\lambda_{Ci} = \frac{1}{2} \sqrt{4 \det(\nabla\mathbf{V}) - \text{tr}(\nabla\mathbf{V})^2}, \text{ if defined} \quad (3.3)$$

and $\lambda_{Ci} = 0$ otherwise. It means that an element of fluid at the position (x, z) will rotate around the nearest vortex core in $2\pi/\lambda_{Ci}(x, y)$. Cambonie *et al.* (2013) demonstrated the effectiveness of the 3D version of this criterion (Zhou *et al.*, 1999) to detect vortices despite the presence of shear. Figure 3.3(a) illustrates the criterion for the BFS flow. The activity in the shear layer and the vortex shedding starting at $x^* \sim 4.9$ are both well detected.

Gautier & Aider (2015a) implemented this criterion on the GPU to capture the shedding frequency downstream of the BFS flow at $Re_h \sim 10^3$. They aimed at injecting momentum in the flow at this frequency since it is effective to reduce the recirculation area. A vertical ROI located

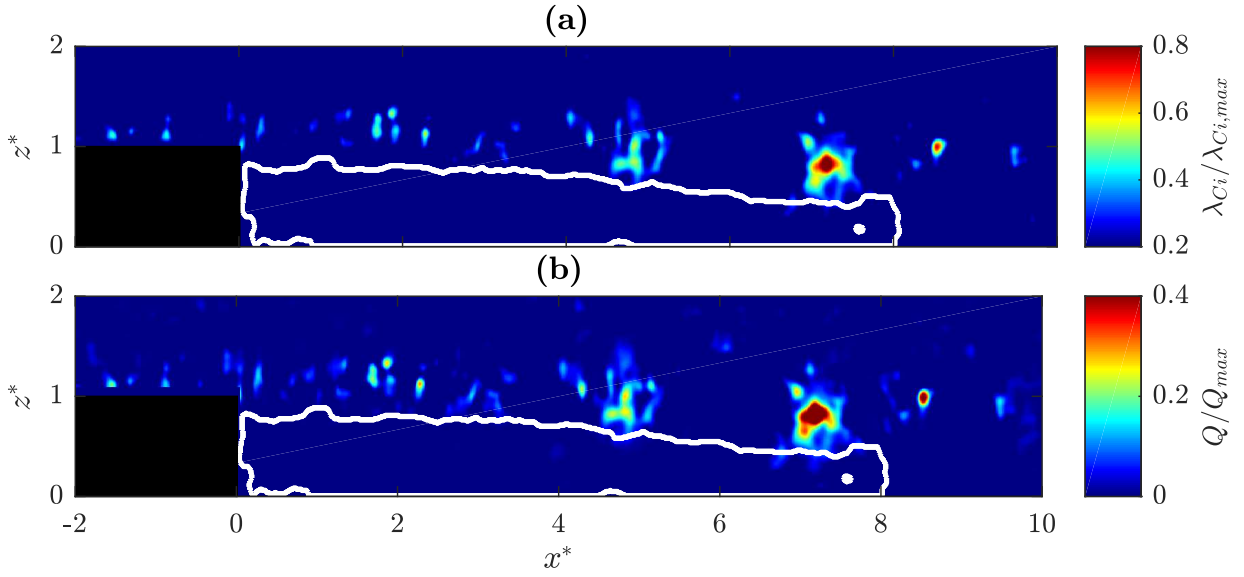


Figure 3.3 – (a) λ_{Ci} and (b) Q -criterion derived from the same instantaneous velocity field. $Re_H = 2 \times 10^3$.

at $x^* \sim 8$ integrates the swirling strength activity for a chosen period and a fast Fourier transform (FFT) highlights the frequency peak corresponding to the vortex shedding. The frequency is computed only if any change in the free-stream is detected since both quantities are linearly related at this Reynolds number range.

3.2.2 Q -criterion

Since the vorticity alone is not enough to distinguish vortices from strain, Hunt *et al.* (1988) defined the Q -criterion as

$$Q = \frac{1}{2}(\|\boldsymbol{\Omega}\|^2 - \|\boldsymbol{S}\|^2) > 0, \quad (3.4)$$

where $\boldsymbol{\Omega} = \frac{1}{2}(\nabla\mathbf{V} - \nabla\mathbf{V}^T)$ and $\boldsymbol{S} = \frac{1}{2}(\nabla\mathbf{V} + \nabla\mathbf{V}^T)$ are the vorticity tensor and the rate of strain tensor respectively. This criterion can be related to the pressure Laplacian $Q = \Delta p / (2\rho)$ via the Poisson equation for the pressure. Figure 3.3(b) gives the Q -criterion derived from the same previous velocity field. Both criteria are in good agreement.

The main issue with the above described criteria appears for 3D fully turbulent flows, where large-scale and small-scale vortices tangle. This is due to the velocity gradient which tends to amplify the inherent noise of turbulence. In these cases, a user-defined threshold is required to detect the vortex cores. This is critical because it can lead to misinterpretation of the flow dynamics by removing apparently low Q values. It shall be stressed that velocity fields obtained via the optical flow allow to derive directly accurate gradients. For velocity fields computed from FFT-PIV this requires time consuming methods (Raffel *et al.*, 2007).

3.3 Separated flow activity

The previous quantities are widely used to characterize and analyze the activity of separated flows. Two important properties already discussed in [chapter 2](#) are the recirculation area A_{rec} , a valuable target for experimental control practice ([Gautier, 2014](#)), and the Kelvin-Helmholtz (KH) instability.

Recirculation area The instantaneous recirculation area $A_{rec}(t)$ is defined as

$$A_{rec}(t) = \iint H(-u^*(x^*, z^*, t)) dx dz, \quad (3.5)$$

where H is the Heaviside function. It allows the study of the time evolution of the recirculation bubble. In [chapter 5](#), the tracking of its barycenter will be of particular interest to understand the dynamics of a 3D fully turbulent wake. This value will even be used as a sensor in a closed-loop control in [chapter 7](#).

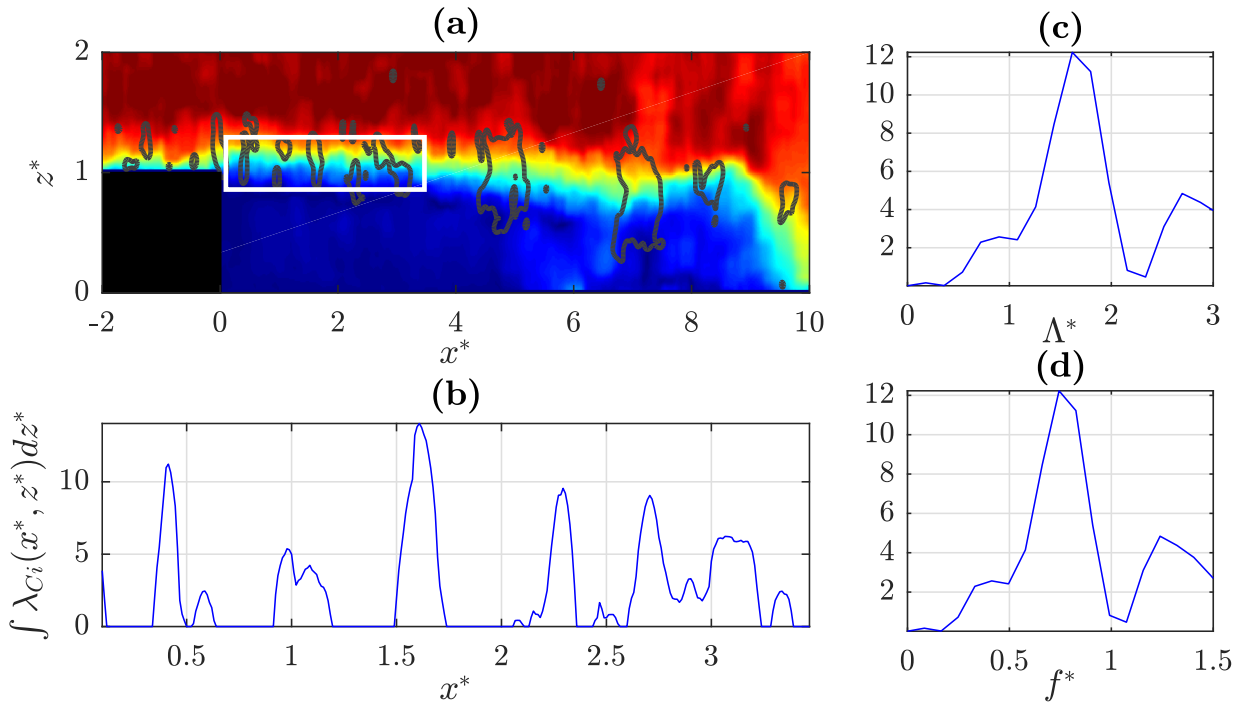


Figure 3.4 – (a) Instantaneous velocity field, together with contour of λ_{Ci} (gray) and the rectangular ROI (white). (b) Integrated λ_{Ci} along the z -axis. (c) FFT of the integrated λ_{Ci} . (d) Previous resulting FFT multiplied by the mean velocity of the vortices. $Re_H = 2 \times 10^3$.

Kelvin-Helmholtz instability Derived from the idea of [Gautier & Aider \(2015a\)](#) mentioned above, a new measurement technique has been implemented. It consists in applying a spatial FFT rather than the temporal one, considering the KH vortices as a wave. The ROI is located in the first half of the shear layer [[Figure 3.4\(a\)](#)] to vertically integrate the criterion $\int \lambda_{Ci}(x^*, z^*) dz$.

Space series of the vortices streamwise position are thus extracted [Figure 3.4(b)]. The wavenumber Λ^* of the vortices train results from the FFT of this signal [Figure 3.4(c)]. Averaging the velocity components where the vortices are detected, $\overline{u_{KH}^*}$ and $\overline{w_{KH}^*}$, enables to measure their mean velocity V_{KH}^* . This leads directly to the shedding frequency $f_{KH}^* = \Lambda^* V_{KH}^*$ [Figure 3.4(d)]. This technique can be used with the Q -criterion as well.

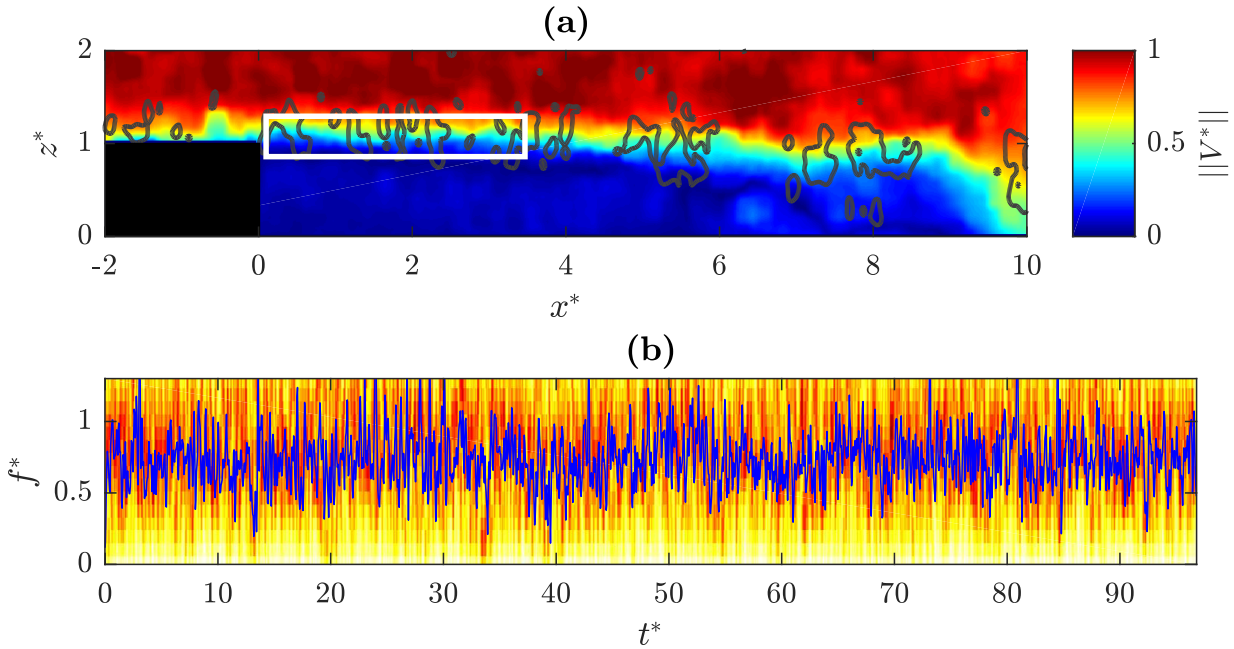


Figure 3.5 – (a) Instantaneous velocity field, together with contour of λ_{Ci} (gray) and the rectangular ROI (white). (b) Estimated KH frequency for each velocity field $f_{KH}^*(t^*)$ (highlighted in blue).

The KH frequency has been estimated for 2000 snapshots, giving $f_{KH}^* = 0.79 \pm 0.12$, as displayed in Figure 3.5. Regarding the vortex shedding frequency (see after), this result is in good agreement with previous experimental (Norberg, 1987) and numerical (Dong *et al.*, 2006; Kim *et al.*, 2015) estimations done for the wake behind a cylinder. It even supports well the $Re_h^{0.67}$ scaling proposed by Prasad & Williamson (1996), predicting $f_{KH}^* = 0.76$.

The first advantage of such a measurement is the possibility to reach a characteristic frequency of the separated flow usually captured only by high sampling rate sensors (see chapter 5). The second advantage resides in the instantaneous measurement itself, giving the information in real-time. It enables indeed to compute the shedding frequency online without building time series. Moreover, the measurements are spatially averaged when extracted from the instantaneous fields. This is even better than a local sensor, especially an intrusive one like the hot-wire, which is critical for a noise amplifier flow. For example, a second, larger, ROI can be defined in the second part of the shear layer as shown by Figure 3.6(a). The results are displayed in Figure 3.6(b), where the mean estimated shedding frequency is $f_{shed}^* = 0.2 \pm 0.04$, in good agreement with the expected value. The high standard deviation is due to the low spatial resolution for the FFT, the ROI being limited in the streamwise direction.

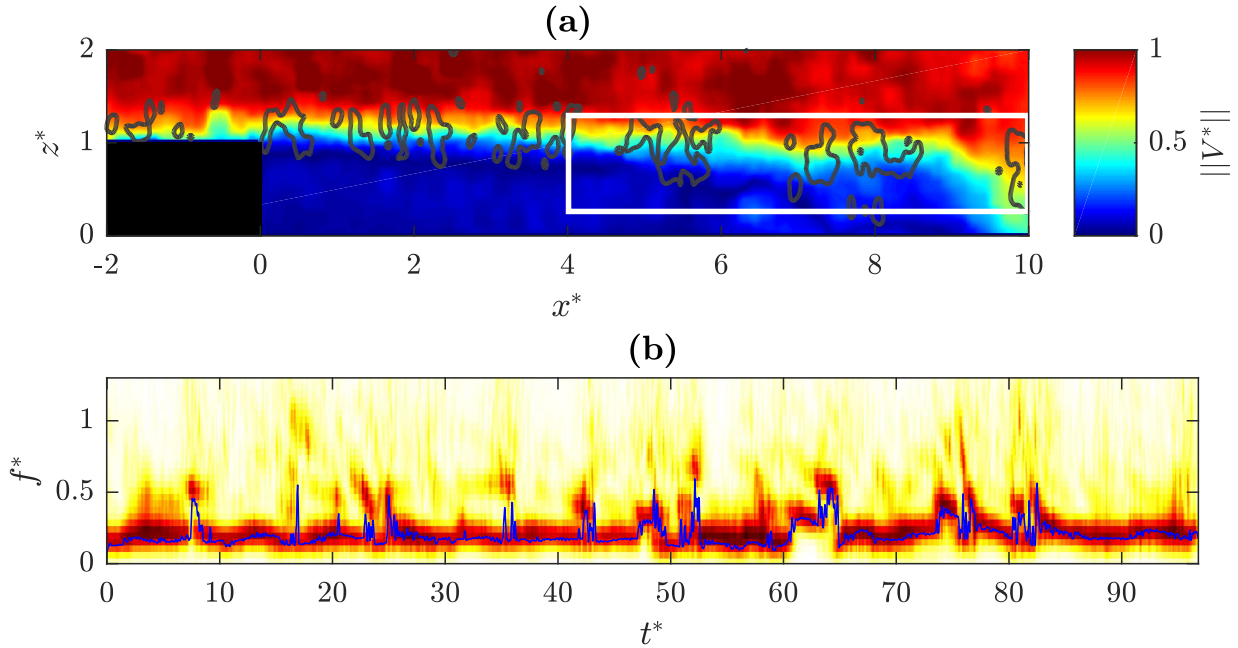


Figure 3.6 – (a) Instantaneous velocity field, together with contour of λ_{Ci} (gray) and the rectangular ROI (white). (b) Estimated shedding frequency for each velocity field $f_{shed}^*(t^*)$ (highlighted in blue). $Re_H = 2 \times 10^3$.

3.4 Conclusions and perspectives

Building linear controllers to manipulate the recirculation area in a BFS flow at $Re_h \sim 10^3$, N. Gautier has implemented numerous quantities derived from the instantaneous fields in the CUDA/LabVIEW environment (Gautier & Aider, 2013, 2014a,b, 2015a). These RT processes have even enabled an experimental application of machine learning on this flow (Gautier *et al.*, 2015b). The CUDA codes computing these variables have been improved, especially to fulfil the requirements of the measurement conditions of a bluff-body in a wind-tunnel (see chapter 7): higher Reynolds number, 3D wake and low frame rate of the streaming double-frame camera. Quantities like the Reynolds stress tensor, the Q -criterion and the boundary layer characteristics (see chapter 4) have been added. A new method to capture rapid dynamics is now available and needs to be intensively tested on different geometries (see chapter 5).

Known structures in unsteady turbulent flows have low vorticity Ω , such as the counter-rotating longitudinal vortices downstream of a slanted bluff-body (see chapter 5), making them difficult to detect using the presented criteria, highly sensitive to the small-scale turbulence. A solution, introduced by Graftieaux *et al.* (2001), consists in only dealing with the fields topology, excluding the velocities magnitude. This approach defines two scalar functions, detecting both the centre and the boundary of vortices. For instance, using this criterion, Venning *et al.* (2017) have recently highlighted the presence of a twin-horseshoe structure in the wake behind a slanted bluff-body, rather than the usually admitted toroidal vortex (see chapter 5).

A complementary Lagrangian technique could be added to the previous Eulerian tools. This would require data storage since the vortex detection is based on an ensemble of velocity fields. Furthermore, it is a time-dependent method, meaning that the frame rate and the computation speed of the optical flow have to be higher than the characteristic frequencies of the flow. Nonetheless, [Rockwood & Green \(2016\)](#) have recently coupled the FTLE analysis to RT pressure sensor, reaching online accurate tracking of the vortices behind a cylinder. Furthermore, [Guéniat \(2013\)](#) proposed a faster computation of the FTLE, based on GPU interpolation and applied to an open cavity flow.

Bibliography

- CAMBONIE, T., GAUTIER, N. & AIDER, J.L. (2013) Experimental study of counter-rotating vortex pair trajectories induced by a round jet in cross-flow at low velocity ratios. *Experiments in Fluids* **54** (3), p. 1475. doi:10.1007/s00348-013-1475-9. 55
- CHONG, M.S., PERRY, A.E. & CANTWELL, B.J. (1990) A general classification of three-dimensional flow fields. *Physics of Fluids A: Fluid Dynamics* **2** (5), pp. 765–777. doi:10.1063/1.857730. 55
- DONG, S., KARNIADAKIS, G.E., EKMEKCI, A. & ROCKWELL, D. (2006) A combined direct numerical simulation–particle image velocimetry study of the turbulent near wake. *Journal of Fluid Mechanics* **569**, p. 185–207. doi:10.1017/S0022112006002606. 58
- GAUTIER, N. (2014) Flow control using optical sensors. PhD thesis, PMMH, EPSCI, France. 57
- GAUTIER, N. & AIDER, J.L. (2013) Control of the separated flow downstream of a backward-facing step using visual feedback. *Proceedings of the Royal Society of London A: Mathematical, Physical and Engineering Sciences* **469** (2160). doi:10.1098/rspa.2013.0404. 59
- GAUTIER, N. & AIDER, J.L. (2014a) Upstream open-loop control of the recirculation area downstream of a backward-facing step. *Comptes Rendus Mécanique (CRAS II B)* **342**, pp. 382–388. doi:10.1016/j.crme.2014.05.004. 59
- GAUTIER, N. & AIDER, J.L. (2014b) Feed-forward control of a perturbed backward-facing step flow. *Journal of Fluid Mechanics* **759**, p. 181–196. doi:10.1017/jfm.2014.518. 55, 59
- GAUTIER, N. & AIDER, J.L. (2015a) Frequency-lock reactive control of a separated flow enabled by visual sensors. *Experiments in Fluids* **56**, p. 16. doi:10.1007/s00348-014-1869-3. 55, 57, 59
- GAUTIER, N., AIDER, J.L., DURIEZ, T., NOACK, B.R., SEGOND, M. & ABEL, M. (2015b) Closed-loop separation control using machine learning. *Journal of Fluid Mechanics* **770**, pp. 442–457. doi:10.1017/jfm.2015.95. 59
- GRAFTIEAUX, L., MICHARD, M. & GROSJEAN, N. (2001) Combining PIV, POD and vortex identification algorithms for the study of unsteady turbulent swirling flows. *Measurement Science and Technology* **12** (9), p. 1422. doi:10.1088/0957-0233/12/9/307. 59
- GUÉNIAT, F. (2013) Detection of coherent structures in fluid flows and interactive interface for the exploration of scientific dataset. PhD thesis, LIMSI, Université Paris-Sud, France. 60
- HALLER, G. (2002) Lagrangian coherent structures from approximate velocity data. *Physics of Fluids* **14** (6), pp. 1851–1861. doi:10.1063/1.1477449. 55
- HERVÉ, A., SIPP, D., SCHMID, P. & SAMUELIDES, M. (2012) A physics-based approach to flow control using system identification. *Journal of Fluid Mechanics* **702**, pp. 26–58. doi:10.1017/jfm.2012.112. 55

- HUNT, J.C.R., WRAY, A. & MOIN, P. (1988) Eddies, stream, and convergence zones in turbulent flows. *Tech. Rep.*. Center for Turbulence Research Report. 56
- JEONG, J. & HUSSAIN, F. (1995) On the identification of a vortex. *Journal of Fluid Mechanics* **285**, p. 69–94. doi:10.1017/S0022112095000462. 55
- KIM, S., WILSON, P.A. & CHEN, Z.M. (2015) Large-eddy simulation of the turbulent near wake behind a circular cylinder: Reynolds number effect. *Applied Ocean Research* **49**, pp. 1 – 8. doi:http://dx.doi.org/10.1016/j.apor.2014.10.005. 58
- MEZIĆ, I., LOIRE, S., FONOBEROV, V.A. & HOGAN, P. (2010) A new mixing diagnostic and gulf oil spill movement. *Science* **330** (6003), pp. 486–489. doi:10.1126/science.1194607. 55
- NORBERG, C. (1987) Effects of Reynolds number and a low-intensity freestream turbulence on the flow around a circular cylinder. *Chalmers University, Goteborg, Sweden, Technological Publications* **87** (2). 58
- PRASAD, A. & WILLIAMSON, C.H.K. (1996) The instability of the separated shear layer from a bluff body. *Physics of Fluids* **8** (6), pp. 1347–1349. doi:10.1063/1.868942. 58
- RAFFEL, M., WILLERT, C.E., WERELEY, S.T. & KOMPENHANS, J. (2007) *Particle Image Velocimetry*. Springer. doi:10.1007/978-3-540-72308-0. 56
- ROCKWOOD, M. & GREEN, M. (2016) Correlation of the surface pressure distribution on a circular cylinder with objective identification of vortex formation and shedding. In *54th AIAA Aerospace Sciences Meeting, San Diego, USA*. 60
- SHADDEN, S.C., LEKIEN, F. & MARSDEN, J.E. (2005) Definition and properties of Lagrangian coherent structures from finite-time Lyapunov exponents in two-dimensional aperiodic flows. *Physica D: Nonlinear Phenomena* **212**, pp. 271 – 304. doi:10.1016/j.physd.2005.10.007. 55
- VENNING, J., LO JACONO, D., BURTON, D., THOMPSON, M.C. & SHERIDAN, J. (2017) The nature of the vortical structures in the near wake of the Ahmed body. In *Proceedings of the Institution of Mechanical Engineers, Part D: Journal of Automobile Engineering*. doi:10.1177/0954407017690683. 59
- ZHOU, J., ADRIAN, R.J., BALACHANDAR, S. & KENDALL, T.M. (1999) Mechanisms for generating coherent packets of hairpin vortices in channel flow. *Journal of Fluid Mechanics* **387**, p. 353–396. doi:10.1017/S002211209900467X. 55

The dynamic observer

This chapter presents the dynamic observer, a reduced-order model well suited for amplifier flows. After explaining its functioning in the system identification framework, this method is experimentally applied to the transient boundary layer over a flat plate.

4.1	Introduction	64
4.1.1	Reduced-order model	64
4.1.2	Dynamic observer principle	65
4.1.2.1	From the amplifier flow dynamics to a linear system	65
4.1.2.2	POD reduced-order model	65
4.1.2.3	System identification	66
4.2	Experimental application	67
4.2.1	The boundary layer over a flat plate	67
4.2.1.1	Dynamics description	68
4.2.1.2	Flow characteristics	69
4.2.2	Experimental setup	70
4.2.2.1	Water channel	70
4.2.2.2	Boundary layer	70
4.2.2.3	Forcing noise	70
4.2.2.4	Real-time PIV as a sensor	71
4.2.3	Flow characterization	72
4.2.3.1	Base flow	72
4.2.3.2	Forced flow	73
4.2.4	Experimental dynamic observer	75
4.2.4.1	POD modes	76
4.2.4.2	Sensors definition	77
4.2.4.3	Reduced-order model and validation	79
4.2.4.4	Other tested sensors	80
4.3	Conclusions and perspectives	81
4.3.1	Discussion	82
4.3.2	Perspectives	82

The camera has its own sense of being a person observing, rather than being something clever that's manipulating, shooting up on a crane, and zooming over the fields and down at floor level. Who on earth ever watches anything from floor level?

4.1 Introduction

The presented work, done in collaboration with J. Guzmán Iñigo (Imperial College London, former ONERA), D. Sipp (ONERA DAAA) and P. J. Schmid (Imperial College London), is the experimental realization of the numerical investigation into dynamic observer by Guzmán Iñigo *et al.* (2014); Guzmán Iñigo *et al.* (2016). The theory will therefore only be summarized in this section since complete details can be found in the given references.

4.1.1 Reduced-order model

In their classification of unsteadiness in open flows, Huerre & Monkewitz (1990) define two main categories exhibiting strong non-linearities. On one hand, the oscillator-type flows are characterized by a global instability resulting in self-sustained oscillatory fluid behaviour (wake, jets). On the other hand, the noise amplifiers category contains fluid systems which are globally stable even if they selectively amplify upstream perturbations by convective instabilities (boundary layer).

Directly controlling a fluid system requires to handle its numerous degrees of freedom, which is not realistic yet. The idea consists thus in simplifying the system as a reduced-order model (ROM). If the physics are deeply understood, then a physical model can be set. Unfortunately, such level of knowledge is still difficult to reach.

Galerkin projection Projecting the Navier-Stokes (NS) equations onto a reduced basis, purpose-built to capture the most essential dynamics, is another way called Galerkin projection. The reduced basis may be computed either through global stability analysis or through statistical decomposition like proper orthogonal decomposition (Berkooz & Titi, 1993) and dynamic mode decomposition (Tissot *et al.*, 2014). This technique is appropriate for oscillator-type flows (Jackson, 1987), like the cylinder wake (Bergmann & Cordier, 2008) and the open cavity (Barbagallo *et al.*, 2009), but not for amplifier flows. Indeed, due to their nature, the dynamics driven by environmental noise cannot be distinguished from the intrinsic dynamics by global stability analysis (Trefethen *et al.*, 1993; Chomaz, 2005; Brandt *et al.*, 2011). In the same manner, a statistical decomposition cannot detect the statistically steady noise, which prevents the system from creating the corresponding output. In fact, the model would need an access to the noise distribution to avoid this issue, which is experimentally realizable with data-based techniques. It shall be mentioned that the transient growth of the perturbations, characteristic of such a flow, can be captured using the resolvent operator (Sipp & Marquet, 2013).

System identification By highlighting the role of system identification as a design problem, especially for control, rather than solely a tool to match the real dynamics, Ljung (1999) proposed, amongst other things, an alternative approach to Galerkin projection. The system identification algorithm aims at predicting the dynamics of the entire flow through a statistical learning process from local measurements of input and output data, as explained hereafter. For instance,

Hervé *et al.* (2012) used the system identification method to numerically predict and control the dynamics of a back-facing step between an upstream sensor and a downstream one. For the same flow, Henning *et al.* (2007) delayed the vortex shedding using an array of pressure sensors as an input of a model identification.

4.1.2 Dynamic observer principle

4.1.2.1 From the amplifier flow dynamics to a linear system

The complete dynamics of a forced amplifier flow are represented by the incompressible NS equations including an unknown upstream forcing term $\mathbf{F}_w w(t)$

$$\partial_t \mathbf{V} + \mathbf{V} \cdot \nabla \mathbf{V} = -\nabla \mathbf{P} + Re^{-1} \Delta \mathbf{V} + \mathbf{F}_w w(t), \quad (4.1a)$$

$$\nabla \cdot \mathbf{V} = 0, \quad (4.1b)$$

where the velocity \mathbf{V} and the pressure \mathbf{P} are dimensionless and the physical meaning of $w(t)$ is given in the following section. Expressing the velocity and the pressure in Equation 4.1 such as $\mathbf{V} = \mathbf{V}_{base} + \mathbf{v}'$ and $\mathbf{P} = \mathbf{P}_{base} + \mathbf{p}$, where \mathbf{V}_{base} and \mathbf{P}_{base} are respectively the velocity and the pressure when $w = 0$ (base-flow), and \mathbf{v}' and \mathbf{p} are the velocity and pressure disturbances, leads to

$$\partial_t \mathbf{v}' + \mathbf{V}_{base} \cdot \nabla \mathbf{v}' + \mathbf{v}' \cdot \nabla \mathbf{V}_{base} = -\nabla \mathbf{p} + Re^{-1} \Delta \mathbf{v}' + \mathbf{F}_w w(t), \quad (4.2a)$$

$$\nabla \cdot \mathbf{v}' = 0, \quad (4.2b)$$

where linear perturbation dynamics are assumed (second order perturbations are negligible).

The objective is thus to obtain the following linear time invariant (LTI) multiple-input-multiple-output (MIMO) system

$$x(n+1) = \mathcal{A}x(n) + \mathcal{B}u(n) + w(n), \quad (4.3a)$$

$$y(n) = \mathcal{C}x(n) + \mathcal{D}u(n) + v(n), \quad (4.3b)$$

where $y(n)$ is the system output, $x(n)$ is the system state, $u(n)$ is the system input, $w(n)$ is the state noise, $v(n)$ is the sensor noise, and \mathcal{A} , \mathcal{B} , \mathcal{C} and \mathcal{D} are the system matrices. $w(n)$ and $v(n)$ being unknown, the state space model described in Equation 4.3 rather predicts an estimated output denoted y_e when $w = v = 0$. The system matrices are consequently chosen to minimize the difference between the estimated output, and the measured output y .

4.1.2.2 POD reduced-order model

N consecutive velocity fields $\{\mathbf{V}(\mathbf{n})\}_{n=1\dots N}$ are computed to form the so-called learning data set. The proper orthogonal decomposition (POD) of this data set enables to build a ranked and orthonormal basis containing N modes (Lumley, 1967; Sirovich, 1987) thanks to the snapshots

method. The first K modes $\{\Phi_k\}_{k=1\dots K}$ with $K \leq N$ are chosen to compute the approximated velocity field $\tilde{\mathbf{V}}(\mathbf{n})$

$$\tilde{\mathbf{V}}(\mathbf{n}) = \sum_{k=1}^K \langle \Phi_k, \mathbf{V}(\mathbf{n}) \rangle \Phi_k, \quad (4.4)$$

where the scalar product $\langle \cdot, \cdot \rangle$ is the energy-based inner product. By gathering all the POD coefficients $a_k(n)$, defined as $a_k(n) = \langle \Phi_k, \mathbf{V}(\mathbf{n}) \rangle$, the system output is obtained through the reduced state vector $Y(n) = [a_1(n) \ a_2(n) \ \dots \ a_K(n)]^T$. The modes dynamics are contained in their coefficients.

The dynamics of the estimation $Y_e(n)$ of the reduced state vector $Y(n)$ can therefore be captured from sensor measurements $s(n)$ by

$$Y_e(n+1) = \tilde{A}_s Y_e(n) + \tilde{L} s(n), \quad (4.5a)$$

$$s(n) = \tilde{C} Y_e(n), \quad (4.5b)$$

where \tilde{A}_s is the linear evolution matrix, \tilde{L} is the observer matrix, while \tilde{C} is the measurement matrix. These matrices are determined using system identification techniques based on the input-output relation only and described hereafter. Assuming $\mathcal{D} = 0$, the matrices of the desired LTI MIMO system in Equation 4.3 are related to Equation 4.5 through $\tilde{A}_s = \mathcal{C} \mathcal{A} \mathcal{C}^{-1}$ and $\tilde{L} = \mathcal{C} \mathcal{B}$. Actually, the model has to consider the physical perturbations rather than the measurements in Equation 4.5a and also the noise in Equation 4.5b to capture the real dynamics

$$Y_e(n+1) = \tilde{A}_w Y_e(n) + \tilde{B}_w w(n) \quad (4.6a)$$

$$s(n) = \tilde{C} Y_e(n) + g(n), \quad (4.6b)$$

where $\tilde{B}_w w(n)$ is the unknown driving term and $g(n)$ is the measurement noise. The real linear evolution matrix \tilde{A}_w is directly computed from the other matrices, using Equation 4.6a, Equation 4.5a and Equation 4.6b

$$\tilde{A}_w = \tilde{A}_s + \tilde{L} \tilde{C}. \quad (4.7)$$

4.1.2.3 System identification

The system identification comprises three steps summarized in Figure 4.1. The POD modes are first computed from the learning data set which is made of velocity fields recorded while the flow is randomly perturbed upstream. This data set must contain enough events to build an efficient reduced-order model. The number of velocity fields to retain depends consequently on the perturbation generation settings and the sampling frequency of the PIV setup. According to Sirovich (1987), the number of POD modes to conserve is defined through the percentage of energy they contain. However the most important criteria to select the appropriate number of modes are the sensor nature and position. The position is thereby verified by computing the relative error between the measures by the sensors and the reconstructed measures from a certain amount of POD modes (observability of the system). Then a subspace identification algorithm (Qin, 2006) is applied to calculate the state matrices of the stochastic linear system in Equation 4.3. The so-called "N4SID" algorithm (Van Overschee & De Moor, 1994, 1995) is well suited for this step.

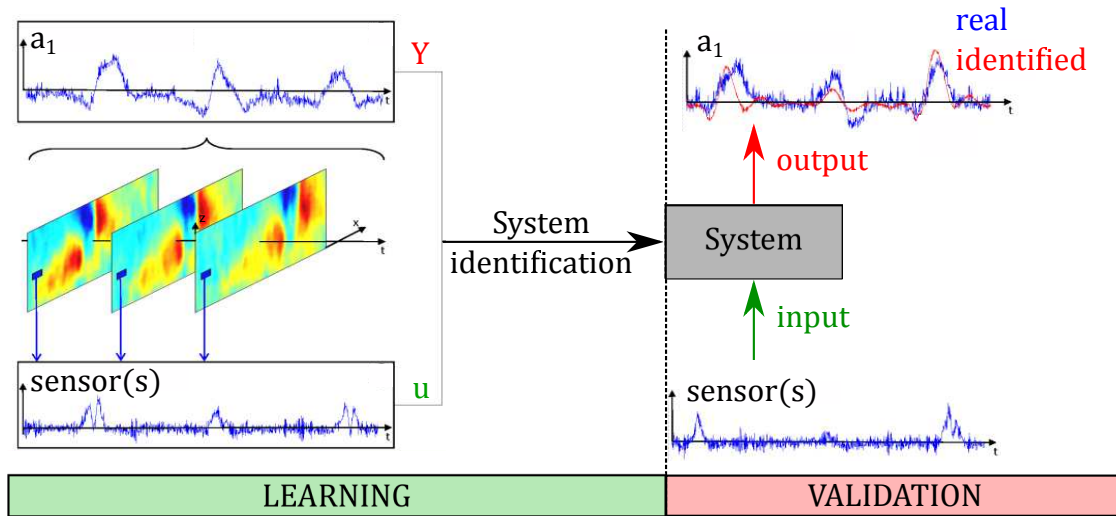


Figure 4.1 – Sketch of a system identification method using POD coefficients a_i as output.

Finally the model is tested on a validation data set by comparing the predicted output POD coefficients to the real ones. Contrary to the learning step, a high temporal resolution is required because of the nature of the system itself.

4.2 Experimental application

As it has been specifically designed for amplifier flows, the dynamic observer is applied to the transient boundary layer. The results are evaluated as the ones numerically obtained by Guzmán Iñigo *et al.* (2014).

4.2.1 The boundary layer over a flat plate

The noise amplifier studied in the present chapter is the zero pressure gradient two-dimensional (2D) boundary layer flow over a flat plate. Even if this flow is less complex than the adverse pressure gradient case, it contains interesting dynamics to capture, which have been intensively studied and theorized (Kachanov, 1994). Thereby, this flow may be delimited in three successive regions: the laminar one also called the Blasius flow (Schlichting & Gersten, 2017), the transient one and the turbulent one. Two convective instabilities work in the two first regions. They produce different structures described hereafter, depending on the nature of the small upstream perturbations.

4.2.1.1 Dynamics description

Due to its viscosity ν and the free-stream U_∞ , the flow near the wall undergoes shear stress τ_w , as explained by Prandtl first. At low Reynolds numbers the dissipative effect of the viscosity is more important than the shearing: this is the laminar regime. Increasing the Reynolds number inverts the trend and the kinetic energy rises: this is the turbulent regime. It produces vorticity which is diffused vertically and advected downstream and the boundary layer thickness δ grows consequently.

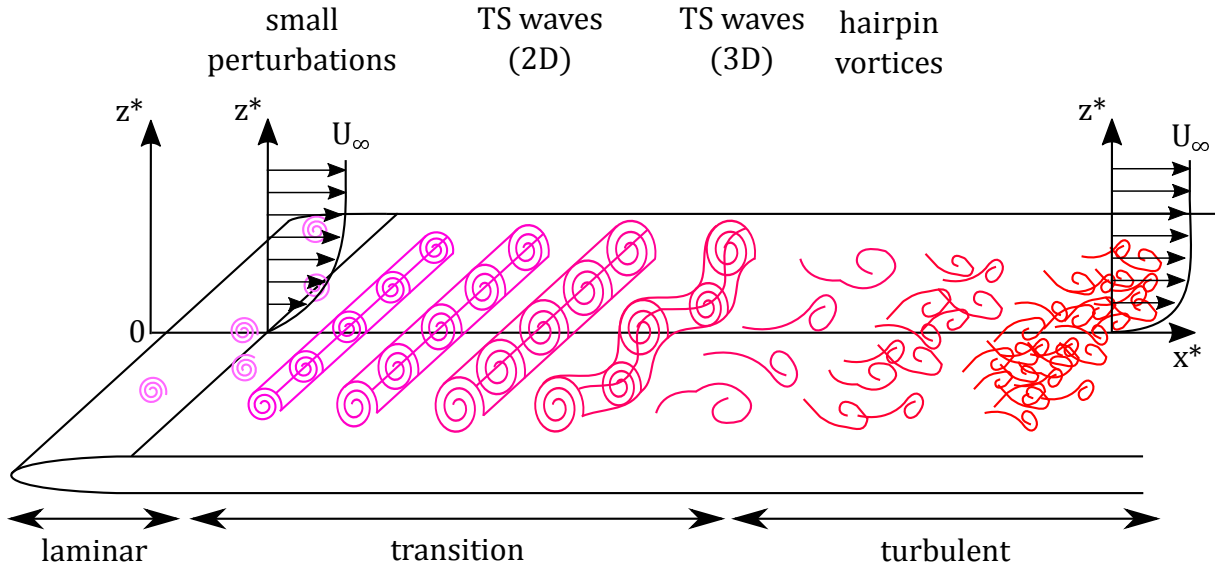


Figure 4.2 – Sketch of a transient boundary layer undergoing a T-S instability.

Small free-stream vortices penetrating or generated in the boundary layer are transformed into the so-called Tollmien-Schlichting (T-S) waves by the natural instability¹. The amplitude of these waves increases downstream until the emergence of alternating peaks and valleys (Figure 4.2), going from two-dimensional stable to three-dimensional unstable structure (Klebanoff *et al.*, 1962). The waves finally breakdown into hairpin eddies, becoming then a fully turbulent flow with small-scale structures (spots, eddies) and intense fluctuations. This instability is referred as a receptivity problem since it linearly amplifies small specific upstream perturbations (Kachanov, 1994).

Another transition process may occur if the turbulence intensity of the flow is higher than 1% (Morkovin, 1985): the bypass transition. It is referred as the secondary instability and it generates groups of streaks, which are streamwise structures periodically distributed in the spanwise direction Matsubara & Alfredsson (2001). This instability can be well forced and observed in a laboratory environment as Duriez *et al.* (2009) did to exhibit the self-sustaining process between the streaks and the streamwise vorticity. The streaks finally collapse into turbulent spots (Schlatter *et al.*, 2008) like the T-S waves.

Both transitions are not completely uncorrelated since the streaky structures of the bypass tran-

1. History of the works leading to their study is well detailed by Eckert (2017).

sition looks like the 3D shape of the T-S waves and the natural transition spectrum signature is also identified in the streaks dynamics (Hughes & Walker, 2000). Modelling these instability mechanisms in a control purpose is therefore of interest since the growing structures advected downstream and tilted by the free-stream provoke finally the flow breakdown into turbulence (Butler & Farrell, 1992). Delaying this transition is thus a good strategy to reduce the drag related to the skin friction. For instance, at moderate turbulence intensity, the T-S waves can be stabilized by streaks of low amplitude forced (Cossu & Brandt, 2002; Fransson *et al.*, 2006) or appearing naturally (Martin *et al.*, 2015). The reconstruction and the prediction of the T-S waves only are investigated in the present experiment.

4.2.1.2 Flow characteristics

Defining some characteristics of the flow allows to know the instant when the different dynamics described above are triggered and the position where they are. The most imaginable value is the boundary layer thickness δ . It conventionally corresponds to the height where

$$v_x(y = \delta) = 0.99U_\infty. \quad (4.8)$$

The displacement thickness $\delta^*(x)$ is the vertical deflection imposed by the boundary layer existence to the potential flow² incoming over the flat plate. It is defined as

$$\delta^*(x) = \int_0^\infty \left(1 - \frac{v_x(x, y)}{U_\infty}\right) dy. \quad (4.9)$$

The Reynolds number $Re_{\delta^*}(x)$ in Equation 4.2a will be consequently based on the displacement thickness

$$Re_{\delta^*}(x) = \frac{\delta^*(x)U_\infty}{\nu}. \quad (4.10)$$

The streamwise position allows also a common alternative definition Re_x .

In a similar way as the displacement thickness, the momentum thickness $\theta(x)$ is the vertical shift required for the boundary layer flow to recover from the lost in momentum due to the shear stress τ_w , in comparison of the potential flow. It is defined as

$$\theta(x) = \int_0^\infty \frac{v_x(x, y)}{U_\infty} \left(1 - \frac{v_x(x, y)}{U_\infty}\right) dy, \quad (4.11)$$

whose flux deficit is equal to the 2D skin friction drag $\rho U_\infty^2 \theta = \int_0^x \tau_w dx$.

The last two thickness definitions lead to the shape factor $\mathcal{H}(x)$

$$\mathcal{H}(x) = \frac{\delta^*(x)}{\theta(x)}. \quad (4.12)$$

The turbulent separation is assumed to occur when $1.8 < \mathcal{H} < 2.4$ according to Head (1960) and Cebeci *et al.* (1972). Theoretical values for the laminar and the turbulent³ regions are summarized in Table 4.1.

2. Flow in absence of vorticity.

3. There is also another power-law used in some engineering books: $Re_x^{1/5}$.

Characteristics	Laminar profile	Turbulent profile
	Blasius	Prandtl
$\delta(x)/x$	$4.91/\sqrt{Re_x}$	$0.16/Re_x^{1/7}$
$\delta^*(x)/x$	$1.73/\sqrt{Re_x}$	$0.020/Re_x^{1/7}$
$\theta(x)/x$	$0.664/\sqrt{Re_x}$	$0.016/Re_x^{1/7}$
\mathcal{H}	2.59	1.29

Table 4.1 – Theoretical characteristic values for the boundary layer flow.

4.2.2 Experimental setup

4.2.2.1 Water channel

The experiments are carried out in the closed hydrodynamic channel mentioned in the previous chapter and sketched with the investigated flat plate installed in [Figure 4.5](#). For the present study, the free-stream velocity range is $U_\infty \in [3; 7; 12]$ cm.s⁻¹.

4.2.2.2 Boundary layer

A homemade leading edge, designed as a NACA 00020 profile, is used to smoothly start the boundary layer. The flat plate along which the boundary layer grows entirely spans the test section width to manage 2D dynamics at best. The channel height is $H = 8.5$ cm. The origin is located at the beginning of the leading edge ($x = 0$), in the vertical symmetry plane ($y = 0$) and on the flat plate ($z = 0$).

4.2.2.3 Forcing noise

The perturbation is induced by a span-wise inclined slotted jet, whose angle to the wall is 45° ([Figure 4.3](#)). The injection system is composed of glass beads between two pierced grids to avoid undesired structures. It is located 5 cm downstream the leading edge ([Figure 4.5](#)). The jet outlet has a rectangular cross-section which is 0.4 cm long (in the streamwise direction) and 9 cm wide (spanwise direction). Thanks to this geometry, the perturbation can be considered as homogeneous along the spanwise direction.

As described in [Figure 4.4](#), the slotted jet is supplied by a pressurized water tank, monitored by an electro-pneumatic regulator to control the jet velocity $u_{forcing}$, which can be set regarding the frequency $f_{forcing}$, the amplitude $U_{forcing}$, and the length $\delta T_{forcing}$. This setup enables to induce random perturbations by changing these parameters after each pulse. The command signal between the impulses remains at the value avoiding any perturbation generation, as if the slot does not exist.

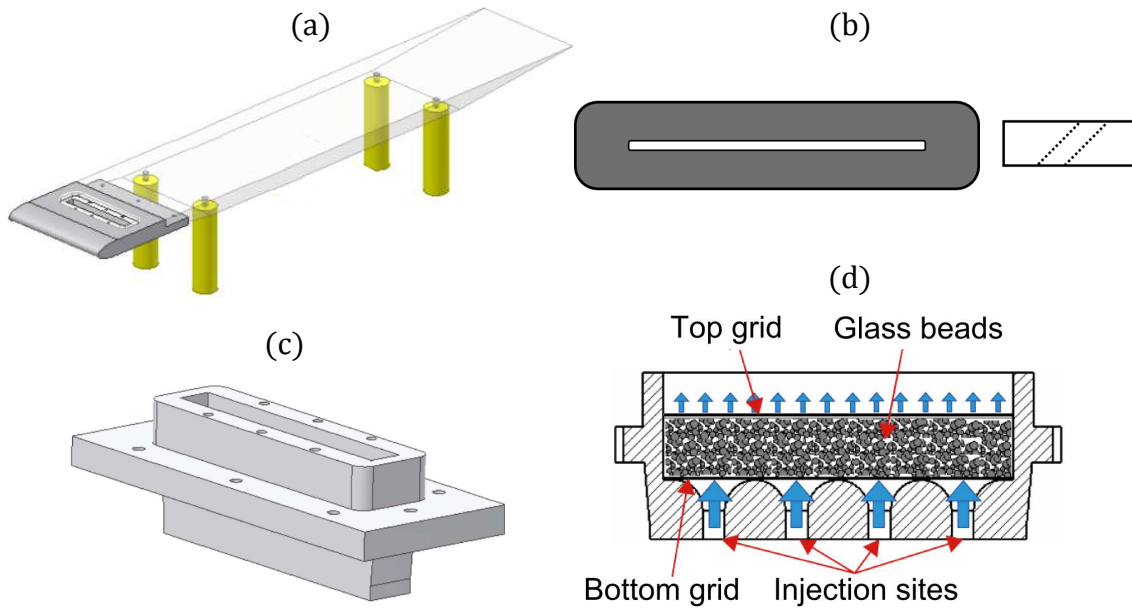


Figure 4.3 – (a) Computer-aided design of the modified flat plate used in the water channel. (b) Inclined slot sketch. (c) 3D view and (d) side view of the jet injection system.

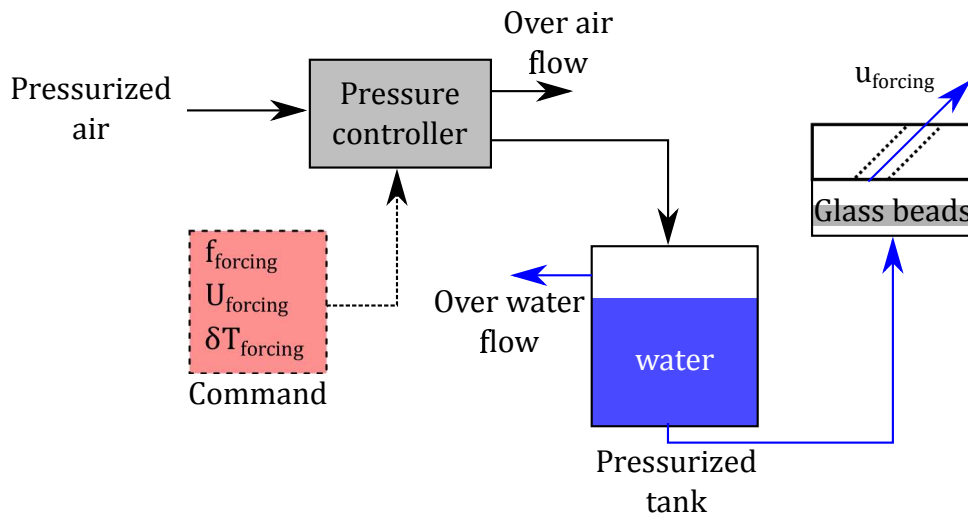


Figure 4.4 – Jet supply circuit.

4.2.2.4 Real-time PIV as a sensor

The flow is seeded with $20\ \mu\text{m}$ neutrally buoyant polyamid seeding particles. The vertical symmetry plane of the test section is illuminated by a laser sheet created by the 8 W continuous laser beam operating at a 532-nm wavelength and passing through a cylindrical lens. A very thin layer of the fluorescent paint *FP Rhodamine 6G* has been applied on the surface illuminated by the laser sheet to reduce the reflections. The snapshots of the illuminated particles are recorded

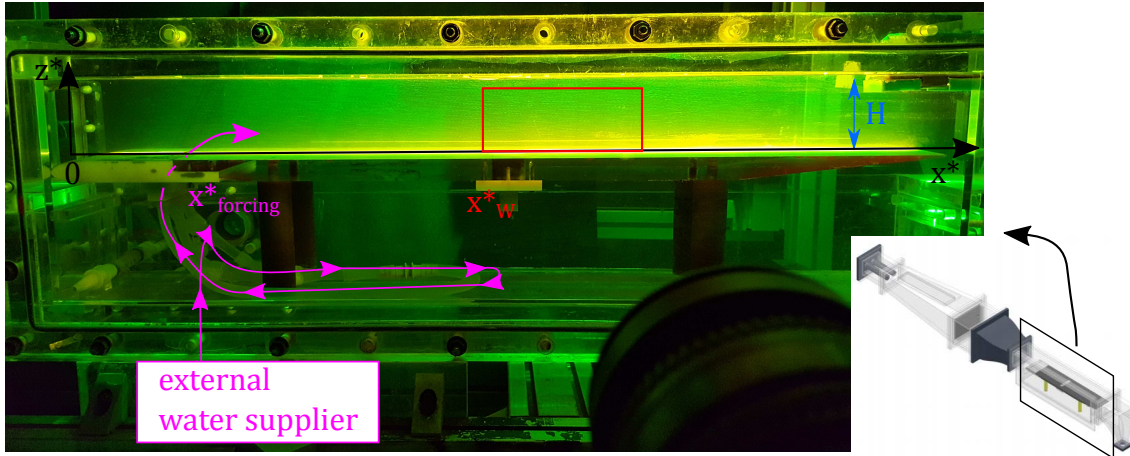


Figure 4.5 – Experimental setup with the PIV plane (red rectangle) and forcing jet (pink arrow) positions. Sketch of the water channel is displayed on the bottom right.

using the hydraulic configuration given in [chapter 2](#). The PIV plane starts 35.1 cm downstream of the leading edge. This position is denoted x_W^* , as illustrated in [Figure 4.5](#). This position is used in [Equation 4.9](#) to define the characteristic length of the flow $\delta_0^* = \delta^*(x_W^*)$ and the resulting Reynolds number taken as reference $Re_{\delta_0^*}$. In the same way, the dimensionless time is $t^* = tU_\infty/\delta_0^*$.

The two dimensional two components (2D-2C) velocity fields $v_x(x, z)$ and $v_z(x, z)$ (respectively the streamwise and wall normal components) are computed at the frequency f_{PIV} using the optical flow algorithm described in [chapter 2](#). Finally a low-pass filter has been applied to the raw data sets with a cutoff frequency f_{cut} at least ten times higher than the highest measured frequency of the forced boundary layer dynamics.

Instead of the wall sensor as in the numerical work of [Guzmán Iñigo *et al.* \(2014\)](#), a different sensor has been used in the present experiment. Indeed, different values such as the vorticity ω_y and the λ_{Ci} -criterion, have been monitored directly from the local fluctuations of the velocity fields in the region of the instantaneous PIV snapshot. The size and location of the sensor may play a role in the efficiency of the learning process because the former will act as a spatial filter and the later will be crucial for its ability to detect relevant flow variations ([Guzmán Iñigo *et al.*, 2016](#)). This point will be discussed later.

4.2.3 Flow characterization

4.2.3.1 Base flow

The unforced flow is first studied for three Reynolds numbers, $Re_{\delta_0^*} = [224, 297, 337]$, detailed in this section. The base flow $\mathbf{V}_{base} = (\bar{v}_x, \bar{v}_z)$ is processed over $t^* = 50$, $t^* = 250$ and $t^* = 500$ respectively.

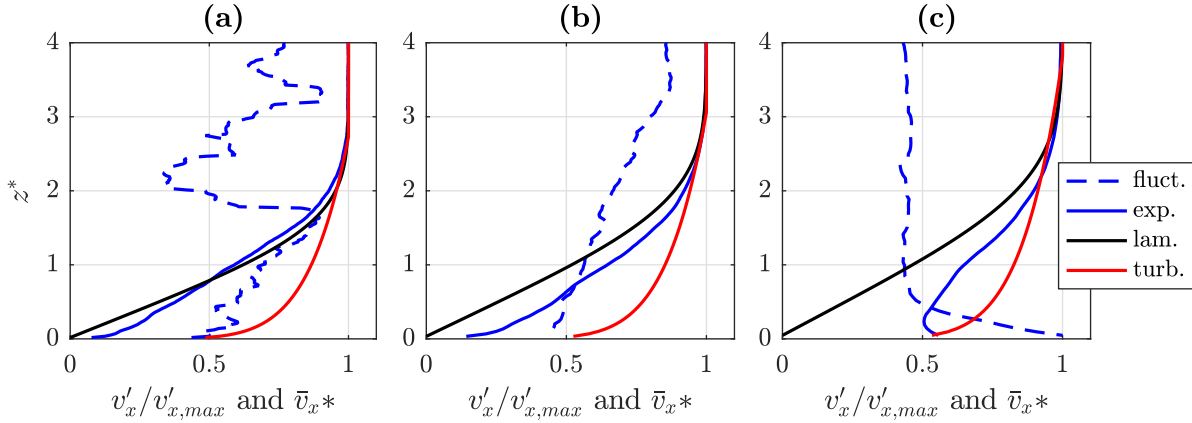


Figure 4.6 – Experimental (solid blue), theoretical laminar (solid black) and theoretical turbulent (solid red) time-averaged velocity profiles, together with the fluctuations (dashed blue) for **(a)** $Re_{\delta_0^*} = 224$, **(b)** $Re_{\delta_0^*} = 297$ and **(c)** $Re_{\delta_0^*} = 337$. Profiles measured at x_W^* .

The nature of the main stream is first quantified in terms of flow uniformity. The standard deviation σ and the mean velocity profile are measured at x_W^* . The maximum turbulence intensity is $T_u = \sigma/U_\infty = 0.23\%$. **Figure 4.6(a-b)** show a laminar behavior for $Re_{\delta_0^*} = 224$ and $Re_{\delta_0^*} = 297$ since the maximum of their fluctuations is located in the free-stream. On the other hand the fluctuations are slightly stronger near the wall for $Re_{\delta_0^*} = 337$ [**Figure 4.6(c)**]. According to [Morkovin \(1985\)](#), this enables to obtain the natural transition to turbulence with T-S waves as desired. This indeed keeps only 2D dynamics by avoiding the bypass transition characterized by streaks.

The streamwise velocity profiles are also compared to the theoretical ones in **Figure 4.6**. At $Re_{\delta_0^*} = 224$, the experimental velocity is rather well approximated by the Blasius profile. It begins to go slightly closer to the turbulent approximation when increasing the Reynolds number. At $Re_{\delta_0^*} = 337$ it is clearly in the transitional dynamics [**Figure 4.6(c)**]. These observations are confirmed by computing the boundary layer characteristics.

Like the velocity profile, **Figure 4.7(d-f)** highlight that the computed displacement thickness progress from the laminar model to the turbulent one as soon as the corresponding Reynolds number increases **Figure 4.7(j-l)**. The shape factor leads consequently to expected values, decreasing from $\mathcal{H} \sim 2$ at $Re_{\delta_0^*} = 224$ to $\mathcal{H} \sim 1.5$ at $Re_{\delta_0^*} = 337$. As the flow in the observed region is desired to be transitional, the perturbations will be generated for $Re_{\delta_0^*} \geq 337$ but not too high to remain in the linear approximation imposed by the system identification method.

4.2.3.2 Forced flow

Experimentally the forcing design is one of the toughest aspects since the same perturbations cannot be brought out as in [Guzmán Iñigo et al. \(2014\)](#). In the present work, a random 2D jet is created by sending a square signal, similar to the one in **Figure 4.9**, to the air pressure controller with the following settings (0 being equivalent to a closed slot): the jet frequency

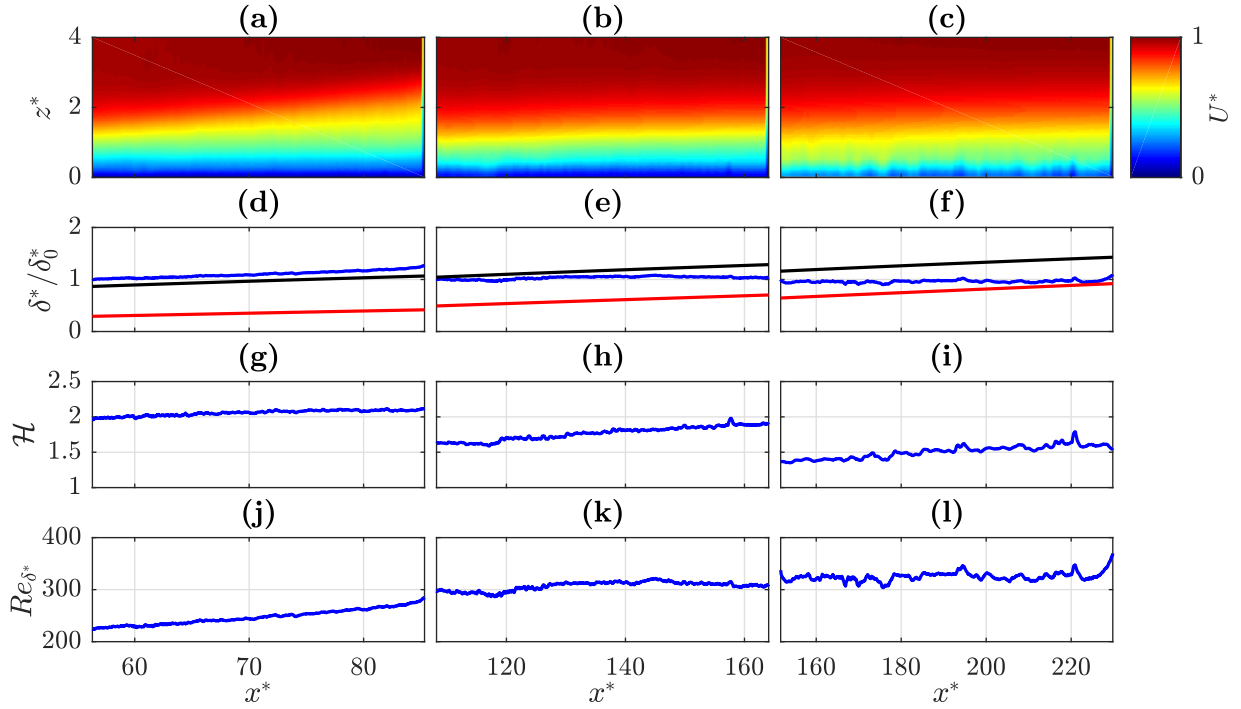


Figure 4.7 – Flow characteristics for the different Reynolds numbers, $Re_{\delta_0^*} = 224$ (left), $Re_{\delta_0^*} = 297$ (middle) and $Re_{\delta_0^*} = 337$ (right): **(a-c)** the streamwise velocity, **(d-f)** the displacement thickness, **(g-i)** the shape factor and **(j-l)** the Reynolds number along the streamwise direction. Theoretical values are also indicated for the displacement thickness: laminar (black) and turbulent (red).

$f_{forcing}^* \in [0; 0.12]$, the output velocity $U_{forcing}^* \in [0; 0.75]$, and the pulse length $\delta T_{forcing}^* \in [0; 4.2]$. A resulting T-S wave is displayed in Figure 4.8.

The kinetic energy (KE) k^* , previously defined in chapter 3, is analyzed to study the generated perturbations. Figure 4.10 shows the KE evolution in time at two streamwise positions, x_W^* and $x_W^* + 25$. The lag between the two curves gives the length of time which perturbations travel the distance between the measurements locations. The resulting velocity of the T-S waves is 0.373, in agreement with Guzmán Iñigo *et al.* (2014). As expected most of the perturbations are increased by the instability, even if some of them seem to decrease downstream. It may be due to a too high jet amplitude, generating a strong forcing but without the proper dynamics to be amplified (Luchini, 2000). A surprising aspect of these results concerns the Reynolds value at which the T-S waves are obtained since it is under the theoretical one ($Re_{\delta_0^*}^{crit} = 520$). At the time of the thesis submission, this is still under investigation and it is planned to be discussed in further works.

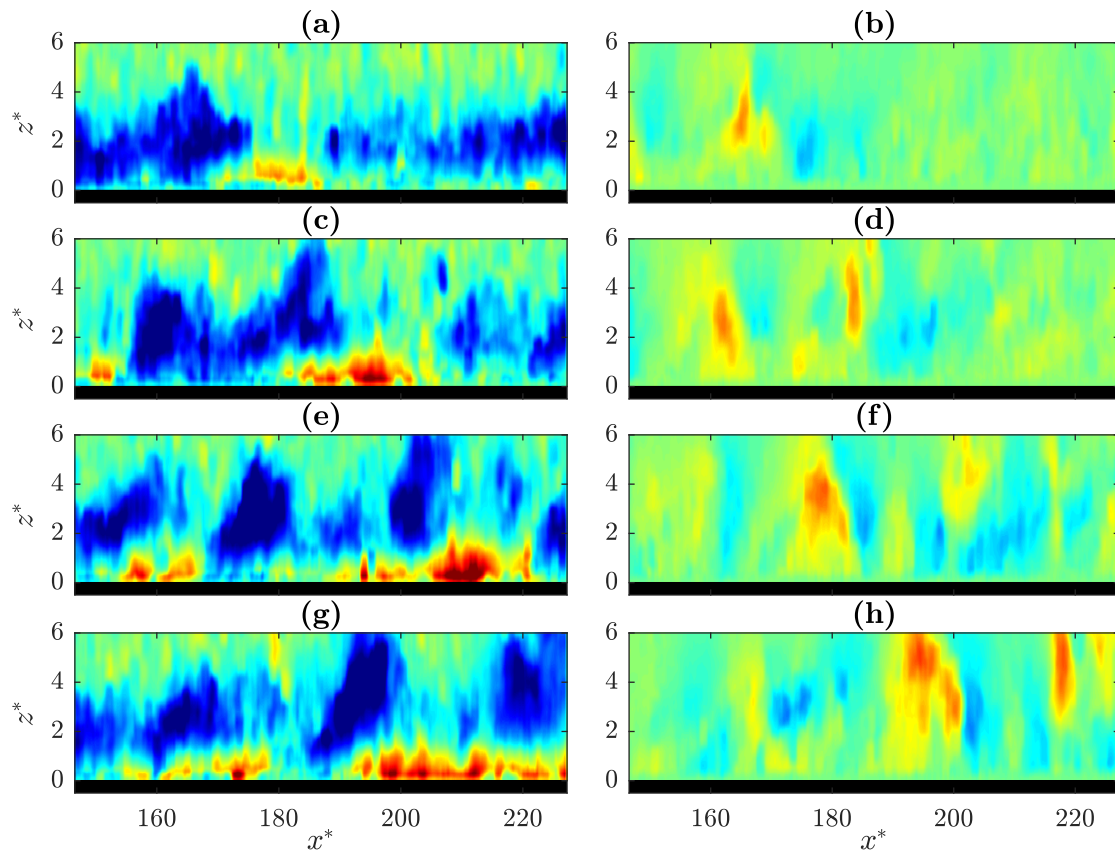


Figure 4.8 – Successive instantaneous streamwise (left) and vertical (right) components of the velocity fields while a T-S wave propagates.

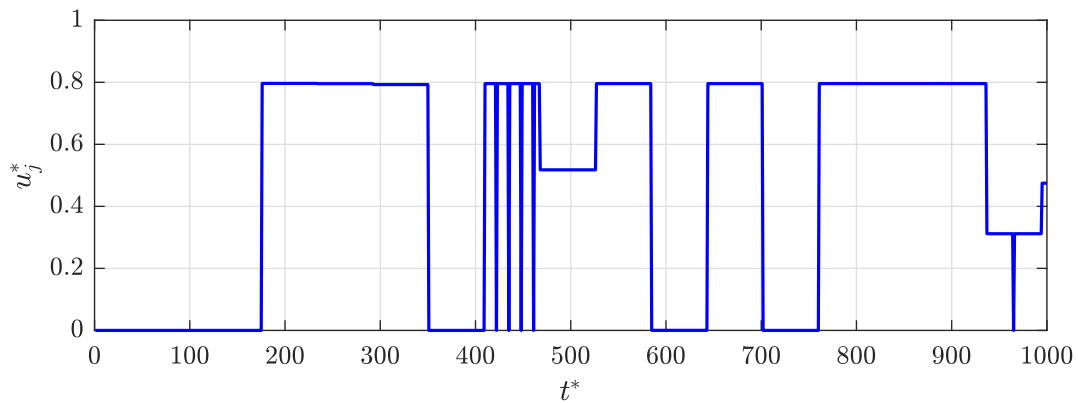


Figure 4.9 – Example of a random signal created to perturb the flow upstream.

4.2.4 Experimental dynamic observer

The retaining learning data set is composed of 1500 velocity fields sampled at $f_{PIV}^* = 1.1$ with a spatial resolution of 0.24 mm.px^{-1} , containing about ten events perturbing the base flow. The length of the learning data set is related to the occurrence of recorded events: it is useless to

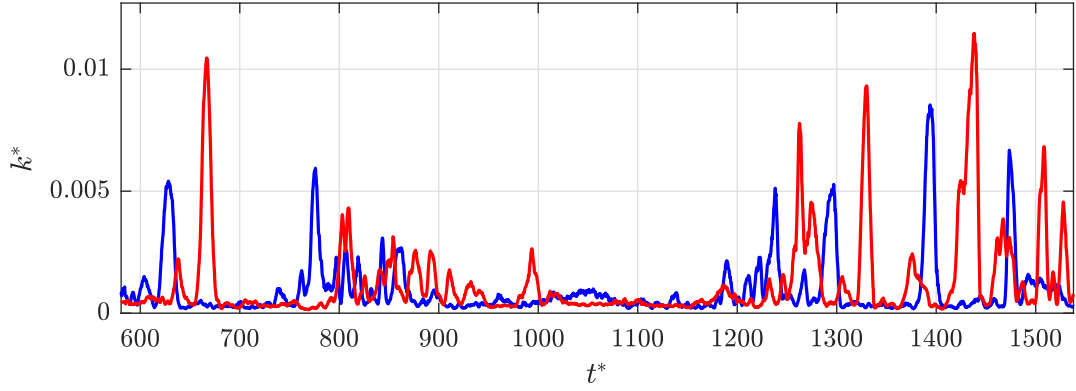


Figure 4.10 – Mean kinetic energy $k^*(t^*)$ in the vertical pixels at x_W^* (blue) and at $x_W^* + 25$ (red).

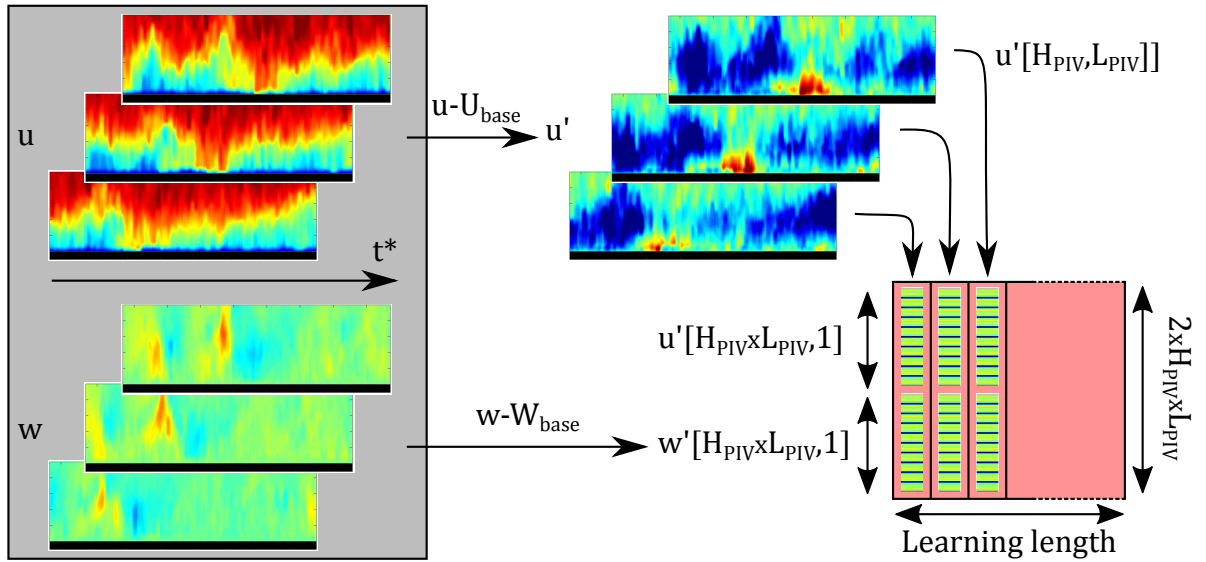


Figure 4.11 – Sketch of the learning matrix (red) construction from the data set (gray), explaining how the data are stored.

increase the number of velocity fields without increasing the number of perturbations. Directly extracted by subtracting the base flow obtained before, the fluctuations fields are gathered in the learning matrix as explained in Figure 4.11. The size of this matrix can be reduced by spatially down-sampling the fields and/or sub-sampling the data set. The POD is then applied to the learning matrix.

4.2.4.1 POD modes

The POD energy and the normalized POD modes of the streamwise velocity v_x^* are given in Figure 4.12. The first 32 modes accumulate more than 80% of the total energy, the first one being at 46%. Beyond the eleventh POD mode, each other mode contains less than 1% of the

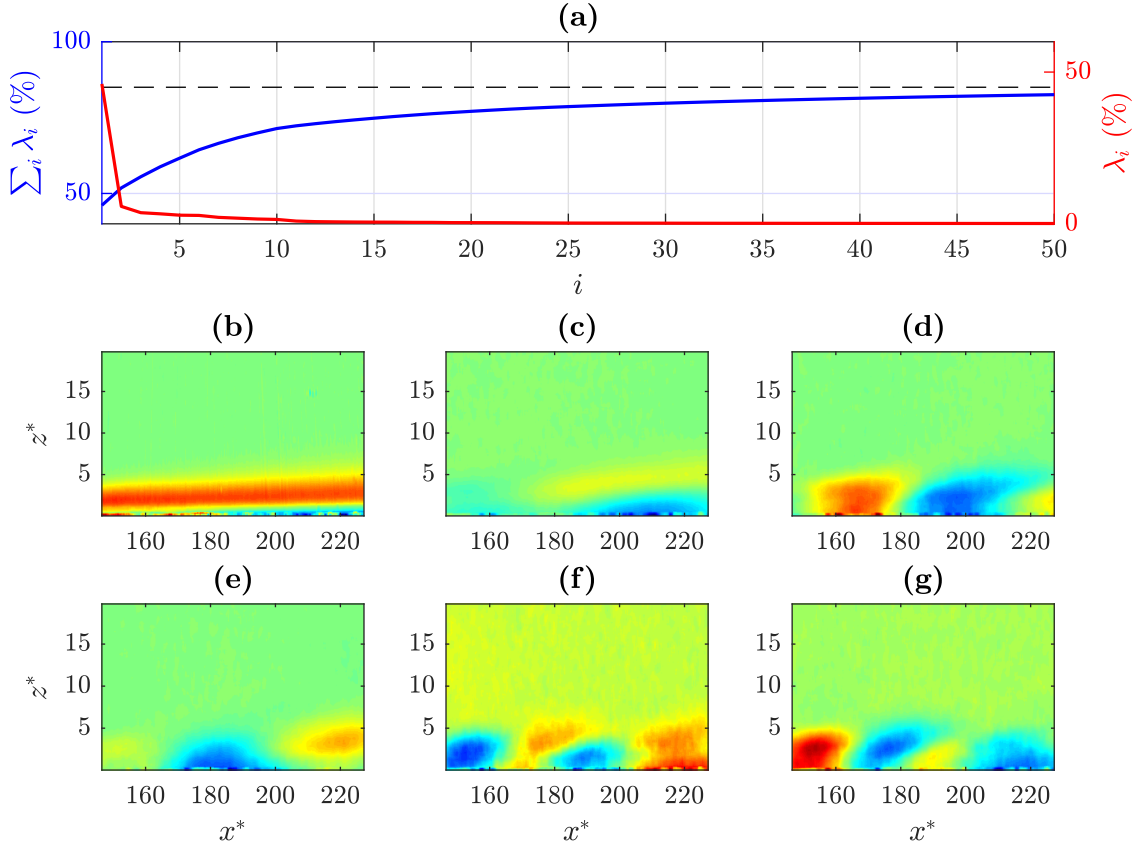


Figure 4.12 – (a) POD energy (red) and cumulated energy (blue). The 85%-threshold is displayed (dashed black). Normalized POD modes of the streamwise velocity v_x^* : (b) Φ_1 , (c) Φ_2 , (d) Φ_3 , (e) Φ_4 , (f) Φ_5 and (g) Φ_6 .

energy of the first one. The spatial organization of the first mode contains all the structures advected downstream. The T-S waves are globally well captured by the following modes. The most energetic structures, rather downstream, look indeed like the most developed T-S waves [Figure 4.12(c-e)], whereas the lowest energetic modes contain weaker shapes of the T-S waves localized upstream [Figure 4.12(f) and (g)].

4.2.4.2 Sensors definition

The sensors used are directly derived from the velocity fields. Various natures, positions and numbers of sensors have been tested. The streamwise v_x^* and the vertical components v_z^* are first both monitored in the same region Ω_S placed upstream at $x_s^* = 150$ as shown in Figure 4.13(a) and (b). The sensor does not contain the ten first pixels (interrogation window radius) the closest to the wall to limit noisy data. It is also not too large too avoid a smoothing effect. The nature of this sensor $s = [\langle v_x^* \rangle_{\Omega_S}, \langle v_z^* \rangle_{\Omega_S}]$ is based on the sensitivity of such values to the T-S waves. The position of Ω_S has been chosen to detect the perturbations incoming in the PIV window as soon as possible. A downstream sensor is avoided in purpose in the present study since the final

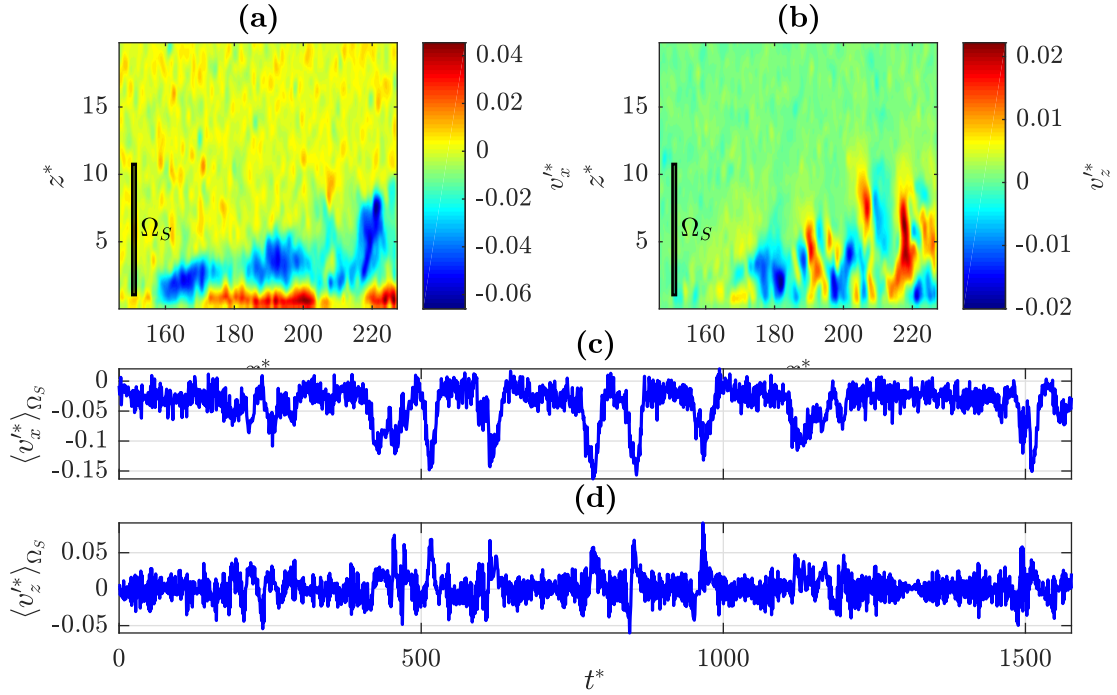


Figure 4.13 – Instantaneous (a) streamwise and (b) vertical components of the fluctuating velocities at $t^* = 310$, together with the sensors area Ω_S (rectangles). Time series of (c) the streamwise and (d) the vertical components of the fluctuating velocity, both space-averaged over Ω_S .

objective will be the design of a feedforward control.

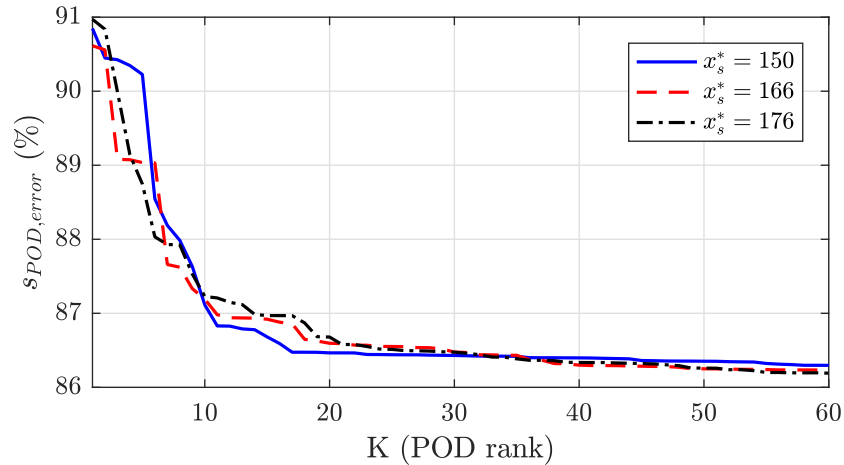


Figure 4.14 – Relative error between the real and the POD sensor at different streamwise positions.

The observability of the sensor s regarding the POD modes $\{\Phi_i\}_{i=1..K}$ is given by measuring the same values in the K modes as in the velocity fields. The resulting sensor $s_{POD}(K)$ is then

compared to the real sensor s :

$$s_{POD,error}(K) = \frac{\|s_{POD}(K) - s\|}{\|s\|}. \quad (4.13)$$

Figure 4.14 shows the results for the considered sensors at different streamwise positions. Taking a low number of POD modes into account leads to slightly better results for the sensors localized in the most upstream part of the PIV window. This is due to the spatial organization of the first POD modes as previously observed. Adding more modes compensates this difference. Beyond a threshold, there is almost no more gain. For the present case, the most important gain without requiring too extra modes is obtained with the first 17 modes for $x_s^* = 150$. Nevertheless the error remains high since the noise has a huge impact for the defined sensors which fluctuate around 0 when there is no perturbation. Only considering snapshots when perturbation occurs should improve this evaluation.

4.2.4.3 Reduced-order model and validation

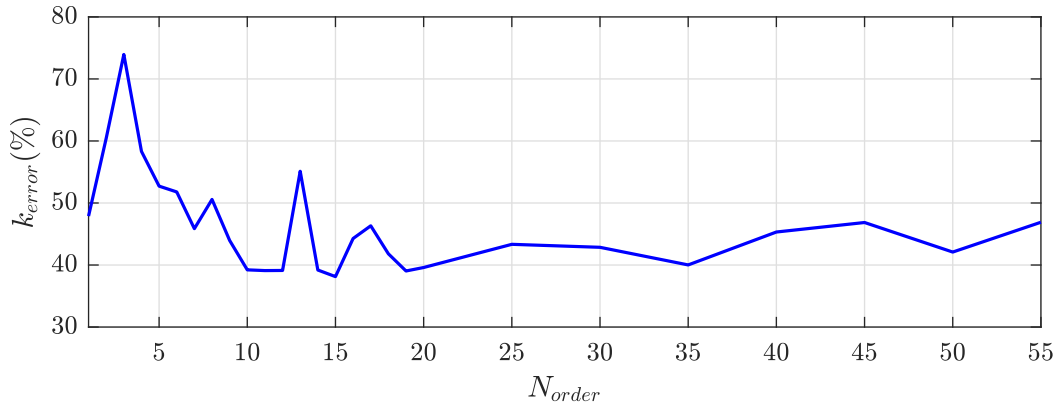


Figure 4.15 – Difference between the real POD coefficients and the ones estimated by ROMs computed with various state orders N_{order} for the sensor $s = [\langle v_x^* \rangle_{\Omega_S}, \langle v_z^* \rangle_{\Omega_S}]$.

The ROM is finally computed using N4SID. Different model orders $N_{order} \in [1 : 55]$ have been tested since there is no explicit rule to select it. Even if the validation data set is recorded with the same settings as the ones generating the perturbations, it is independent from the learning data set. To evaluate the global accuracy of the prediction for the validation data set, the KE is computed from the POD coefficients $k_{POD}^* = \sum_{i=1}^K a_i^2$ (Guzmán Iñigo *et al.*, 2014). The difference between the real POD coefficients and the ones estimated by the ROM is then estimated via k_{error} , defined as

$$k_{error} = 100 \frac{\|k_{POD,real}^*(t^*) - k_{POD,model}^*(t^*)\|}{\|k_{POD,real}^*(t^*)\|}. \quad (4.14)$$

Figure 4.15 gives the resulting k_{error} with respect to N_{order} for the sensor $s = [\langle v_x^* \rangle_{\Omega_S}, \langle v_z^* \rangle_{\Omega_S}]$. It reveals that the best recover, $k_{error} = 38.1\%$ is obtained for $N_{order} = 15$.

For this state order, Figure 4.16(a) compares the KE resulting from the output POD coefficients of the model (red) and the real ones (blue). Even if the amplitudes do not match during the

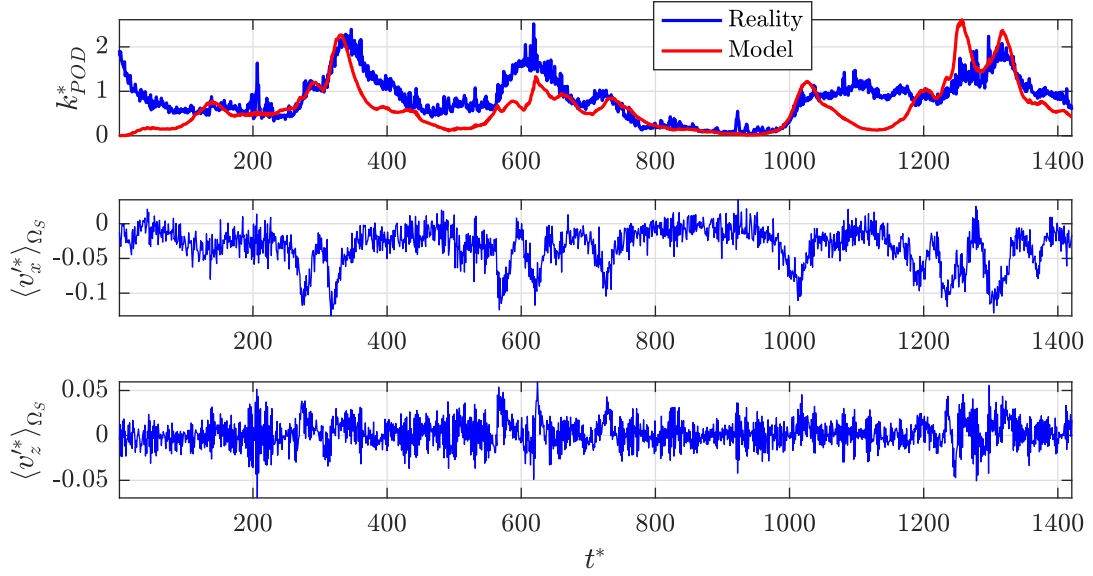


Figure 4.16 – (a) KE from the POD coefficients k_{POD}^* for the real validation data (blue) and the output of the dynamic observer (red). Time series of (b) the streamwise and (c) the normal components averaged over Ω_S .

validation step, the fluctuations are close after a delay $\Delta t^* \sim 48$, meaning that the model effectively captured the dynamics. The minimization of such fluctuations are a good objective for a closed-loop control. The missing T-S wave around $t^* \sim 1100$ can be related to the sensors time series since it seem undetected by both of them. Nevertheless, any perturbation well detected by both sensors appears in the model output.

A passing T-S wave is depicted by three successive instantaneous fields in Figure 4.17(a,d,g). Their corresponding POD reconstructions are given in Figure 4.17(b,e,h). As expected from Figure 4.12(a), most of the large-scale structures are well contained by those 17 POD modes. The noise of the velocity fields is filtered by their projection onto the POD modes. Finally the corresponding output of the system are shown in Figure 4.17(c,f,i). The fields appear to be rather close to their real projections, confirming the results obtained with the KE.

4.2.4.4 Other tested sensors

Other sensors have been tested: the velocity components alone, the swirling strength criterion λ_{C_i} alone (see chapter 3), then combined with the streamwise component. As shown by Figure 4.18, the streamwise and vertical velocity proved the best sensors for $N_{order} \in [5 : 37]$ and $N_{order} > 49$, whereas it is the vortex identification criterion otherwise. As the vertical component lead to the worst results, the swirling strength criterion and the streamwise component have been tested together. They turn out to only improve the ROM computed for $N_{order} = 20$. Even if this sensor lead to an error of the same order as the first presented one, the obtained ROM requires a higher state order.

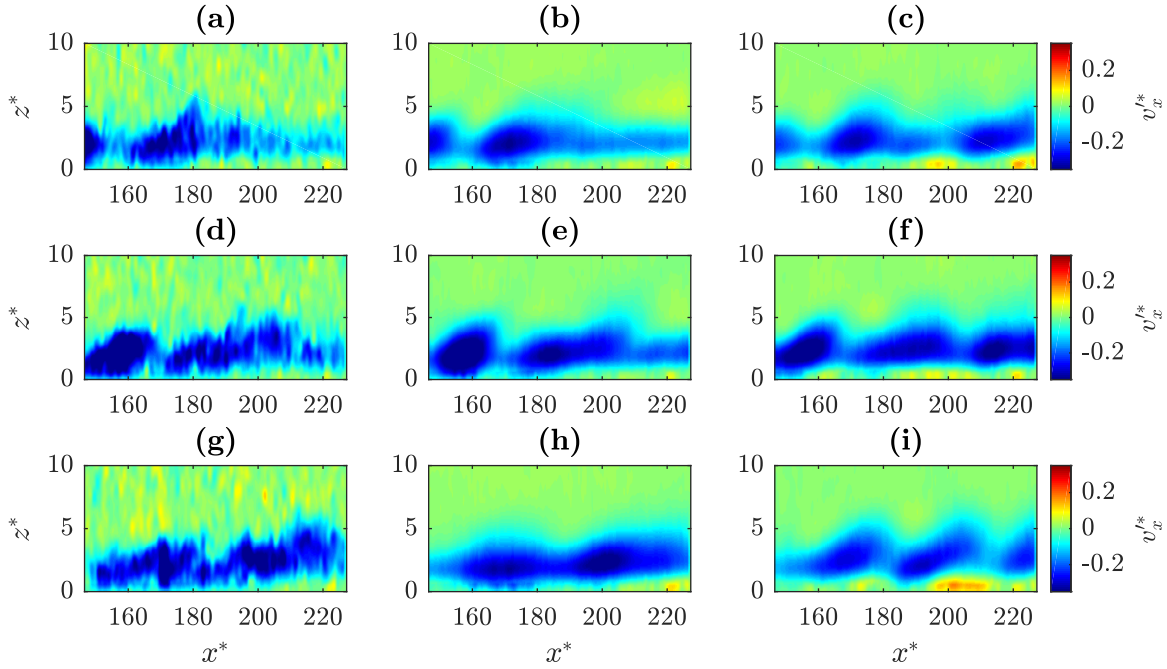


Figure 4.17 – Real (left), reconstructed by POD (middle) and estimated (right) streamwise component of successive instantaneous velocity fields (from top to bottom) separated of $\Delta t^* = 18$.

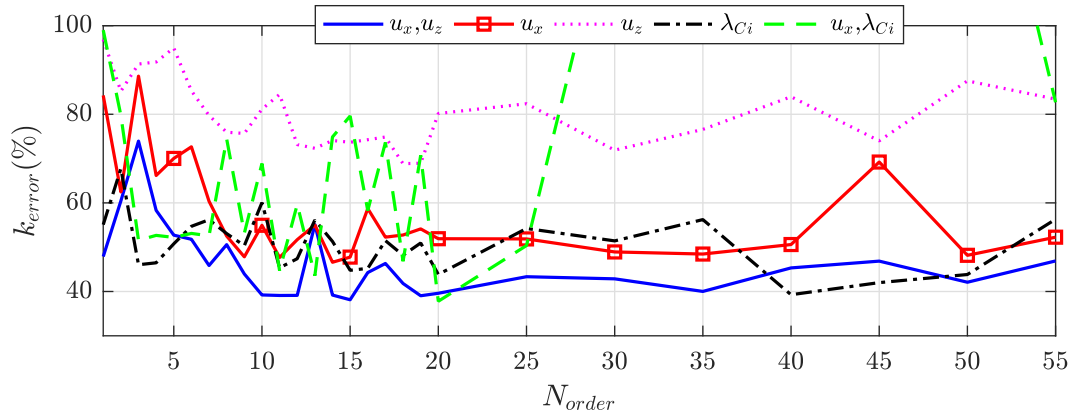


Figure 4.18 – Difference between the real POD coefficients and the ones estimated by ROMs computed with various state orders N_{order} for different natures of sensor.

4.3 Conclusions and perspectives

A system identification method based on the N4SID algorithm has been successfully implemented for the forced boundary layer flow developing T-S waves. The input data have been obtained from optical flow PIV measurements, retaining in a small area of the velocity fields a double visual sensor of the streamwise fluctuating velocity and either the vertical fluctuating velocity or the swirling strength criterion. The KE increase induced by the T-S waves propagating along the flat plate has been identified with acceptable agreement between the model and the real flow via

a POD.

4.3.1 Discussion

The computation of the POD modes and coefficients requires large usage of memory regarding the dense fields obtained via optical flow. The high data density inherent to this velocimetry method may thus become a drawback in the present case, as it was foreseen by [Champagnat *et al.* \(2011\)](#). Nonetheless, spatially down-sampling the field turns out to be a good solution, giving the choice (if the hardware allows it) between high space accuracy and computation cost, the reduced-order model being still available.

A larger PIV window would be better to capture a longer T-S waves evolution, giving more distributed POD modes along the flat plate. The description of the flow dynamics would be improved but it would consequently increase the system state order. This would require to change the camera objective to keep the spatial accuracy without extending the number of vectors and therefore the size of the learning matrix.

4.3.2 Perspectives

The motivation of the presented work is to delay the laminar-turbulent transition by suppressing the captured T-S waves. Further works will therefore concern the closed-loop control based on the flow reconstruction ([Ottonelli, 2014](#); [Guzmán Iñigo *et al.*, 2014](#)) since the actuator is already installed. The region investigated in this chapter contains indeed a slotted jet designed like the one forcing the T-S waves, which was covered with a plate visible in [Figure 4.5](#). This experimental application will first require a similar study as the one presented here, including an additional random forcing by the actuator. The command signal sent to the actuator will be associated to the sensor(s) to create the input u of the system. The reduction of the KE may be finally a good objective to fix to the built system since it can also be tracked in real-time.

Bibliography

- BARBAGALLO, A., SIPP, D. & SCHMID, P. (2009) Closed-loop control of an open cavity flow using reduced-order models. *Journal of Fluid Mechanics* **641** (1), pp. 1–50. [64](#)
- BERGMANN, M. & CORDIER, L. (2008) Control of the circular cylinder wake by trust-region methods and POD reduced-order models. *Tech. Rep.* RR-6552. INRIA. [64](#)
- BERKOOZ, G. & TITI, E.S. (1993) Galerkin projections and the proper orthogonal decomposition for equivariant equations. *Physics Letters A* **174** (1-2), pp. 94–102. [64](#)
- BRANDT, L., SIPP, D., PRALITS, J.O. & MARQUET, O. (2011) Effect of base-flow variation in noise amplifiers: the flat-plate boundary layer. *Journal of Fluid Mechanics* **687**, p. 503–528. doi:10.1017/jfm.2011.382. [64](#)
- BUTLER, K.M. & FARRELL, B.F. (1992) Three-dimensional optimal perturbations in viscous shear flow. *Physics of Fluids A: Fluid Dynamics (1989-1993)* **4** (8), pp. 1637–1650. [69](#)
- CEBECI, T., MOSINSKIS, G.J. & SMITH, A.M.O. (1972) Calculation of separation points in incompressible turbulent flows. *Journal of Aircraft* **9**, pp. 618–624. [69](#)
- CHAMPAGNAT, F., PLYER, A., LE BESNERAIS, G., LECLAIRE, B., DAVOUST, S. & LE SAINT, Y. (2011) Fast and accurate PIV computation using highly parallel iterative correlation maximization. *Experiments in Fluids* **50**, pp. 1169–1182. doi:10.1007/s00348-011-1054-x. [82](#)
- CHOMAZ, J.M. (2005) Global instabilities in spatially developing flows: non-normality and nonlinearity. *Annual Review of Fluid Mechanics* **37**, pp. 357–392. [64](#)
- COSSU, C. & BRANDT, L. (2002) Stabilization of Tollmien–Schlichting waves by finite amplitude optimal streaks in the Blasius boundary layer. *Physics of Fluids* **14** (8), pp. L57–L60. doi:10.1063/1.1493791. [69](#)
- DURIEZ, T., AIDER, J.L. & WESFREID, J.E. (2009) Self-sustaining process through streak generation in a flat-plate boundary layer. *Phys. Rev. Lett.* **103**, p. 144502. doi:10.1103/PhysRevLett.103.144502. [68](#)
- ECKERT, M. (2017) A kind of boundary-layer ‘flutter’: The turbulent history of a fluid mechanical instability. *arXiv* 1706.00334. [68](#)
- FRANSSON, J.H.M., BRANDT, L., TALAMELLI, A. & COSSU, C. (2006) Experimental study of the stabilization of Tollmien–Schlichting waves by finite amplitude streaks. In *IUTAM Symposium on Laminar-Turbulent Transition* (ed. R. Govindarajan), pp. 299–304. Dordrecht: Springer Netherlands. doi:10.1007/1-4020-4159-4_41. [69](#)
- GUZMÁN IÑIGO, J., SIPP, D. & SCHMID, P.J. (2016) Recovery of the inherent dynamics of noise-driven amplifier flows. *Journal of Fluid Mechanics* **797**, pp. 130–145. doi:10.1017/jfm.2016.266. [64](#), [72](#)

- GUZMÁN IÑIGO, J., SIPP, D. & SCHMID, P.J. (2014) A dynamic observer to capture and control perturbation energy in noise amplifiers. *Journal of Fluid Mechanics* **758**, pp. 728–753. doi:10.1017/jfm.2014.553. 64, 67, 72, 73, 74, 79, 82
- HEAD, M.R. (1960) Entrainment in the turbulent boundary layer. *Tech. Rep. R. and M. No. 3152*. Aeronautical Research Council. Ministry of Aviation, England. 69
- HENNING, L., PASTOOR, M., KING, R., NOACK, B.R. & TADMOR, G. (2007) Feedback control applied to the bluff body wake. In *Active Flow Control: Papers contributed to the Conference “Active Flow Control 2006”, Berlin, Germany, September 27 to 29, 2006* (ed. R. King), pp. 369–390. Berlin, Heidelberg: Springer Berlin Heidelberg. doi:10.1007/978-3-540-71439-2_23. 65
- HERVÉ, A., SIPP, D., SCHMID, P. & SAMUELIDES, M. (2012) A physics-based approach to flow control using system identification. *Journal of Fluid Mechanics* **702**, pp. 26–58. doi:10.1017/jfm.2012.112. 65
- HUERRE, P. & MONKEWITZ, P. (1990) Local and global instabilities in spatially developing flows. *Annual Review of Fluid Mechanics* **22** (1), pp. 473–537. doi:10.1146/annurev.fl.22.010190.002353. 64
- HUGHES, J.D. & WALKER, G.J. (2000) Natural transition phenomena on an axial compressor blade. In *Turbo Expo 2000: Power for Land, Sea, and Air. Volume 3: Heat Transfer; Electric Power; Industrial and Cogeneration. Munich, Germany, May 8–11, 2000*. ASME. doi:10.1115/2000-GT-0264. 69
- JACKSON, C.P. (1987) A finite-element study of the onset of vortex shedding in flow past variously shaped bodies. *Journal of Fluid Mechanics* **182**, p. 23–45. doi:10.1017/S0022112087002234. 64
- KACHANOV, Y.S. (1994) Physical mechanisms of laminar-boundary-layer transition. *Annual Review of Fluid Mechanics* **26** (1), pp. 411–482. doi:10.1146/annurev.fl.26.010194.002211. 67, 68
- KLEBANOFF, P.S., TIDSTROM, K.D. & SARGENT, L.M. (1962) The three-dimensional nature of boundary-layer instability. *Journal of Fluid Mechanics* **12** (1), p. 1–34. doi:10.1017/S0022112062000014. 68
- LJUNG, L. (1999) *System identification: Theory for the user. Second edition*. Prentice-Hall PTR. 64
- LUCHINI, P. (2000) Reynolds-number-independent instability of the boundary layer over a flat surface: optimal perturbations. *Journal of Fluid Mechanics* **404**, p. 289–309. doi:10.1017/S0022112099007259. 74
- LUMLEY, J.L. (1967) The structure of inhomogeneous turbulent flows. In *Atmospheric turbulence and radio propagation* (ed. A.M. Yaglom & V.I. Tatarski), pp. 166–178. Moscow: Nauka. 65

- MARTIN, J.A., MARTEL, C., PAREDES, P. & THEOFILIS, V. (2015) Numerical studies of non-linear intrinsic streaks in the flat plate boundary layer. *Procedia IUTAM* **14**, pp. 479–486. doi:10.1016/j.piutam.2015.03.076. IUTAM ABCM Symposium on Laminar Turbulent Transition. 69
- MATSUBARA, M. & ALFREDSSON, P.H. (2001) Disturbance growth in boundary layers subjected to free-stream turbulence. *Journal of Fluid Mechanics* **430**, p. 149–168. doi:10.1017/S0022112000002810. 68
- MORKOVIN, M.V. (1985) Bypass transition to turbulence and research desiderata. *Transition in Turbines* pp. 161–204. 68, 73
- OTTONELLI, C. (2014) Apprentissage statistique de modèles réduits non-linéaires par approche expérimentale et design de contrôleurs robustes: le cas de la cavité ouverte. PhD thesis, Ecole Polytechnique X, France. 82
- QIN, S. (2006) An overview of subspace identification. *Comp. & Chem. Eng.* **30** (10), pp. 1502–1513. 66
- SCHLATTER, P., BRANDT, L., DE LANGE, H.C. & HENNINGSON, D.S. (2008) On streak breakdown in bypass transition. *Physics of Fluids* **20** (10), p. 101505. doi:10.1063/1.3005836. 68
- SCHLICHTING, H. & GERSTEN, K. (2017) *Boundary Layer Theory*, 9th edn. Springer. doi:10.1007/978-3-662-52919-5. 67
- SIPP, D. & MARQUET, O. (2013) Characterization of noise amplifiers with global singular modes: The case of the leading-edge flat-plate boundary layer. *Theoretical and Computational Fluid Dynamics* **27** (5), pp. 617–635. doi:10.1007/s00162-012-0265-y. 64
- SIROVICH, L. (1987) Turbulence and the dynamics of coherent structures. *Quarterly of Applied Mathematics* **45**, pp. 561–571. 65, 66
- TISSOT, G., CORDIER, L., BENARD, N. & NOACK, B.R. (2014) Model reduction using dynamic mode decomposition. *Comptes Rendus Mecanique* **342**, pp. 410–416. doi:10.1016/j.crme.2013.12.011. 64
- TREFETHEN, L.N., TREFETHEN, A.E., REDDY, S.C. & DRISCOLL, T.A. (1993) Hydrodynamic stability without eigenvalues. *Science* **261** (5121), pp. 578–584. doi:10.1126/science.261.5121.578. 64
- VAN OVERSCHEE, P. & DE MOOR, B. (1994) N4SID: Subspace algorithms for the identification of combined deterministic-stochastic systems. *Automatica* **30** (1), pp. 75–93. 66
- VAN OVERSCHEE, P. & DE MOOR, B. (1995) A unifying theorem for three subspace system identification algorithms. *Automatica* **31** (12), pp. 1853–1864. 66

Turbulent square-back bluff body wake

This chapter summarizes first the cutting-edge knowledge about the flow around a simple car model: the square-back Ahmed body. After presenting the experimental setup, the natural flow is studied by investigating time-averaged and instantaneous measurements of the flow velocity in the wake, the rear pressure and the aerodynamic forces.

5.1 Introduction	88
5.1.1 A model to rule them all...	88
5.1.2 The slanted rear configuration	89
5.1.3 The square-back Ahmed body	91
5.2 Experimental setup	93
5.2.1 Bluff body	93
5.2.2 Wind tunnel	93
5.2.3 Measurements and the Holy Grail: No intrusion	94
5.2.3.1 Pressure	94
5.2.3.2 Velocity	96
5.2.3.3 Aerodynamics forces	97
5.3 Time-averaged characteristics of the unforced wake	98
5.3.1 Incoming flow	98
5.3.2 Mean wake topology	99
5.3.3 Global aerodynamic indicators	101
5.4 Unsteady characteristics and large-scale dynamics	102
5.4.1 Unsteady characteristics	103
5.4.2 Bimodality and more	104
5.4.2.1 Relation between the recirculation bubble and the pressure over the rear part	107
5.4.2.2 Large-scale activity	108
5.4.2.3 Transient symmetric state	115
5.4.3 Coherent structures	118
5.5 Conclusions	120

Vous vous en doutez, on va bifurquer !

5.1 Introduction

The flow over a real vehicle is very complex but most of the aerodynamics forces are related to various flow separations over the front part (A-pillar vortices, wake of the rear-view mirrors) to the massive flow separation over the rear part, which is responsible of 50% to 70% of the drag, depending on the geometry. Studying the structure and dynamics of the three-dimensional (3D) wake downstream of the vehicle is then crucial to optimize and reduce the overall drag and related fuel consumption (Hucho, 2013). As a consequence, one can focus on simplified geometries that could mimic the wake of a real vehicle.

The turbulent wakes downstream of 3D bluff bodies, like cylinders (circular or square) (Williamson, 1996; Bailey *et al.*, 2002), spheres (Gumowski *et al.*, 2008; Yun *et al.*, 2006; Grandemange *et al.*, 2014b) or cubes (Castro & Robins, 1977; Klotz *et al.*, 2014), either wall-mounted or in the freestream, can also be multifaceted, exhibiting large-scale and small-scale coherent structures, either spanwise or streamwise, with strongly intermittent behaviors. Passenger cars or trucks can be considered as 3D bluff-bodies interacting with a wall (underbody flow).

5.1.1 A model to rule them all...

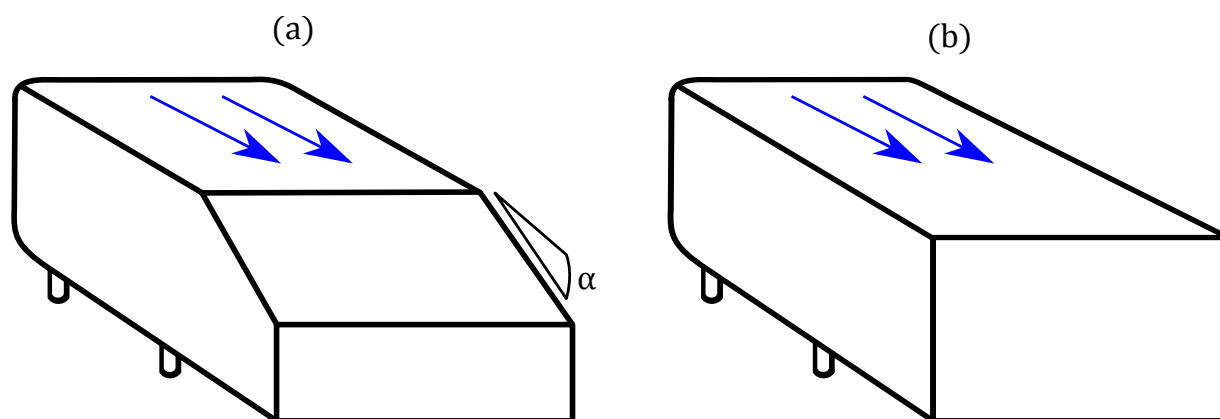


Figure 5.1 – Ahmed body sketched with (a) a slanted and (b) a square-back rear surfaces. Free-stream direction is given by the blue arrows (no drift).

In response to the need of a simplified 3D model for automotive aerodynamics studies, the so-called Ahmed body (Ahmed *et al.*, 1984) has thus been designed obeying a reflectional symmetry. Based on the previous works of Morel (1978), its adjustable shape has been essentially made to investigate the drag due to the rear part of ground vehicles. No wing mirrors to keep clear of structures generation. No heat exchanger to avoid a pressure drop. Wheels are replaced by cylinder supports. In this geometry, only the rear-slant angle α can be changed ($0^\circ \leq \alpha \leq 90^\circ$) as illustrated by Figure 5.1. This simple modification leads to drastic changes in the overall structure of the wake, together with large variations of the aerodynamic drag coefficient. This angle enables to select a simplified rear profile from the sport utility vehicle (SUV) one (slanted configuration) to the truck or bus one (square-back configuration).

Historically, the Reynolds number for this flow is based on the height of the model H ,

$$Re_H = \frac{U_\infty H}{\nu_{air}}, \quad (5.1)$$

where ν_{air} is the kinematic viscosity of the air at ambient temperature. This definition enables to gather and compare numerous investigations, which involve reduced scales of the bluff body and different aspect ratios $AR = H/W$.

Until recent improvements in the experimental (TR-PIV) and the numerical instruments (LES), the first analysis of the wake rested essentially on time- and space-averaged values, without obtaining a complete description of the wake unsteady behavior. The following *brief* presentation of the flow over different Ahmed body configurations is based on the abundant literature on the subject, hopefully recently reviewed (Joseph, 2012; Choi *et al.*, 2014).

The front surface The forebody is strongly rounded to limit structures generation, and separated zones over the roof and the lateral sides. Even if they have been experimentally observed for $1.8 \times 10^3 < Re_H < 9 \times 10^4$ (Spohn & Gilliéron, 2002; Courtine & Spohn, 2004) and numerically obtained at $Re_H = 1.3 \times 10^3$ (Lamballais *et al.*, 2008), their average size decreases at higher Reynolds number. Indeed, laser-Doppler anemometer measurements done by Lienhart *et al.* (2002) shows that the flow remains attached to the roof at $Re_H = 7.3 \times 10^5$.

5.1.2 The slanted rear configuration

The slanted configuration described in Figure 5.2 involves three mean flow arrangements, determined by two threshold angles: $\alpha_m \sim 12.5^\circ$ and $\alpha_M = 30^\circ$. Most of the studies focus on the Ahmed body with $\alpha = 25^\circ$ slant angle, since the comprehension of these wake dynamics is still challenging, as well as its control.

$0 < \alpha \lesssim \alpha_m$ The flow coming from the roof keeps being tangential to the slanted surface, before it separates at the sharp rear edge. This separation occurs also at each other edge of the base area and creates consequently a counter-rotary vortex system with a toroidal shape, defining the contour of recirculation bubbles behind the vertical base (Gilliéron, P. & Chometon, F., 1999). In this configuration, the drag is essentially due to the massive depression contained in the bubbles (Ahmed *et al.*, 1984). As α increases, the flow over the slanted surface encounters a larger adverse pressure gradient, making the contribution of this area to the drag more important. Concurrently, the recirculation bubbles decrease, up to the base surface reduction, and it finally results in a total drag lowering until $\alpha \sim \alpha_m$.

$\alpha_m \lesssim \alpha \leq \alpha_M$ A first separation of the incoming flow happens at the front edge of the inclined surface, followed by a reattachment, giving birth to a recirculation bulk over the upper part of the surface. The bulk is composed of small-scale vortices, which aggregate inside until

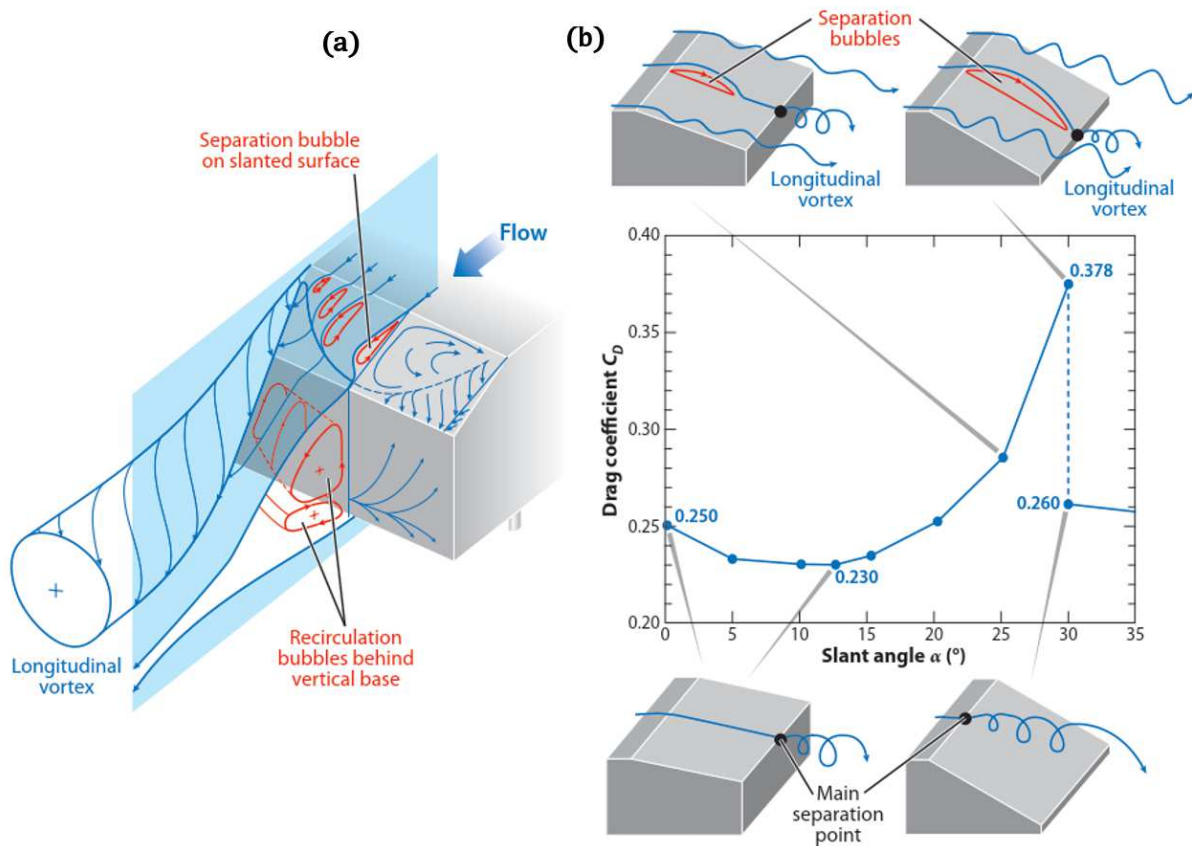


Figure 5.2 – (a) Sketch of the different large coherent structures generated by the Ahmed body with a slanted rear surface with $12.5^\circ < \alpha < 30^\circ$. (b) Resulting time-averaged drag coefficient with respect to the slant angle, together with some sketches of streamlines over the slant surface. Figure extracted from the works of Choi *et al.* (2014).

being advected far from the surface by the shear layer between the bulk and the freestream (Krajnović S., 2005). The position of the reattachment lines fluctuates, such as the flow may be fully separated periodically at large values of α (Hinterberger *et al.*, 2004; Thacker, 2010).

The separatrix adopts a D-shape, occasioned by the top corners, from where a pair of counter-rotating longitudinal vortices develops downstream. Each of these vortices is supplied continuously by the flow coming from its lateral edge (Lehuteur, 2007; Rouméas *et al.*, 2008) and intermittently by small-scale structures from the bulk (Minguez *et al.*, 2008). Then, it follows a slightly deviated line from the inclined surface (Spohn & Gilliéron, 2002; Leclerc, 2008), going downwards into the upper wake, where it is dissipated quite far away (Lienhart *et al.*, 2002). The complex structure of such vortices above the slanted surface still interacts with the bulk by delimiting its reattachment line close to the sides (Spohn & Gilliéron, 2002; Krajnović S., 2005; Vino *et al.*, 2005). These vortices are well studied because their path corresponds to the lowest pressure region (Krajnović & Davidson, 2004; Beaudoin *et al.*, 2004), making them responsible for the so-called *induced drag* (like the ones produced by the end of the airplane wings).

The recirculation region behind the vertical base is composed of two bubbles: a large one above a small one. The large recirculation feeds the counter-rotating longitudinal vortices (Venning *et al.*, 2015). The interaction between the incoming underflow and the small recirculation makes the flow separate from the floor, generating a transverse bulk (Drouin V. & P., 2002; Joseph, 2012). The location of this separation seems to oscillate with the location of the recirculation reattachment. Downstream of this bulk, a horseshoe vortex arises (Venning *et al.*, 2015). Each bubble is included in a horseshoe vortex (Venning *et al.*, 2017). It can be noted that in some studies where the lateral cylindrical supports are missing, a longitudinal vortex develops along the lower part of each lateral surface (Krajnović & Davidson, 2004; Strachan *et al.*, 2007) and merge with the pair of counter-rotating vortices and the horseshoe vortex (Venning *et al.*, 2015). The main hypothesis to explain the absence of such structures in other studies is that the depression caused by the supports suppress them.

The unsteady flow consists thus in a competition between the large-scale streamwise longitudinal vortices, the spanwise Kelvin-Helmholtz vortices emerging from each separation zone, the recirculation bulks oscillations, and the twin horseshoe vortices over the base surface. As α rises, the bulk enlarges in average and the two longitudinal vortices amplify. Therefore, the global drag critically increases until $\alpha = \alpha_m$.

$\alpha_M \leq \alpha$ The bulk and the bubbles behind the base area becomes suddenly a unique large separated region.

5.1.3 The square-back Ahmed body

Like the slanted configuration of the Ahmed body, the flow around the square-back version ($\alpha = 0^\circ$) has been considerably investigated since it corresponds to the profile of a rear truck. Yet, if the mean fields are relatively simple and well defined, the instantaneous fields remain complicated and exhibit together large- and small-scale structures, leading to a very puzzling 3D turbulent flows.

Indeed, time-averaged velocity and pressure fields reveal a toroidal vortex in the near wake (Duell & George, 1999; Krajnović & Davidson, 2003) and spectral analyses highlight a low-frequency mechanism, the bubble pumping (Duell & George, 1999; Volpe *et al.*, 2015).

Bimodality Recently, a right-left switching of the global turbulent wake has been observed experimentally (Grandemange *et al.*, 2013a) and numerically (Östh *et al.*, 2014), defining the so-called reflectional symmetry breaking (RSB) modes and leading to the bimodal (or bi-stable) wake. In fact, this phenomenon emerges in the laminar regime (Grandemange *et al.*, 2012b; Evstafyeva *et al.*, 2017) and is maintained when increasing the Reynolds number. For such dynamics, two different time scales are notable: a long one, $T_{RSB}^* \sim 10^3 H/U_\infty$, is associated to the symmetry-breaking process, whereas the switching itself is characterized by a short time scale T_{switch} which will be discussed hereafter.

Wake behaviors similar to the bimodality are reported for other 3D bluff bodies. The 3D turbulent wakes behind a sphere (Grandemange *et al.*, 2014a) or a bullet-like body (Grandemange *et al.*, 2012a; Rigas *et al.*, 2014) adopt actually instantaneous asymmetric patterns. Due to the axisymmetric shape of those obstacles, there are an infinite number of RSB modes. As well as the square-back body, such dynamics arise in the laminar regime (Bury & Jardin, 2012), occasioned by a supercritical pitchfork bifurcation (Fabre *et al.*, 2008; Meliga *et al.*, 2009). Through long time observation, it is possible to statistically recover a symmetric wake since each state is equiprobable. These observations lead Rigas *et al.* (2015) to use a generic Langevin equation to capture the large-scale dynamics of the axisymmetric wake downstream of the bullet-like body. This equation is based on a deterministic model for the persistent laminar instabilities coupled with a stochastic representation of the turbulent fluctuations. The same approach has subsequently been applied to the turbulent wake behind the square-back Ahmed body by Brackston *et al.* (2016), who stress the key role of the turbulence intensity in the switching trigger. Indeed, they highlighted that the switching time T_{switch} is larger than the vortex shedding period ($T_{shedding}^* \sim 5H/U_\infty$) and depends on the increase in the turbulent fluctuations, which thus drive the large-scale instability. The general theory of the noise-induced breaking symmetry has been demonstrated by Van den Broeck *et al.* (1994).

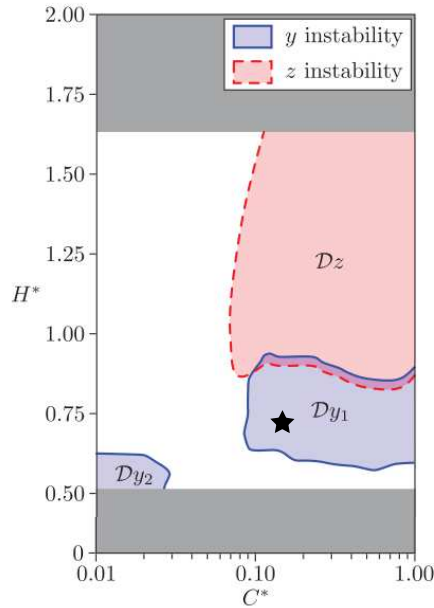


Figure 5.3 – Present study configuration (black star) in the instabilities map experimentally made by Grandemange *et al.* (2013c). D_y and D_z are the domains of spanwise and vertical bimodality respectively. $H^* = H/W$ and $C^* = C/W$.

The bimodality refers to two metastable asymmetric states of the wake but the switching process suggests a third one, less stable. In fact it will be shown that this mode can be defined experimentally, as the one found numerically by Kaiser *et al.* (2014) when they statistically computed a cluster-based reduced-order model of the wake. Finally the bimodality is sensitive to other geometric parameters like the aspect ratio of the bluff-body's cross-section AR and the ground clearance C , which can even trigger a vertical bimodal behavior as shown in Figure 5.3 (Grande-

mange *et al.*, 2013c), and to experimental conditions like the yaw angle β (Cadot *et al.*, 2015; Volpe *et al.*, 2015).

References	Re_H	AR	$C^* = C/W$	Remarks
Krajnović & Davidson (2003)	2.1×10^5	1.0	0.08	No supports
Rouméas <i>et al.</i> (2009)	7.7×10^5	0.74	0.13	No supports
Grandemange <i>et al.</i> (2012b) Evstafyeva <i>et al.</i> (2017)	$[3.1; 4.2] \times 10^2$		0.44	
Grandemange <i>et al.</i> (2013c) Volpe <i>et al.</i> (2015)	9.2×10^4 $[5.1; 7.7] \times 10^5$	0.74	0.13	
Brackston <i>et al.</i> (2016) Cadot <i>et al.</i> (2015)	$[2.3; 4.4] \times 10^5$ $[1.8; 16] \times 10^4$		[0.007; 0.208]	
Barros <i>et al.</i> (2014) Östh <i>et al.</i> (2014) Barros <i>et al.</i> (2016)	3.0×10^5 $[2.0; 4.0] \times 10^5$	0.85	0.14	
Lahaye <i>et al.</i> (2014) Eulalie (2014)	5.3×10^5 3.9×10^5	0.74	0.18	Supplementary pod across the underbody

Table 5.1 – Square-back Ahmed geometries reported in the literature.

5.2 Experimental setup

The dynamics of a 3D bimodal turbulent wake downstream of a square-back Ahmed body are experimentally studied in a wind tunnel through high-frequency wall-pressure probes mapping the rear of the model and a horizontal two-dimensional (2D) velocity field.

5.2.1 Bluff body

The blunt body is a 0.7 scale of the original Ahmed body ($L=0.731$ m long, $H=0.202$ m high, and $W=0.272$ m wide), previously used by Lahaye *et al.* (2014) and Eulalie (2014). The rear part of the model is a square-back geometry with sharp edges (Figure 5.4), which corresponds to trucks, buses or mini-van geometries.

5.2.2 Wind tunnel

Like some of the previous studies on a square-back bluff body (Lahaye *et al.*, 2014; Eulalie, 2014; Volpe *et al.*, 2015), our experiments are carried out in the PRISME laboratory wind tunnel (Orléans, France). The test section of this closed wind tunnel is a 2 m \times 2 m square, resulting in a ratio blockage lower than 3%, and extends over 5 m. The model is mounted on a raised

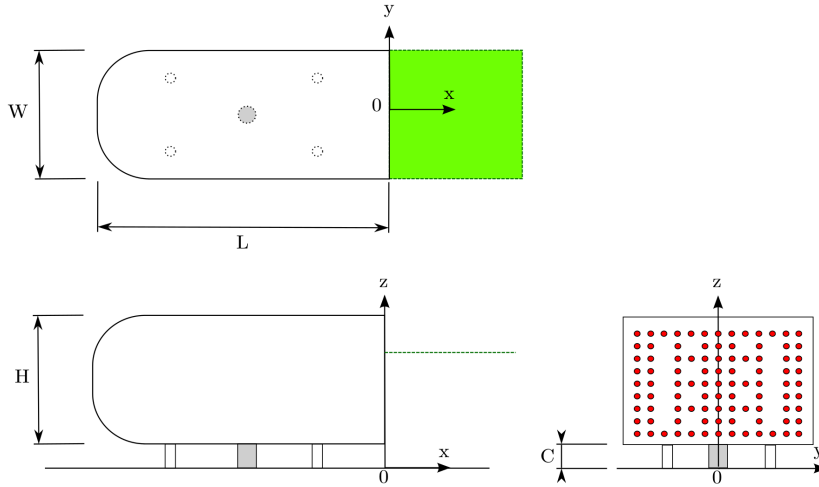


Figure 5.4 – Upper view (top figure) and side view (lower left figure) and view from behind (lower right figure) of the Ahmed body. The PIV measurement plane is shown on top (green rectangle) and lower left (green line) figure. The rear part of the model is mapped with 95 pressure sensors (red circles on lower right figure). Cables pass through a supplementary pipe (grey part on lower figures).

floor with a properly profiled leading edge, to ensure a fully turbulent incoming boundary layer, and an adjustable trailing edge to avoid undesired flow separations (see [Figure 5.5](#)). The ground clearance is set to $C = 5$ cm, higher than the boundary layer thickness (~ 2.1 cm). In the following, the free-stream velocity is $U_\infty = 30$ m.s⁻¹, corresponding to $Re_H = 3.9 \times 10^5$. The origin is located on the rear of model ($x = 0$), in the vertical symmetry plane ($y = 0$) and on the raised floor ($z = 0$). Nondimensionalization is applied to spatial variables such as $x^* = x/H$, $y^* = y/H$, $z^* = z/H$, while the convective time and the Strouhal number are respectively defined as $t^* = tU_\infty/H$ and $St_H = fH/U_\infty$. Although this kind of definition of the Strouhal number does not suit correctly to qualify all the observed dynamics in separated flows ([Roshko, 1955](#); [Bearman, 1967](#); [Griffin, 1981](#); [Williamson & Brown, 1998](#); [Ponta, 2006](#)), it is used here to help comparisons with other studies using it.

5.2.3 Measurements and the Holy Grail: No intrusion

5.2.3.1 Pressure

The wall-pressure over the rear part of the model is studied using a set of 95 taps defining an area denoted S_p and covering 70% of the entire rear surface $S_r = H \times W$, as shown on [Figure 5.4](#). Each hole is 2 cm away from each of its closest neighbors and is connected through a vinyl tube to a 32-channels microDAQ pressure scanner (Chell Instruments, UK), insuring an accuracy of ± 17 Pa and located inside the body. The scanner computes the pressure difference between the rear pressures $p(i, j)$ and the reference static pressure p_∞ , measured by a Prandtl tube located above the leading edge of the raised floor. This tube sends also the reference dynamic pressure,

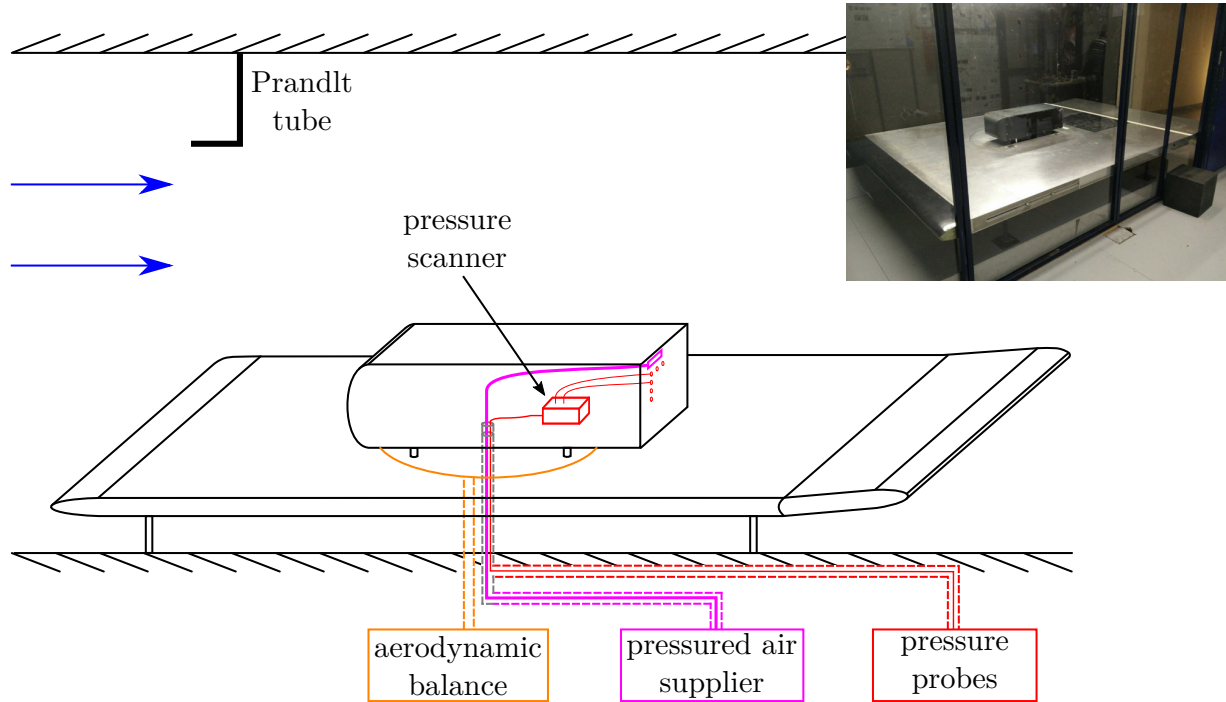


Figure 5.5 – Sketch and picture of the 0.7 scaled square-back Ahmed body mounted inside the Malavard wind tunnel facility (Orléans, France).

$q_\infty = \frac{1}{2}\rho U_\infty^2$, synchronously to easily calculate C_p (see Equation 5.2). Therefore, a total of three scanners are linked to an external computer over Ethernet, through a cylindrical pipe of diameter 32 mm at the center of the bottom face (see the gray part in Figure 5.4). The need of such a pipe comes from the pneumatic tubes for the actuators introduced in chapter 7. Even if this pipe does not break the reflexive symmetry of the body, it has certainly an influence on the near wake, which will be discussed. The data are processed by a Chell software, then stored in the RAM during the record time and finally given in a file per scanner. The number of samples per acquisition is bounded to $N = 30\,000$ ¹, making the sampling frequency for the pressure f_P^* dependent on the acquisition time T_P^* : $f_P^* = N/T_P^*$. Only the 95 pressure values $p(i, j)$ measured by the scanners are used to calculate the pressure-linked values below.

The pressure coefficient $C_p(t)$ is defined as:

$$C_p(t, i, j) = \frac{p(t, i, j) - p_\infty(t)}{q_\infty(t)}, \quad (5.2)$$

where $p(t, i, j)$ is the local pressure (i, j) measured at time t , and S_r is the rear area of the bluff body mentioned above. A typical instantaneous pressure coefficient field is shown in Figure 5.7(a). It shall be mentioned that such a smooth imagery is obtained by using a cubic interpolation². Denoting the space average of a quantity a over an area S as $\langle a \rangle_S$, we call for convenience the

1. After N recorded samples, a lag occurs, shifting the next N samples in time.
 2. Thanks to the Matlab files *inpaint_nans*, from J. D'Errico, and *interp2*.

instantaneous spatially-averaged pressure coefficient as the base coefficient $C_b(t)$

$$C_b(t) = \langle C_p(t) \rangle_{S_p}. \quad (5.3)$$

We are interested in the large-scale dynamics of the global wake. This is the reason why we define the instantaneous wall-pressure barycenter at $x^* = 0$, which can be seen as the footprint of the wake,

$$\overrightarrow{OG_p(t)} = \begin{pmatrix} y_p^*(t) \\ z_p^*(t) \end{pmatrix} = \begin{pmatrix} \frac{\langle y^* p(t) \rangle_{S_p}}{\langle p(t) \rangle_{S_p}} \\ \frac{\langle z^* p(t) \rangle_{S_p}}{\langle p(t) \rangle_{S_p}} \end{pmatrix}. \quad (5.4)$$

5.2.3.2 Velocity

The air flow is seeded with oil droplets via a nozzle located just downstream of the test section. The velocity fields are obtained using the aero configuration given in chapter 2, able to stream the $2048 \text{ px} \times 2048 \text{ px}$ snapshots to the LabVIEW program. Because it is the best suited to characterize the bimodality, the main investigated PIV plane is the near wake horizontal XY-plane at $z^* = 1$, displayed in Figure 5.5, with a 0.21 mm.px^{-1} resolution. Other PIV planes are studied.

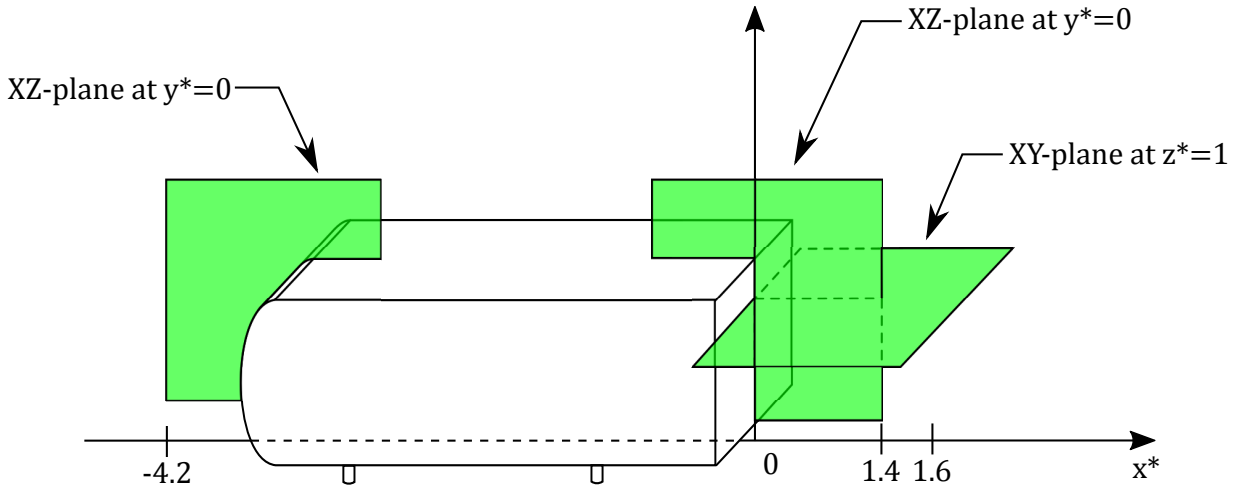


Figure 5.6 – PIV planes investigated in this chapter.

The 2D velocity fields are computed at the frequency $f_{PIV}^* = 2.8 \times 10^{-2}$ ($f_{PIV} = 4.2 \text{ Hz}$) using the optical flow algorithm described in chapter 2. The interrogation window size is 16×16 pixels and the calculation is based on three iterations for each of the three pyramid reduction levels. An example of a 2D instantaneous velocity field is shown in Figure 5.7(b). One can see the complexity of the turbulent wake, with large and small-scale strongly fluctuating vortices.

In the same way as the pressure center we define another global indicator of the state of the wake through the computation of the instantaneous recirculation intensity barycenter (also called

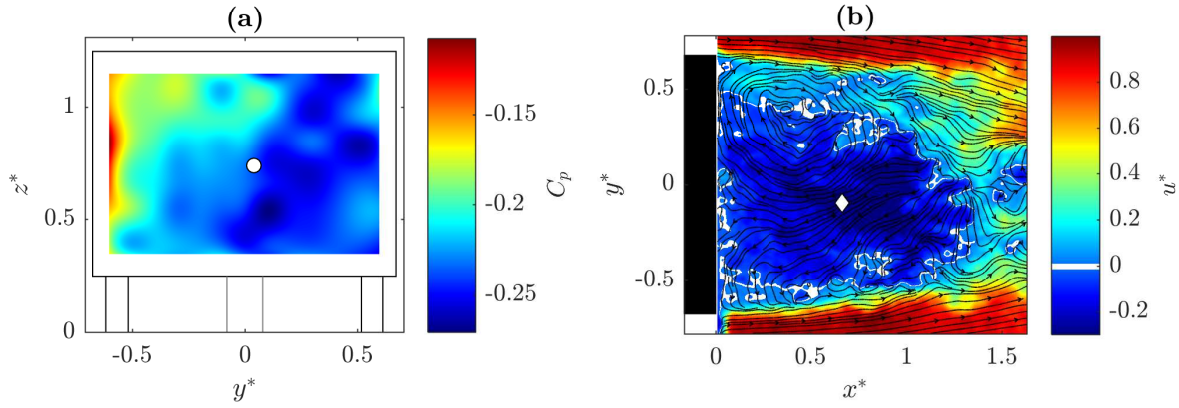


Figure 5.7 – Typical (a) instantaneous pressure field over the rear part of the model with the pressure center G_p indicated as a white circle, and (b) instantaneous normalized longitudinal velocity field with streamlines and the recirculation barycenter G_{rec} shown as a white diamond in the horizontal XY-plane at $z^* = 1$.

backflow centroid) $G_{rec}(t)$, from the velocity fields in the horizontal PIV plane at $z^* = 1$,

$$\overrightarrow{OG_{rec}(t)} = \begin{pmatrix} x_{rec}^*(t) \\ y_{rec}^*(t) \end{pmatrix} = \begin{pmatrix} \frac{\langle x^* u_{rec}(t) \rangle_{A_{rec}(t)}}{\langle u_{rec}(t) \rangle_{A_{rec}(t)}} \\ \frac{\langle y^* u_{rec}(t) \rangle_{A_{rec}(t)}}{\langle u_{rec}(t) \rangle_{A_{rec}(t)}} \end{pmatrix}, \quad (5.5)$$

where $u_{rec}(t) = u_{rec}(x^*, y^*, t)$ and $A_{rec}(t)$ are respectively the local streamwise component of the recirculation velocity and the recirculation area at time t . The instantaneous barycenter of the depression can thus be tracked at each time step. An example of the evolution in time is given in Figure 5.21 for y_p^* (a) and y_{rec}^* (b). Table 5.2 indicates the different dimensionless parameters of the runs.

$T^*(\times 10^3)$	Runs nb.	PIV planes	Nb. of fields
8.9	12	XY at $z^* = 1$	256
18	2	XZ at $y^* = 0$ and XY at $z^* = 1$	510
45	1	None	-

Table 5.2 – Parameters of the different runs.

5.2.3.3 Aerodynamics forces

The bluff body is linked to an aerodynamic balance through a supporting turntable (see the orange part in Figure 5.5). As the influence of the free-stream orientation is not studied here, the yaw angle β is fixed to 0° . The drag and the lift forces are respectively measured with an accuracy of 0.08 N and 0.24 N. The precision for the drift measurements is the same as the drag one.

Investigations on the sensitivity of the balance to the model vibrations, like those provoked by actuators (see chapter 7), have highlighted possible bias in measurements when forcing is active. Consequently, the mean aerodynamics indicators will be only presented for the reference case.

5.3 Time-averaged characteristics of the unforced wake

First, the incoming flow is described. The wake topology is then characterized before presenting and discussing the aerodynamics behavior together with the rear pressure maps and the velocity fields.

5.3.1 Incoming flow

The time-averaged velocities are first computed over 510 fields at the front of the bluff body in a XZ-plane at $y^* = 0$. Figure 5.8(a) shows a slowing down of the flow until reaching the bluff body. Then it starts to accelerate along the curved edge, where a depression takes place [Figure 5.8(b)]. Close to the wall, it encounters an adverse pressure gradient near the end of the curvature, making it strongly slow down for a short distance. This region of the mean flow is detailed in Figure 5.9 for three different Reynolds numbers. It shall be specified that the instantaneous fields are very similar to the mean fields.

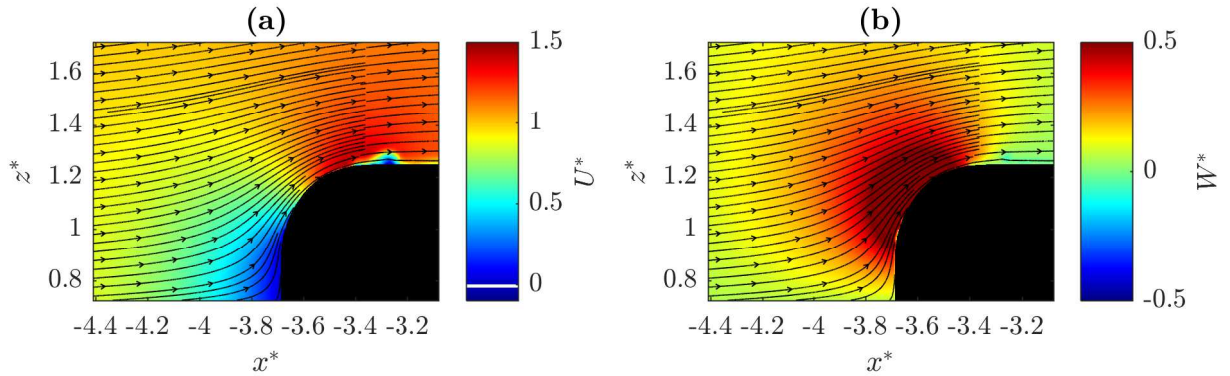


Figure 5.8 – (a) Streamwise and (b) normal components of the mean velocity field, together with streamlines, in the front XZ-plane at $y^* = 0$. $Re_H = 3.9 \times 10^5$.

At the lowest Reynolds numbers, the boundary layer may separate: the velocity decreases near the wall because of the adverse pressure Figure 5.9(a). Figure 5.9(b) and (c) show that the upstream area where the speed decreases is reduced when increasing the Reynolds number, as reported numerically by Krajnović S. (2005) and experimentally by Spohn & Gilliéron (2002); Grandemange *et al.* (2013a).

The mean flow over the roof has previously been detailed by Lahaye *et al.* (2014). Only its behavior at the top trailing edge is thus described, moving the previous longitudinal median PIV

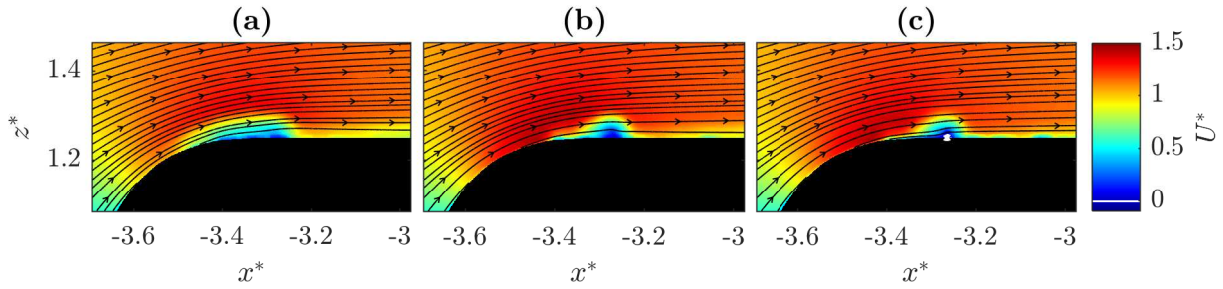


Figure 5.9 – Streamwise component of the mean velocity field and streamlines in the front XZ-plane at $y^* = 0$ for (a) $Re_H = 2.6 \times 10^5$, (b) $Re_H = 3.9 \times 10^5$, and (c) $Re_H = 5.1 \times 10^5$.

plane to the rear part.

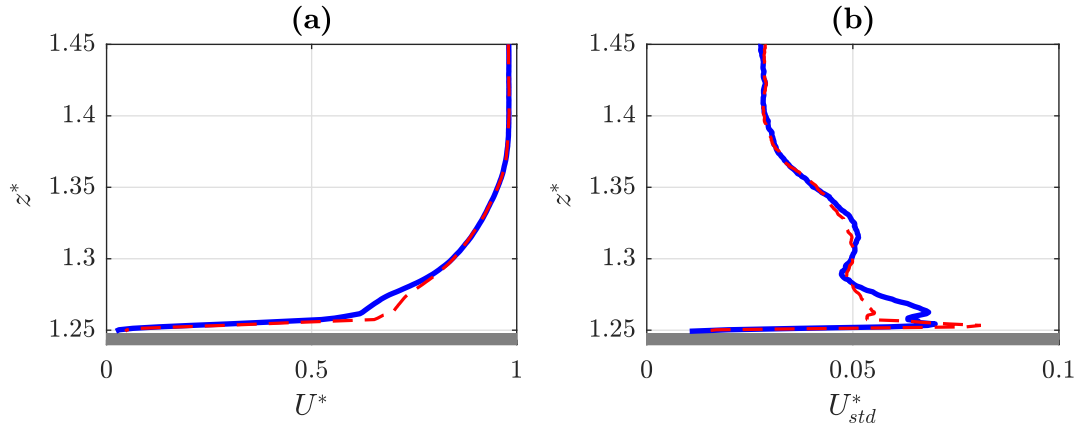


Figure 5.10 – (a) Mean streamwise velocity profile and (b) its standard deviation at the top trailing edge $(x^*, y^*) = (0, 0)$ (blue solid lines), and at an upstream position $(x^*, y^*) = (-0.15, 0)$ (red dashed lines).

The boundary layer is first evaluated from the dense PIV data at the top trailing edge for $Re_H = 3.9 \times 10^5$. The profiles of streamwise velocity [Figure 5.10(a)] and of its standard deviation [Figure 5.10(b)] are characteristic of a turbulent boundary layer: highest fluctuations close to the wall reduce the loss of momentum with respect to the free-stream. This is confirmed by the computation of the shape factor $\bar{H} = 1.35$, the displacement thickness and the momentum thickness being respectively $\delta^* = 0.036$ and $\theta^* = 0.027$. The nearby separation tends nonetheless to increase the loss of momentum, as attested by the change in the curvature of the velocity profile between the trailing edge and an upstream position in Figure 5.10(a).

5.3.2 Mean wake topology

The same average wake organization as Lahaye *et al.* (2014) is unsurprisingly found. Figure 5.11(a) and (b) show indeed two vortices on both sides of the recirculation, the bottom

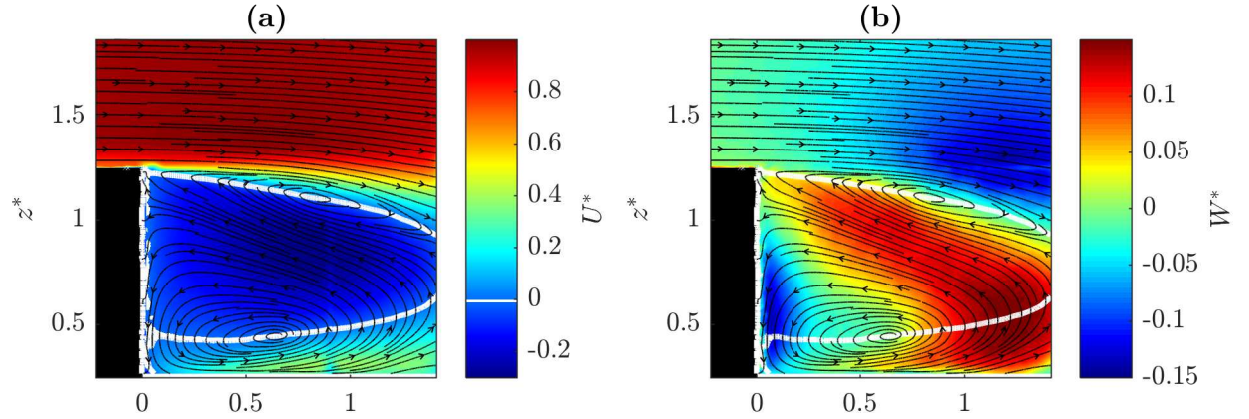


Figure 5.11 – (a) Streamwise and (b) normal components of the mean velocity field, together with streamlines (black) and the separatrix (white), in the rear XZ-plane at $y^* = 0$. $Re_H = 3.9 \times 10^5$.

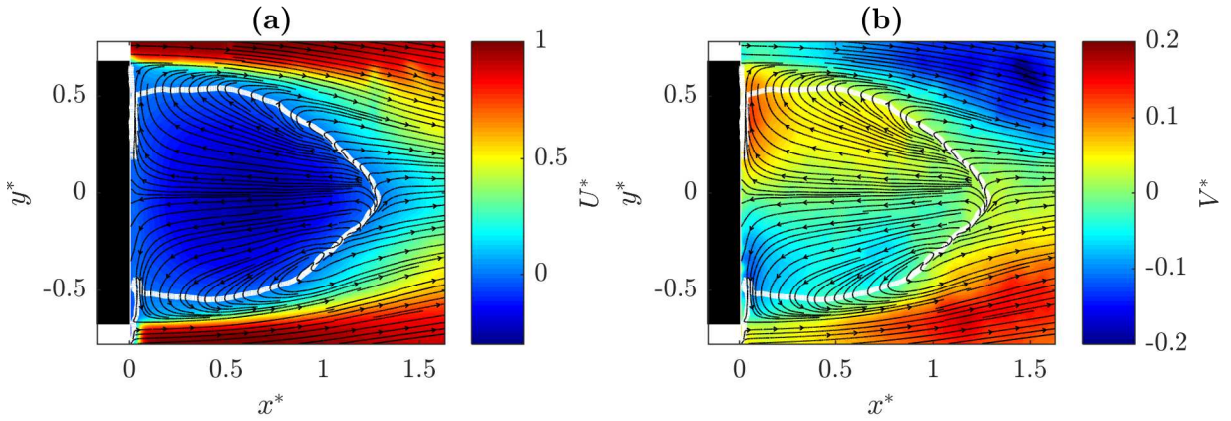


Figure 5.12 – (a) Streamwise and (b) spanwise components of the mean velocity field, together with streamlines (black) and the separatrix (white), in the XY-plane at $z^* = 1$. $Re_H = 3.9 \times 10^5$.

one being bigger and closer to the bluff body than the top one. This asymmetry is due to the ground proximity and the structures coming from the underbody flow. An asymmetric distribution is also observed by Barros *et al.* (2016) but with inverted roles for the vortices. However, other studies obtain an almost symmetric mean wake, where the vortices are vertically aligned (Grandemange *et al.*, 2013a; Volpe *et al.*, 2015). Comparisons with such references have therefore to be cautious regarding the near wake dynamics in the z -direction, since the central pipe across the underbody flow clearly modifies it. Finally, although the wake expansion is not completely visible, the mean recirculation length is estimated to $L_{rec}^* = 1.5$.

The time-averaged pressure coefficient $\langle C_p \rangle_{T_p^*}$ and the pressure fluctuations C_{pSTD} are computed for $T_p^* = 44 \times 10^3$. As expected for such a bluff body, Figure 5.13(a) shows a symmetric spatial distribution for $\langle C_p \rangle_{T_p^*}$ with the lowest pressure values at the bottom part. This can be compared to the spatial distribution of the fluctuations of the wall pressure displayed in Figure 5.13(b). Two regions in the upper part of the rear of the model exhibits large pressure

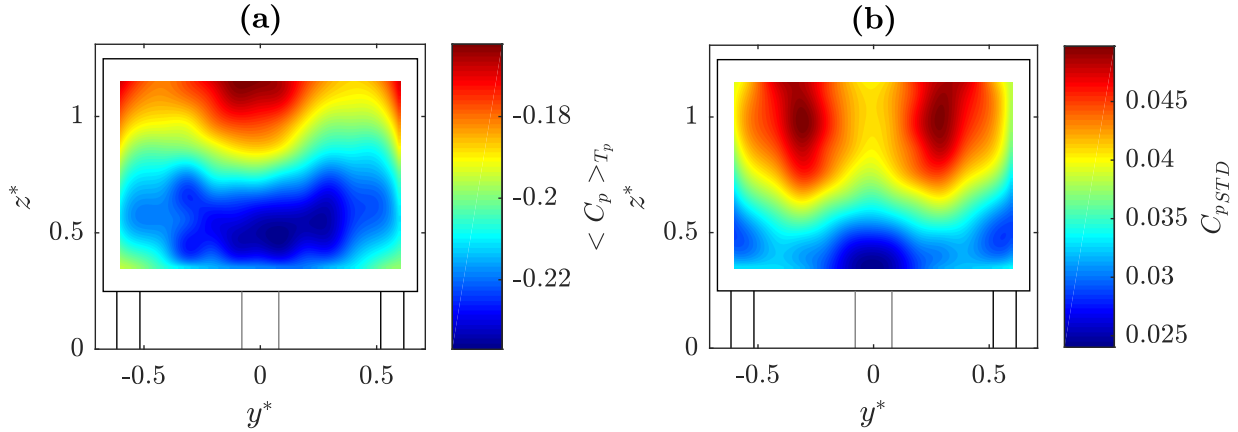


Figure 5.13 – Spatial distribution of (a) the time-averaged pressure coefficient $\langle C_p \rangle_{T_p}$, and of (b) the pressure fluctuations C_{pSTD} over the rear of the Ahmed body.

fluctuations.

5.3.3 Global aerodynamic indicators

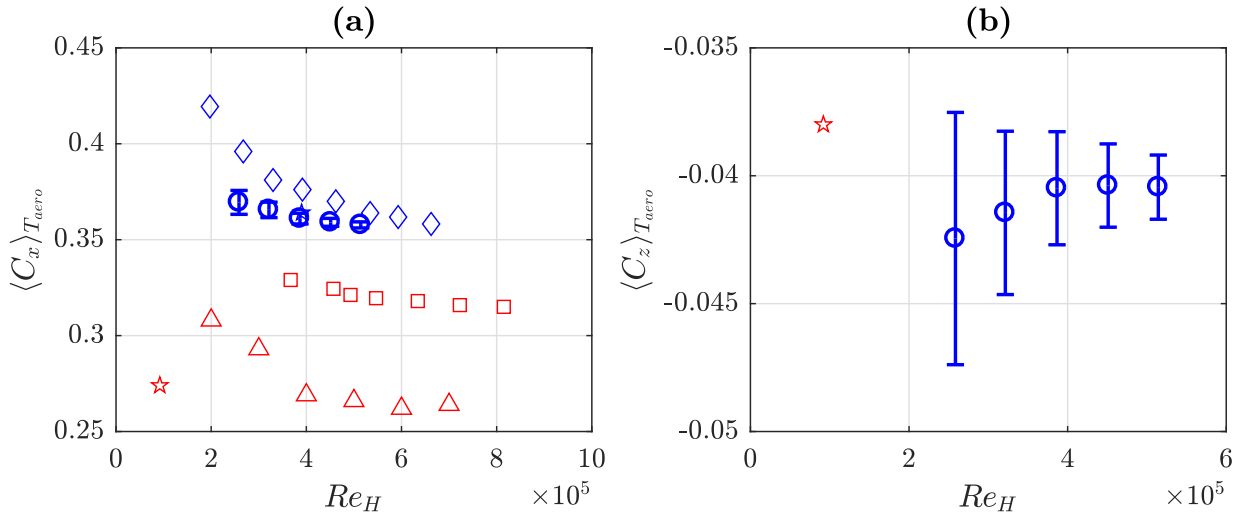


Figure 5.14 – (a) $\langle C_x \rangle_{T_{aero}}$ and (b) $\langle C_z \rangle_{T_{aero}}$ with errorbars (blue circles) for different Re_H . Extra data come from Grandemange *et al.* (2013c) (\star), Eulalie (2014) (\star), Lahaye *et al.* (2014) (\diamond), Volpe *et al.* (2015) (\square), and Barros (2015) (\triangle).

The time-averaged drag coefficients for $Re_H = [2.6; 5.1] \times 10^5$ are displayed in Figure 5.14(a), together with data from previous studies. Each point results from two independent 2-min runs, sampled at the frequency $f_{aero}^* = 6.7$ ($f_{aero} = 1000$ Hz). The drag coefficients are only comparable when model geometries (ground clearance, aspect ratio) are close to each other (Table 5.1), which explains some important differences between the references. It is noteworthy that the experiments involving the central pipe have the highest drag coefficients. Nevertheless, most of the studies

exhibit a Reynolds effect, $\langle C_x \rangle_{T_{aero}}$ depending on Re_H until a critical value. In the present study, this value is $Re_H = 3.9 \times 10^5$. The influence of the Reynolds number is also visible for the lift coefficient in Figure 5.14(b). Beyond the critical Reynolds number, this coefficient remains constant: $\langle C_z \rangle_{T_{aero}} \sim -4.0(\pm 0.22) \times 10^{-2}$. As there is no yaw angle ($\beta = 0^\circ$) breaking the reflexive symmetry of the experiment, the mean drift statistically cancels: $\langle C_y \rangle_{T_{aero}} \sim 1.2 \times 10^{-4}$.

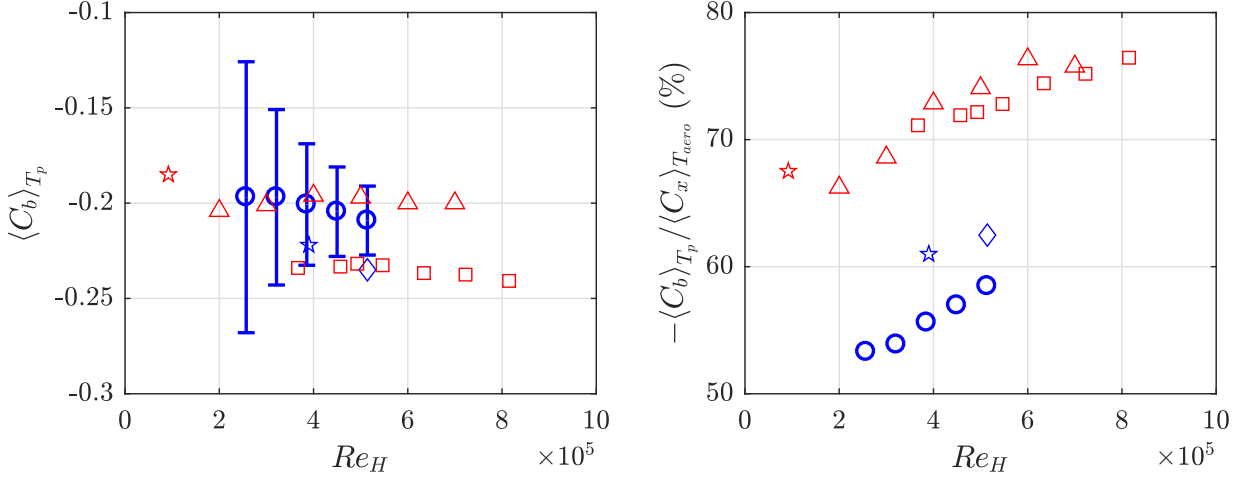


Figure 5.15 – (a) $\langle C_b \rangle_{T_p}$ with errorbars (blue circles) and (b) base-pressure-to-drag ratio $-\langle C_b \rangle_{T_p} / \langle C_x \rangle_{T_{aero}}$ for different Re_H . Extra data come from Grandemange *et al.* (2013c) (\star), Eulalie (2014) (\star), Lahaye *et al.* (2014) (\diamond), Volpe *et al.* (2015) (\square), and Barros (2015) (\triangle).

The base pressure is given for different Reynolds numbers and compared with previous studies in Figure 5.15(a). The depression seems curiously³ less stronger than the ones previously measured for the same bluff body (Eulalie, 2014; Lahaye *et al.*, 2014). Indeed Figure 5.15(b) shows a 56% mean base-pressure-to-drag ratio for the present wake, whereas it was 62%. Even so, the base suction represents the dominant part of the drag and its recover remains a good objective for drag reduction. Finally $-\langle C_b \rangle_{T_p} / \langle C_x \rangle_{T_{aero}}$ linearly increases with Re_H since the viscous forces tangential to the surface decline.

5.4 Unsteady characteristics and large-scale dynamics

In this section, several representations of the measurements will be displayed to precisely describe the unsteady natural wake through the large-scale dynamics in the flow control perspective. If there is no precision, the Reynolds number is always $Re_H = 3.9 \times 10^5$.

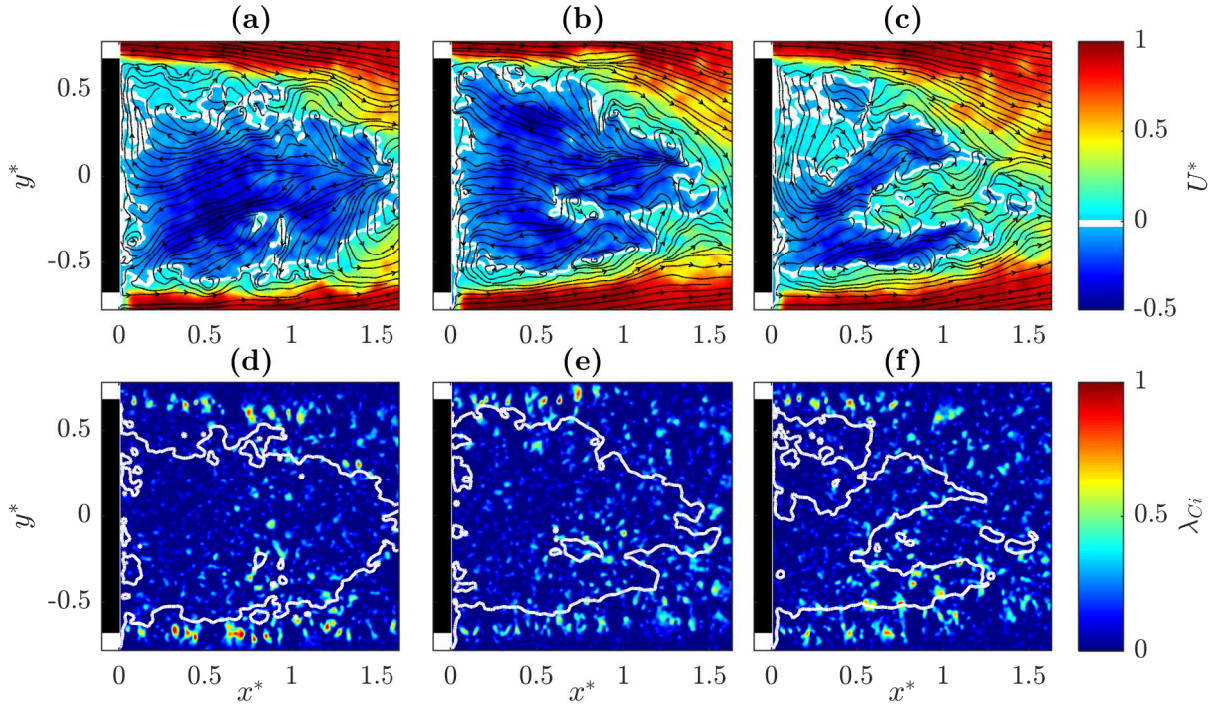


Figure 5.16 – (a-c) Streamwise velocity component with superposed streamlines and (d-f) λ_{Ci} -criterion of three successive instantaneous velocity fields, together with the separatrix (white), in the rear XY-plane at $z^* = 1$.

5.4.1 Unsteady characteristics

Studying successive instantaneous fields gives a more complete description of the involved in-wake phenomena. Thereby, λ_{Ci} -criterion highlights the vortex roll-up due to the Kelvin-Helmholtz instability along the upper and lateral shear layers in Figure 5.17(d-e-f) and in Figure 5.16(d-e-f) respectively. As well as in the backward-facing step wake (chapter 2) or in the circular cylinder wake (Kovasznay, 1949), those growing perturbations will here also cause the downstream vortex shedding. The bottom vortex of the toroidal structure can be either far from the rear surface [Figure 5.17(a)] or close to it [Figure 5.17(c)]. Even if the recirculation area globally keeps its shape and size of the same order of the bluff body height, it can be elongated [Figure 5.17(c)] or even strongly collapses [Figure 5.16(c) and Figure 5.17(b)].

In fact, the recirculation area seems to have periodic dynamics. Plotting its time evolution in Figure 5.18(a) and (c), a long-time periodic pattern, evaluated at $T^* \sim 3.5 \times 10^3$, partly appears for the smoothed data. This can be referred to the periodic oscillations of the recirculation length in the BFS wake as reported by Aider *et al.* (2007).

When analyzing the power spectra of the pressure sensors along the height of the model for various Reynolds numbers, Figure 5.19 reveals that the low frequencies dominate, especially in

3. Investigations have been *a posteriori* made and are still in progress to understand these values which may be due to air temperature, update of the pressure scanners...

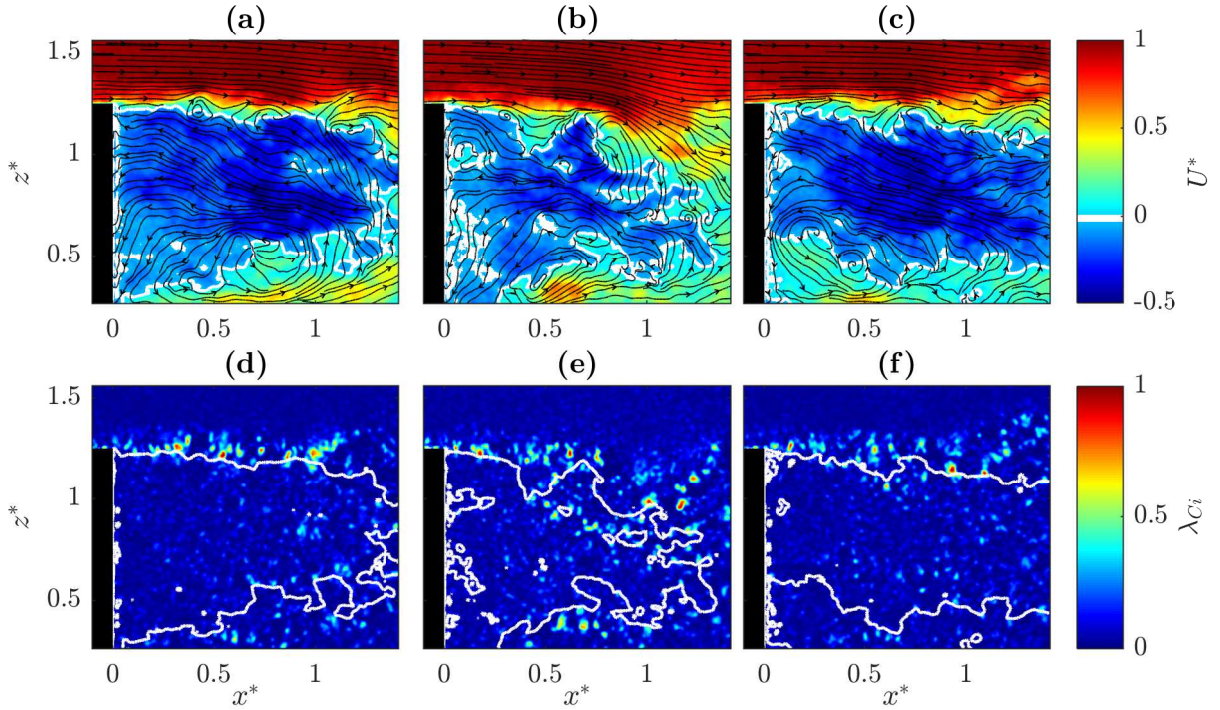


Figure 5.17 – (a-c) Streamwise velocity component with superposed streamlines and (d-f) λ_{Ci} -criterion of three successive instantaneous velocity fields, together with the separatrix (white), in the rear XZ-plane at $y^* = 0$.

the upper part, where the recirculation bubble essentially is.

Along the bottom trailing edge, there is clear peak at $St_H = 0.19$. This peak is also present at the middle of the upper trailing edge [Figure 5.20(d) and (g)]. There is a peak at $St_H \sim 0.3$ along the upper edge. There is a peak at $St_H \sim 0.4$ along the upper edge. The centre of the rear surface seems to have higher level of energy according to Figure 5.20(b-e-h).

5.4.2 Bimodality and more

As we are interested in the global wake dynamics, the probability density function (PDF) is computed for both barycenters. Regarding their spanwise position, Figure 5.21 shows clearly the bimodal behavior of the turbulent wake, whether it is through the pressure barycenter PDF $P_{y_p^*}$ (b) or the recirculation barycenter PDF $P_{y_{rec}^*}$ (d).

Indeed each barycenter moves from one side to the other [Figure 5.21(a) and (c)], between two more probable locations, one located in the negative part of the y^* -axis and the other one in the positive part. This is the kind of sidewise bimodal configurations that is expected for a square-back bluff body with such geometric parameters (aspect ratio $H/W = 0.743$, and ground clearance $C/W = 0.248$), as shown by Grandemange *et al.* (2013c) at $Re_H = 3.3 \times 10^4$ (Figure 5.3). The difference in the peaks value is due to the low acquisition time as observed by

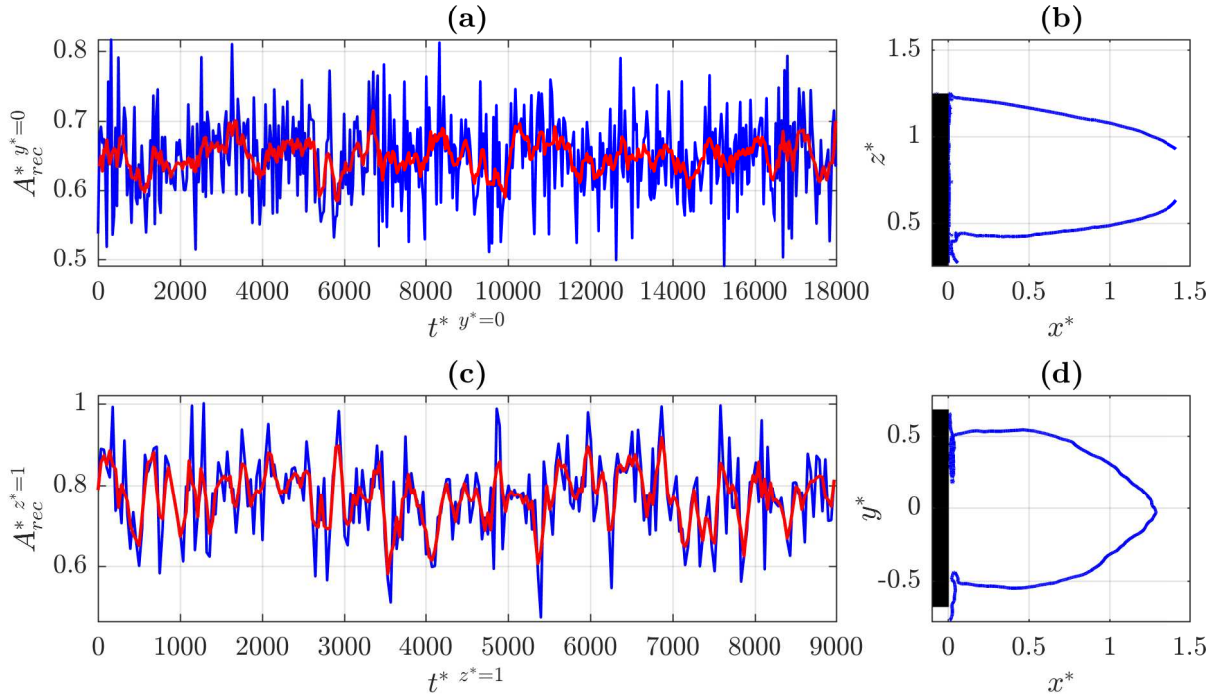


Figure 5.18 – Evolution of the recirculation area and the separatrix computed in **(a-b)** the XZ-plane at $y^* = 0$ and **(c-d)** the XY-plane at $z^* = 1$. Red curves are smoothed data over $\Delta t^* = 300$.

Cadot *et al.* (2015) but longer acquisitions only done for the pressure show well two peaks of the same level. The small amount of data regarding the PIV explains the noisy aspect of $P_{y_{rec}^*}$. The two RSB modes are temporarily identified only with respect to the sign of y_p^* , calling “N” the one when $y_p^* < 0$ ($y_{rec}^* > 0$) and “P” the one when the $y_p^* > 0$ ($y_{rec}^* < 0$).

The normal to the wall positions z_p^* of the pressure center [Figure 5.22(a) and (b)] and of the recirculation barycenter [Figure 5.22(c) and (d)] respectively alternate between two positions. In fact, their respective PDFs, $P_{z_p^*}$ and $P_{z_{rec}^*}$, show only one mode, but smoothing the pressure data over $\Delta t^* = 1.5 \times 10^2$ (and even less) exhibits a second peak. Unfortunately this second peak is difficult to obtain from the PIV data due to the sample size. Nevertheless, it suggests the existence of a weak top-down switching, hidden by the strong transverse oscillation.

The streamwise position x_{rec}^* seems to fluctuate around one mean position as its PDF is roughly Gaussian and reveals one peak.

The evolution of the wake in the XY-plane at $z^* = 1$ and in the XZ-plane at $y^* = 0$ during a switch from a RSB mode to another one are respectively displayed in Figure 5.24 and Figure 5.25. The two sets of successive instantaneous fields presented here have been selected regarding y_p and for a transition long enough each to obtain comprehensive fields and understand the process. They are representative of most of the observed transitions in the data set but one has to keep

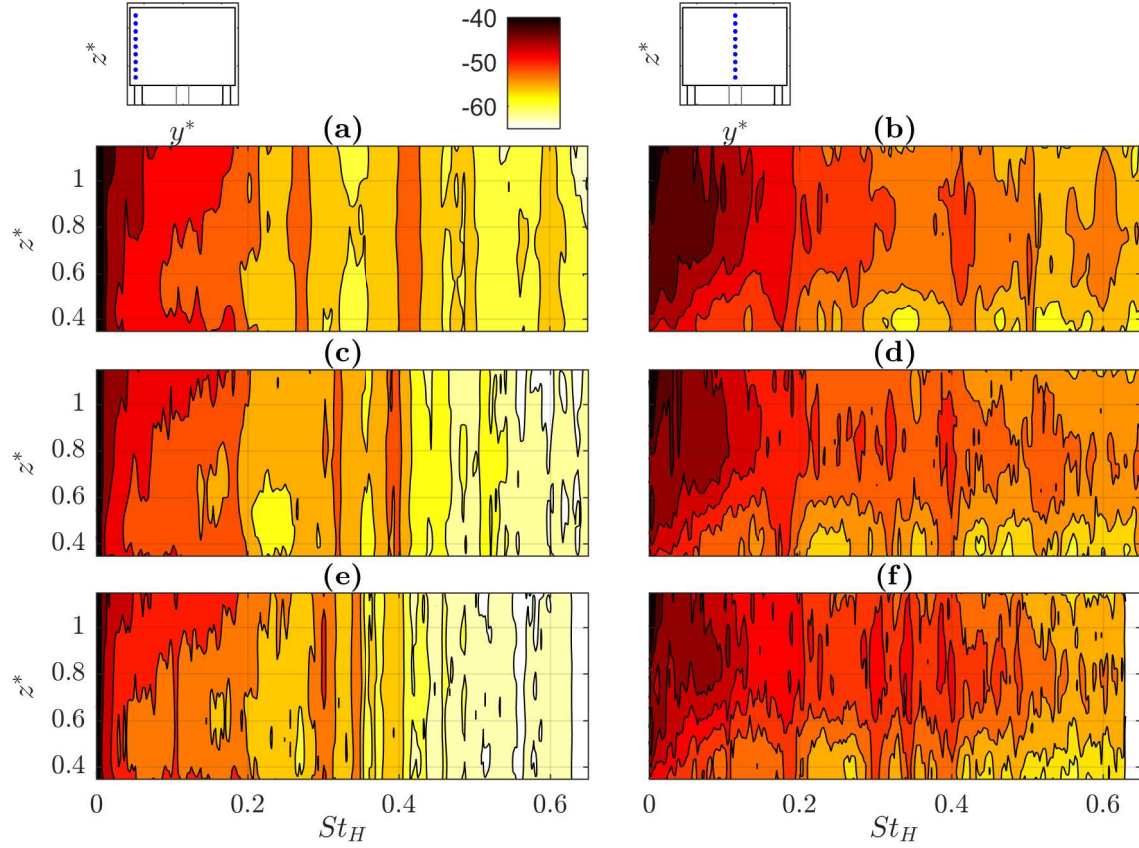


Figure 5.19 – Spatial PSD of the pressure fluctuations for (a-b) $Re_H = 2.6 \times 10^5$, (c-d) $Re_H = 3.9 \times 10^5$, and (e-f) $Re_H = 5.1 \times 10^5$.

in mind that other phenomena are captured. Figure 5.24(a) shows that, in an asymmetric state, one of the lateral vortex defining the toroidal structure is near the rear surface, whereas the other lateral vortex is $1H$ distant from it. The closest vortex to the body gives the depression localization. The recirculation area in the XZ-plane spread along $0.75H$ in height and the bottom vortex seems $0.5H$ distant from the body.

Thus the same lateral symmetry-breaking mechanism is observed in the wake topology as the ones presented by Grandemange *et al.* (2013a); Cadot *et al.* (2015); Volpe *et al.* (2015). Figure 5.26 shows that other physical quantities enable to track the bimodality, such as the spanwise pressure gradient $\partial C_p / \partial y^*$ and the drift coefficient C_y . The further analyses about the pressure center hold consequently for these quantities. The effects of the modified ground clearance on the wake reversal behind a square-back bluff body have been studied by Barros *et al.* (2017). It was reported in particular that the presence of a circular cylinder, very similar to the central pipe in our experiments but closer to the rear part, changes the vertical position of the modes but does not cancel the lateral bimodality.

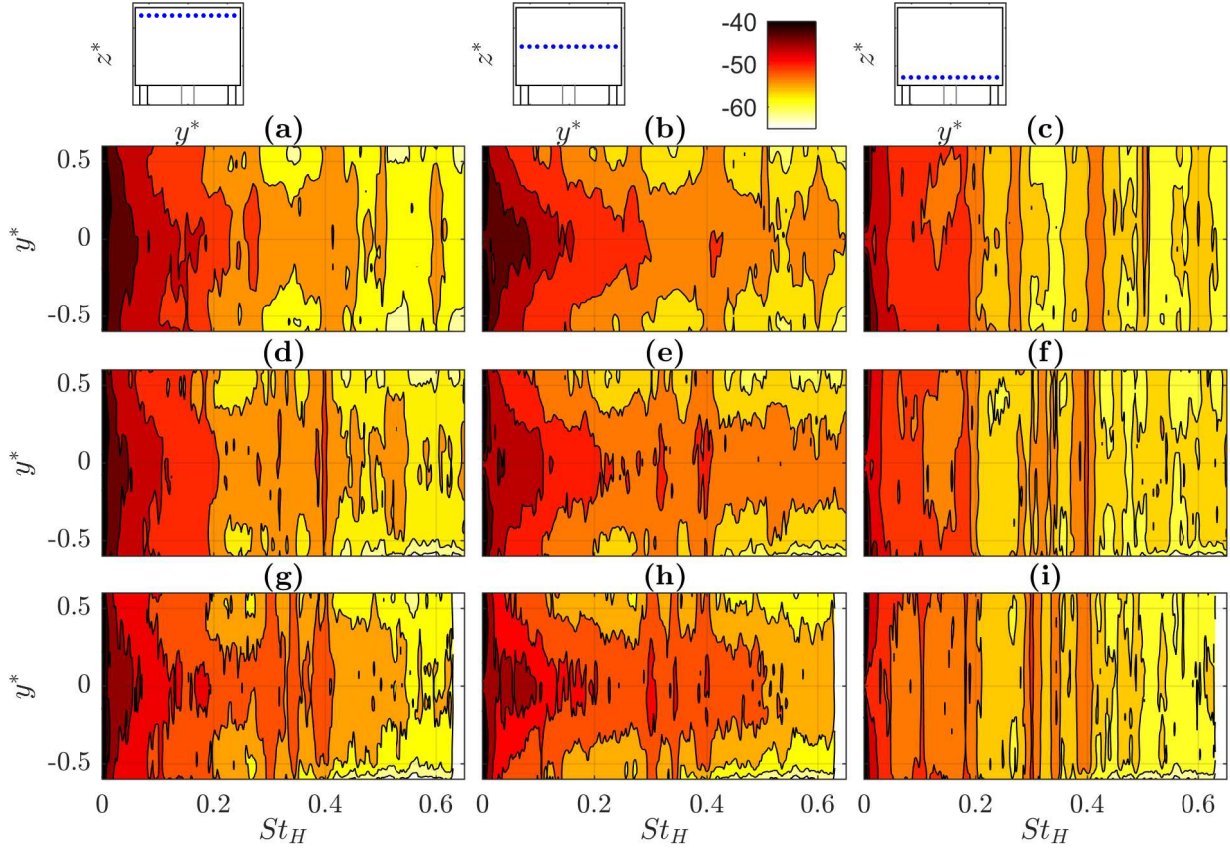


Figure 5.20 – Spatial PSD of the pressure fluctuations for (a-b-c) $Re_H = 2.6 \times 10^5$, (d-e-f) $Re_H = 3.9 \times 10^5$, and (g-h-i) $Re_H = 5.1 \times 10^5$.

5.4.2.1 Relation between the recirculation bubble and the pressure over the rear part

The relation between the dynamics of the wake, characterized by its instantaneous recirculation area, and the dynamics wall pressure is not straightforward because of the complex 3D flow. To study the linear part of their relationship, the cross correlations between y_p^* and y_{rec}^* , and between z_p^* and z_{rec}^* have been fist computed for five $T^* = 8.9 \times 10^3$ runs and one $T^* = 1.8 \times 10^4$ run respectively:

$$\Gamma_{y_p^*, y_{rec}^*}(\tau^*) = y_p^*(\tau^*) \otimes y_{rec}^*(\tau^*) \text{ and } \Gamma_{z_p^*, z_{rec}^*}(\tau^*) = z_p^*(\tau^*) \otimes z_{rec}^*(\tau^*), \quad (5.6)$$

where τ^* is the dimensionless evaluated lag. Even if the results are similar with the raw data, [Figure 5.27](#) is obtained from time-series smoothed over $\Delta t^* = 150$ for visibility. The results show a strong correlation and an almost non-existent delay between the two measurements as illustrated by [Figure 5.27](#). The values of the strongest peak are indeed $\Gamma_{y_p^*, y_{rec}^*}(\tau^* \sim 60) = -0.84 \pm 0.05$ and $\Gamma_{z_p^*, z_{rec}^*}(\tau^* \sim 77) = -0.53$, meaning that both barycenters are in phase opposition. When the depression is located in the negative part of the rear surface ($y_p^* < 0$), the recirculation bubble is located in the positive one ($y_{rec}^* > 0$) and *vice versa*.

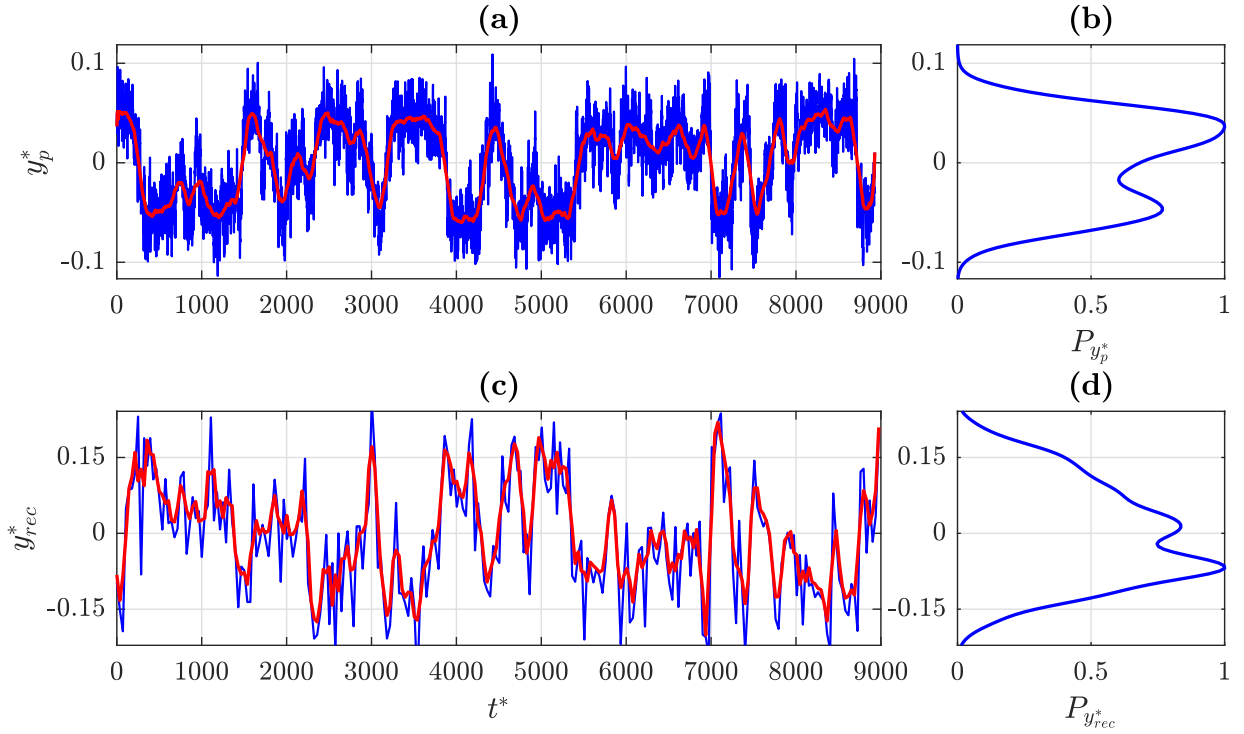


Figure 5.21 – Pressure barycenter spanwise position y_p^* : (a) evolution in time and (b) normalized PDF, $P_{y_p^*}$. Recirculation intensity barycenter spanwise position y_{rec}^* : (c) evolution in time and (d) normalized PDF $P_{y_{rec}^*}$. Red curves show the data smoothed over $\Delta t^* = 150$.

Furthermore, Figure 5.28(a) displays the vertical fluctuations of the depression \tilde{z}_P^* and the absolute value of the corresponding spanwise position $|y_p^*|$. It reveals that, while in one of the RSB mode ($|y_p^*| > 0$), the depression is higher localized ($\tilde{z}_P^* > 0$) than when it comes closer to the reflexive axis ($|y_p^*| \sim 0$ and $\tilde{z}_P^* < 0$). This linear relation is confirmed by the centred peak of $\Gamma_{|y_p^*|, \tilde{z}_P^*}(\tau^*)$ in Figure 5.28(b). It is consequently the inverse for the recirculation intensity. The wake states can therefore be characterized either by the pressure barycenter or by the recirculation intensity one. Due to the higher sampling rate, we essentially present results in the following regarding pressure measurements for several independent experiments of various lengths acquisition runs ($T_P^* = \{1.8; 4.4\} \times 10^4$).

5.4.2.2 Large-scale activity

For different Reynolds numbers, the power spectra density (PSD) of the sidewise position y_p^* [Figure 5.29(a)] and the vertical position z_p^* , noted $S_{y_p^* y_p^*}$ and $S_{z_p^* z_p^*}$ respectively, contain high amplitude at a very-low-frequency range ($St_H < 0.02$). The observation of high energy level in this part of the spectrum is common in measurements close to the rear body (Grandemange *et al.*, 2013a; Volpe *et al.*, 2015). Considering the average time spent in a RSB mode ($\sim 7 \times 10^2$), it may be associated to the lateral bimodal behavior.

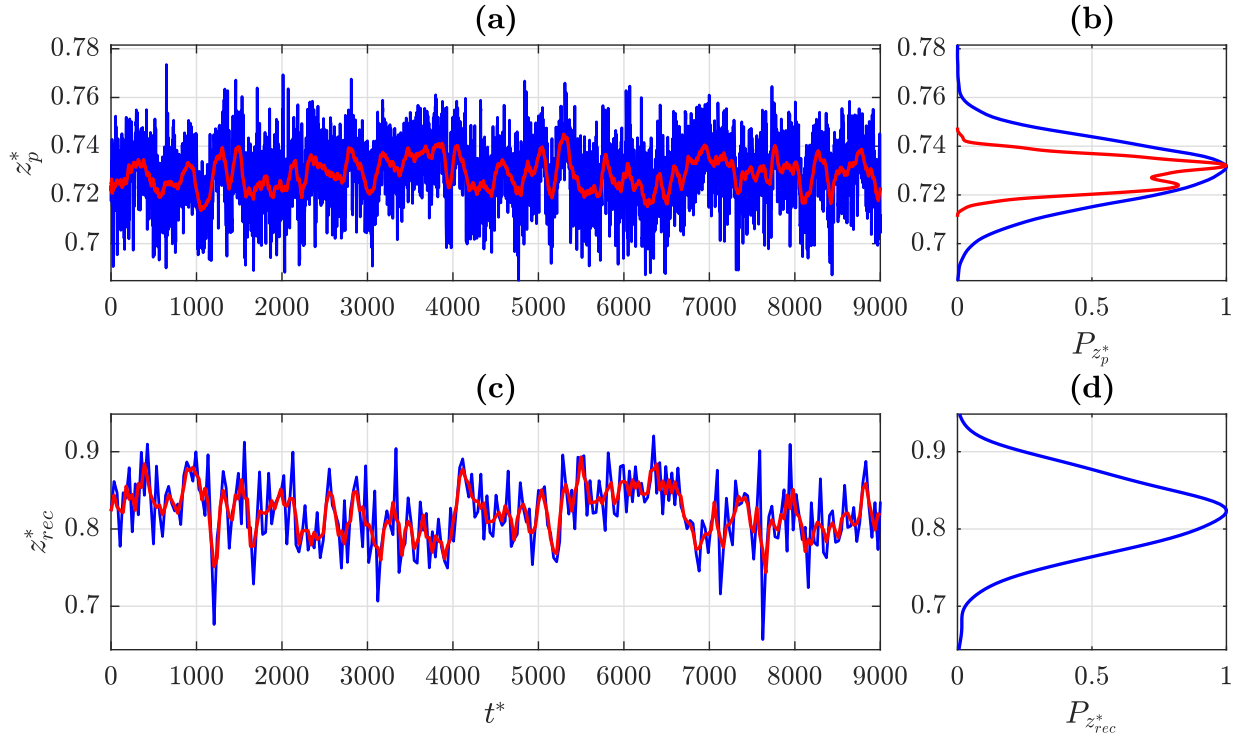


Figure 5.22 – Pressure barycenter vertical position z_p^* : (a) evolution in time and (b) normalized PDF, $P_{z_p^*}^*$. Recirculation intensity barycenter vertical position z_{rec}^* : (c) evolution in time and (d) normalized PDF $P_{z_{rec}^*}^*$. Red curves show the data smoothed over $\Delta t^* = 150$.

A decaying but still high level of energy is then observed in $S_{y_p^* y_p^*}$ for $St_H \in [0.02, 0.08]$. Khalighi *et al.* (2012); Volpe *et al.* (2015) and McArthur *et al.* (2016) linked 0.08 to the bubble pumping phenomenon. Then a plateau appears until $St_H \sim 0.14$. It contains the value 0.13 previously found with hot-wire measurements in the lateral shear layers, indicator of vortex shedding (Lahaye *et al.*, 2014; Eulalie, 2014; Volpe *et al.*, 2015).

Recent frequency measurements in a simulated turbulent wake behind a circular disk confirm the presence of two close low frequencies: 0.02 and 0.03 (Yang *et al.*, 2015). The lowest one is associated to the asymmetric changes in the wake orientation at such low frequency, whereas the highest one is related to the bubble pumping. Similar results have been obtained for a turbulent axisymmetric body wake by Gentile *et al.* (2016). Through a POD analysis of the velocity fluctuations, they find very-low-frequency peaks, $St_H \sim 10^{-4}$ and $St_H = 10^{-3}$, in the dynamics of the modes associated respectively to the symmetry breaking process and to the bubble pumping.

The PSD of the vertical position z_p^* , $S_{z_p^* z_p^*}$, alone reveals a peak at $St_H = 0.19$, independent from the Reynolds number, as displayed in Figure 5.29(b). This Strouhal number is characteristic of the signature of vortex shedding from the top-bottom shear layers interaction (Parezanović & Cadot, 2012; Lahaye *et al.*, 2014; Volpe *et al.*, 2015; Barros *et al.*, 2016), meaning that the z -position of the depression over the rear part is influenced by these far wake dynamics. This natural feedback inside the wake has been reported by Broze & Hussain (1994) for a turbulent

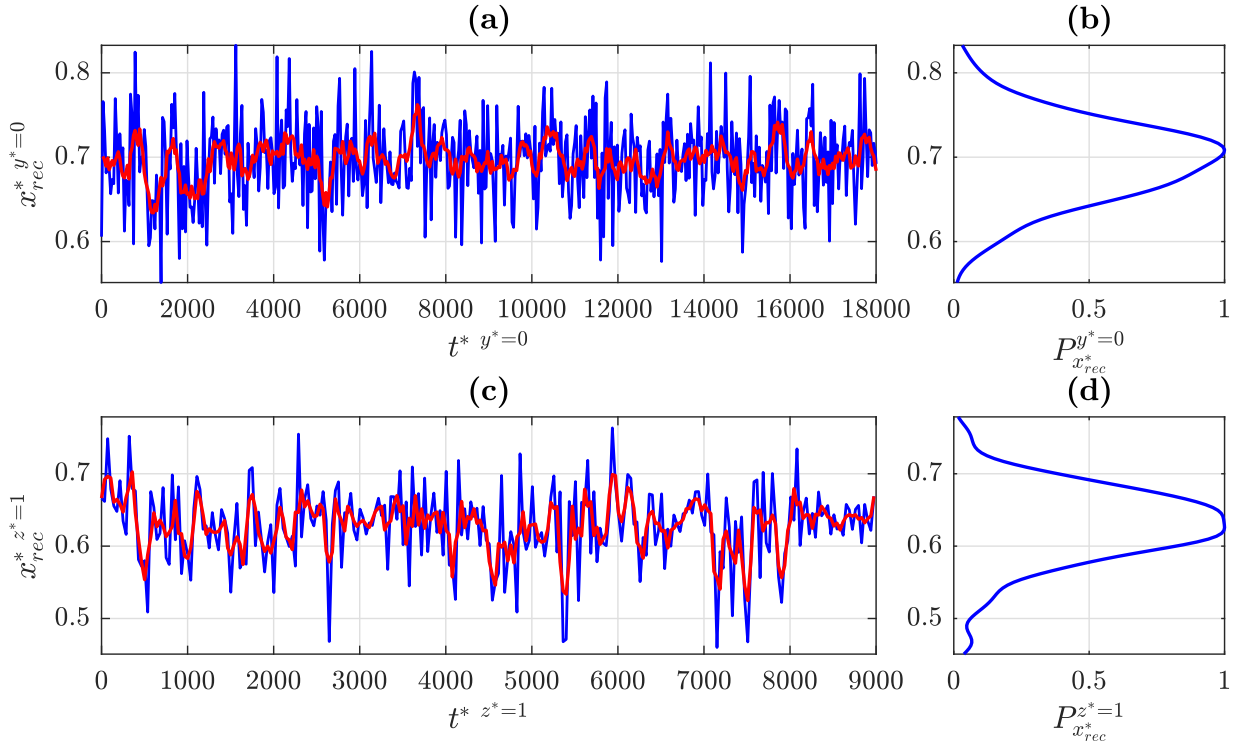


Figure 5.23 – Recirculation intensity barycenter spanwise position x_{rec}^* and its normalized PDF $P_{x_{rec}^*}$ in (a-b) the XZ-plane at $y^* = 0$ and (c-d) the XY-plane at $z^* = 1$. Red curve shows the data smoothed over $\Delta t^* = 150$. Unlike the previous figures, these measurements come from different runs but are done at the same Reynolds number.

axisymmetric jet, where the spectral signature of vortex pairings downstream of a nozzle appears in the velocity fluctuations measured at the nozzle exit. For the turbulent axisymmetric body wake, the characteristic vortex shedding frequency also appears in the spectrum of the POD mode describing the switching behavior (Gentile *et al.*, 2016). Physically, the feedback is due to upstream propagating pressure fluctuations.

The vortex roll-up generated by the Kelvin-Helmholtz (KH) instability and visible for instantaneous velocity fields in Figure 5.16 and in Figure 5.17 cannot be detected through PSD. In fact, their high frequency can be estimated from the instantaneous velocity fields using the method based on the vortex detection described in chapter 3. As a reminder, computing the λ_{C_i} -criterion in a region of interest which comprises the starting shear layer enables the detection of the KH vortices, as shown in Figure 5.30(a). Depending on the λ_{C_i} values, a wavenumber $\Lambda_{KH,i}^*$ and a convective velocity $U_{KH,i}^*$ are estimated for the instantaneous field i , giving an estimate of the instantaneous KH frequency $f_{KH,i}^* = \|U_{KH,i}^*\| \Lambda_{KH,i}^*$ [Figure 5.30(b)]. Applying this method to the upper and lateral shear layers returns respectively $f_{KH,up}^* = 3.6 \pm 0.8$ and $f_{KH,lat}^* = 3.6 \pm 0.9$. The deviation remains important since the instability is not steady. Nevertheless, these values are in good agreement with $f_{KH}^* = 3.8$ predicted by the scaling law $Re^{0.52}$ for such high Reynolds number from Thompson & Hourigan (2005), rather than the model mentioned in chapter 3 for lower Reynolds numbers.

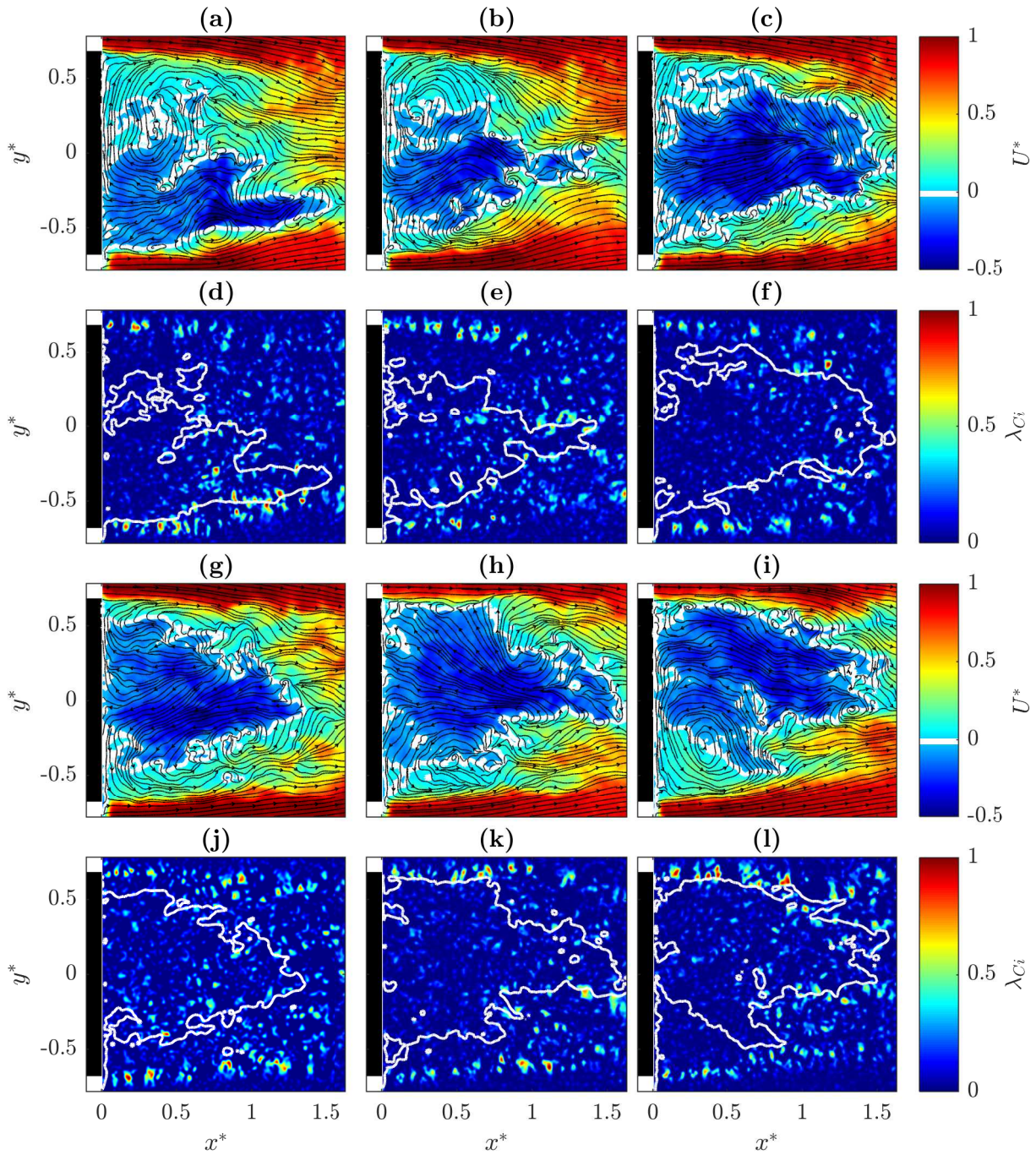


Figure 5.24 – (a-b-c-g-h-i) Streamwise velocity component with superposed streamlines and (d-e-f-j-k-l) λ_{Ci} -criterion of three successive instantaneous velocity fields, together with the separatrix (white), in the rear XZ-plane at $y^* = 0$ during spanwise switching of the wake.

Thus, the dynamics of the depression seem to be rather dominated by the spanwise bimodal behavior of the recirculation and the top-bottom shear layers interaction. The central pipe may

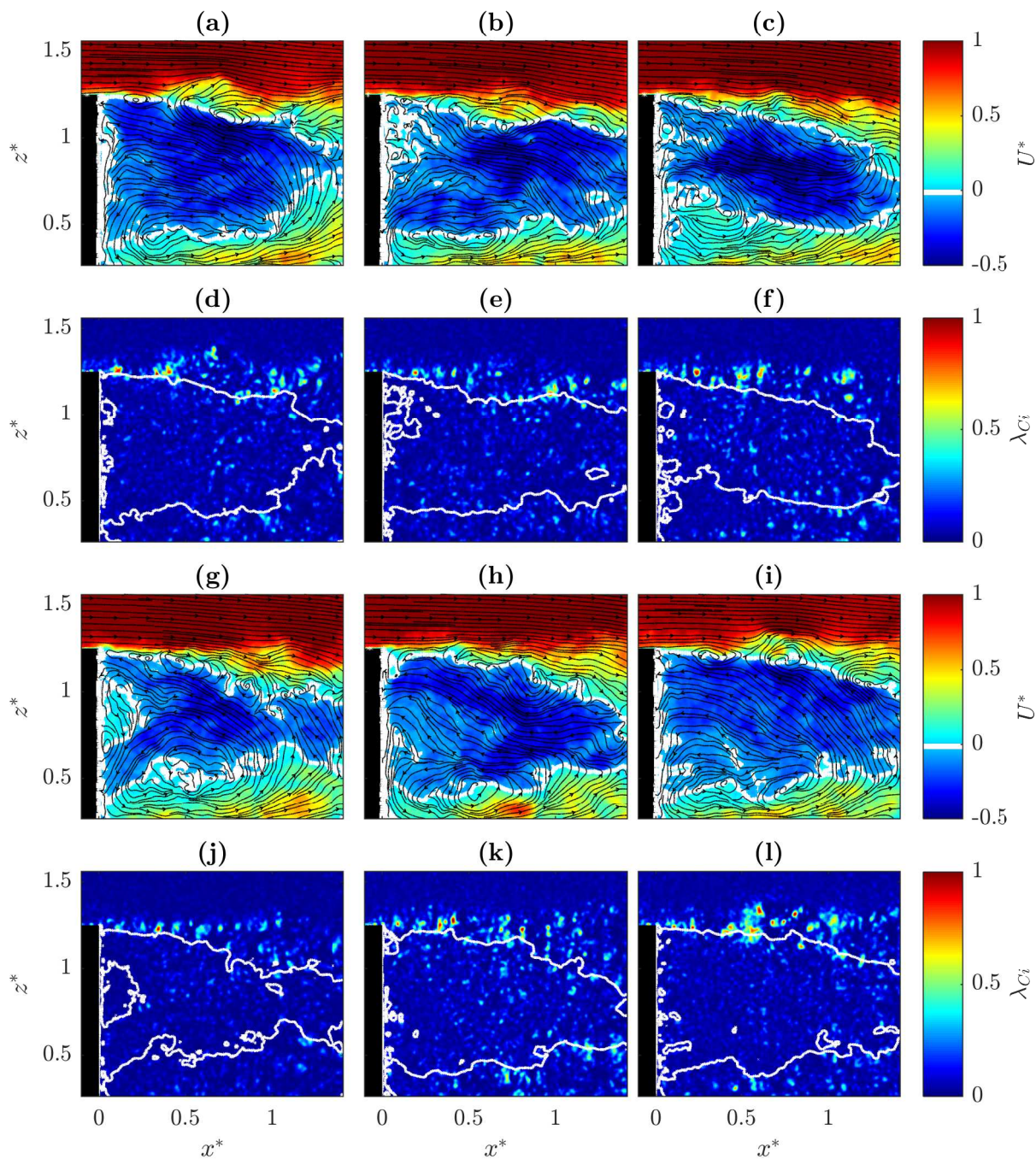


Figure 5.25 – (a-f) Streamlines and streamwise component of six successive instantaneous velocity fields in the rear XZ-plane at $y^* = 0$ during spanwise switching of the wake.

partly intensify this interaction, as highlighted by Lahaye *et al.* (2014), but most of the added structures in the underbody flow have higher frequency signatures like the Karman vortex street at $St_H = 1$ and $St_H = 1.6$ (Eulalie, 2014). It shall be recalled that the switching process is linked

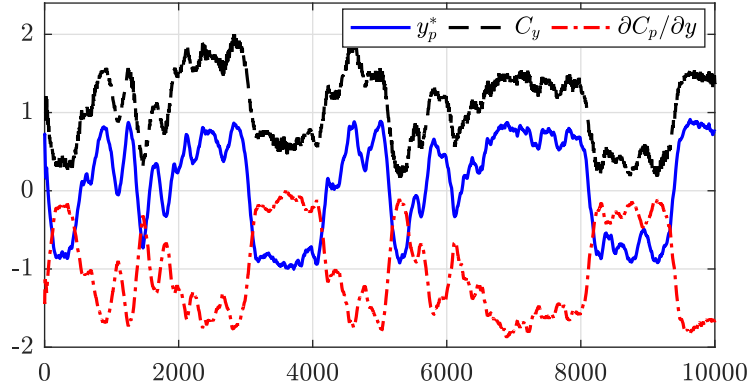


Figure 5.26 – Bimodality highlighted by normalized y_p^* (blue solid), C_y (black dashed) and $\partial C_p/\partial y^*$ (red dash-dotted) time-series. Data are normalized and shifted for clarity.

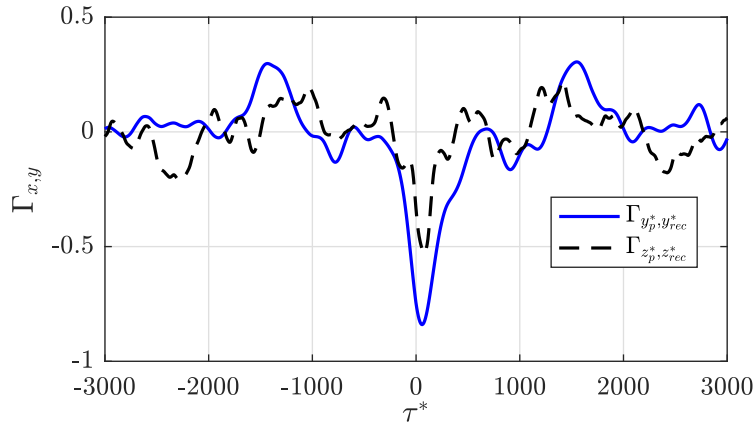


Figure 5.27 – Cross-correlation of $\Gamma_{y_p^*, y_{rec}^*}(\tau^*)$ (blue solid line) and $\Gamma_{z_p^*, z_{rec}^*}(\tau^*)$ (black dashed line).

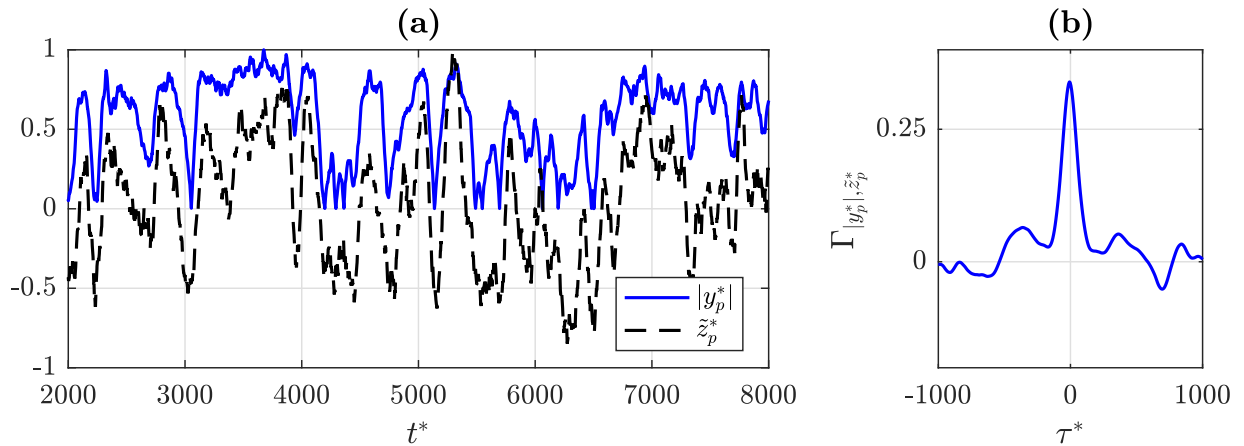


Figure 5.28 – (a) Normalized time series of $|y_p^*|$ (blue solid line) and z_p^* (black dashed line) and (b) their cross-correlation $\Gamma_{|y_p^*|, z_p^*}(\tau^*)$. Plotted data are smoothed over $\Delta t^* = 150$ for clarity.

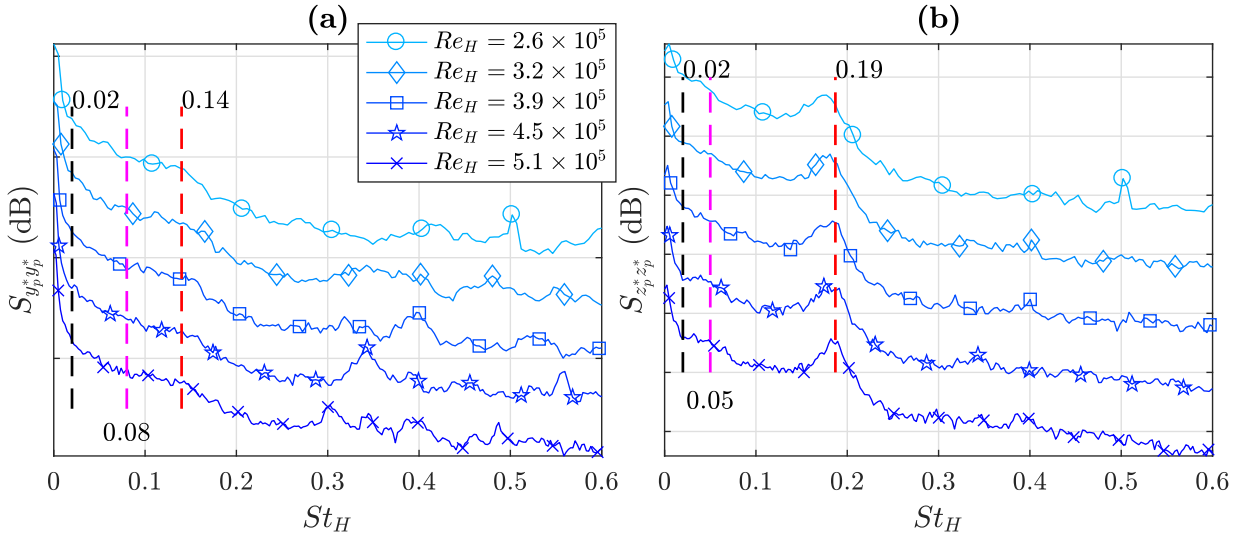


Figure 5.29 – PSD of the fluctuations of (a) y_p^* and (b) z_p^* for five Reynolds number: 2.6×10^5 (circle), 3.2×10^5 (diamond), 3.9×10^5 (square), 4.5×10^5 (star) and 5.1×10^5 (cross). Curves are shifted for clarity. The frequency resolution is $\Delta St_H = 2 \times 10^{-3}$.

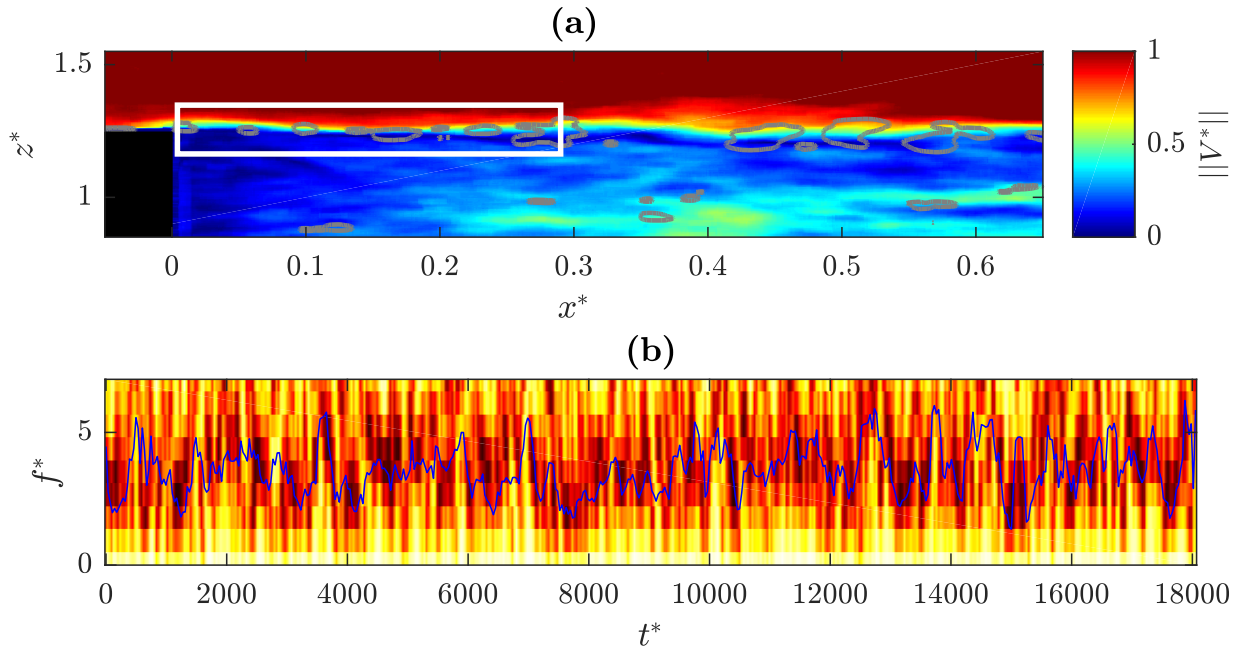


Figure 5.30 – (a) Instantaneous velocity field, together with contour of λ_{Ci} (gray) and the rectangular ROI (white). (b) Estimated KH frequency for each velocity field $f_{shed}^*(t^*)$ (highlighted in blue).

to the turbulent perturbations growth (Brackston *et al.*, 2016).

5.4.2.3 Transient symmetric state

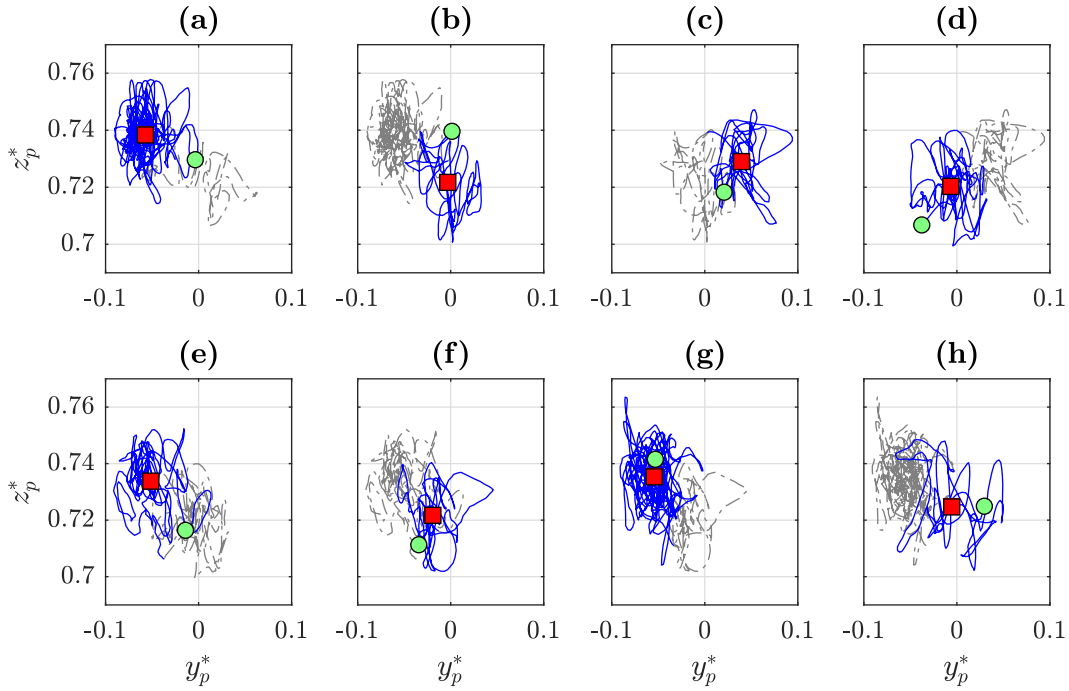


Figure 5.31 – Successive trajectories of $G_p(y_p^*, z_p^*)$ during periods of (a) $\Delta t^* = 367$, (b) $\Delta t^* = 105$, (c) $\Delta t^* = 126$, (d) $\Delta t^* = 145$, (e) $\Delta t^* = 194$, (f) $\Delta t^* = 111$, (g) $\Delta t^* = 414$, and (h) $\Delta t^* = 96$. The solid blue line shows the barycenter trajectory and the grey dashed line displays its previous one. The green circle and the red square are respectively the last position and the most probable location in the corresponding sub-figure of G_p .

The positions of the pressure barycenter G_P for successive stays in the RSB modes are displayed in Figure 5.31. The most probable location (red square plots) near which G_p evolves during each stay alternates between two opposite spanwise positions, keeping the same vertical position [Figure 5.31(a-c-e)]. During most of the flipping processes, the pressure center goes around a central position $y_p^* \sim 0$, as shown by Figure 5.31(b-d-f-h). In average, this step lasts for well shorter time than the RSB modes. It is noteworthy that, after being in this transient state, the wake may also go back in the previous RSB mode as illustrated by Figure 5.31(e-f-g).

As mentioned hereinbefore, three states can be considered for the system: two corresponding to the RSB modes, and a third one being a transient mode. For a more quantitative analysis, two thresholds for $y_p^*(t)$ has consequently been defined. Above a given positive threshold $y_{p,P}^*$, the wake is in the P mode, and lower than a given negative threshold $y_{p,N}^*$, it is in the N mode. Between these values, it is the transient state. The thresholds are computed as

$$y_{p,N}^* = w_{th} \times y_{p,\max(P_{y_p^*|y_p^* < \bar{y}_p^*})}^* \quad \text{and} \quad y_{p,P}^* = w_{th} \times y_{p,\max(P_{y_p^*|y_p^* > \bar{y}_p^*})}^*, \quad (5.7)$$

where P_X is the PDF of the variable X , \bar{X} is the temporal mean of X , and w_{th} is a positive weight to avoid too large thresholds ($w_{th} = 0.25$ is chosen). From now on, the state of the wake is

defined as negative (N), positive (P) or transient symmetric (TS), where respectively $y_p^* < y_{p,N}^*$, $y_p^* > y_{p,P}^*$ and $y_{p,N}^* < y_p^* < y_{p,P}^*$.

Even if the switching process seems to randomly occur, some characteristic time scales can be statistically estimated. Hence, the time the wake spent on each mode is evaluated from all runs, giving $T_{RSB}^* \sim 7 \times 10^2$ for each asymmetric mode, whereas the switch itself lasts for $T_{switch}^* \sim 4 \times 10^1$. As expected, these results have a high dispersion caused by the turbulent noise, their respective standard deviations being $\sigma_{T_{RSB}^*} = 10^2$ and $\sigma_{T_{switch}^*} = 10^1$. A mean switching frequency is also computed by counting the switching occurrences during runs: $f_{switch}^* \sim 3.4 \times 10^{-3}$. In probability terms, the RSB modes exist 83.4% (± 5.3) of the time (41.1% for the N state, and 42.3% for the P one), whereas the wake is in the unstable TS mode during the remaining 16.6% (± 1.2). This is the reason why the present wake can also be considered thereafter exhibiting a trimodal dynamics.

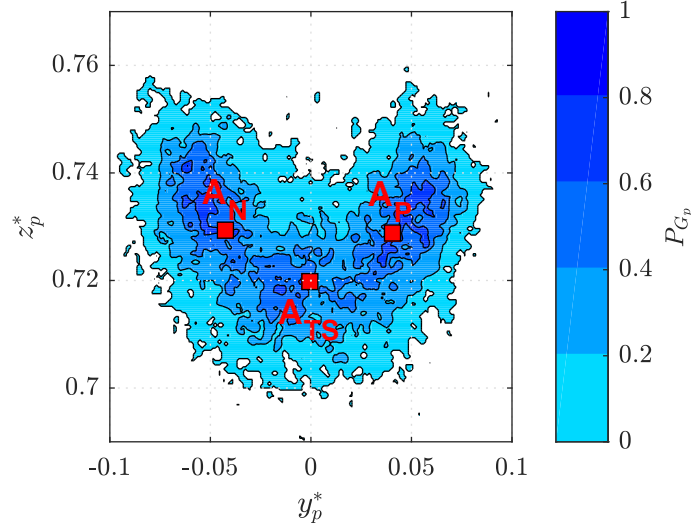


Figure 5.32 – Normalized 2D PDF of $G_p(y_p^*, z_p^*)$ for a 2-min run, together with the conditional-mean positions of G_p (red squares) for each identified mode.

The 2D PDF of the pressure barycenter is computed and shown in Figure 5.32. It gives a global overview of its most frequent positions on the rear. As revealed by the time series, three main areas corresponding to the wakes states are highlighted, confirming the trimodal behavior. We calculate then the positions of the identified centers of these areas, denoted $A_N(y_{A_N}^*, z_{A_N}^*)$, $A_P(y_{A_P}^*, z_{A_P}^*)$ and $A_{TS}(y_{A_{TS}}^*, z_{A_{TS}}^*)$ for the N, P and TS states respectively, such as

$$\overrightarrow{OA_N} = \begin{pmatrix} y_p^*|_{y_p^* < y_{p,N}^*} \\ z_p^*|_{y_p^* < y_{p,N}^*} \end{pmatrix}, \overrightarrow{OA_P} = \begin{pmatrix} y_p^*|_{y_p^* > y_{p,P}^*} \\ z_p^*|_{y_p^* > y_{p,P}^*} \end{pmatrix} \text{ and } \overrightarrow{OA_{TS}} = \begin{pmatrix} y_p^*|_{y_{p,N}^* < y_p^* < y_{p,P}^*} \\ z_p^*|_{y_{p,N}^* < y_p^* < y_{p,P}^*} \end{pmatrix}. \quad (5.8)$$

For each area a quasi-attractive center can be identified, such as $y_{C_1}^* \sim -y_{C_2}^*$ and $z_{C_1}^* \sim z_{C_1}^*$. During the switch between these two positions, the pressure barycenter follows preferentially a trajectory along a well-defined path.

It is then interesting to visualize the corresponding time-averaged pressure and velocity fields using conditional averaging. Figure 5.33(a-c) display the conditional time-averaged pressure

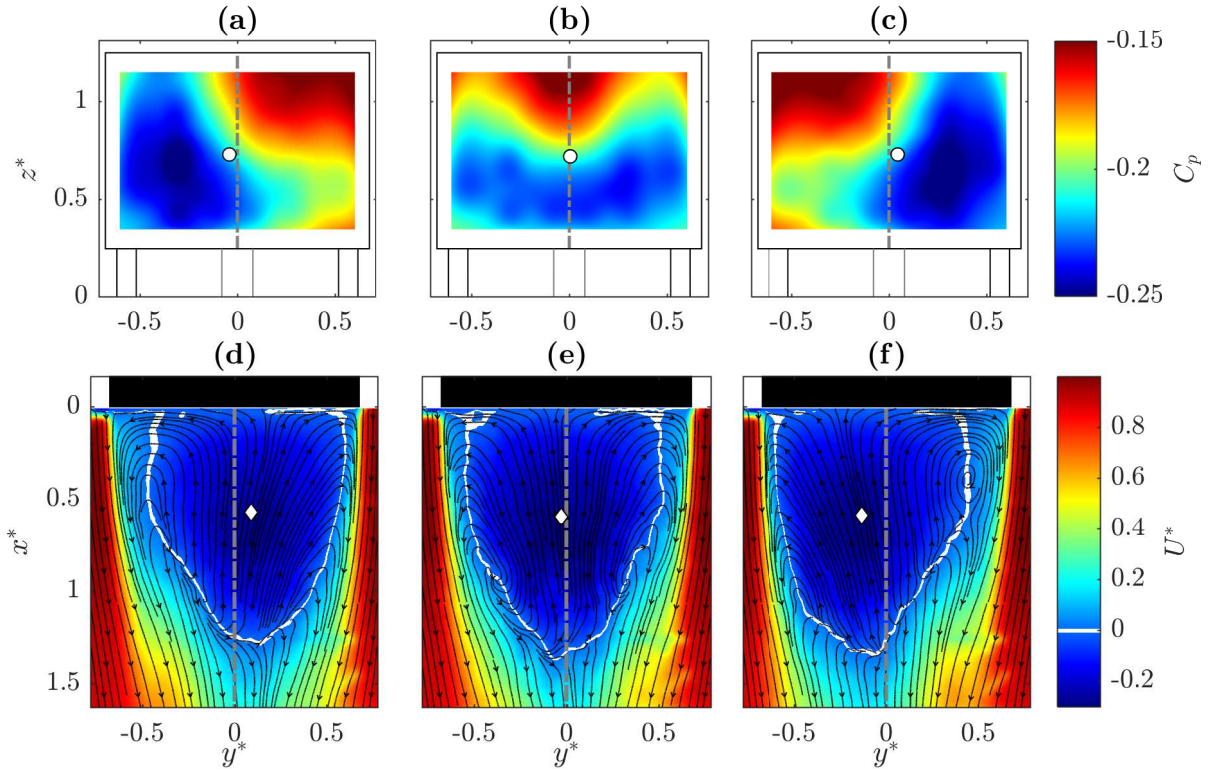


Figure 5.33 – Conditional averages of the pressure coefficient at the rear body and the velocity field at $z^* = 1$ for the modes **(a-d)** N, **(b-e)** TS and **(c-f)** P. The average position of the pressure center G_p (white circle) and of the recirculation barycenter G_{rec} (white diamond) are displayed. $y^* = 0$ is also displayed (dash-dotted grey lines). Some streamlines are plotted over the streamwise component of the velocity to localize the coherent large-scale structures.

fields of the three modes, while [Figure 5.33\(d-f\)](#) correspond to their conditional time-averaged velocity fields. The RSB modes presented here have identical pressure and velocity topologies as the ones without considering the transient state ([Volpe *et al.*, 2015](#)): the depression is localized on the same side as the vortex being the closest to the rear surface. In the TS state, the wake appears to be a perfect mean of the two RSB modes. These results are in good agreement with the transient state revealed in the cluster-based modelling by [Kaiser *et al.* \(2014\)](#). Once again, the phase opposition between the pressure and velocity barycenters clearly appears.

The conditional time-averaged velocity fields is also computed in the reflexive XZ-plane from a $T_{PIV}^* = 18 \times 10^3$ run. The RSB modes have the same vertical configuration, which is given in [Figure 5.34\(a\)](#). In the TS state [[Figure 5.34\(b\)](#)], the toroidal structure seems to globally move closer to the rear body and the recirculation barycenter is slightly higher than for the asymmetric states. It shall be mentioned that 80 velocity fields were detected as describing a TS mode to compute the corresponding mean field.

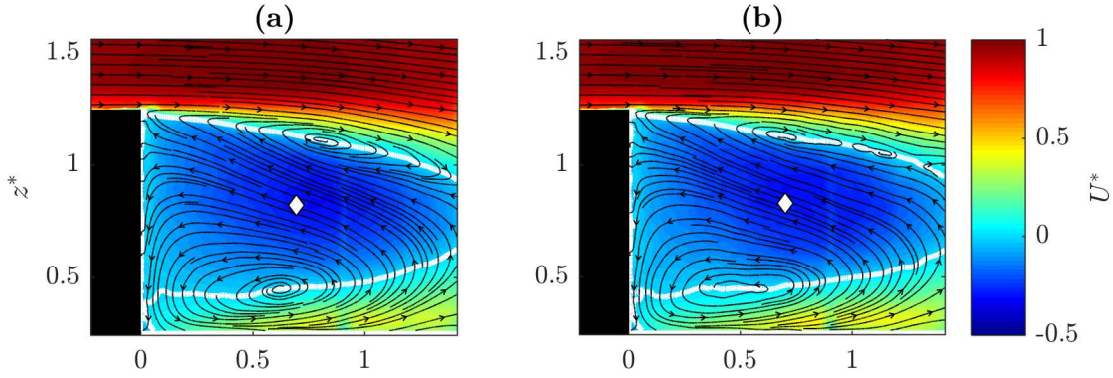


Figure 5.34 – Conditional averages of the velocity field at $y^* = 0$ for the modes (a) N and P, and (b) TS. The average position of the recirculation barycenter G_{rec} (white diamond) is also displayed. Some streamlines are plotted over the streamwise component of the velocity to localize the large-scale structures.

5.4.3 Coherent structures

As we are interested in the dynamics of the large-scale structures, we quantify the spatio-temporal organization of the wall pressure spatial distributions using POD on each entire studied data set. As a reminder, it is an efficient approach to detect coherent structures in turbulent flows (Lumley, 1967; Sirovich, 1987). Thus we apply the POD on the rear pressure coefficient fluctuations \tilde{c}_p :

$$\tilde{c}_p(t) \sim \sum_{i=1}^k a_i(t) \Phi_i, \quad (5.9)$$

where k is the number of POD modes Φ_i carrying most of the coherent structures energy and a_i are the corresponding temporal coefficients. The energy distribution of the first 20 POD modes is given in Figure 5.35 showing that the first five modes contain 75% of the total energy.

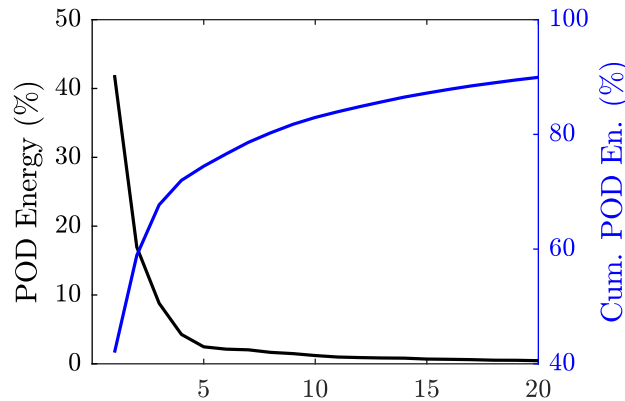


Figure 5.35 – Energy distribution (black) and cumulative energy (blue) of the first 20 POD modes of the rear pressure fluctuations.

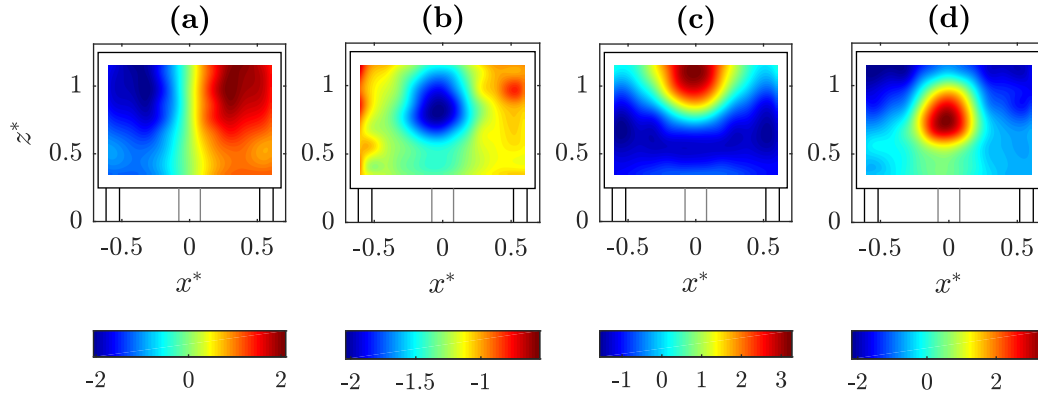


Figure 5.36 – Four first POD modes of the rear pressure fluctuations: (a) Φ_1 (42%), (b) Φ_2 (17%), (c) Φ_3 (8.8%) and (d) Φ_4 (4.3%).

The most remarkable results are that the first mode Φ_1 represents 42% of the total energy (Figure 5.35) and that its spatial organization exhibits the global symmetry breaking presented in Figure 5.36(a). Perry *et al.* (2016) found a similar result by analyzing the PDF of its temporal coefficient a_1 , exhibiting two peaks like in Figure 5.21(b) and Figure 5.21(d). Φ_2 (17%) and Φ_4 (4.3%) can be paired, since they display the same central symmetry and their amplitude are in opposition. Both have a spatial singularity centred in the same position as the G_p resident zone. With 8.8% of the total energy, Φ_3 has an uniform distribution with a strong singularity localized in the middle of the top edge.

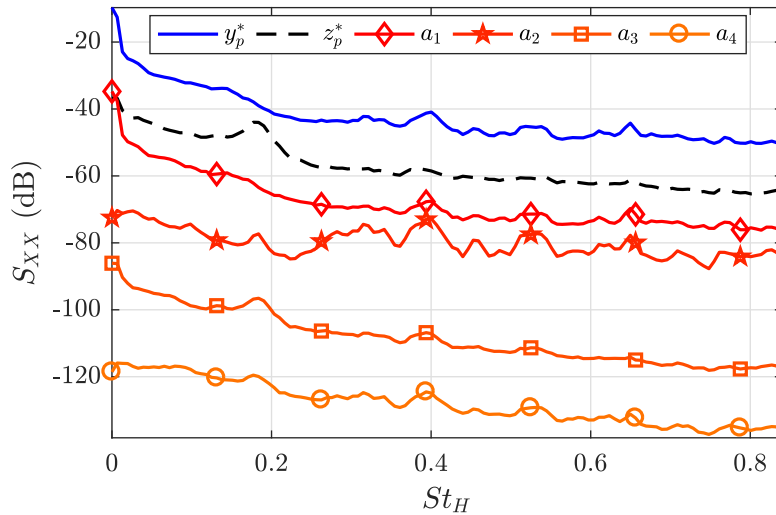


Figure 5.37 – PSD of the four first POD coefficients of the rear pressure fluctuations, together with $S_{y_p^* y_p^*}$ (solid blue line) and $S_{z_p^* z_p^*}$ (dashed black line).

The spectral signature of the first POD coefficient a_1 is identical to the one of the pressure barycenter, displayed in Figure 5.37. This confirms that the pressure barycenter is a direct measure of the most energetic large-scale coherent structure governed by a long time scale. The POD modes pair Φ_2 and Φ_4 are multifaceted since they contain the peak at $St_H = 0.19$, characteristic of $S_{z_p^* z_p^*}$ alone, and they partly share the same higher-frequency spectrum as $S_{y_p^* y_p^*}$. As expected

from the Φ_3 spatial organization, a_3 behaves like z_p^* . Finally, at least three POD modes carrying 30.1% of the total energy have the vortex shedding signature in their spectra, confirming the influence of the top shear layer on the depression dynamics.

5.5 Conclusions

The square-back configuration of the Ahmed body has been investigated. The barycenters of the pressure distribution over the rear part of this model and of the intensity recirculation are found highly correlated. Both described the most energetic large-scale structures dynamics, confirming the relation between the large-scale recirculation bubble and its wall-pressure footprint. The switching process and the vortex shedding from the top shear layer seem to dominate the depression dynamics. A third state, transient symmetric, is highlighted when analysing the bimodality.

Future investigations on the square-back version should involve only the four classic pods to avoid the clear fixing of the vertical bimodal behavior (Barros *et al.*, 2017). They could eventually be designed with NACA profile McArthur *et al.* (2016). Also, the sharp edges of the after-body are far from real modern cars design. Recently, Thacker *et al.* (2012) rounded the roof/backlight intersection and Rossitto *et al.* (2016) completed with curved sides/backlight edges for the slanted configuration of the Ahmed body. Such modifications of the square-back model should be considered in further works.

Bibliography

- AHMED, S., RAMM, G. & FALTIN, G. (1984) Some salient features of the time-averaged ground vehicle wake. In *SAE Technical Paper 840300*. SAE International. doi:[10.4271/840300](https://doi.org/10.4271/840300). 88, 89
- AIDER, J.L., DANET, A. & LESIEUR, M. (2007) Large-eddy simulation applied to study the influence of upstream conditions on the time-dependant and averaged characteristics of a backward-facing step flow. *Journal of Turbulence* **8**, p. N51. doi:[10.1080/14685240701701000](https://doi.org/10.1080/14685240701701000). 103
- BAILEY, S.C.C., MARTINUZZI, R.J. & KOPP, G.A. (2002) The effects of wall proximity on vortex shedding from a square cylinder: Three-dimensional effects. *Physics of Fluids* **14** (12), pp. 4160–4177. doi:[10.1063/1.1514972](https://doi.org/10.1063/1.1514972). 88
- BARROS, D. (2015) Wake and drag manipulation of a bluff body using fluidic forcing. PhD thesis, École Nationale Supérieure de Mécanique et d'Aérotechnique, Poitiers, France. 101, 102
- BARROS, D., BORÉE, J., CADOT, O., SPOHN, A. & NOACK, B.R. (2017) Forcing symmetry exchanges and flow reversals in turbulent wakes. *Journal of Fluid Mechanics* **829**. doi:[10.1017/jfm.2017.590](https://doi.org/10.1017/jfm.2017.590). 106, 120
- BARROS, D., BORÉE, J., NOACK, B.R. & SPOHN, A. (2016) Resonances in the forced turbulent wake past a 3D blunt body. *Physics of Fluids* **28** (6), p. 065104. doi:[10.1063/1.4953176](https://doi.org/10.1063/1.4953176). 93, 100, 109
- BARROS, D., RUIZ, T., BORÉE, J. & NOACK, B.R. (2014) Control of a three-dimensional blunt body wake using low and high frequency pulsed jets. *International Journal of Flow Control* **6** (1), pp. 61–74. doi:[10.1260/1756-8250.6.1.61](https://doi.org/10.1260/1756-8250.6.1.61). 93
- BEARMAN, P.W. (1967) On vortex street wakes. *Journal of Fluid Mechanics* **28** (4), p. 625–641. doi:[10.1017/S0022112067002368](https://doi.org/10.1017/S0022112067002368). 94
- BEAUDOIN, J.F., CADOT, O., AIDER, J.L., GOSSE, K., PARANTHOËN, P., HAMELIN, B., TISSIER, M., ALLANO, D., MUTABAZI, I., GONZALES, M. *et al.* (2004) Cavitation as a complementary tool for automotive aerodynamics. *Experiments in Fluids* **37** (5), pp. 763–768. doi:[10.1007/s00348-004-0879-y](https://doi.org/10.1007/s00348-004-0879-y). 90
- BRACKSTON, R., GARCÍA DE LA CRUZ, J., WYNN, A., RIGAS, G. & MORRISON, J. (2016) Stochastic modelling and feedback control of bistability in a turbulent bluff body wake. *Journal of Fluid Mechanics* **802**, pp. 726–749. doi:[10.1017/jfm.2016.495](https://doi.org/10.1017/jfm.2016.495). 92, 93, 114
- VAN DEN BROECK, C., PARRONDO, J.M.R. & TORAL, R. (1994) Noise-induced nonequilibrium phase transition. *Physical Review Letters* **73**, pp. 3395–3398. doi:[10.1103/PhysRevLett.73.3395](https://doi.org/10.1103/PhysRevLett.73.3395). 92

- BROZE, G. & HUSSAIN, F. (1994) Nonlinear dynamics of forced transitional jets: periodic and chaotic attractors. *Journal of Fluid Mechanics* **263**, p. 93–132. doi:10.1017/S0022112094004040. 109
- BURY, Y. & JARDIN, T. (2012) Transitions to chaos in the wake of an axisymmetric bluff body. *Physics Letters A* **376** (45), pp. 3219 – 3222. doi:10.1016/j.physleta.2012.09.011. 92
- CADOT, O., EVRARD, A. & PASTUR, L. (2015) Imperfect supercritical bifurcation in a three-dimensional turbulent wake. *Physical Review E* **91** (6), p. 063005. doi:10.1103/PhysRevE.91.063005. 93, 105, 106
- CASTRO, I.P. & ROBINS, A.G. (1977) The flow around a surface-mounted cube in uniform and turbulent streams. *Journal of Fluid Mechanics* **79** (2), p. 307–335. doi:10.1017/S0022112077000172. 88
- CHOI, H., LEE, J. & PARK, H. (2014) Aerodynamics of heavy vehicles. *Annual Review of Fluid Mechanics* **46** (1), pp. 441–468. doi:10.1146/annurev-fluid-011212-140616. 89, 90
- COURTINE, S. & SPOHN, A. (2004) Dynamics of separation bubbles formed on rounded edges. In *12th International Symposium on Applications of Laser Techniques to Fluid Mechanics. Lisbon, Portugal*. 89
- DROUIN V., G.A. & P., G. (2002) Topology and characterization of the vortical near-wake flow over a simplified car model. In *Proceedings of the bluff body wakes and vortex induced vibrations (BBVIV3) conference, Port-Douglas, Australia*. 91
- DUELL, E.G. & GEORGE, A.R. (1999) Experimental study of a ground vehicle body unsteady near wake. In *SAE Technical Paper*. SAE International. doi:10.4271/1999-01-0812. 91
- EULALIE, Y. (2014) Aerodynamic analysis and drag reduction around an Ahmed bluff body. PhD thesis, Université de Bordeaux, Bordeaux, France. 93, 101, 102, 109, 112
- EVSTAFYEVA, O., MORGANS, A.S. & DALLA LONGA, L. (2017) Simulation and feedback control of the Ahmed body flow exhibiting symmetry breaking behaviour. *Journal of Fluid Mechanics* **817**. doi:10.1017/jfm.2017.118. 91, 93
- FABRE, D., AUGUSTE, F. & MAGNAUDET, J. (2008) Bifurcations and symmetry breaking in the wake of axisymmetric bodies. *Physics of Fluids* **20** (5), p. 051702. doi:10.1063/1.2909609. 92
- GENTILE, V., SCHRIJER, F.F.J., VAN OUDHEUSDEN, B.W. & SCARANO, F. (2016) Low-frequency behavior of the turbulent axisymmetric near-wake. *Physics of Fluids* **28** (6), p. 065102. doi:10.1063/1.4953150. 109, 110
- GILLIÉRON, P. & CHOMETON, F. (1999) Modelling of stationary three-dimensional separated air flows around an ahmed reference model. *ESAIM: Proceedings and Surveys* **7**, pp. 173–182. doi:10.1051/proc:1999016. 89
- GRANDEMANGE, M., CADOT, O. & GOHLKE, M. (2012b) Reflectional symmetry breaking of the separated flow over three-dimensional bluff bodies. *Physical Review E* **86** (3), p. 035302. doi:10.1103/PhysRevE.86.035302. 91, 93

- GRANDEMANGE, M., GOHLKE, M. & CADOT, O. (2013a) Turbulent wake past a three-dimensional blunt body. Part 1. Global modes and bi-stability. *Journal of Fluid Mechanics* **722**, pp. 51–84. doi:10.1017/jfm.2013.83. 91, 98, 100, 106, 108
- GRANDEMANGE, M., GOHLKE, M. & CADOT, O. (2013c) Bi-stability in the turbulent wake past parallelepiped bodies with various aspect ratios and wall effects. *Physics of Fluids* **25** (9). doi:10.1063/1.4820372. 92, 93, 101, 102, 104
- GRANDEMANGE, M., GOHLKE, M. & CADOT, O. (2014a) Turbulent wake past a three-dimensional blunt body. Part 2. Experimental sensitivity analysis. *Journal of Fluid Mechanics* **752**, pp. 439 — 461. doi:10.1017/jfm.2014.345. 92
- GRANDEMANGE, M., GOHLKE, M. & CADOT, O. (2014b) Statistical axisymmetry of the turbulent sphere wake. *Experiments in Fluids* **55** (11), p. 1838. doi:10.1007/s00348-014-1838-x. 88
- GRANDEMANGE, M., GOHLKE, M., PAREZANOVIĆ, V. & CADOT, O. (2012a) On experimental sensitivity analysis of the turbulent wake from an axisymmetric blunt trailing edge. *Physics of Fluids* **24**, pp. 51–84. doi:10.1063/1.3694765. 92
- GRIFFIN, O.M. (1981) Universal similarity in the wakes of stationary and vibrating bluff structures. *Journal of Fluids Engineering* **103** (1), pp. 52–58. doi:10.1115/1.3240780. 94
- GUMOWSKI, K., MIEDZIK, J., GOUJON-DURAND, S., JENFFER, P. & WESFREID, J. (2008) Transition to a time-dependent state of fluid flow in the wake of a sphere. *Physical Review E* **77** (5), p. 055308. doi:10.1103/PhysRevE.77.055308. 88
- HINTERBERGER, C., GARCÍA-VILLALBA, M. & RODI, W. (2004) Large eddy simulation of flow around the ahmed body. In *The Aerodynamics of Heavy Vehicles: Trucks, Buses, and Trains* (ed. R. McCallen, F. Browand & J. Ross), pp. 77–87. Berlin, Heidelberg: Springer. doi:10.1007/978-3-540-44419-0_7. 90
- HUCHO, W.H. (2013) *Aerodynamics of road vehicles: From fluid mechanics to vehicle engineering*. Elsevier. 88
- JOSEPH, P. (2012) Application of control by pulsed jets on a bluff body. PhD thesis, Université Pierre et Marie Curie, Paris, France. 89, 91
- KAISER, E., NOACK, B.R., CORDIER, L., SPOHN, A., SEGOND, M., ABEL, M., DAVILLER, G., ÖSTH, J., KRAJNOVIĆ, S., NIVEN, R.K. & ET AL. (2014) Cluster-based reduced-order modelling of a mixing layer. *Journal of Fluid Mechanics* **754**, p. 365–414. doi:10.1017/jfm.2014.355. 92, 117
- KHALIGHI, B., CHEN, K. & IACCARINO, G.G. (2012) Unsteady aerodynamic flow investigation around a simplified square-back road vehicle with drag reduction devices. *Journal of Fluids Engineering* **134** (6), p. 061101. doi:10.1115/1.4006643. 109
- KLOTZ, L., GOUJON-DURAND, S., ROKICKI, J. & WESFREID, J. (2014) Experimental investigation of flow behind a cube for moderate Reynolds numbers. *Journal of Fluid Mechanics* **750**, pp. 73 – 98. doi:10.1017/jfm.2014.236. 88

- KOVASZNAVY, L.S.G. (1949) Hot-wire investigation of the wake behind cylinders at low Reynolds numbers. *Proceedings of the Royal Society of London A: Mathematical, Physical and Engineering Sciences* **198** (1053), pp. 174–190. doi:10.1098/rspa.1949.0093. 103
- KRAJNOVIĆ, S. & DAVIDSON, L. (2003) Numerical study of the flow around a bus-shaped body. *Journal of Fluids Engineering* **125** (3), pp. 500–509. doi:10.1115/1.1567305. 91, 93
- KRAJNOVIĆ, S. & DAVIDSON, L. (2004) Large-eddy simulation of the flow around simplified car model. *SAE Paper 2004-01-0227* . 90, 91
- KRAJNOVIĆ S., D.L. (2005) Flow around a simplified car. Part 1: Large eddy simulation. *Journal of Fluids Engineering* **127** (5), pp. 907–918. doi:10.1115/1.1989371. 90, 98
- LAHAYE, A., LEROY, A. & KOURTA, A. (2014) Aerodynamic characterisation of a square back bluff body flow. *International Journal of Aerodynamics* **4** (1-2), pp. 43–60. doi:10.1504/IJAD.2014.057804. PMID: 57804. 93, 98, 99, 101, 102, 109, 112
- LAMBALLAIS, E., SILVESTRINI, J. & LAIZET, S. (2008) Direct numerical simulation of a separation bubble on a rounded finite-width leading edge. *International Journal of Heat and Fluid Flow* **29** (3), pp. 612 – 625. doi:10.1016/j.ijheatfluidflow.2008.03.006. The Fifth International Symposium on Turbulence and Shear Flow Phenomena (TSFP5). 89
- LECLERC, C. (2008) Réduction de la traînée d’un véhicule automobile simplifié à l’aide du contrôle actif par jet synthétique. PhD thesis, Institut National Polytechnique de Toulouse, Toulouse, France. 90
- LEHUGEUR, B. (2007) Characterization and control of longitudinal vortices in automotive aerodynamics. PhD thesis, Université Pierre et Marie Curie, Paris, France. 90
- LIENHART, H., STOOT, C. & BECKER, S. (2002) Flow and turbulence structures in the wake of a simplified car model (ahmed model). In *New Results in Numerical and Experimental Fluid Mechanics III: Contributions to the 12th STAB/DGLR Symposium Stuttgart, Germany 2000* (ed. S. Wagner, U. Rist, H.J. Heinemann & R. Hilbig), pp. 323–330. Berlin, Heidelberg: Springer. doi:10.1007/978-3-540-45466-3_39. 89, 90
- LUMLEY, J.L. (1967) The structure of inhomogeneous turbulent flows. In *Atmospheric turbulence and radio propagation* (ed. A.M. Yaglom & V.I. Tatarski), pp. 166–178. Moscow: Nauka. 118
- MCCARTHER, D., BURTON, D., THOMPSON, M. & SHERIDAN, J. (2016) On the near wake of a simplified heavy vehicle. *Journal of Fluids and Structures* **66**, pp. 293 – 314. doi:10.1016/j.jfluidstructs.2016.07.011. 109, 120
- MELIGA, P., CHOMAZ, J.M. & SIPP, D. (2009) Global mode interaction and pattern selection in the wake of a disk: A weakly nonlinear expansion. *Journal of Fluid Mechanics* **633**, p. 159–189. doi:10.1017/S0022112009007290. 92
- MINGUEZ, M., PASQUETTI, R. & SERRE, E. (2008) High-order large-eddy simulation of flow over the “ahmed body” car model. *Physics of Fluids* **20** (9), p. 095101. doi:10.1063/1.2952595. 90

- MOREL, T. (1978) The effect of base slant on the flow pattern and drag of three-dimensional bodies with blunt ends. In *Aerodynamic Drag Mechanisms of Bluff Bodies and Road Vehicles* (ed. G. Sovran, T. Morel & W.T. Mason), pp. 191–226. Boston, MA: Springer US. doi:10.1007/978-1-4684-8434-2_8. 88
- ÖSTH, J., NOACK, B.R., KRAJNOVIĆ, S., BARROS, D. & BORÉE, J. (2014) On the need for a nonlinear subscale turbulence term in pod models as exemplified for a high-reynolds-number flow over an ahmed body. *Journal of Fluid Mechanics* **747**, pp. 518–544. doi:10.1017/jfm.2014.168. 91, 93
- PAREZANOVIĆ, V. & CADOT, O. (2012) Experimental sensitivity analysis of the global properties of a two-dimensional turbulent wake. *Journal of Fluid Mechechanics* **693**, p. 115–149. doi:10.1017/jfm.2011.495. 109
- PERRY, A.K., PAVIA, G. & PASSMORE, M. (2016) Influence of short rear end tapers on the wake of a simplified square-back vehicle: wake topology and rear drag. *Experiments in Fluids* **57** (11), p. 169. doi:10.1007/s00348-016-2260-3. 119
- PONTA, F. (2006) Effect of shear-layer thickness on the Strouhal–Reynolds number relationship for bluff-body wakes. *Journal of Fluids and Structures* **22** (8), pp. 1133 – 1138. doi:10.1016/j.jfluidstructs.2006.03.005. 94
- RIGAS, G., MORGANS, A.S., BRACKSTON, R.D. & MORRISON, J.F. (2015) Diffusive dynamics and stochastic models of turbulent axisymmetric wakes. *Journal of Fluid Mechanics* **778**, p. R2. doi:10.1017/jfm.2015.390. 92
- RIGAS, G., OXLADE, A.R., MORGANS, A.S. & MORRISON, J.F. (2014) Low-dimensional dynamics of a turbulent axisymmetric wake. *Journal of Fluid Mechanics* **755**, p. R5. doi:10.1017/jfm.2014.449. 92
- ROSHKO, A. (1955) On the wake and drag of bluff bodies. *Journal of the Aeronautical Sciences* **22** (2), pp. 124–132. doi:10.2514/8.3286. 94
- ROSSITTO, G., SICOT, C., FERRAND, V., BORÉE, J. & HARAMBAT, F. (2016) Influence of afterbody rounding on the pressure distribution over a fastback vehicle. *Experiments in Fluids* **57** (3), p. 43. doi:10.1007/s00348-016-2120-1. 120
- ROUMÉAS, M., GILLIÉRON, P. & KOURTA, A. (2008) Separated flows around the rear window of a simplified car geometry. *Journal of Fluids Engineering* **130** (2), p. 021101. doi:10.1115/1.2829566. 90
- ROUMÉAS, M., GILLIÉRON, P. & KOURTA, A. (2009) Analysis and control of the near-wake flow over a square-back geometry. *Computers & Fluids* **38** (1), pp. 60 – 70. doi:10.1016/j.compfluid.2008.01.009. 93
- SIROVICH, L. (1987) Turbulence and the dynamics of coherent structures. *Quarterly of Applied Mathematics* **45**, pp. 561–571. 118

- SPOHN, A. & GILLIÉRON, P. (2002) Flow separations generated by a simplified geometry of an automotive vehicle. In *IUTAM Symposium: unsteady separated flows, Toulouse, France*. 89, 90, 98
- STRACHAN, R.K., KNOWLES, K. & LAWSON, N.J. (2007) The vortex structure behind an ahmed reference model in the presence of a moving ground plane. *Experiments in Fluids* **42** (5), pp. 659–669. doi:10.1007/s00348-007-0270-x. 91
- THACKER, A. (2010) Experimental contribution to the steady and unsteady analysis of the flow behind a bluff body. PhD thesis, Université d'Orléans, Orléans, France. 90
- THACKER, A., AUBRUN, S., LEROY, A. & DEVINANT, P. (2012) Effects of suppressing the 3D separation on the rear slant on the flow structures around an Ahmed body. *Journal of Wind Engineering and Industrial Aerodynamics* **107**, pp. 237 – 243. doi:10.1016/j.jweia.2012.04.022. 120
- THOMPSON, M.C. & HOURIGAN, K. (2005) The shear-layer instability of a circular cylinder wake. *Physics of Fluids* **17** (2), p. 021702. doi:10.1063/1.1852581. 110
- VENNING, J., LO JACONO, D., BURTON, D., THOMPSON, M.C. & SHERIDAN, J. (2015) The effect of aspect ratio on the wake of the Ahmed body. *Experiments in Fluids* **56** (6), p. 126. doi:10.1007/s00348-015-1996-5. 91
- VENNING, J., LO JACONO, D., BURTON, D., THOMPSON, M.C. & SHERIDAN, J. (2017) The nature of the vortical structures in the near wake of the Ahmed body. In *Proceedings of the Institution of Mechanical Engineers, Part D: Journal of Automobile Engineering*. doi:10.1177/0954407017690683. 91
- VINO, G., WATKINS, S., MOUSLEY, P., WATMUFF, J. & PRASAD, S. (2005) Flow structures in the near-wake of the ahmed model. *Journal of Fluids and Structures* **20** (5), pp. 673 – 695. doi:10.1016/j.jfluidstructs.2005.03.006. 90
- VOLPE, R., DEVINANT, P. & KOURTA, A. (2015) Experimental characterization of the unsteady natural wake of the full-scale square back Ahmed body: Flow bi-stability and spectral analysis. *Experiments in Fluids* **56** (5), p. 99. doi:10.1007/s00348-015-1972-0. 91, 93, 100, 101, 102, 106, 108, 109, 117
- WILLIAMSON, C.H.K. (1996) Vortex dynamics in the cylinder wake. *Annual review of fluid mechanics* **28** (1), pp. 477–539. doi:10.1146/annurev.fl.28.010196.002401. 88
- WILLIAMSON, C.H.K. & BROWN, G.L. (1998) A series in $1/\sqrt{Re}$ to represent the Strouhal-Reynolds number relationship of the cylinder wake. *Journal of Fluids and Structures* **12** (8), pp. 1073 – 1085. doi:10.1006/jfs.1998.0184. 94
- YANG, J., LIU, M., WU, G., LIU, Q. & ZHANG, X. (2015) Low-frequency characteristics in the wake of a circular disk. *Physics of Fluids* **27** (6), p. 064101. doi:10.1063/1.4922109. 109
- YUN, G., KIM, D. & CHOI, H. (2006) Vortical structures behind a sphere at subcritical Reynolds numbers. *Physics of Fluids* **18** (1), p. 015102. doi:10.1063/1.2166454. 88

Turbulent wake as a dynamical system

In this chapter, the 3D full turbulent wake dynamics can be characterized by the single trajectory of its projected barycenter. After recovering a classic chaotic pattern, its inner characteristics are analyzed more thoroughly, by evaluating, in particular, the family of random process to which it belongs, the largest Lyapunov exponent of the system and the correlation dimension. This chapter is an extended version of the article published in Physical Review Fluids (Varon et al., 2017).

6.1	Quasi strange attractor dynamics	127
6.1.1	Clues to weak chaos	129
6.1.1.1	Structure function	129
6.1.1.2	Phase space reconstruction	130
6.1.2	A chaos portrait	132
6.1.2.1	Largest Lyapunov exponent	133
6.1.2.2	Correlation dimension	133
6.1.2.3	Telegraph-like signal	135
6.2	Conclusions and discussion	137

The most exciting phrase to hear in science, the one that heralds new discoveries, is not 'Eureka!' (I found it!) but 'That's funny ...'

ascribed to Isaac Asimov in the source code Fortune (1987)

6.1 Quasi strange attractor dynamics

The results, gathered in [Figure 5.32](#), disclose two areas highly preferred by the barycenter, corresponding to the two RSB states and a third one less visited, which is referred as the TS state. This pattern can bring back the strange attractors dynamics to us since two y -axis symmetric points attracts successively the depression center, passing through a preferential path when switching. We are interested here in the characterization of the bimodal oscillation of the near wake in the framework of dynamical systems theory and, more precisely, as a chaotic system ¹.

1. The term *chaos* is used to qualify a deterministic system, highly depending on the initial conditions

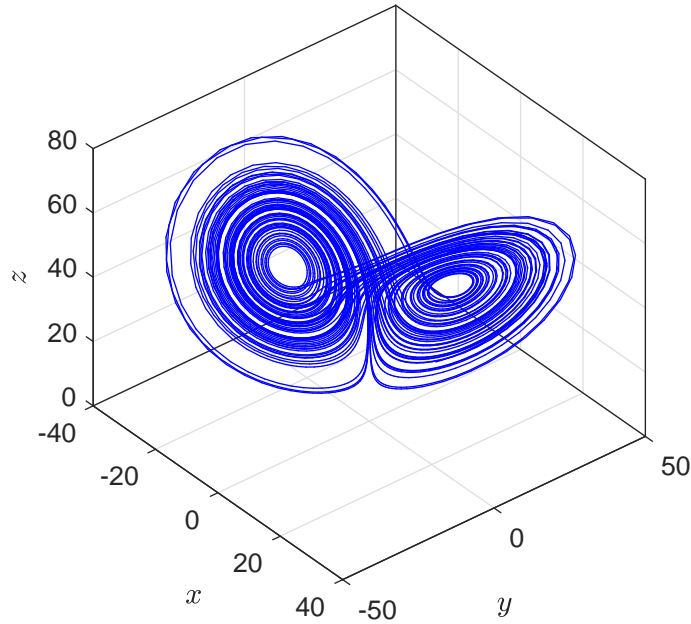


Figure 6.1 – Lorenz attractor with the parameters ($\sigma = 16$, $R = 45.92$, and $\beta = 4$).

A classic example of a chaotic system is the Lorenz attractor and corresponding Lorenz system, whose characteristic butterfly shape is famous (Lorenz, 1963). The so-called Lorenz system is a simplified weather model defined by the set of three ordinary differential equations:

$$\begin{cases} \dot{x} = \sigma(y - x) \\ \dot{y} = x(R - z) - y \\ \dot{z} = xy - \beta z \end{cases} \quad (6.1)$$

With the correct choice for the three parameters ($\sigma = 16$, $R = 45.92$, and $\beta = 4$), the trajectory plotted in Figure 6.1 exhibits a chaotic behavior, circling in an apparent random manner between two stable attractors.

Since the pioneering work of Lorenz, it has been shown that many biological, natural, or artificial systems, either at very small or very large scales, follow a chaotic dynamics. The brain wave activity (EEG) (Achermann *et al.*, 1994) or the heart rate activity (ECG) (Fojt & Holcik, 1998) can exhibit chaotic behaviors. In some cases, chaotic excitations can be used to study the response of mechanical systems. A variation in correlation dimensions can be used as an indicator of a fracture in the overall mechanical structure (Yan *et al.*, 2013). Chaotic behavior has also been found in trading market time series (Orlando, 2016). One can even find chaotic behavior for large-scale phenomena like earthquakes (Matcharashvili *et al.*, 2002).

The link between turbulence and strange attractors, has been a challenging question since the introduction of the chaos concept in fluid mechanics by Ruelle & Takens (1971). May the wake state be predicted at any time? In the laminar regime, Depending on the nature and the strength of the turbulences, some dynamics can be categorized as low-dimensional chaotic (Ruelle, 1991). For instance, Guckenheimer (1983) report that weakly turbulent convective flows contain strange

attractors. On the other hand, fully turbulent wakes are rather related to high-dimensional system and, because of this, are well captured by stochastic representations (Swinney & Gollub, 1986). Indeed, Östh *et al.* (2014) need 100 POD modes to recover the bimodal behavior for a reduced-order model of the turbulent wake behind a square-back Ahmed body, while Grandemange *et al.* (2013) use a Markovian process and Brackston *et al.* (2016) rely on a Langevin equation to statistically match it.

6.1.1 Clues to weak chaos

Analysing the signal to know whether the dynamics of the wake are chaotic or stochastic is therefore of prime interest. Different statistical methods may enable to properly categorize the wake (Guckenheimer, 1983; Provenzale *et al.*, 1992). Since such computations are only efficient through the use of long time series regarding the natural time scales (Eckmann *et al.*, 1986), the longest y_p^* signal is used in this section ($T^* = 45 \times 10^3$).

6.1.1.1 Structure function

An effective approach is to study its self-affinity by computing its first order ($k = 1$) (Osborne & Provenzale, 1989) or its second order ($k = 2$) (Provenzale *et al.*, 1992) structure function S_k , defined as

$$S_k(n) = \langle |y_p^*(i+n) - y_p^*(i)|^k \rangle_i, \quad (6.2)$$

where n is the lag and $\langle \cdot \rangle_i$ stands for the average over $N - n$ points. According to Mandelbrot (1982), if y_p^* is fractal, S_k follows a scaling law for small n :

$$S_k(n) \propto n^{kh}, \quad (6.3)$$

where h is the so-called scaling exponent. If the signal is chaotic then $h = 1$. If it is stochastic then its power spectrum follows a power-law $PSD(St_W) \propto St_W^{-\alpha}$ and $\alpha = 2h + 1$.

However, Provenzale *et al.* (1992) demonstrate that S_k alone is not enough to conclude and the structure function of the first derivative of the signal y_p^* , denoted as $S_{k,d}$, needs to be also computed. Thus, if it is stochastic then $S_{k,d}$ is almost constant and if the signal is chaotic then $S_{k,d}(n)$ follows a scaling law for small n . Figure 6.2 displays S_2 and $S_{2,d}$ for the raw signal y_p^* (a) and for the signal on which we apply a low-pass (LP) filter (b) to only select very low frequencies modes which have the highest magnitudes: $St_H < 10^{-3}$ [Figure 5.29(a)]. The raw signal behaves clearly like a fractal noise with $h = 1/2$ implying $\alpha = 2$, which is in agreement with Grandemange *et al.* (2013); Brackston *et al.* (2016). Conversely the LP filtered data appear to be chaotic since $h = 1$ and $S_{2,d}$ is not constant. It is noteworthy that the same observations hold for $k = 1$.

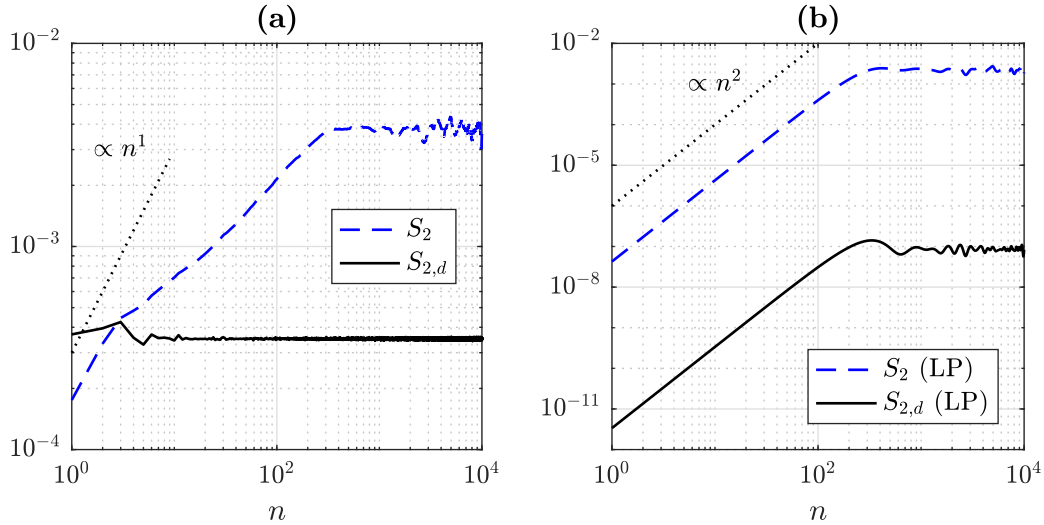


Figure 6.2 – (a) Second order structure functions of y_p^* (dashed blue line) and of its first derivative (solid black line). (b) Second order structure functions of the LP filtered y_p^* (dashed blue line) and of its first derivative (solid black line).

6.1.1.2 Phase space reconstruction

As we only observe a part of the non-linear wake dynamics (rear body pressure and 2D-2C velocity fields of the near-wake), we cannot experimentally access to its complete phase space. But [Eckmann & Ruelle \(1985\)](#) and [Sauer *et al.* \(1991\)](#) provide the so-called embedding methods to reconstruct a pseudo phase space from scalar N -points time series, which are $Y^N = \{y_p^*(i)\}_{i=1\dots N}$ in the present study. Thus, according to the pioneering Takens's time-delay embedding method ([Takens, 1981](#)), we build the M state vectors $\{\hat{Y}_i\}_{i=1\dots M}$:

$$\hat{Y}_i(m) = \left[y_p^*(i) \ y_p^*(i+J) \ \dots \ y_p^*(i+(m-1)J) \right], \quad (6.4)$$

where m is the embedding dimension and J the reconstruction delay², implying $M = N - (m - 1)J$.

J is determined first to avoid *redundance* - J too small, the extra components of Y_i are not independent - and *irrelevance* - J too large, information is lost due to the possible chaotic separation (see the Lyapunov exponent section) - in phase space reconstruction ([Casdagli *et al.*, 1991](#)). It is thus interesting to estimate the relation between the time series Y^M and its shifted version $Y_J^M = \{y_p^*(i+J)\}_{i=1\dots M}$ for various time-delays J . To manage it, a practical quantity is the mutual information (MI) between two time series X_1 and X_2 , denoted $I(X_1, X_2)$, which gives the information (bits) on X_1 , contained in X_2 ([Fraser & Swinney, 1986](#)). The best J to choose corresponds either to the first minimum of $I(Y^M, Y_J^M)$ if it exists, or to the moment a significant low rate of reduction in MI. Two recently improved algorithms are finally used: one computes directly the MI ([Cellucci *et al.*, 2005](#); [Jiang *et al.*, 2010](#)), and the other derives a quantity from it, the averaged mutual information (AMI) $\hat{I}(Y^M, Y_J^M)$, based on a kernel density estimation

2. J is the notation index and J^* is the corresponding dimensionless time.

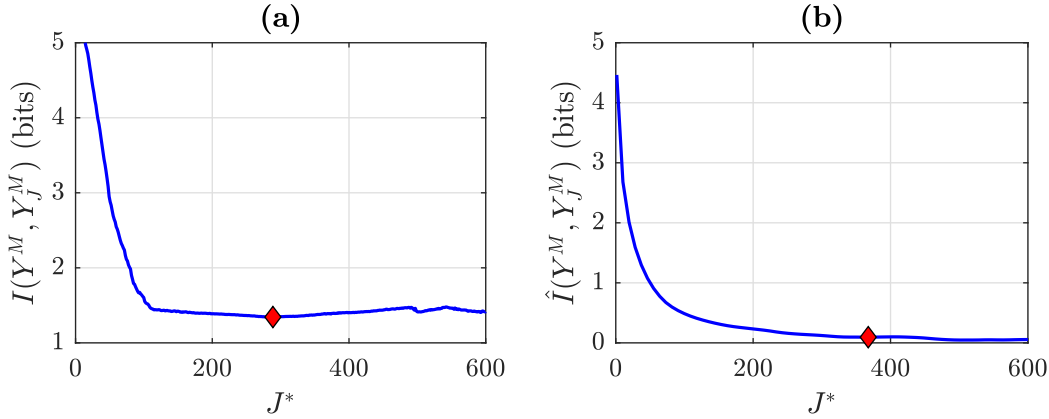


Figure 6.3 – (a) MI $I(Y^M, Y_J^M)$ and (b) AMI $\hat{I}(Y^M, Y_J^M)$, together with their respected minimum (red diamond)

(Silverman, 1986; Thomas *et al.*, 2014). Figure 6.3(a) and (b) show that the minima of MI and AMI are respectively obtained for $J^* \sim 2.9 \times 10^2$ and $J^* \sim 3.7 \times 10^2$. The first value is chosen since it corresponds also to the end of the rapid AMI decay.

We then determine the minimum value of m from y_p^* , following Cao’s method (Cao, 1997), which emanates from the false nearest neighbor algorithm of Kennel *et al.* (1992). This method enables also to distinguish deterministic and stochastic time series. The idea is to evaluate how the mean distance between close state vectors in dimension m evolves in the dimension $m+1$. Over the real embedding dimension, their ratio, denoted $E(m)$, does not change anymore. We look initially for the closest neighbor $\hat{Y}_{\mathcal{N}(i,m)}(m)$ of each state vector $\hat{Y}_i(m)$:

$$\min_{\mathcal{N}(i,m) \neq i} \|\hat{Y}_i(m) - \hat{Y}_{\mathcal{N}(i,m)}(m)\|, \quad i \in \llbracket 1; M \rrbracket, \quad (6.5)$$

where $\|\cdot\|$ stands for the Euclidean distance³. The ratio of the distances in m and $m+1$ dimensions for \hat{Y}_i is

$$a_{i,m} = \frac{\|\hat{Y}_i(m+1) - \hat{Y}_{\mathcal{N}(i,m)}(m+1)\|}{\|\hat{Y}_i(m) - \hat{Y}_{\mathcal{N}(i,m)}(m)\|}. \quad (6.6)$$

Finally $E(m)$ is computed:

$$E(m) = \frac{1}{M} \sum_{i=1}^M a_{i,m}. \quad (6.7)$$

For convenience its evolution is evaluated through $E_1(m)$,

$$E_1(m) = \frac{E(m+1)}{E(m)}, \quad (6.8)$$

and if $\exists m \setminus \forall k \geq m, E_1(k+1) = E_1(k)$ then m is the minimum embedding dimension. In parallel the mean difference between the raw data $E^*(m)$ is evaluated with respect to m , relating

3. The infinite norm has also been tested, giving same results not presented here.

to $\mathcal{N}(m)$ obtained in Equation 6.5:

$$E^*(m) = \frac{1}{M} \sum_{i=1}^M |y_p^*(i + mJ) - y_p^*(\mathcal{N}(i, m) + mJ)|. \quad (6.9)$$

In the same manner as Equation 6.8, the evolution is analyzed through $E_2(m)$:

$$E_2(m) = \frac{E^*(m+1)}{E^*(m)}, \quad (6.10)$$

and if $\exists k \setminus E_2(k) \neq 1$ then the signal is deterministic, otherwise it is stochastic.

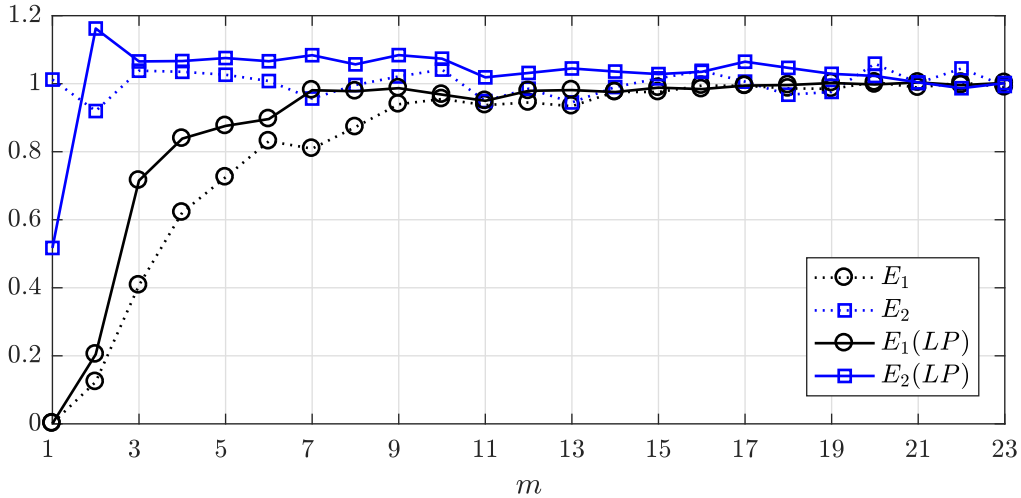


Figure 6.4 – $E_1(m)$ (black circle) and $E_2(m)$ (blue square) computed from raw (dashed line) and LP filtered (solid line) signal y_p^* . The large-scale dynamics associated with the LP filtered signal show a chaotic signature.

As shown by Figure 6.4, the raw signal appears stochastic but the LP filtered one is indeed deterministic, confirming the results obtained with the structure function. The minimum embedding dimension seems to be $m = 12$, which tends towards a high-dimensional system for the low-frequency large scales. It should be noted that a new reconstruction delay J^* is computed for the filtered data ($J^* \sim 4.4 \times 10^2$ and $J^* \sim 4.9 \times 10^2$ through MI and AMI evaluations respectively).

Thus the complete large-scale bimodal dynamics of such a fully turbulent wake are well composed of a stochastic part and a deterministic part. In the following sections only the chaotic behavior of these dynamics is characterized through the analysis of the LP filtered signal directly denoted as $y_p^*(t)$ for convenience.

6.1.2 A chaos portrait

There are many ways to characterize and quantify chaos. Among the most popular quantities, one can cite the correlation dimension (Grassberger & Procaccia, 1983) which gives an estimate

of the system complexity and characteristic exponents which give an estimate of the level of chaos in the dynamical system. In this section we focus on the Lyapunov exponent.

6.1.2.1 Largest Lyapunov exponent

The spectrum of Lyapunov exponents is well known for detecting and quantifying chaotic systems from the experimental time series (Wolf *et al.*, 1985). Indeed chaos exists if a system is sensitive to its initial conditions. Thus the principle consists in following the evolution of the distance d between two initial neighbouring state vectors in the phase space. For a chaotic attractor, the distance d exponentially increases in time at an average rate equal to the largest Lyapunov exponent (LLE) λ_1 (Eckmann & Ruelle, 1985):

$$d(t) = d(0)e^{\lambda_1 t}. \quad (6.11)$$

Due to its efficiency on small data sets, Rosenstein's algorithm (Rosenstein *et al.*, 1992; Sato *et al.*, 1987) is applied to the LP filtered N -points time series $\{y_p^*(i)\}_{i=1\dots N}$, rather than Wolf's algorithm (Wolf *et al.*, 1985). The M state vectors $\{\hat{Y}_i\}_{i=1\dots M}$ and their closest neighbor $\{\hat{Y}_{\mathcal{N}(i)}\}_{i=1\dots M}$ as previously to compute the distances evolution,

$$d_i(j) = \|\hat{Y}_{i+j} - \hat{Y}_{\mathcal{N}(i)+j}\|, \quad (6.12)$$

where $j = \lfloor f_p^* t^* \rfloor$ verifies $i + j \leq M$ and $\mathcal{N}(i) + j \leq M$. The distance $d(t)$ is approximated by averaging over i the distances $d_i(j)$:

$$d(j) = \langle d_i(j) \rangle_i. \quad (6.13)$$

By taking the logarithm of Equation 6.13 with respect to j the slope, extracted through a least-square fit, gives directly the LLE. The distance $d(t)$ computed for the LP filtered data is given in Figure 6.5 and it appears to follow the Equation 6.11 for small t^* , typically $t \in [50 : 1500]$. The LLE is thus computed in this range.

The estimated dimensionless positive LLE is $\lambda_1^* = 2.8(\pm 0.3) \times 10^{-4}$. The relative error is due to the main difficulty to define the right linear region of the curve to fit. The low frequencies dynamics associated to large-scale structures may thus be considered as a weak chaotic strange attractor.

6.1.2.2 Correlation dimension

The fractal dimension (or Hausdorff dimension) D of a strange attractor can be rigorously approximated by its correlation dimension D_2 which is directly computed from experimental time series according to the works of Grassberger & Procaccia (1983). The previous M state vectors $\{\hat{Y}_i\}_{i=1\dots M}$ are also used to compute the correlation integral function $\mathcal{C}(r)$, defined as

$$\mathcal{C}(r) = \frac{2}{M(M-1)} \sum_{i=1}^{M-1} \sum_{j=i+1}^M \Theta(r - \|\hat{Y}_i - \hat{Y}_j\|), \quad (6.14)$$

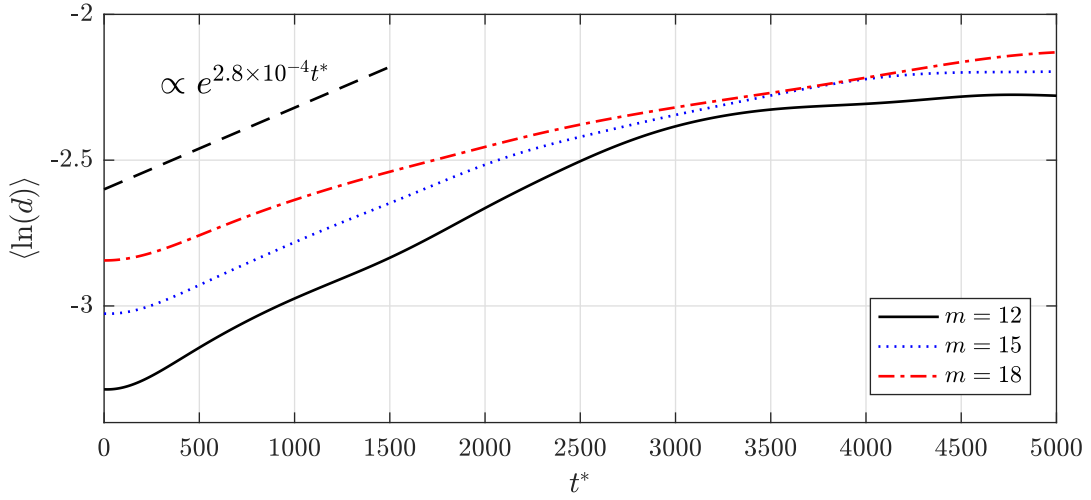


Figure 6.5 – $\langle \ln(d(t)) \rangle_{i=1..M}$ and exponential approximation $e^{1.8 \times 10^{-4} t^*}$ (black dashed line).

where Θ is the Heaviside function and r is an evaluated size. The correlation dimension D_2 can be derived from the correlation integral function $\mathcal{C}(r)$ which scales as a power-law for small r :

$$\mathcal{C}(r) \propto r^{D_2}, \quad (6.15)$$

The correlation integral function of the LP filtered signal y_p^* is computed using the Grassberger-Procaccia method improved by Ning *et al.* (2008), who normalize the Euclidean distance in Equation 6.14 by the embedding dimension m . Figure 6.6 shows the resulting correlation integral function in logarithmic scale.

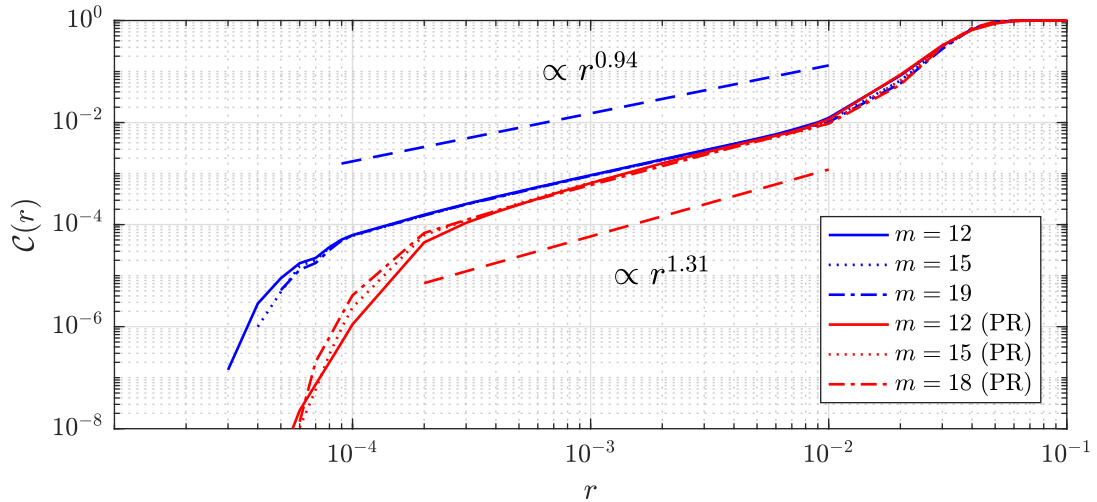


Figure 6.6 – Correlation integral function $\mathcal{C}(r)$ of LP filtered y_p^* (blues lines) and their corresponding surrogate PR data (red lines). Power law approximations (dashed lines) are also given in logarithmic scale.

Regarding the whole experimental LP signals we obtain $D_2 = 0.94 \pm 0.01$, from a fit over two decades. The result well verifies the validation condition on the length of the studied time series

$D_2 \leq 2 \log N$ (Ruelle, 1990). This low value, close to 1, confirms the weak chaotic nature of the low-frequency dynamics, which are even so validated thanks to the phase randomization (PR) test provided by Provenzale *et al.* (1992): for a stochastic signal the correlation dimension does not change when its Fourier phases are randomized. Figure 6.6 reveals a modified correlation dimension for the surrogate PR data obtained from the original LP time series, $D_{2,rand} = 1.31 \pm 0.01$, which is indicative of chaotic dynamics.

6.1.2.3 Telegraph-like signal

Another interesting way to characterize chaotic oscillator is to analyze the properties of its auto-correlation function (ACF). Considering Equation 5.6, the ACF of a given function $x(t)$ is

$$\Gamma_x(\tau^*) = \Gamma_{x,x}(\tau) = x(\tau^*) \otimes x(\tau^*), \quad (6.16)$$

which will be normalized by $\Gamma_x(0)$. The ACF of a random process has different properties depending on the nature of the system. Two famous models used to describe the behavior of many applied random systems are the noisy harmonic oscillations and the telegraph signal (Anishchenko *et al.*, 2002). The model of telegraph signal is particularly well-suited to describe the statistics of random switching of a bimodal system in the presence of noise, which is a close description of the bimodal wake as previously mentioned. Two main kinds of telegraph signals can be distinguished, namely, the random and quasirandom telegraph signals. The random telegraph signal is characterized by a Poisson distribution of switching moments while quasirandom telegraph signal corresponds to random switching between two equi-probable states (probability of switching events equal to $\frac{1}{2}$). For instance, the latter is very well suited to the Lorenz attractor (Anishchenko *et al.*, 2002).

To characterize the time series as telegraph signals, the first step is then to define two states as the symmetric spanwise positions of the pressure centers given by Equation 5.8. It is then possible to construct a telegraph-like signal Y_p^* such as

$$Y_p^*(t) = \begin{cases} y_{AN}^* & \text{if } y_p^*(t) \leq 0 \\ y_{AP}^* & \text{if } y_p^*(t) > 0 \end{cases}. \quad (6.17)$$

Figure 6.7 shows a part of the LP filtered signal y^* together with the resulting telegraph signal Y_p^* .

The normalized ACF $\Gamma_{y_p^*}(\tau^*)$ and $\Gamma_{Y_p^*}(\tau^*)$ are computed for the raw signal and the LP filtered one. According to Anishchenko *et al.* (2002), the ACF approximation of a random telegraph signal, $\Psi_R(\tau^*)$, is given by the following function:

$$\Psi_R(\tau^*) = e^{-2n_1^*|\tau^*|}, \quad (6.18)$$

where n_1^* corresponds to the normalized mean switching frequency, while the ACF of a random telegraph signal can be linearly approximated on short times by the following function $\Psi_{QR}(\tau^*)$:

$$\Psi_{QR}(\tau^*) = \begin{cases} 1 - \frac{|\tau^*|}{\xi_0^*} & \text{if } |\tau^*| < \xi_0^* \\ 0 & \text{if } |\tau^*| \geq \xi_0^* \end{cases}, \quad (6.19)$$

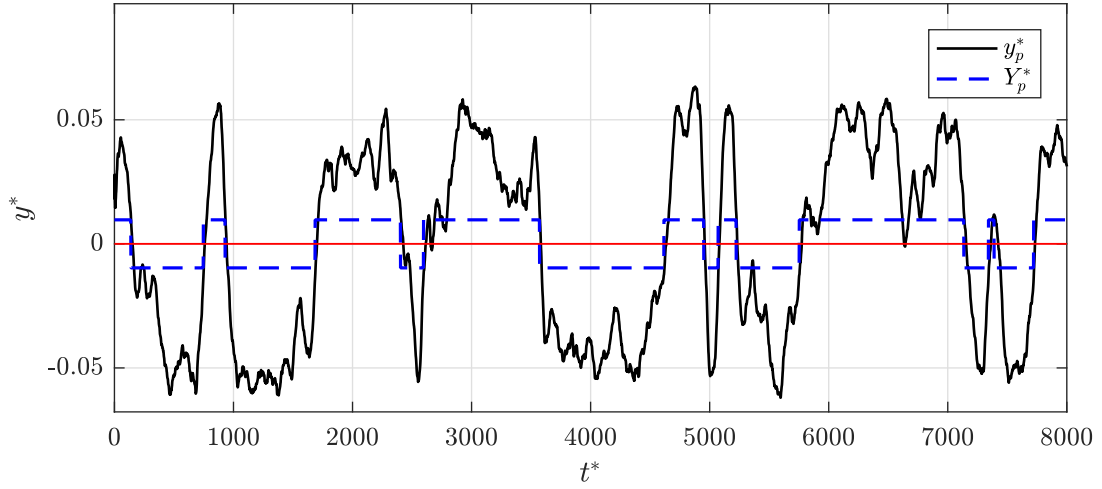


Figure 6.7 – Part of the telegraph signal Y_p^* (blue) obtained for the pressure barycenter spanwise position y_p^* (black). For clarity the telegraph signal is plotted with a 0.25 factor.

where ξ_0^* corresponds to the minimal residence time in one state, denoted T_{min} . $\Gamma_{y_p^*}(\tau^*)$, $\Gamma_{Y_p^*}(\tau^*)$ and the ACF approximations are plotted in Figure 6.8.

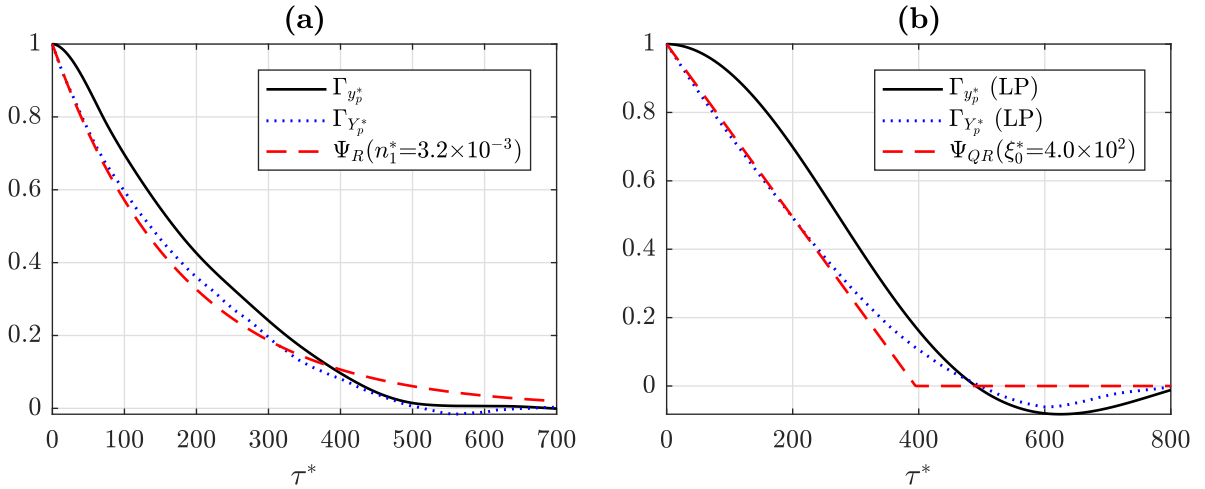


Figure 6.8 – Normalized autocorrelation functions of the pressure barycenter spanwise position $\Gamma_{y_p^*}$ (black solid line) and of the resulting telegraph-like signal $\Gamma_{Y_p^*}$ (blue dotted line) for (a) the raw signal and (b) the LP filtered one, together with their respective ACF approximations: $\Psi_R(n_1^* = 3.2 \times 10^{-3})$ and $\Psi_{QR}(\xi_0^* = 4.0 \times 10^2)$ (red dashed line).

Figure 6.8(a) shows that $\Psi_R(n_1^* = 3.2 \times 10^{-3})$ is a good approximation of the ACF of the telegraph signal obtained from the raw data. The estimated mean switching frequency $n_1^* = 3.2 \times 10^{-3}$ is close to the directly measured one $f_{switch}^* \sim 3.4 \times 10^{-3}$. The ACF of the telegraph-like signal extracted from the LP filtered time series is well approximated by the linear function $\Psi_{QR}(\xi_0^* = 4.0 \times 10^2)$ in Figure 6.8(b). From the linear approximation we thus find $\xi_0^* = 4.0 \times 10^2$, which is not far from the filtered experimental results, $T_{min}^* = 0.8 \times 10^2$ for the studied run. The same kind of ACF approximation is obtained for the Lorenz attractor described by Equation 6.1

(Anishchenko *et al.*, 2002).

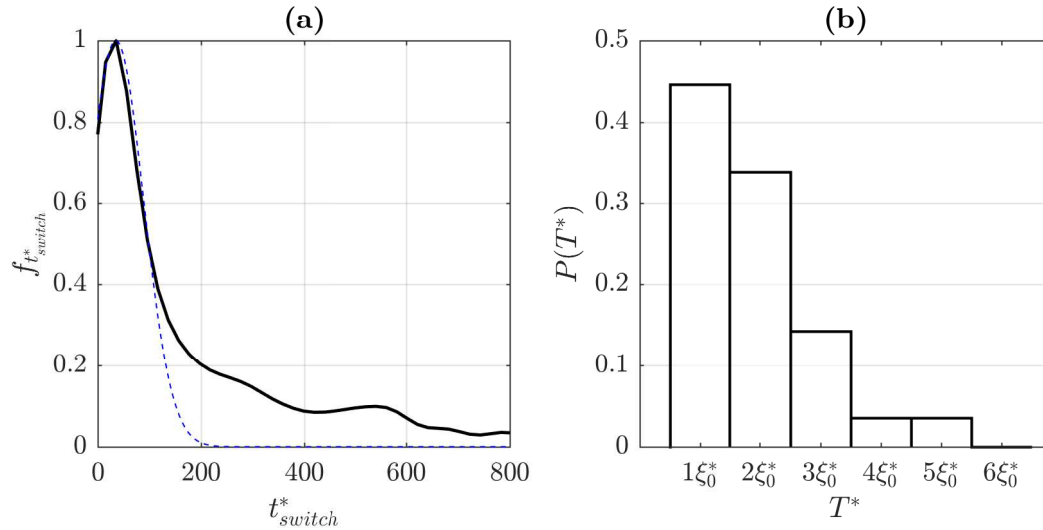


Figure 6.9 – (a) PDF of the switching time t_{switch}^* for the raw data (black solid line) together with a Poisson distribution (parameter set to 2.9×10^3 , blue dashed line) and (b) probabilities of switching at times T^* multiple to $\xi_0^* = 4.0 \times 10^2$ for the LP filtered signal.

Furthermore the PDF of the switching times t_{switch}^* of the raw time series is given in Figure 6.9(a), revealing itself close to a Poisson distribution whose parameter is 2.9×10^3 . The mean switching time, which is the parameter of the Poisson distribution, is of the same order as the residential time T_{RSB}^* seen previously. Regarding the corresponding LP filtered data, the probability of switching $P(T^*)$ occurring at times T^* multiple to ξ_0^* is computed in Figure 6.9(b). The results show that the probability of switching at time $T^* = \xi_0^*$ is $P(\xi_0^*) = 0.45$, agreeing with the ACF approximation of Equation 6.19. Anishchenko *et al.* (2002) obtained $P(\xi_0^*) = 0.52$ for the Lorenz system of Equation 6.1, which is also close to 0.5 as expected for such a strange chaotic attractor.

6.2 Conclusions and discussion

The trajectory of the pressure barycenter over the rear part of the model is first characteristic of a stochastic behavior. But the low-frequency part of this signal reveals a chaotic aspect: the instantaneous pressure barycenter circles around two stable areas acting like strange attractors and randomly switches from one attractor to the other. The nonlinear dynamics of the pressure center are therefore investigated by reconstructing its phase space from the spanwise component. The largest Lyapunov exponent is first estimated, leading to a low positive value, characteristic of strange attractors and weak chaotic systems. The weak aspect is then confirmed by the correlation dimension found close to one. Afterwards, the low-frequency signal is transformed and studied as a telegraph signal, showing that its dynamics correspond to a quasirandom telegraph signal. All of these elements tend therefore to describe the dynamics of a complex 3D turbulent wake as a weak chaotic system with physical noise.

In fluid dynamics, the turbulence problem is associated either to chaotic (Landau, 1944) or to probabilistic (Ruelle & Takens, 1971) representation. Due to the high embedding dimension and the weak Lyapunov exponent evaluated, the “chaotic” term has to be consequently used with caution for the present turbulent wake. The deterministic model of the turbulent wake is indeed very difficult to completely prove (Noack & Eckelmann, 1992) because of the turbulent noise itself. Nevertheless, a research team from CEA has recently obtained very close experimental results for the turbulent Von Kàrmàn flow (Faranda *et al.*, 2017), applying the same tools from dynamical system theory. Qualifying the dynamics as “stochastic chaos”, they suggest to use the stochastic Duffing attractor to model the flow.

Apart from its fundamental interest, this result is also of great practical interest. Indeed, if the wake dynamics can be modelled as a chaotic attractor, it opens the path to different closed-loop control strategies, similar to the one used to control chaotic systems.

Bibliography

- ACHERMANN, P., HARTMANN, R., GUNZINGER, A., GUGGENBÜH, W. & BORBÉLY, A.A. (1994) Correlation dimension of the human sleep electroencephalogram: Cyclic changes in the course of the night. *European Journal of Neuroscience* **6** (3), pp. 497–500. doi:[10.1111/j.1460-9568.1994.tb00292.x](https://doi.org/10.1111/j.1460-9568.1994.tb00292.x). 128
- ANISHCHENKO, V.S., VADIVASOVA, T.E., OKROKVERTSKHOV, G.A. & STRELKOVA, G.I. (2002) Correlation analysis of dynamical chaos. *Journal of Physics A* **325** (1–2), pp. 199–212. doi:[10.1016/S0378-4371\(03\)00199-7](https://doi.org/10.1016/S0378-4371(03)00199-7). 135, 137
- BRACKSTON, R., GARCÍA DE LA CRUZ, J., WYNN, A., RIGAS, G. & MORRISON, J. (2016) Stochastic modelling and feedback control of bistability in a turbulent bluff body wake. *Journal of Fluid Mechanics* **802**, pp. 726–749. doi:[10.1017/jfm.2016.495](https://doi.org/10.1017/jfm.2016.495). 129
- CAO, L. (1997) Practical method for determining the minimum embedding dimension of a scalar time series. *Journal of Physics D* **110** (1), pp. 43 – 50. doi:[10.1016/S0167-2789\(97\)00118-8](https://doi.org/10.1016/S0167-2789(97)00118-8). 131
- CASDAGLI, M., EUBANK, S., DOYNE FARMER, J. & GIBSON, J. (1991) State space reconstruction in the presence of noise. *Journal of Physics D* **51** (1), pp. 52 – 98. doi:[10.1016/0167-2789\(91\)90222-U](https://doi.org/10.1016/0167-2789(91)90222-U). 130
- CELLUCCI, C.J., ALBANO, A.M. & RAPP, P.E. (2005) Statistical validation of mutual information calculations: Comparison of alternative numerical algorithms. *Physical Review E* **71** (6), p. 066208. doi:[10.1103/PhysRevE.71.066208](https://doi.org/10.1103/PhysRevE.71.066208). 130
- ECKMANN, J.P., KAMPHORST, S.O., RUELLE, D. & CILIBERTO, S. (1986) Liapunov exponents from time series. *Phys. Rev. A* **34** (6), pp. 4971–4979. doi:[10.1103/PhysRevA.34.4971](https://doi.org/10.1103/PhysRevA.34.4971). 129
- ECKMANN, J.P. & RUELLE, D. (1985) Ergodic theory of chaos and strange attractors. *Reviews of Modern Physics* **57** (3), pp. 617–656. doi:[10.1103/RevModPhys.57.617](https://doi.org/10.1103/RevModPhys.57.617). 130, 133
- FARANDA, D., SATO, Y., SAINT-MICHEL, B., WIERTEL, C., PADILLA, V., DUBRULLE, B. & DAVIAUD, F. (2017) Stochastic chaos in a turbulent swirling flow. *Phys. Rev. Lett.* **119** (1), p. 014502. doi:[10.1103/PhysRevLett.119.014502](https://doi.org/10.1103/PhysRevLett.119.014502). 138
- FOJT, O. & HOLCIK, J. (1998) Applying nonlinear dynamics to ECG signal processing. *IEEE Engineering in Medicine and Biology Magazine* **17** (2), pp. 96–101. doi:[10.1109/51.664037](https://doi.org/10.1109/51.664037). 128
- FRASER, A.M. & SWINNEY, H.L. (1986) Independent coordinates for strange attractors from mutual information. *Physical Review A* **33** (2), pp. 1134–1140. doi:[10.1103/PhysRevA.33.1134](https://doi.org/10.1103/PhysRevA.33.1134). 130

- GRANDEMANGE, M., GOHLKE, M. & CADOT, O. (2013) Turbulent wake past a three-dimensional blunt body. Part 1. Global modes and bi-stability. *Journal of Fluid Mechanics* **722**, pp. 51–84. doi:10.1017/jfm.2013.83. 129
- GRASSBERGER, P. & PROCACCIA, I. (1983) Characterization of strange attractors. *Physical Review Letters* **50** (5), pp. 346–349. doi:10.1103/PhysRevLett.50.346. 132, 133
- GUCKENHEIMER, J. (1983) Strange attractors in fluid dynamics. In *Dynamical System and Chaos: Proceedings of the Sitges Conference on Statistical Mechanics Sitges, Barcelona/Spain September 5–11, 1982* (ed. L. Garrido), pp. 149–156. Berlin, Heidelberg: Springer. doi:10.1007/3-540-12276-1_10. 128, 129
- JIANG, A.H., HUANG, X.C., ZHANG, Z.H., LI, J., ZHANG, Z.Y. & HUA, H.X. (2010) Mutual information algorithms. *Mechanical Systems and Signal Processing* **24** (8), pp. 2947 – 2960. doi:10.1016/j.ymssp.2010.05.015. 130
- KENNEL, M.B., BROWN, R. & ABARBANEL, H.D.I. (1992) Determining embedding dimension for phase-space reconstruction using a geometrical construction. *Physical Review A* **45** (6), pp. 3403–3411. doi:10.1103/PhysRevA.45.3403. 131
- LANDAU, L.D. (1944) On the problem of turbulence. *Doklady Akademii Nauk SSSR* **44**, pp. 339–342. 138
- LORENZ, E.N. (1963) Deterministic nonperiodic flow. *Journal of the Atmospheric Sciences* **20**, pp. 130–141. doi:10.1175/1520-0469(1963)020<0130:DNF>2.0.CO;2. 128
- MANDELBROT, B. (1982) *The fractal geometry of nature*. Henry Holt and Company. 129
- MATCHARASHVILI, T., CHELIDZE, T., JAVAKHISHVILI, Z. & GHLONTI, E. (2002) Detecting differences in temporal distribution of small earthquakes before and after large events. *Computers & Geosciences* **28** (5), pp. 693–700. doi:10.1016/S0098-3004(01)00047-4. 128
- NING, T., TRANQUILLO, J.V., GRARE, A.C. & SARAF, A. (2008) Computing correlation integral with the euclidean distance normalized by the embedding dimension. In *2008 9th International Conference on Signal Processing, Beijing, China*, pp. 2708–2712. IEEE. doi:10.1109/ICOSP.2008.4697707. 134
- NOACK, B.R. & ECKELMANN, H. (1992) On chaos in wakes. *Physica D: Nonlinear Phenomena* **56** (2), pp. 151 – 164. doi:10.1016/0167-2789(92)90021-E. 138
- ORLANDO, G. (2016) A discrete mathematical model for chaotic dynamics in economics: Kaldor’s model on business cycle. *Mathematics and Computers in Simulation* **125**, pp. 83–98. doi:10.1016/j.matcom.2016.01.001. 128
- OSBORNE, A. & PROVENZALE, A. (1989) Finite correlation dimension for stochastic systems with power-law spectra. *Journal of Physics D* **35** (3), pp. 357 – 381. doi:10.1016/0167-2789(89)90075-4. 129

- ÖSTH, J., NOACK, B.R., KRAJNOVIĆ, S., BARROS, D. & BORÉE, J. (2014) On the need for a nonlinear subscale turbulence term in pod models as exemplified for a high-reynolds-number flow over an ahmed body. *Journal of Fluid Mechanics* **747**, pp. 518–544. doi:10.1017/jfm.2014.168. 129
- PROVENZALE, A., SMITH, L., VIO, R. & MURANTE, G. (1992) Distinguishing between low-dimensional dynamics and randomness in measured time series. *Physica D: Nonlinear Phenomena* **58** (1), pp. 31 – 49. doi:10.1016/0167-2789(92)90100-2. 129, 135
- ROSENSTEIN, M.T., COLLINS, J.J. & DE LUCA, C.J. (1992) A practical method for calculating largest Lyapunov exponents from small data sets. *Journal of Physics D* **65**, pp. 117–134. doi:10.1016/0167-2789(93)90009-P. 133
- RUELLE, D. (1990) The Claude Bernard lecture, 1989. deterministic chaos: The science and the fiction. *Proceedings of the Royal Society A* **427** (1873), pp. 241–248. doi:10.1098/rspa.1990.0010. 135
- RUELLE, D. (1991) The turbulent fluid as a dynamical system. In *New Perspectives in Turbulence* (ed. L. Sirovich), pp. 123–138. New York, USA: Springer. doi:10.1007/978-1-4612-3156-1_4. 128
- RUELLE, D. & TAKENS, F. (1971) On the nature of turbulence. *Communications in Mathematical Physics* **20** (3), pp. 167–192. doi:10.1007/BF01646553. 128, 138
- SATO, S., SANO, M. & SAWADA, Y. (1987) Practical Methods of Measuring the Generalized Dimension and the Largest Lyapunov Exponent in High Dimensional Chaotic Systems. *Progress of Theoretical and Experimental Physics* **77**, pp. 1–5. doi:10.1143/PTP.77.1. 133
- SAUER, T., YORKE, J.A. & CASDAGLI, M. (1991) Embedology. *Journal of Statistical Physics* **65** (3), pp. 579–616. doi:10.1007/BF01053745. 130
- SILVERMAN, B. (1986) Density estimation for statistics and data analysis. In *Monographs on Statistics and Applied Probability*. London: Chapman and Hall. 131
- SWINNEY, H.L. & GOLLUB, J. (1986) Characterization of hydrodynamic strange attractors. *Physica D: Nonlinear Phenomena* **18** (1), pp. 448 – 454. doi:10.1016/0167-2789(86)90213-7. 129
- TAKENS, F. (1981) Detecting strange attractors in turbulence. In *Dynamical Systems and Turbulence, Warwick 1980: Proceedings of a Symposium Held at the University of Warwick 1979/80* (ed. D. Rand & L.S. Young), pp. 366–381. Berlin, Heidelberg: Springer Berlin Heidelberg. doi:10.1007/BFb0091924. 130
- THOMAS, R.D., MOSES, N.C., SEMPLE, E.A. & STRANG, A.J. (2014) An efficient algorithm for the computation of average mutual information: Validation and implementation in Matlab. *Journal Of Mathematical Psychology* **61**, pp. 45 – 59. doi:10.1016/j.jmp.2014.09.001. 131
- VARON, E., EULALIE, Y., EDWIGE, S., GILOTTE, P. & AIDER, J.L. (2017) Chaotic dynamics of large-scale structures in a turbulent wake. *Physical Review Fluids* **2**, p. 034604. doi:10.1103/PhysRevFluids.2.034604. 127

WOLF, A., SWIFT, J.B., SWINNEY, H.L. & VASTANO, J.A. (1985) Determining Lyapunov exponents from a time series. *Journal of Physics D* **16** (3), pp. 285–317. doi:[10.1016/0167-2789\(85\)90011-9](https://doi.org/10.1016/0167-2789(85)90011-9). 133

YAN, G., DE STEFANO, A., MATTA, E. & FENG, R. (2013) A novel approach to detecting breathing-fatigue cracks based on dynamic characteristics. *Journal of Sound and Vibration* **332** (2), pp. 407–422. doi:[10.1016/j.jsv.2012.09.008](https://doi.org/10.1016/j.jsv.2012.09.008). 128

Control of the chaotic dynamics of a turbulent wake

This chapter presents a closed-loop control of the turbulent wake behind the square-back Ahmed body described in [chapter 5](#) and in [chapter 6](#). After introducing the micro-jets system used to force the flow, different control strategies are tested. An opposition strategy is finally applied, based on the real-time PIV.

7.1 Introduction	143
7.1.1 Turbulent wake control	143
7.1.2 Micro-jets system	145
7.2 Open-loop forcing of the wake	147
7.2.1 Continuous blowing in different regions	147
7.2.2 Pulsed blowing in different regions	149
7.3 Closed-loop control of the wake dynamics	153
7.3.1 Principle of the closed-loop experiments	153
7.3.2 Stabilization of the wake	154
7.3.3 Creation of a multimodal state	157
7.4 Conclusions and issues raised	160
7.4.1 Perspectives	162

7.1 Introduction

7.1.1 Turbulent wake control

In some cases, controlling the large-scale fluctuations of a turbulent wake is a key step toward the control of various global quantities like the drag coefficient. Actually, stabilization of the wake by suppressing the bimodal behavior behind a square-back bluff body is of interest to industrial applications since it can lead to drag reduction ([Grandemange *et al.*, 2014a](#); [Cadot *et al.*, 2015](#)). Previous experimental studies show how different control strategies manipulate the wake dynamics. For instance, such a wake has been stabilized toward a symmetric state by adding a well-designed cavity behind the rear surface ([Evrard *et al.*, 2016](#)). Using pulsed jets along continuous slits at the trailing edges, the unsteady dynamics of the wake can be amplified

by selecting either the vortex shedding frequency for an asymmetric forcing configuration, or its subharmonic for a symmetric forcing configuration (Barros *et al.*, 2016a). Inversely, selecting higher actuating frequencies damps the dynamics (Barros *et al.*, 2016b). Feedback controls achieve the suppression of the RSB modes, based either on a stochastic model of the complete wake dynamics using flaps (Brackston *et al.*, 2016), or on an opposition strategy using lateral slit jets (Li *et al.*, 2016).

Drag modifications have also been investigated on modified square-back bluff-bodies, closer to real ground vehicles. For example, Grandemange *et al.* (2015) chamfered rear edges and replaced the pods by wheels. They reached a 10% drag reduction via a cavity effect coupled to boat tail effect. McNally *et al.* (2015) achieved 2.6% by symmetrizing the wake behind a rounded Ahmed body via micro-jets distributed along the lateral and upper faces just upstream of the separation. It is interesting to note how prolific have been the experimental research teams on this subject during the last three years (Table 7.1).

References	Re_H	AR	C/W	Controls
Bruneau <i>et al.</i> (2010)	8.3×10^3	0.74	0.44	Porous surface and jets (no supports)
Grandemange <i>et al.</i> (2013b)	7.4×10^5	0.74	0.09	Horizontal rear flaps
Grandemange <i>et al.</i> (2015)	2.5×10^6		0.12	Real wheels and chamfering
Evrard <i>et al.</i> (2016)	4.0×10^5	0.85	0.09	Base cavity
Evstafyeva <i>et al.</i> (2017)	$[3.1; 4.2] \times 10^2$	0.74	0.44	Synthetic jets
Brackston <i>et al.</i> (2016)	$[2.3; 4.4] \times 10^5$		0.13	Vertical lateral flaps
Barros <i>et al.</i> (2014)	3.0×10^5	0.85	0.14	Pulsed jets
Barros <i>et al.</i> (2016a)	$[2.0; 4.0] \times 10^5$			Pulsed jets
Barros <i>et al.</i> (2016b)	3.0×10^5			Pulsed jets and Coanda effect
Li <i>et al.</i> (2016)	6.0×10^5			Micro-jets
Eulalie (2014)	3.9×10^5	0.74	0.18	Micro-jets
McNally <i>et al.</i> (2015)	3.6×10^5	1	0.23	Micro-jets

Table 7.1 – Square-back Ahmed geometries for control studies reported in the literature.

In the previous chapter the wake dynamics have been characterized as weakly chaotic with two well defined attractors. The objective is thus to control these chaotic dynamics. Because of the sensitive dependence on initial conditions, chaos was believed for a long time to be neither predictable nor controllable. The OGY control method proposed by Ott *et al.* (1990) changed completely this point of view. They showed that it is possible to use small time-dependent perturbations to force a chaotic attractors system in a time-periodic motion, defined from one of its unstable periodic orbits (UPOs) (Grebogi *et al.*, 1988). Since this pioneering work, control of chaotic systems has become a very active research field and many new control methods have been proposed such as linear-feedback (Yassen, 2005), adaptive control (Tian & Yu, 2000), impulsive or intermittent control (Li *et al.*, 2007).

Controlling chaotic systems is a challenge encountered in various domains such as laser, plasma, electronics, communications, brain activity or fluid dynamics. For instance, the dynamics of a convective fluid confined in a vertical toroidal channel are well described by a Lorenz system, whose one of the two strange attractors can be removed through a feedback control (Singer *et al.*, 1991). In simulated fluid flows, the Lorenz model (Lorenz, 1963) is often used as a benchmark case for closed-loop control algorithms. Thereby, a control law is established from limited information on the full Lorenz system and can stabilize it in one of the foci (Guéniat *et al.*, 2016). Machine learning control is also applied to such system as a training exercise (Duriez *et al.*, 2017). Finally, a first control of a chaotic open flow has been recently experimentally achieved. After slightly forcing the dynamics of an axisymmetric jet into a low-dimensional chaotic attractor (Broze & Hussain, 1994), a closed-loop control is designed to sustain a selected UPO (Narayanan *et al.*, 2013). The chaotic dynamics correspond to the vortex ring formation downstream of the jet nozzle exit, which includes successive vortex pairings. The control strategy enables to stabilize the ring formation.

The present study aims at controlling *the dynamics* of the bimodal chaotic oscillations of a 3D turbulent wake by applying a reactive control based on measurements obtained from the *real-time* PIV. Unlike the previous examples on the control of the Lorenz system, this implies here to steady an unstable symmetric state. In the present study, we define an opposition strategy similar to Li *et al.* (2016), but the sensors being the velocity fields and the actuators being discontinuous pulsed jets only localized at the top trailing edge. A closed-loop control using scattered velocity fields from real-time PIV has previously been successfully applied to minimize a pole-cart system plunged into water (Roberts, 2012).

7.1.2 Micro-jets system

To realize the present control, the rear part of the Ahmed body used by Eulalie (2014) has been re-designed by Plastic Omnium R&D engineers, P. Gilotte and Y. Eulalie, to have several independent groups of actuators. The wake of the bluff-body is indeed forced using micro-jets which are distributed along the rear body width, 10 mm under the upper trailing edge ($z^* = 1.25$). The jets are either continuous or pulsed at the jet frequency f_j using three solenoid valves (Matrix®) integrated inside the model just upstream the blowing jets. Each solenoid valve controls a group of jets, which corresponds to the three regions of actuation defined in Figure 7.1. The pressurized air is supplied through pneumatic tubes passing inside a cylindrical pipe of diameter 32 mm at the center of the bottom face as the one in previous chapters (see the gray part in Figure 7.1). Even if this pipe does not break the reflexive symmetry of the body, it has certainly an influence on the near wake, which will be discussed.

The outlets of the jets have a rectangular cross-section $l_j \times h_j = 5.5 \times 0.5 \text{ mm}^2$. The distance between each jet is $l = 12.5 \text{ mm}$. The jets angle θ relative to the horizontal axis can be varied but in the following it will be fixed to $\theta = 0^\circ$ (blowing parallel to the freestream velocity). The jet velocity u_j can reach up to $75 \text{ m}\cdot\text{s}^{-1}$, i.e. a velocity ratio $u_{jet}^* = u_{jet}/U_\infty = 2.5$. Based on the

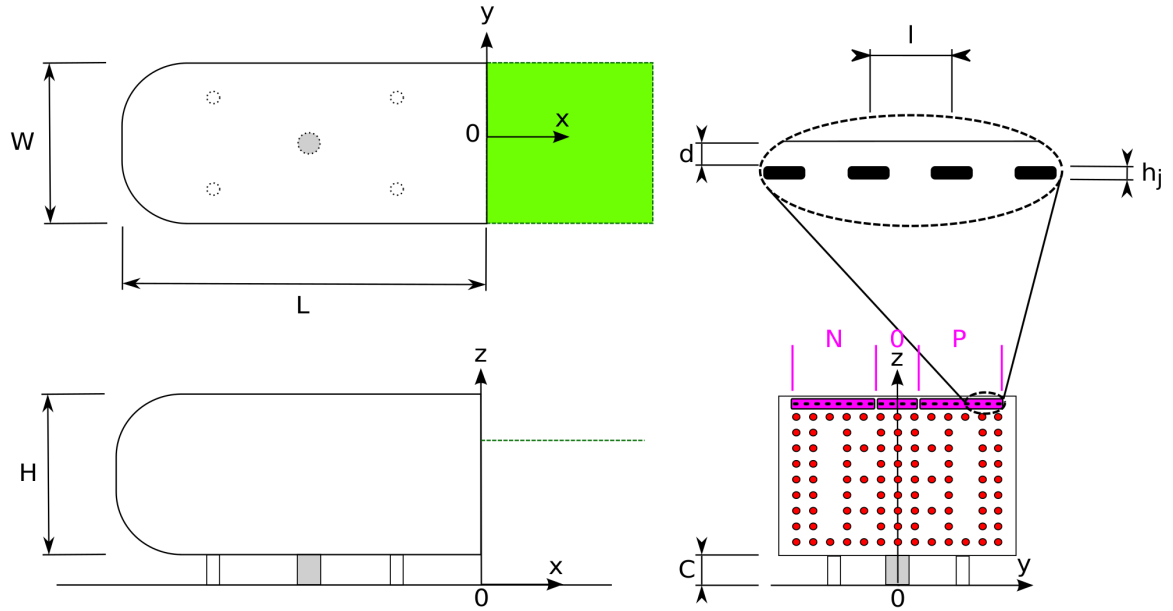


Figure 7.1 – Upper view (top left figure), side view (lower left figure) and view from behind (lower right figure) of the Ahmed body. The jets outputs are gathered in three groups (pink): “N”, “O” and “P”, corresponding respectively to actuations in the left, central or right upper regions. The jets are supplied through pneumatic tubes passing inside a central pipe (grey part on lower figures).

Strouhal number, the normalized jet frequency is defined as

$$f_j^* = \frac{f_j H}{U_\infty}, \quad (7.1)$$

instead of $\frac{f_j h_j}{u_j}$. The momentum coefficient, which is the ratio between the momentum injected by the actuator and the one due to the bluff body,

$$c_\mu = 2 \frac{l_j h_j \overline{u_j^2}}{S_r U_\infty^2}, \quad (7.2)$$

is evaluated at $c_\mu = 0.053\%$ (continuous) and $c_\mu = 0.013\%$ (pulsed) for each jet when $U_\infty = 30 \text{ m.s}^{-1}$.

The three regions of actuations are called “N”, “O” and “P” (Figure 7.1). “N” contains the eight jets located in the Negative part of the y -axis, whereas “P” contains the eight jets located in the Positive part and “O” contains the four y central jets (for a total of 20 jets). Due to the temporal constraints imposed for experiments carried in wind tunnel, all recorded control runs lasted only $T^* = 8.9 \times 10^3$. Regarding the aerodynamics, only the changes in the pressure coefficient will be considered to analyze influences of the control on the wake to avoid the structural response visible in the aerodynamics measurements.

7.2 Open-loop forcing of the wake

Three different open-loop (OL) control strategies are first investigated to evaluate the forcing on the state of the wake. The three open-loop forcings are defined as “OL-P” when only the “P” solenoids group is activated, “OL-0” when only the “0” solenoids group is activated and “OL-P0” when both the “P” and “0” solenoids groups are activated (Figure 7.1). Due to the reflection symmetry the results obtained with the “P” group are expected to be the same as for the “N” configuration. First we used continuous jets, which means only the forcing region is changed. Then pulsed jets are investigated, especially at the normalized frequency $f_j^* = 0.2$.

7.2.1 Continuous blowing in different regions

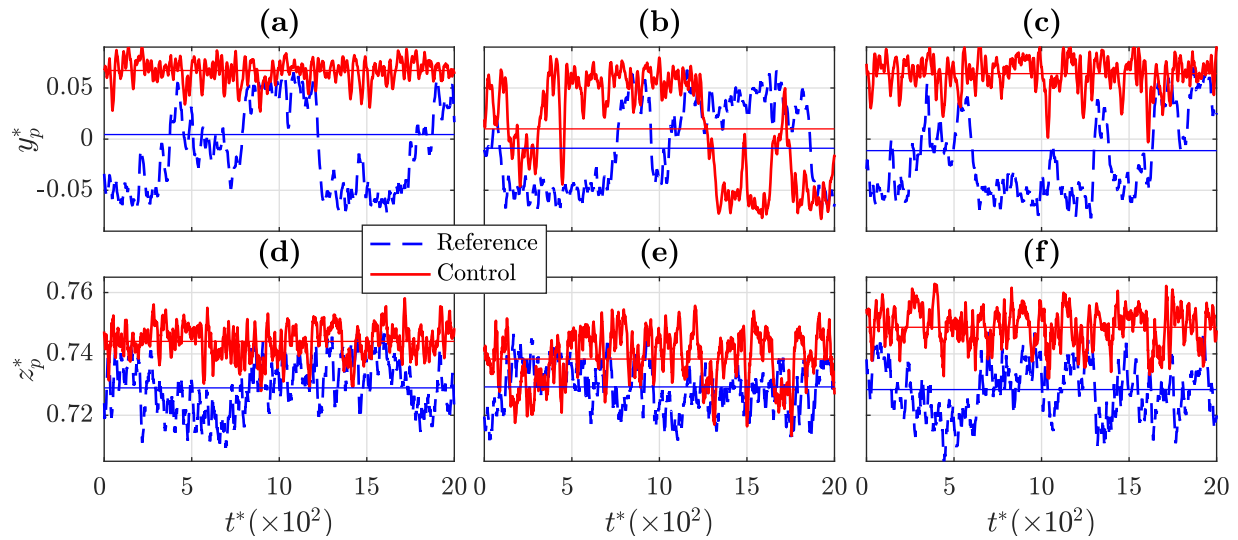


Figure 7.2 – Excerpts of y_p^* and z_p^* time series for the continuous forcing (a-d) OL-P, (b-e) OL-0, and (c-f) OL-P0 (solid red), all compared to a reference time series (dashed blue). Data are smoothed over $\Delta t^* = 15$ for clarity. The horizontal lines are the mean values.

The influence of the location of the continuous blowing on the wake dynamics is studied by analyzing directly the times series of the pressure center obtained for the three open-loop cases. On one hand, as displayed in Figure 7.2(a) and (c), blowing from one side drives the depression to remain localized in this side. On the other hand, Figure 7.2(b) reveals that the symmetric forcing seems not to affect the spanwise bimodal behavior. For all the forcing cases, the vertical position of the depression becomes closer to the upper trailing edge. The averaged z_p^* indeed rises 2.1% for OL-P [Figure 7.2(d)], 1.2% for OL-0 [Figure 7.2(e)] and 2.8% for OL-P0 [Figure 7.2(f)].

The previous observations are also confirmed by the 2D PDFs. Figure 7.3(a) shows that forcing with continuous jets the upper shear layer on one side of the model (OL-P) strongly stabilizes the wake oscillations. The pressure barycenter is now kept on the side of the blowing ($y_p^* > 0$) and oscillates around a single attractor. If the forcing is extended to the central region (OL-P0), the pressure barycenter is still confined on one side of the model but explores a larger region around

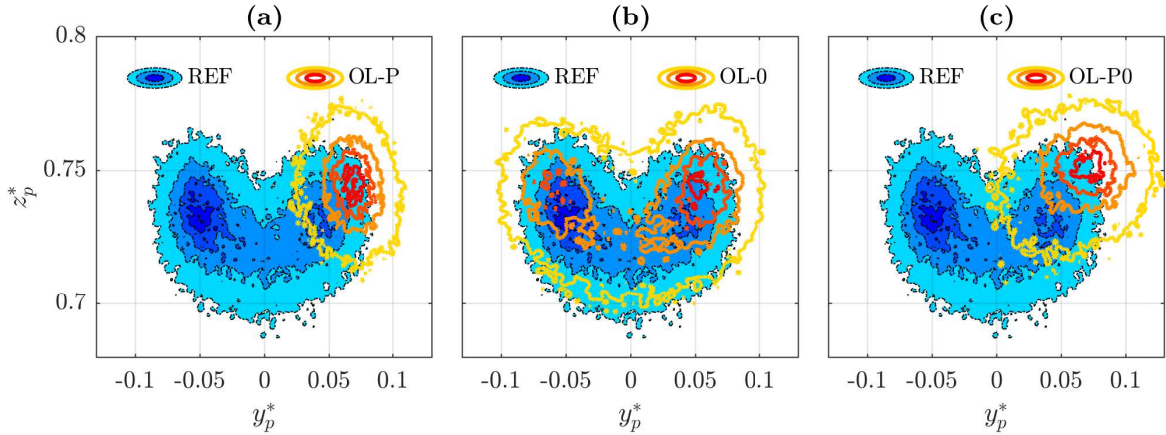


Figure 7.3 – 2D PDF contour of $G_p(y_p^*, z_p^*)$ for the open-loop controls with continuous jets compared to the reference (dashed blue contour): (a) OL-P, (b) OL-0, and (c) OL-P0 (solid red contour). The colormap is the same as Figure 5.32

the attractor [Figure 7.3(c)]. Finally, forcing the wake only in the central region (OL-0) leads to the same kind of PDF as the natural case [Figure 7.3(b)]. Nevertheless, the probability to remain in the TS state is reduced by half compared to the natural state. The TS mode is thus clearly minimized by the central symmetric continuous blowing.

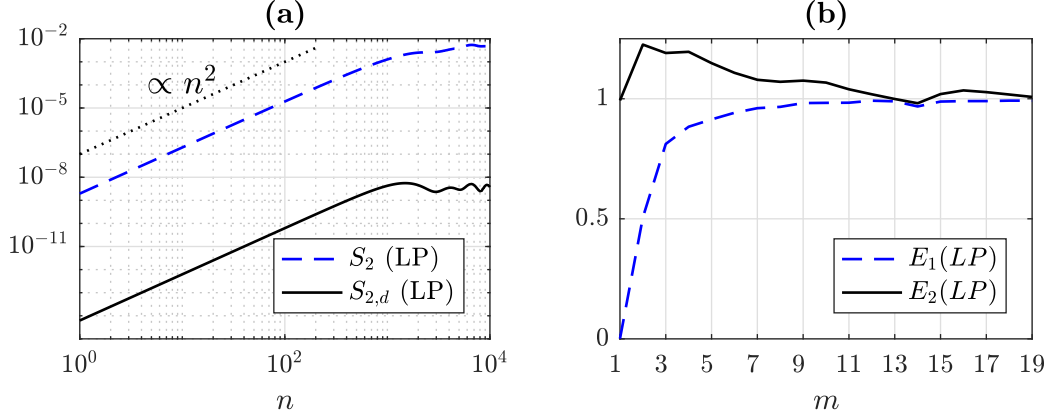


Figure 7.4 – (a) Second-order structure functions of LP y_p^* (dashed blue line) and of its first derivative (solid black line), and (b) $E_1(m)$ (dashed blue line) and $E_2(m)$ (solid black line) computed from LP y_p^* for OL-0.

Concerning the wake dynamics for OL-0, random switches occurs less often but the weak chaotic behavior in the low-frequency range remains ($St_H < 2 \times 10^{-3}$). Indeed, Figure 7.4(a) displays the second order-structure functions of y_p^* and its derivative previously seen in chapter 5. The n^2 slope of these curves is clearly conserved for higher lags than for the unforced wake. Besides, the functions E_1 and E_2 , computed from Cao's method and plotted in Figure 7.4(b), give respectively a minimal embedding dimension $m = 15$ and clue to deterministic dynamics, confirming the weak chaotic character.

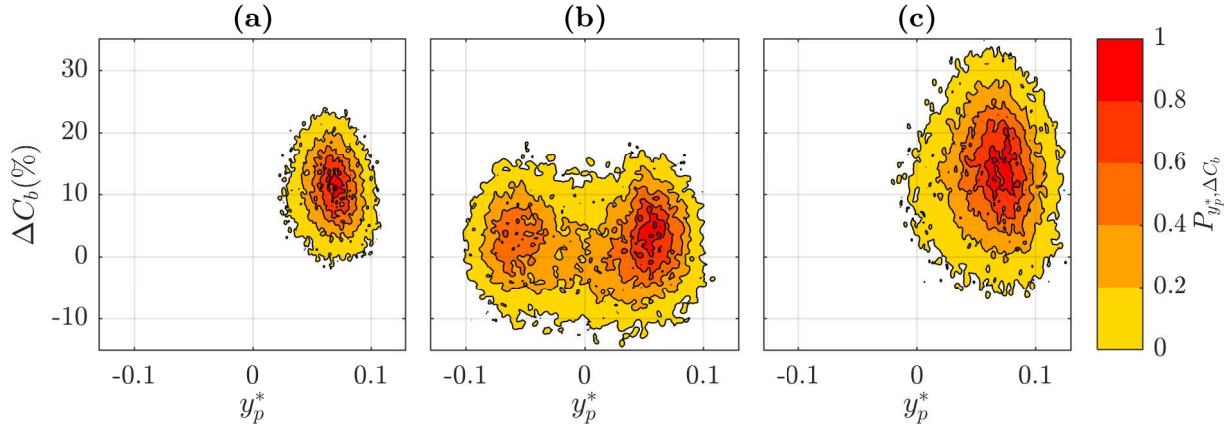


Figure 7.5 – 2D PDF contour of $(y_p^*, \Delta C_b)$ for the open-loop controls (a) OL-P, (b) OL-0, and (c) OL-P0 with continuous blowing.

Instead of looking at the trajectories of the pressure barycenter over the rear of the model in the physical space, it is interesting to look at the trajectory in the phase space. Indeed the state of the wake can be characterized not only by the right-left oscillations (bimodality), through the state parameter y_p^* , but also by the normalized fluctuations of the instantaneous base pressure coefficient $\Delta C_b(t)$

$$\Delta C_b(t) = \frac{C_b(t) - C_{b,ref}}{C_{b,ref}}, \quad (7.3)$$

where $C_{b,ref}$ is the time-averaged value of C_b for the reference flow. In Figure 7.5(a) and (c), forcing the wake into one of the RSB modes increases roughly by 15% the depression. These results are well coherent with the sensibility analysis done by Grandemange *et al.* (2014a). On the contrary, acting on the symmetric mode of the wake leads to similar value for C_b than the reference case [Figure 7.5(b)].

7.2.2 Pulsed blowing in different regions

Finally, the pulsed jets are used with the normalized frequency $f_j^* = 0.2$ for the three previous configurations, since this corresponds to the vortex shedding signature found in the up-down oscillations of the depression position for the reference case. At this actuating frequency, the depression behaves almost as previously for the OL-P and OL-P0 cases, but with more regular oscillations in the z -direction and a reduction of the spanwise fluctuations, amplifying the decrease in the base pressure. On the contrary, the OL-0 case is strongly modified: the average spanwise position of the depression is now centered [Figure 7.6(b)], the amplitude of the vertical fluctuations doubled while the mean vertical position increases much more than for the continuous blowing [Figure 7.6(e)]. For these reasons, the symmetric pulsed forcing will be more detailed in the following.

In average the highest pressure values are localized at the centre of the rear surface, circled by the lowest values, as shown in Figure 7.7(a). The fluctuations have a similar spatial organization

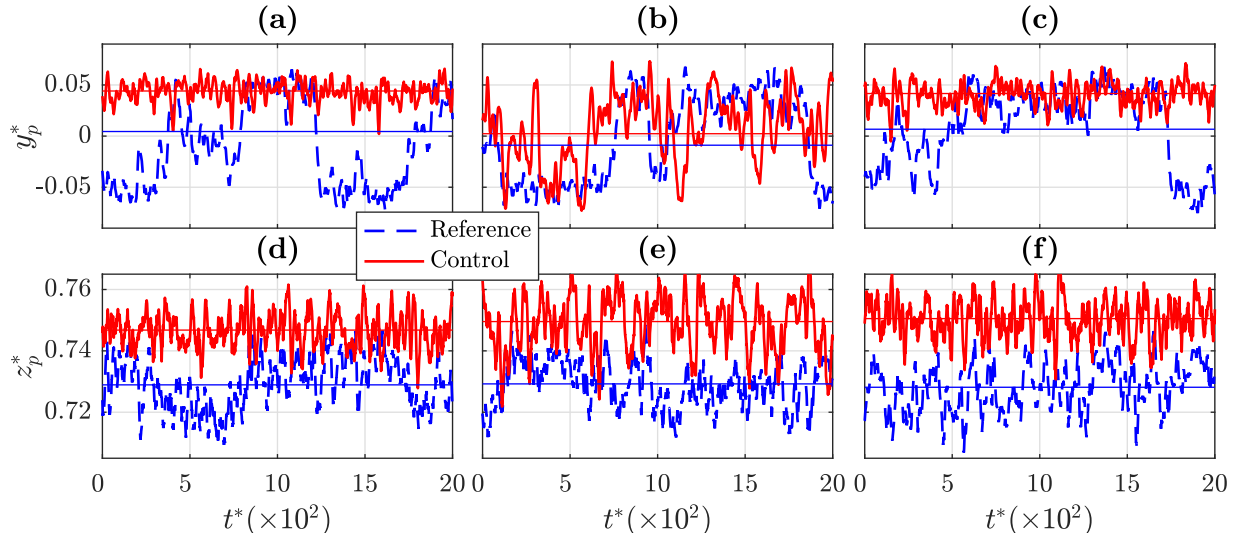


Figure 7.6 – Excerpts of y_p^* and z_p^* time series for the pulsed jets at $f_j^* = 0.2$ in configurations (a-d) OL-P, (b-e) OL-0, and (c-f) OL-P0 (solid red), all compared to a reference time series (dashed blue). Data are smoothed over $\Delta t^* = 15$ for clarity. The horizontal lines are the mean values.

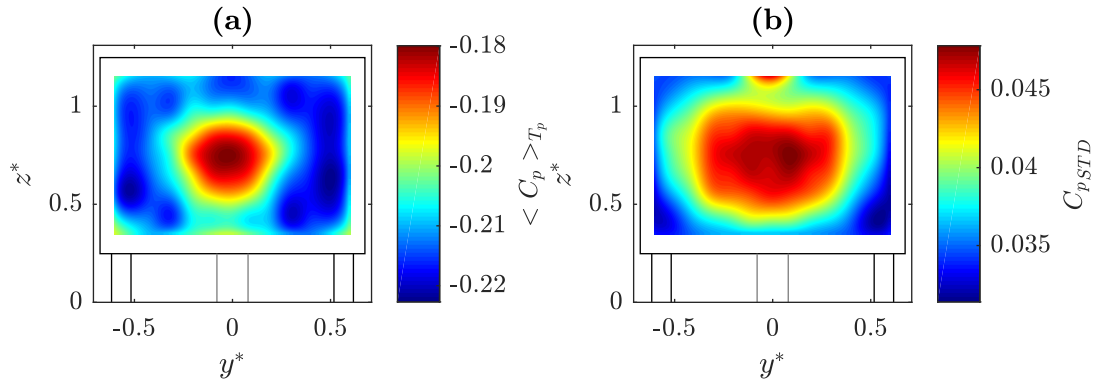


Figure 7.7 – Spatial distribution of (a) the time-averaged pressure coefficient $\langle C_p \rangle_{T_p}$, and of (b) the pressure fluctuations C_{pSTD} over the rear of the Ahmed body for OL-0 with $f_j^* = 0.2$.

in Figure 7.7(b).

Actually, the control with pulsed jets at $f_j^* = 0.2$ leads to a symmetric PDF with a single central attractor for the trajectory of the pressure barycenter, as illustrated by Figure 7.8(a), exhibiting only one central peak. The probability of being in the TS mode is multiplied by two. This has to be compared to the two attractors trajectories obtained with a constant blowing in the same region [Figure 7.3(b)]. Figure 7.8(b) shows that the pressure coefficient is globally unmodified.

Figure 7.9 stresses the peculiarity of the actuation frequency at $f_j^* = 0.2$, since no other frequency enables such a symmetrization of the wake. This dynamic response of the wake to a specific perturbation reminds the one obtained for a forced axisymmetric jet resulting to UPOs (Broze & Hussain, 1994). As the pressure center of the turbulent wake acts like a strange attractor in

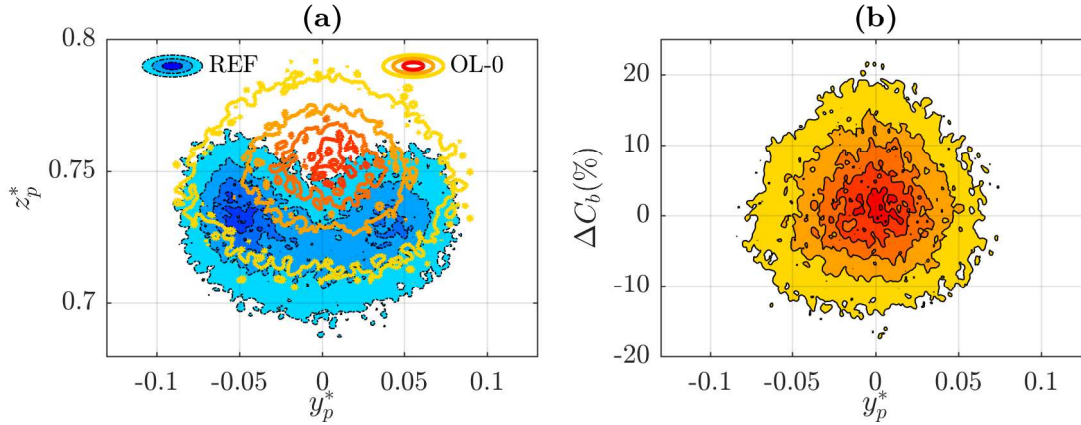


Figure 7.8 – 2D PDF contour of (a) $G_p(y_p^*, z_p^*)$ and (b) $(y_p^*, \Delta C_b)$ with pulsed jets at $f_j^* = 0.2$. The first 2D PDF is compared to the reference (dashed blue contour). Colormaps are respectively the same as Figure 5.32 and Figure 7.5.

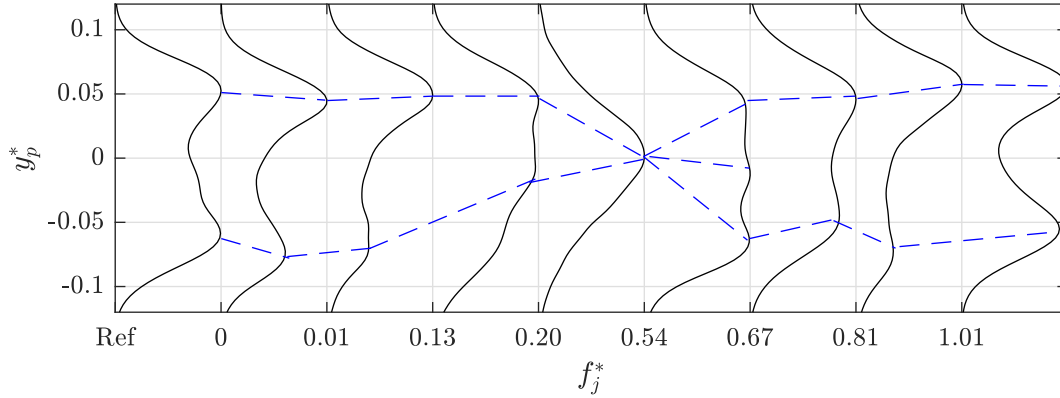


Figure 7.9 – Normalized PDF for the reference flow (Ref), the continuous blow ($f_j^* = 0$) and different actuating frequencies $f_j^* > 0$ for OL-0. Curves are shifted according to the respective cases.

the low-frequency range, its space phase shall embed UPOs according to Auerbach *et al.* (1987). Therefore, the OL-0 forcing at $f_j^* = 0.2$ may have enhanced large UPOs (Grebogi *et al.*, 1988), such as the TS mode dominates. Further investigations to detect and map the UPOs from y_p^* (Ma *et al.*, 2013) are needed to verify this dynamical interpretation which remains an open question.

The four first POD modes are given once again for the natural flow in Figure 7.10(a,d,g,j). These modes are also respectively given for OL-0 in Figure 7.10(b,e,h,k) with continuous blowing and in Figure 7.10(c,f,i,l) with pulsed jets at $f_j^* = 0.2$. The spatial organization of Φ_1 is the same for each run and it is related to the bimodal behavior. Its energy increases for the continuous forcing (+14%), while it decreases with the pulsed jets at $f_j^* = 0.2$ (−50%). It appears that the total energy of POD modes having a spatial organization with a reflexive symmetry with respect to the y -axis [Figure 7.10(f,i,l)] rises for the pulsed forcing.

The sensitivity analysis made by Grandemange *et al.* (2014a) shows that targeting the center of

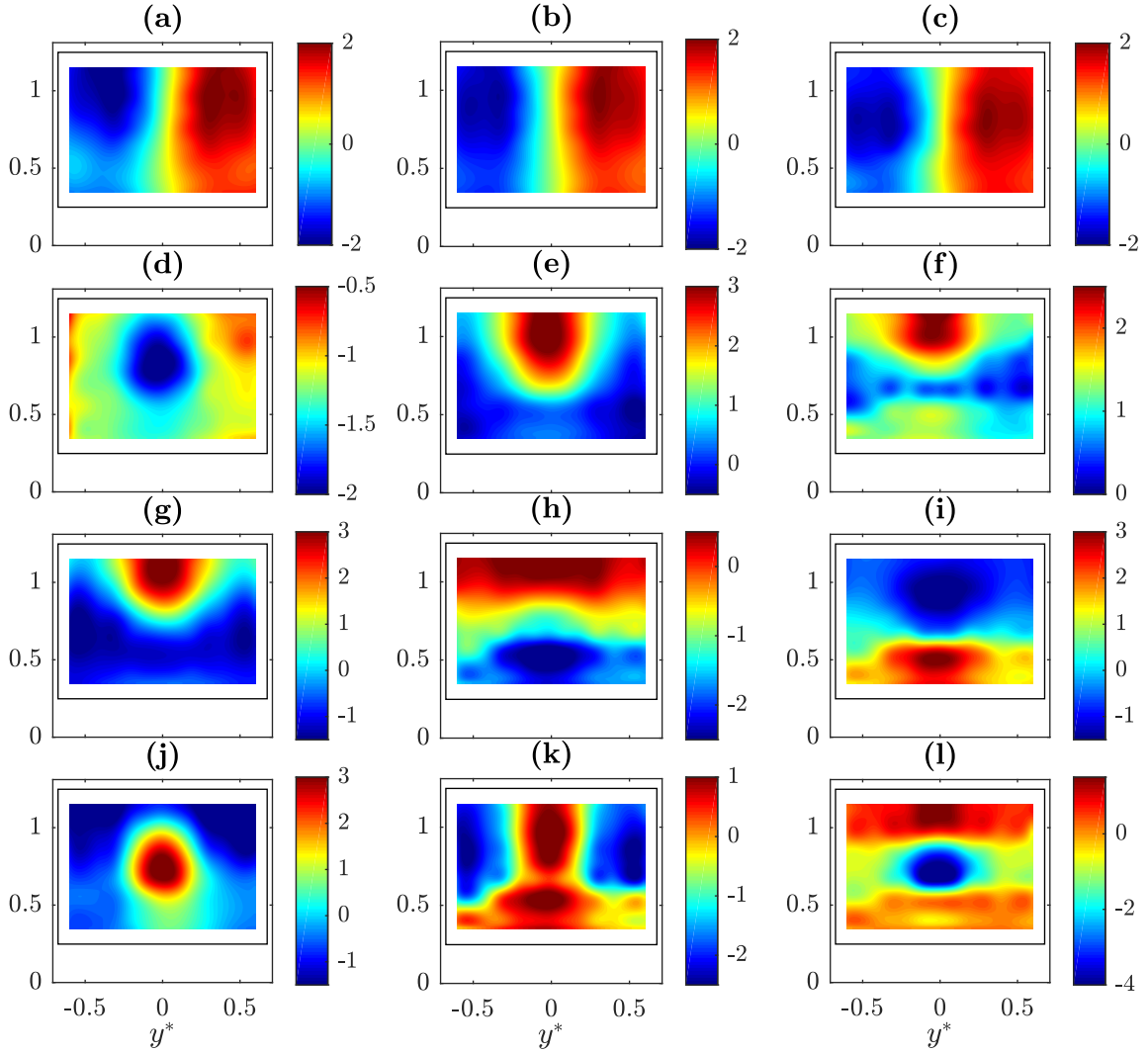


Figure 7.10 – First, second, third, and fourth POD modes (each row of the figure) computed for (a,d,g,j) the reference, (b,e,h,k) OL-0 with continuous jets, and (c,f,i,l) OL-0 with pulsed jets at $f_j^* = 0.2$. For the continuous blowing and the pulsed jets, the associated POD energies are respectively 50% and 22% (Φ_1), 12% and 14% (Φ_2), 6.5% and 12% (Φ_3), 4.0% and 6.8% (Φ_4).

the top or of the bottom shear layer with a control cylinder stabilizes the wake in a symmetric mode. In our case, this wake topology is obtained by forcing the top shear layer at the vortex shedding frequency. As highlighted recently, using this frequency for the actuation frequency leads to a strong increase of the pressure drag (over +25%) by enhancing the entrainment rate of the wake (Barros *et al.*, 2016a,b). Thereby, forcing the wake in its center at one of its main resonant frequency ($St_H = 0.2$) induces two opposite effects on the base pressure, resulting finally to its very slight increase (+0.75% in average), as shown by Figure 7.8(b). The impact of a low pulse frequency previously observed may be attenuated in our case as the exit slit of the jets is discontinuous and only localized in the middle of the upper rear part, unlike the forcing by Barros *et al.* (2016a,b). It is noteworthy that base pressure recovery was also obtained at similar and lower normalized jet frequencies for other bluff body wakes (Brunn & Nitsche, 2006; Joseph,

2012), axisymmetric wakes (Sigurdson, 1995), and 2D wakes (Pastoor *et al.*, 2008).

7.3 Closed-loop control of the wake dynamics

7.3.1 Principle of the closed-loop experiments

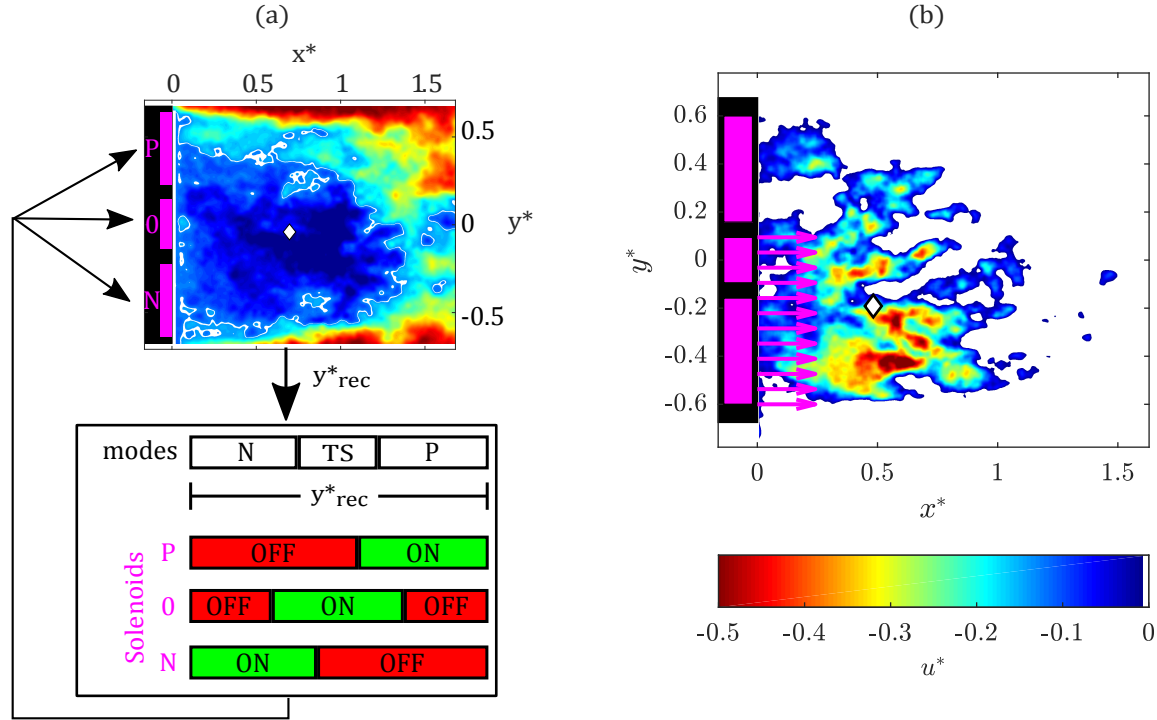


Figure 7.11 – (a) Sketch of the opposition closed-loop control law, based on the detection of the spanwise position of the recirculation barycenter (white diamond), computed from the instantaneous velocity fields. (b) Illustration of the opposition control with the blowing regions chosen as a function of the position of the recirculation barycenter computed in real-time.

The principle of the closed-loop experiments is based on the computation in *real-time* of the recirculation barycenter in the horizontal XY-plane at $z^* = 1$, defining y_{rec}^* as the control parameter. This tracking is then limited by the low acquisition frequency of the PIV setup ($f_{PIV}^* = 2.8 \times 10^{-2}$). It means that we will act on the low-frequency large-scale dynamics of the wake. We then choose an opposition algorithm for the closed-loop experiments. It consists in blowing in the region where the recirculation barycenter is detected, as summarized in Figure 7.11. This is consistent with the three modes defining the state of the wake: the two RSB modes and the TS mode. To these three modes correspond three blowing regions that are activated when the recirculation barycenter is detected in the related region. For each solenoids group we define a range for the spanwise location of the recirculation intensity barycenter y_{rec}^* for which the group is activated. The instantaneous velocity fields and y_{rec}^* are computed in *real-time*. The control variable is updated with a period T_{act}^* , the minimum being $1/f_{PIV}^*$.

To make things more simple, we focus on the detection - blowing algorithm with all other actuation parameters fixed. The parameters for a closed-loop experiment are chosen based on the best or more interesting parameters found in the open-loop experiments. The actuation frequency f_j^* and the mean jet velocity $\overline{u_{jet}}$ are then chosen and set to fixed values before turning the control on.

In the following, two types of actuation are used in the closed-loop experiments: a continuous blowing, denoted “CL-CONT” (“CL” stands for closed-loop.), or a pulsed blowing with different actuation frequencies f_j^* . We will focus on two actuation frequencies: $f_j^* = 0.2$ and $f_j^* = 0.8$, respectively denoted “CL-LF” (for low frequency) and “CL-HF” (for high frequency).

7.3.2 Stabilization of the wake

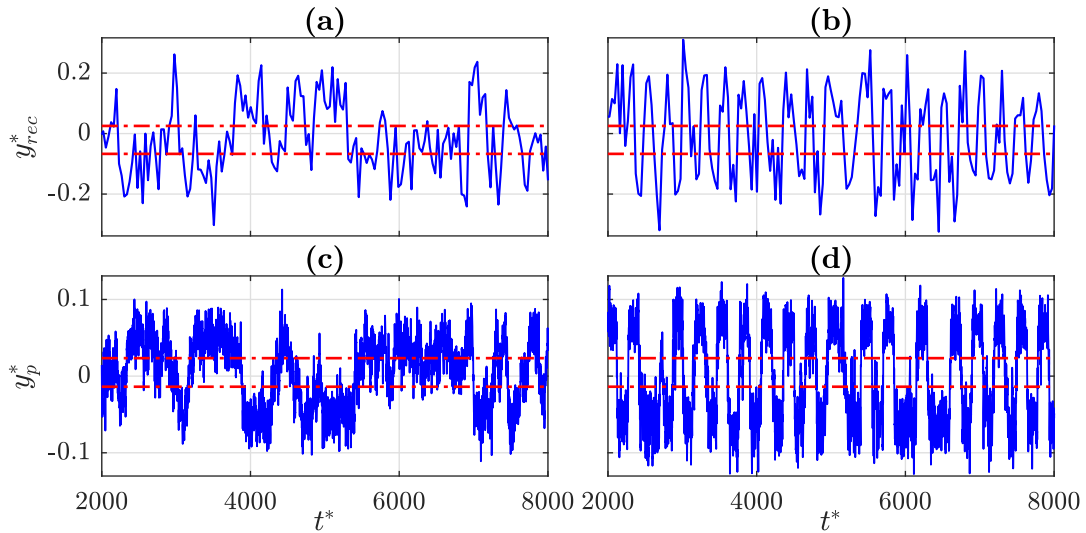


Figure 7.12 – Time series of the y^* -position of the recirculation barycenter and the pressure center for the reference case (a-c), compared to the closed-loop controlled case with continuous blowing jets (b-d). Thresholds are displayed in dash-dotted red.

The objective of these experiments is to control the wake dynamics which are characterized by the fluctuations of the spanwise location of the recirculation barycenter $y_{rec}^*(t)$. Typical time-series of the pressure and recirculation barycenters fluctuations for the reference case are displayed respectively in Figure 7.12(a) and (c) as a reminder. When the closed-loop actuation CL-CONT is triggered, the dynamics of the barycenters [Figure 7.12(b) and (d)] are completely changed. Instead of random large and small fluctuations, the oscillations of the barycenters become very regular and periodic. The right-left switching is now imposed by the characteristic time scale of the closed-loop control law T_{act}^* . This observation holds also for the pulsed actuations.

The trajectories of the pressure barycenter for CL-CONT during four successive control cycles are illustrated in Figure 7.13(a-d). It reveals that the flipping process occurs at the defined period T_{act}^* , only enforcing the presence of the two asymmetric modes, whereas the transient state becomes very short. The bimodal behavior is thus now completely driven by the opposition

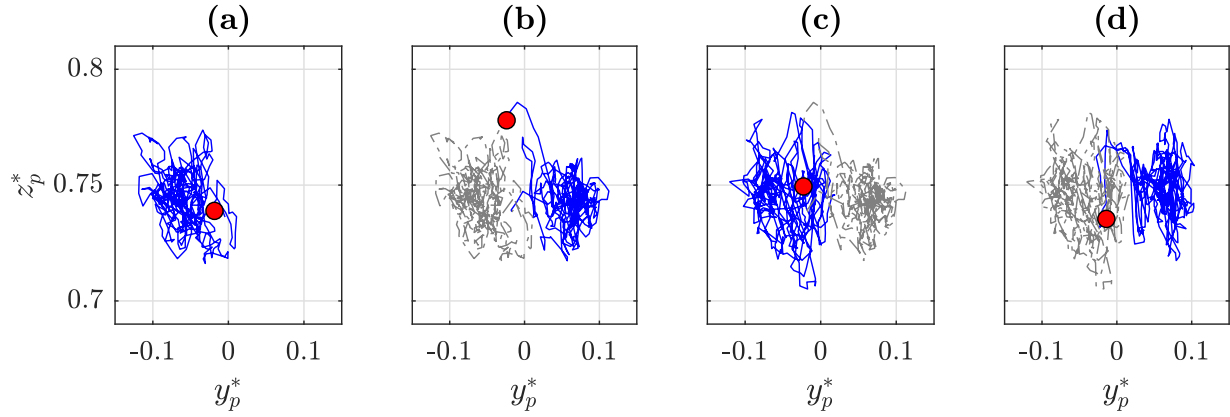


Figure 7.13 – Successive displacements of the pressure center G_p for CL-CONT for (a) $[t_0^* : t_0^* + T_{act}^*]$, (b) $[t_0^* + T_{act}^* : t_0^* + 2T_{act}^*]$, (c) $[t_0^* + 2T_{act}^* : t_0^* + 3T_{act}^*]$, and (d) $[t_0^* + 3T_{act}^* : t_0^* + 4T_{act}^*]$. The red circle is the last position in the corresponding sub-figure, the solid blue line shows the barycenter trajectory whereas the grey dashed line displays its previous one.

control law.

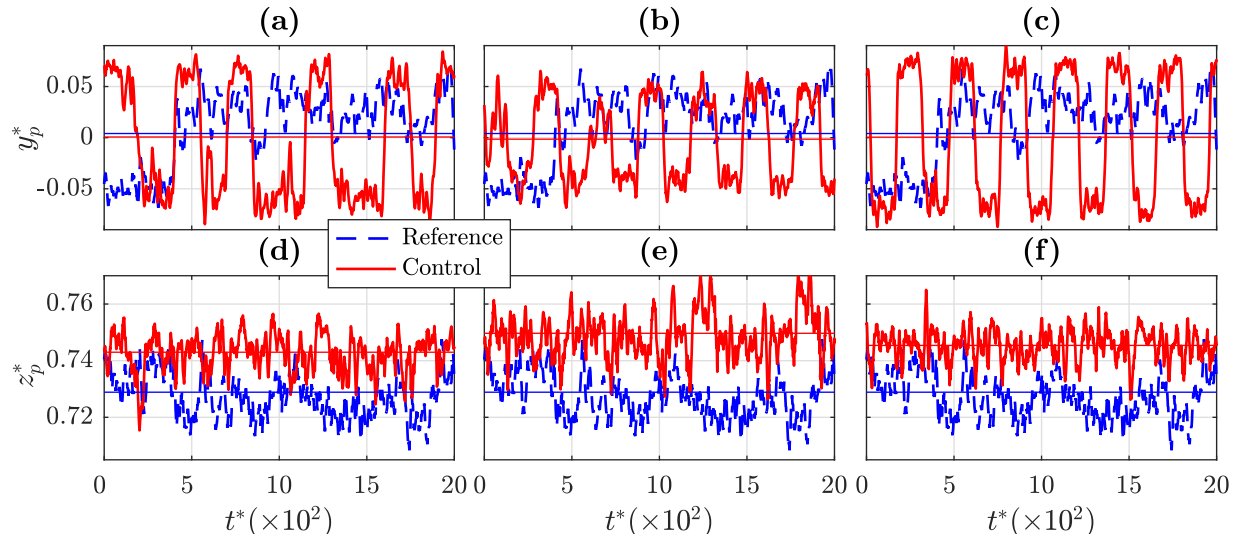


Figure 7.14 – Excerpts of y_p^* and z_p^* time series for (a-d) CL-CONT, (b-e) CL-LF, and (c-f) CL-HF (solid red), all compared to a reference time series (dashed blue). Data are smoothed over $\Delta t^* = 15$ for clarity. The horizontal lines are the mean values.

Introducing again pulsed jets instead of continuous blowing modifies the dynamics, depending on the jet frequency. On one hand, the dynamics obtained for CL-HF [Figure 7.14(c) and (f)] are very close to the ones for CL-CONT [Figure 7.14(a) and (d)]. On the other hand, Figure 7.14(b) shows for CL-LF slightly lower spanwise fluctuations, of the same order as the reference, whereas Figure 7.14(e) reveals a higher mean vertical position of the depression. This is probably due to the central jets which tend to symmetrize the wake and to attract the depression, as seen for the OL-0 case at this jet frequency.

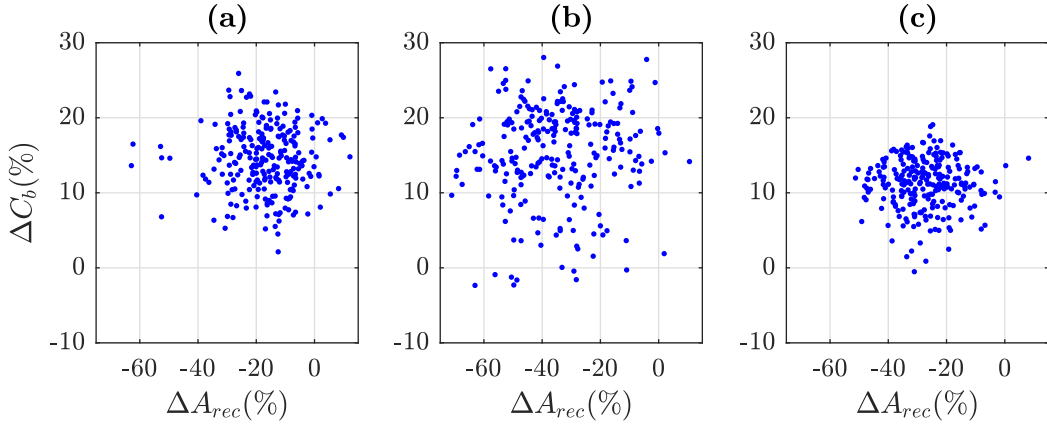


Figure 7.15 – ΔC_b with respect to ΔA_{rec} for (a) CL-CONT, (b) CL-LF, and (c) CL-HF.

It is then interesting to analyze how the pressure at the rear end of the model and the wake size are modified together, depending on the type of actuation used in the closed-loop experiments. Another state parameter for the wake is thus defined: the variation of the recirculation area A_{rec} compared to the mean value of the reference case $A_{rec,ref}$ in the PIV-plane

$$\Delta A_{rec}(t) = \frac{A_{rec}(t) - A_{rec,ref}}{A_{rec,ref}}. \quad (7.4)$$

Instead of following the physical trajectories of the pressure barycenter over the rear part of the model, it is now possible to follow the trajectory of the wake in the state parameter (ΔC_b , ΔA_{rec}). Unfortunately, the acquisition frequency of the PIV fields is much smaller than the ones of the pressure fields, so that it is not possible to correlate all mean pressure coefficients to a corresponding recirculation area. Nevertheless, it is possible to correlate all PIV fields to a corresponding mean pressure coefficient and then plot the two state parameters.

As shown in Figure 7.15, all closed-loop experiments lead to clear reduction of the recirculation area, i.e. of the size of the wake. The type of actuation has also a strong influence: pulsed jets are more efficient (-40% and -32% in average when $f_j^* = 0.2$ and $f_j^* = 0.8$ respectively) than continuous blowing (-18%). On the contrary, the depression over the rear end increases in all cases, with the most important increase for $f_j^* = 0.2$ ($+19\%$). The portion of the phase space explored by the wake is much larger for the CL-LF case [Figure 7.15(b)] than for the two other configurations but there is no clear relation between the changes in ΔA_{rec} and the ones in ΔC_b .

Regarding the RSB modes in particular, the more the CL controls reduce the recirculation area, the more asymmetric the wake is, as highlighted by Figure 7.16(a). Even if the TS state existence is reduced, the separatrices computed for this state [Figure 7.16(b)] have the shape similar to the mean profiles [Figure 7.16(c)]. This is due to the enhanced equiprobability of the BSR states. It is noteworthy that the recirculation barycenter comes also closer to the bluff-body for all types of actuations.

The conditional averages of the pressure and the velocity are computed and displayed in Figure 7.17 for CL-LF. The mean rear pressure of the TS state is higher than the BSR one (-0.227 and -0.234).

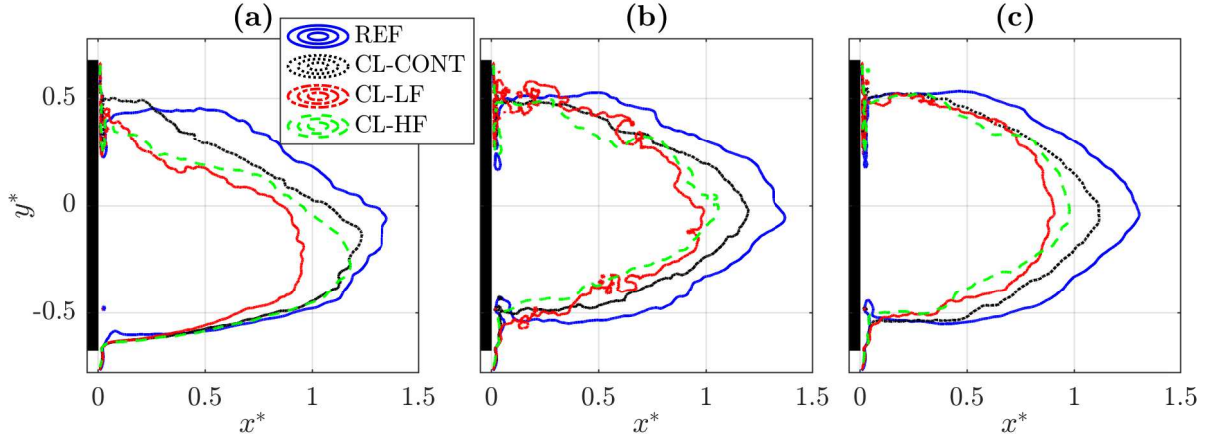


Figure 7.16 – Contour of the recirculation area for the reference (blue solid), CL-CONT (black dotted), CL-LF (red dash-dotted) and CL-HF (green dashed) for (a) the N state, (b) the TS state and (c) the mean velocity field.

7.3.3 Creation of a multimodal state

Another way to characterize the dynamics of the wake is to look again at the full trajectories of the pressure barycenter over the rear part of the model. For the three actuation types, the corresponding 2D PDF are shown in Figure 7.18, where the previously highlighted strange attractors are displayed in blue.

When the recirculation barycenter is tracked and forced by the closed-loop algorithm with a continuous blowing, the PDF is also completely changed and exhibits two strong foci, as shown in Figure 7.18(a). The transient mode is nearly suppressed and the wake switches quickly from one attractor to the other. This modification is also observed with CL-HF [Figure 7.18(c)]. In both cases, the dynamics are marked by a decrease of 50% in the TS mode existence. Interestingly, the PDF is also strongly modified by the lower pulse frequency (CL-LF). In this case, one can see in Figure 7.18(b) a butterfly shape with *four* attractors instead of two for all other cases. These results suggest the occurrence of multi-modal state with a right-left oscillation *and* a top-bottom oscillation, which are undoubtedly enlarged due to the actuating frequency corresponding to the resonant frequency found in the spectral analysis of the $z_p^*(t)$ fluctuations [Figure 5.29(b)]. This harmonic resonance is also highlighted by Barros *et al.* (2016a), through an antisymmetric open-loop forcing, close to the one resulting from our closed-loop control law.

Figure 7.19 displays successive displacements of the pressure center, which oscillates at the constant period $T_j^* = 1/f_j^* = 5$ with a doubled amplitude compared to the natural dynamics.

The multi-modality of the controlled wake dynamics is also analyzed using the POD of the wall-pressure spatial distribution. For the three controlled cases, the spatial organization of Φ_1 remains strictly the same as the natural flow as displayed in Figure 7.20(a-c). Nevertheless, the energy levels are different regarding the control settings: for CL-CONT and CL-HF they reach 57.9%

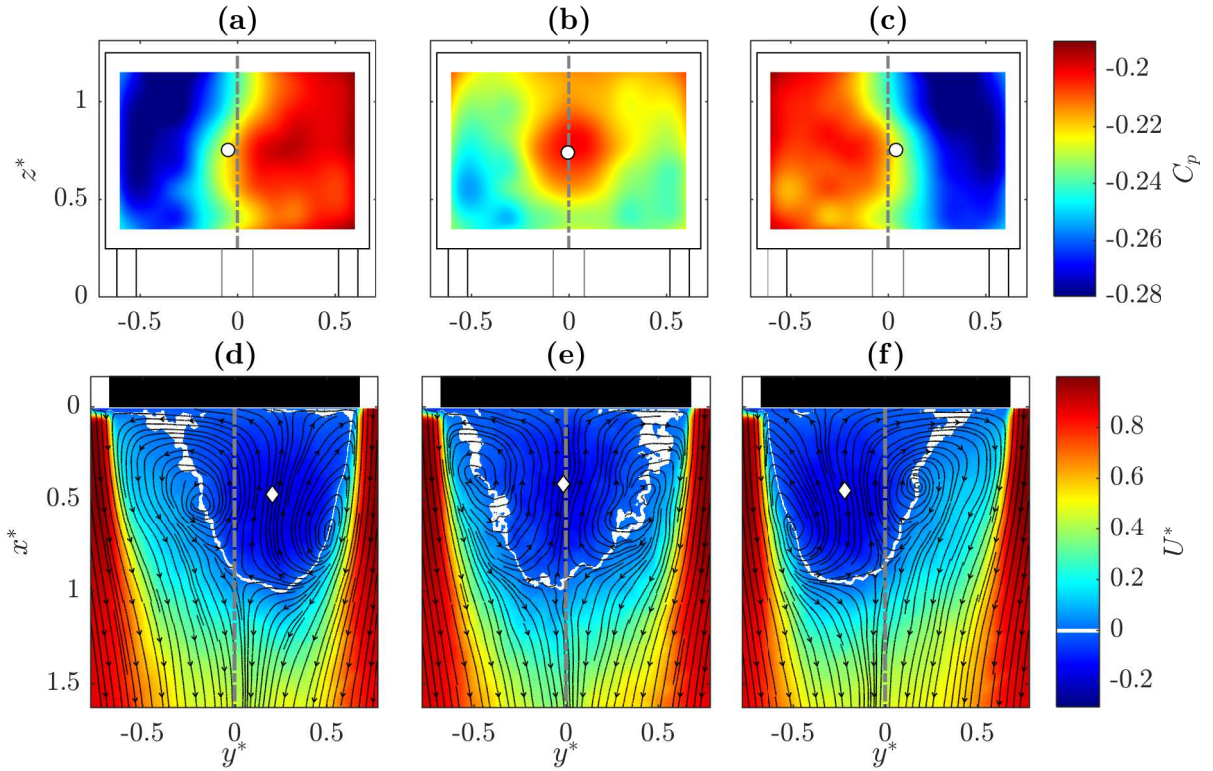


Figure 7.17 – Conditional averages of the pressure coefficient at the rear body and the velocity field at $z^* = 1$ for the modes (a-d) N, (b-e) TS and (c-f) P in the CL-LF case. The average position of the pressure center G_p (white circle) and of the recirculation barycenter G_{rec} (white diamond) are displayed. $y^* = 0$ is also displayed (dash-dotted grey lines). Some streamlines are plotted over the streamwise component of the velocity to localize the coherent large-scale structures.

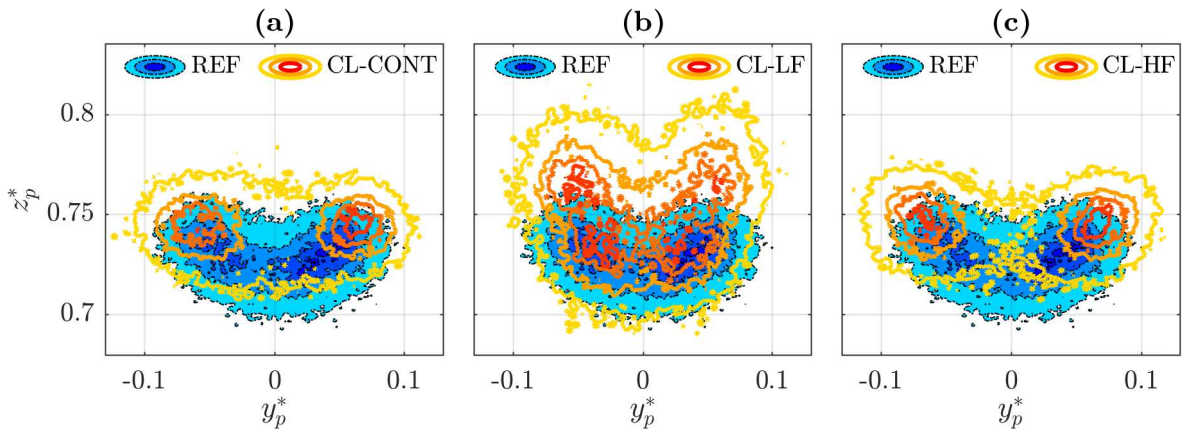


Figure 7.18 – 2D PDF contour of (y_p^*, z_p^*) for the reference flow (blue) and various closed-loop controls (red): (a) CL-CONT, (b) CL-LF, and (c) CL-HF.

and 59.7% respectively, whereas it falls at 34% for CL-LF. The three following POD modes of

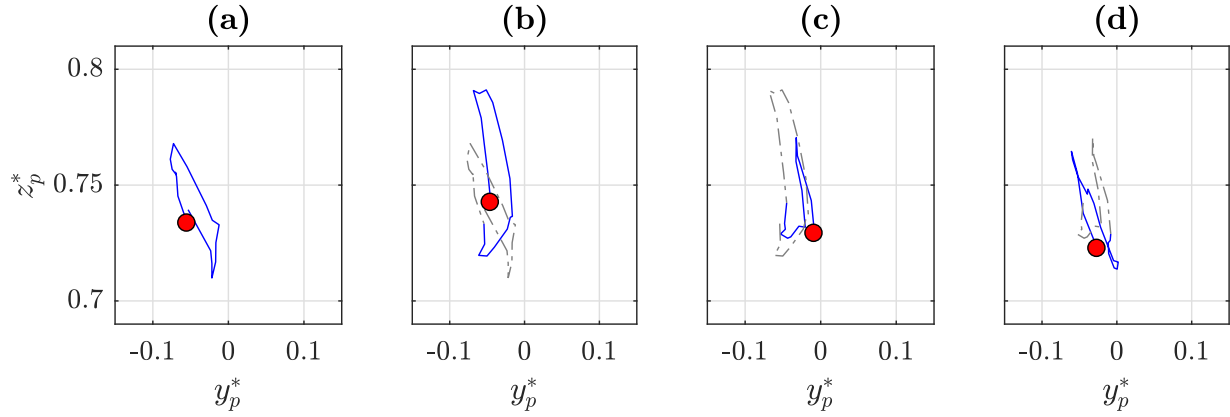


Figure 7.19 – Successive displacements of the pressure center G_p for CL-LF for (a) $[t_0^* : t_0^* + T_j^*]$, (b) $[t_0^* + T_j^* : t_0^* + 2T_j^*]$, (c) $[t_0^* + 2T_j^* : t_0^* + 3T_j^*]$, and (d) $[t_0^* + 3T_j^* : t_0^* + 4T_j^*]$. The red circle is the last position in the corresponding sub-figure, the solid blue line shows the barycenter trajectory whereas the grey dashed line displays its previous one.

CL-CONT are exactly the ones of the reference case [Figure 7.20(d-g-j)]. This remark almost holds for CL-HF, Φ_3 (4.3%) and Φ_4 (4.1%) being simply permuted regarding the POD order of the natural wake [Figure 7.20(f-i-l)]. Actually, only CL-LF exhibits completely new modes. Figure 7.20(e) and (h) show that Φ_2 (18.8%) and Φ_3 (12.3%) have both the identical top-bottom reflexive symmetry. Φ_4 (5.3%) is also a symmetric configuration, but centred in the region of G_p , as displayed by Figure 7.20(k).

Comparing the PSD of the POD modes with the ones of y_p^* and z_p^* also explains how these modes are related to the dynamics of the wake. As expected, Figure 7.21 shows that Φ_1 is clearly linked to the y_p^* activity only, especially for the low frequencies. The $St_H = 0.19$ -peak exclusively present in $S_{z_p^* z_p^*}$ appears in the spectra of the three following POD modes for each control case. Indeed, for CL-CONT and CL-HF, Φ_2 shares some peaks with $S_{y_p^* y_p^*}$ in the high-frequency range, but it contains particularly a similar low frequencies spectrum as $S_{z_p^* z_p^*}$ and a low $St_H = 0.19$ -peak. For CL-LF, this peak is clearly stronger in the Φ_2 and Φ_4 spectra. $S_{a_4 a_4}$ and $S_{z_p^* z_p^*}$ are quasi-identical, meaning Φ_4 is rather only linked to z_p^* dynamics for this case.

The spatial organization and the dynamics of the POD mode enable thus to evaluate the impact of the closed-loop controls on the energy part associated to the large-scale fluctuations tracked by the barycenters. Among the four most energetic POD modes, Φ_1 solely describes a left-right behavior. The other POD modes are rather related to the TS state and slightly to the vortex shedding. The top-bottom variations of the wake fall by 30.2% and 37.9% for CL-CONT and CL-HF with 17.9% (−37.9%). So, these controls enforce vigorously the lateral motion of the wake. Concerning the CL-LF case, the top-bottom characterization is carried by Φ_2 and Φ_3 , which contain 31.2% (+8.3%) of the total energy. This control tends thus to create a multistable state, making the top-bottom dynamics visible as the right-left one.

Table 7.2 summarizes the previous interpretations. For instance, the energy associated to the RSB rises by 37.9% and 42.1% for CL-CONT and CL-HF respectively, whereas it decreases by

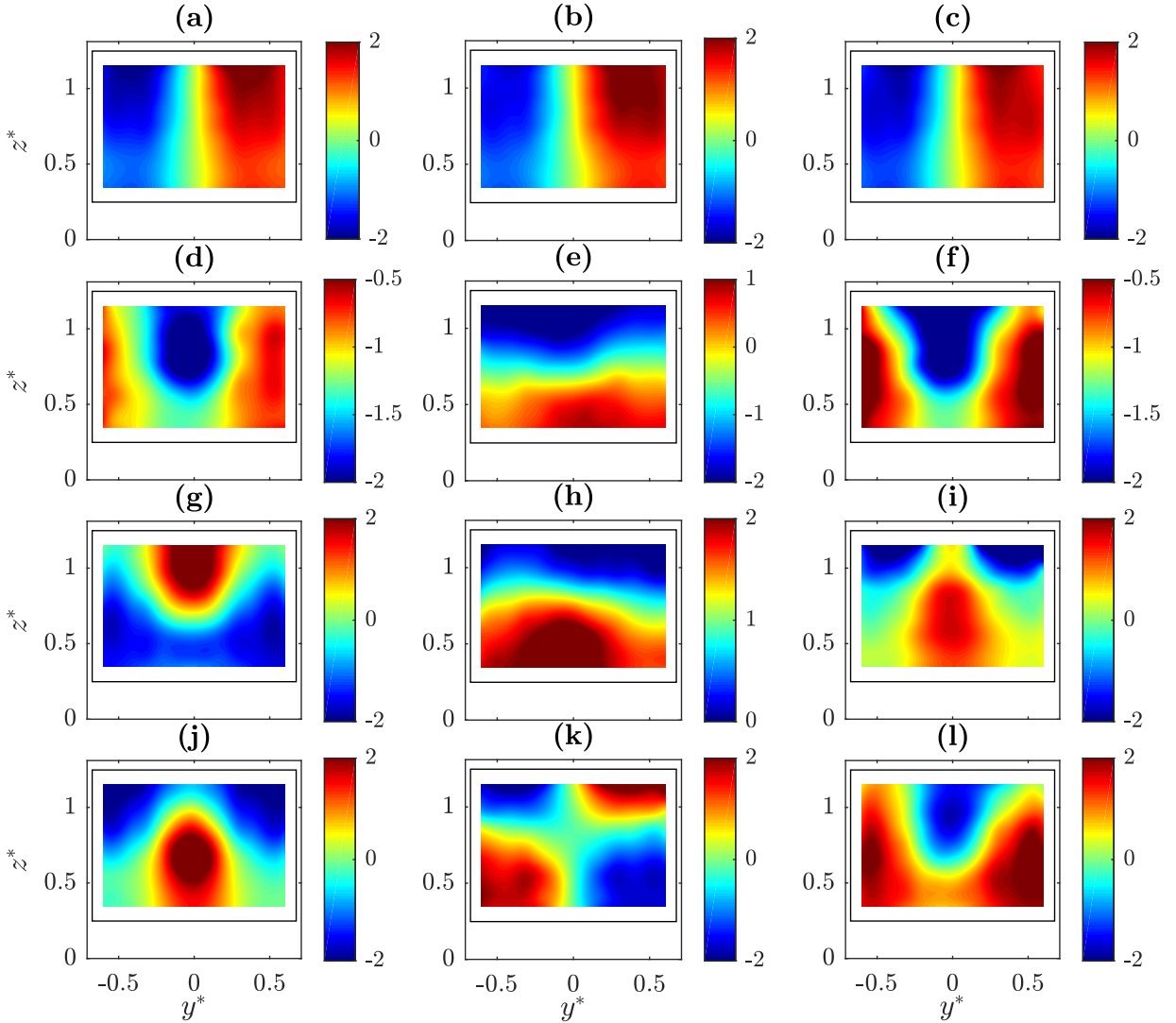


Figure 7.20 – First, second, third, and fourth POD modes (each row of the figure) computed for (a,d,g,j) CL-CONT, (b,e,h,k) CL-LF, and (c,f,i,l) CL-HF.

20.2% for CL-LF.

7.4 Conclusions and issues raised

After testing different open-loop controls with micro jets on the turbulent wake behind a square-back body, a simple opposition control has been based on the real-time computations of the location of the recirculation area barycenter. To our knowledge, this is the first implementation of a closed-loop flow control experiment based on the dense velocity fields computations at such Reynolds numbers (up to 5.1×10^5). The chaotic spanwise oscillations of the location of the recirculation (and pressure) barycenter is then forced into a well-controlled periodic oscillation

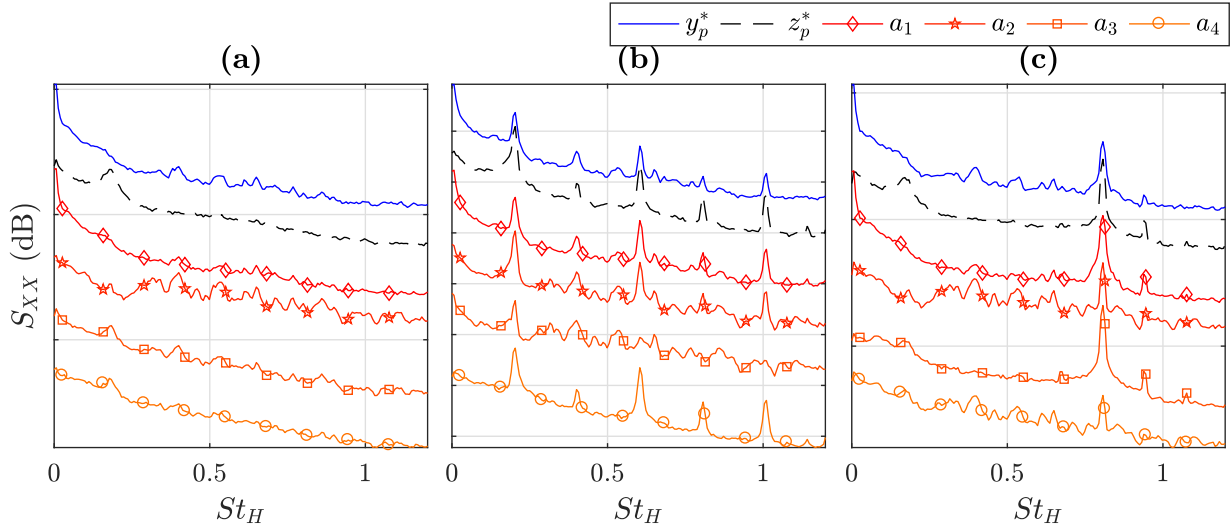


Figure 7.21 – Normalized PSD of the first (diamond), the second (star), the third (square) and the fourth (circle) POD coefficients, together with the PSD of y_p^* (blue solid line) and z_p^* (black dashed line) for the (a) CL-CONT, (b) CL-LF, and (c) CL-HF. Curves are shifted for clarity.

Phenomena	Ref.	CL-CONT	CL-LF	CL-HF
RSB	Φ_1	Φ_1 +37.9%	Φ_1 -20.2%	Φ_1 +42.1%
TS	Φ_2 and Φ_3	Φ_2 and Φ_3 -36.8%	- ?	Φ_2 and Φ_4 -47.7%
Top-bottom interaction	Φ_4	Φ_4 -11.6%	Φ_2, Φ_3 and Φ_4 +749%	Φ_3 +0%
Vortex shedding	Φ_2, Φ_3 and Φ_4	Φ_2, Φ_3 and Φ_4 -33.2%	- ?	Φ_2, Φ_3 and Φ_4 -40.9%

Table 7.2 – Effects of the different closed-loop controls on the wake through the POD modes analysis.

at the time scale imposed by the PIV setup and the control algorithm.

Moreover, a much larger reduction of the recirculation area is obtained when a pulsed actuation is used in the closed-loop control experiments, instead of a continuous blowing. When the frequency of the pulsed actuation used in the closed-loop experiments corresponds to the natural shedding frequency the fluctuations in the phase space are strongly increased. Moreover, if the PDF of trajectories exhibits well-defined stable foci points for most of the configurations, the low-frequency actuation case leads to a new four attractors configuration, suggesting multi-modality behavior with a right-left oscillation together with a top-bottom oscillation of the wake. These results are also confirmed by a POD analysis.

7.4.1 Perspectives

The analysis and the understanding of the open-loop results came after the closed-loop experiments. An interesting strategy to test would involve pulsed jets at $f_j = 0.2$ only at the center, whereas the opposition approach would be defined on the side actuators groups.

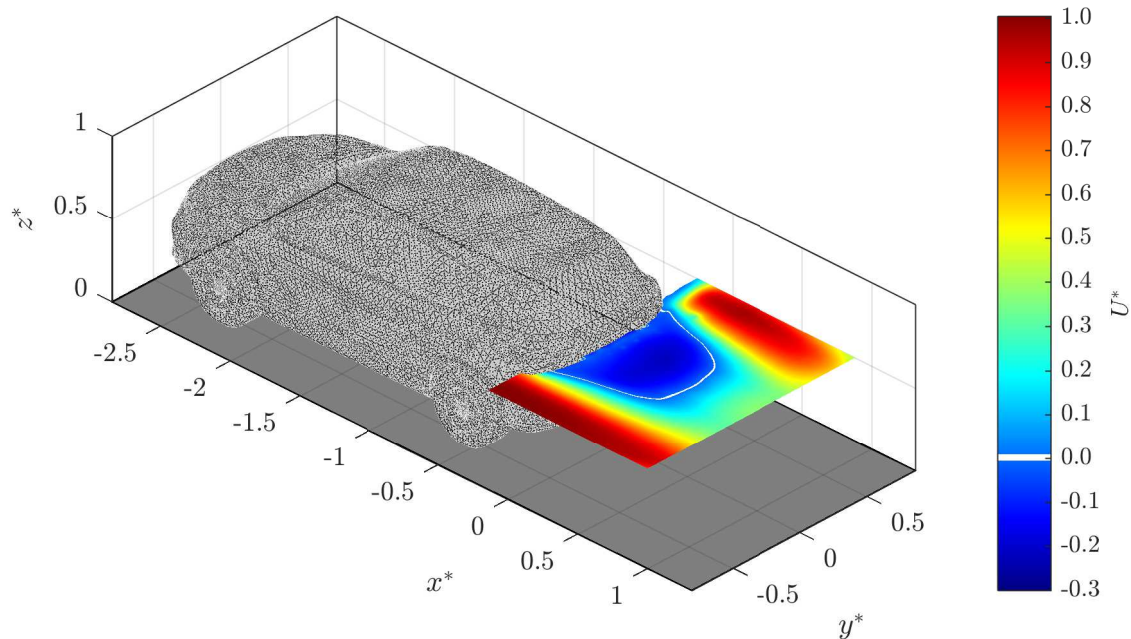


Figure 7.22 – PO SUV sketch with a time-averaged 2D-2C velocity field in the XY-plane at $z^* = 0.56$.

The real-time PIV setup will be used to investigate the flow over a reduced model having the complex shape of a SUV designed by Plastic Omnium. In fact, these experiments have already started through the first characterizations of the natural turbulent wake illustrated in [Figure 7.22](#). This model has been conceived by defining various rear and front profiles, as well as different configurations for the nature of the embedded actuators (discontinuous jets, Coanda effect). A promising machine learning control, recently successfully applied to the square-back Ahmed body ([Li et al., 2017](#)), has even been rapidly tested on the SUV model. This finally requires an improved management of the actuators through the LabVIEW program.

Bibliography

- AUERBACH, D., CVITANOVIĆ, P., ECKMANN, J.P., GUNARATNE, G. & PROCACCIA, I. (1987) Exploring chaotic motion through periodic orbits. *Physical Review Letters* **58**, pp. 2387–2389. doi:10.1103/PhysRevLett.58.2387. 151
- BARROS, D., BORÉE, J., NOACK, B.R. & SPOHN, A. (2016a) Resonances in the forced turbulent wake past a 3D blunt body. *Physics of Fluids* **28** (6), p. 065104. doi:10.1063/1.4953176. 144, 152, 157
- BARROS, D., BORÉE, J., NOACK, B.R., SPOHN, A. & RUIZ, T. (2016b) Bluff body drag manipulation using pulsed jets and Coanda effect. *Journal of Fluid Mechanics* **805**, p. 422–459. doi:10.1017/jfm.2016.508. 144, 152
- BARROS, D., RUIZ, T., BORÉE, J. & NOACK, B.R. (2014) Control of a three-dimensional blunt body wake using low and high frequency pulsed jets. *International Journal of Flow Control* **6** (1), pp. 61–74. doi:10.1260/1756-8250.6.1.61. 144
- BRACKSTON, R., GARCÍA DE LA CRUZ, J., WYNN, A., RIGAS, G. & MORRISON, J. (2016) Stochastic modelling and feedback control of bistability in a turbulent bluff body wake. *Journal of Fluid Mechanics* **802**, pp. 726–749. doi:10.1017/jfm.2016.495. 144
- BROZE, G. & HUSSAIN, F. (1994) Nonlinear dynamics of forced transitional jets: periodic and chaotic attractors. *Journal of Fluid Mechanics* **263**, p. 93–132. doi:10.1017/S00222112094004040. 145, 150
- BRUNEAU, C.H., CREUSÉ, E., DEPEYRAS, D., GILLIÉRON, P. & MORTAZAVI, I. (2010) Coupling active and passive techniques to control the flow past the square back Ahmed body. *Computers & Fluids* **39** (10), pp. 1875 – 1892. doi:10.1016/j.compfluid.2010.06.019. 144
- BRUNN, A. & NITSCHKE, W. (2006) Active control of turbulent separated flows over slanted surfaces. *International Journal of Heat and Fluid Flow* **27** (5), pp. 748 – 755. doi:10.1016/j.ijheatfluidflow.2006.03.006. Special issue of the 6th International Symposium on Engineering Turbulence Modelling and Measurements (ETMM6). 152
- CADOT, O., EVRARD, A. & PASTUR, L. (2015) Imperfect supercritical bifurcation in a three-dimensional turbulent wake. *Physical Review E* **91** (6), p. 063005. doi:10.1103/PhysRevE.91.063005. 143
- DURIEZ, T., BRUNTON, S.L. & NOACK, B.R. (2017) *Machine Learning Control - Taming Nonlinear Dynamics and Turbulence*. Springer. doi:10.1007/978-3-319-40624-4. 145
- EULALIE, Y. (2014) Aerodynamic analysis and drag reduction around an Ahmed bluff body. PhD thesis, Université de Bordeaux, Bordeaux, France. 144, 145

- EVRRARD, A., CADOT, O., HERBERT, V., RICOT, D., VIGNERON, R. & DÉLERY, J. (2016) Fluid force and symmetry breaking modes of a 3D bluff body with a base cavity. *Journal of Fluid Mechanics* **61**, pp. 99 – 114. doi:10.1016/j.jfluidstructs.2015.12.001. 143, 144
- EVSTAFYEVA, O., MORGANS, A.S. & DALLA LONGA, L. (2017) Simulation and feedback control of the Ahmed body flow exhibiting symmetry breaking behaviour. *Journal of Fluid Mechanics* **817**. doi:10.1017/jfm.2017.118. 144
- GRANDEMANGE, M., CADOT, O., COURBOIS, A., HERBERT, V., RICOT, D., RUIZ, T. & VIGNERON, R. (2015) A study of wake effects on the drag of ahmed's squareback model at the industrial scale. *Journal of Wind Engineering and Industrial Aerodynamics* **145**, pp. 282 – 291. doi:10.1016/j.jweia.2015.03.004. 144
- GRANDEMANGE, M., GOHLKE, M. & CADOT, O. (2014a) Turbulent wake past a three-dimensional blunt body. Part 2. Experimental sensitivity analysis. *Journal of Fluid Mechanics* **752**, pp. 439 — 461. doi:10.1017/jfm.2014.345. 143, 149, 151
- GRANDEMANGE, M., MARY, A., GOHLKE, M. & CADOT, O. (2013b) Effect on drag of the flow orientation at the base separation of a simplified blunt road vehicle. *Experiments in Fluids* **54** (5), p. 1529. doi:10.1007/s00348-013-1529-z. 144
- GREBOGI, C., OTT, E. & YORKE, J.A. (1988) Unstable periodic orbits and the dimensions of multifractal chaotic attractors. *Physical Review A* **37**, pp. 1711–1724. doi:10.1103/PhysRevA.37.1711. 144, 151
- GUÉNIAT, F., MATHELIN, L. & HUSSAINI, M.Y. (2016) A statistical learning strategy for closed-loop control of fluid flows. *Theoretical and Computational Fluid Dynamics* **30** (6), pp. 497–510. doi:10.1007/s00162-016-0392-y. 145
- JOSEPH, P. (2012) Application of control by pulsed jets on a bluff body. PhD thesis, Université Pierre et Marie Curie, Paris, France. 152
- LI, C., LIAO, X. & HUANG, T. (2007) Exponential stabilization of chaotic systems with delay by periodically intermittent control. *Chaos: An Interdisciplinary Journal of Nonlinear Science* **17** (1), p. 013103. doi:10.1063/1.2430394. 144
- LI, R., BARROS, D., BORÉE, J., CADOT, O., NOACK, B.R. & CORDIER, L. (2016) Feedback control of bimodal wake dynamics. *Experiments in Fluids* **57** (10), p. 158. doi:10.1007/s00348-016-2245-2. 144, 145
- LI, R., NOACK, B.R., CORDIER, L., BORÉE, J. & HARAMBAT, F. (2017) Drag reduction of a car model by linear genetic programming control. *Experiments in Fluids* **58** (8), p. 103. doi:10.1007/s00348-017-2382-2. 162
- LORENZ, E.N. (1963) Deterministic nonperiodic flow. *Journal of the Atmospheric Sciences* **20**, pp. 130–141. doi:10.1175/1520-0469(1963)020<0130:DNF>2.0.CO;2. 145
- MA, H., LIN, W. & LAI, Y.C. (2013) Detecting unstable periodic orbits in high-dimensional chaotic systems from time series: Reconstruction meeting with adaptation. *Physical Review E* **87**, p. 050901. doi:10.1103/PhysRevE.87.050901. 151

- MCNALLY, J., FERNANDEZ, E., ROBERTSON, G., KUMAR, R., TAIRA, K., ALVI, F., YAMAGUCHI, Y. & MURAYAMA, K. (2015) Drag reduction on a flat-back ground vehicle with active flow control. *Journal of Wind Engineering and Industrial Aerodynamics* **145**, pp. 292 – 303. doi:10.1016/j.jweia.2015.03.006. 144
- NARAYANAN, S., GUNARATNE, G.H. & HUSSAIN, F. (2013) A dynamical systems approach to the control of chaotic dynamics in a spatiotemporal jet flow. *Chaos: An Interdisciplinary Journal of Nonlinear Science* **23** (3), p. 033133. doi:10.1063/1.4820819. 145
- OTT, E., GREBOGI, C. & YORKE, J.A. (1990) Controlling chaos. *Physical Review Letters* **64** (11), pp. 1196–1199. doi:10.1103/PhysRevLett.64.1196. 144
- PASTOOR, M., HENNING, L., NOACK, B.R., KING, R. & TADMOR, G. (2008) Feedback shear layer control for bluff body drag reduction. *Journal of Fluid Mechanics* **608**, pp. 161 – 196. doi:10.1017/S0022112008002073. 153
- ROBERTS, J.W. (2012) Control of underactuated fluid-body systems with real-time particle image velocimetry. PhD thesis, Massachusetts Institute of Technology. Dept. of Mechanical Engineering, Boston, USA. 145
- SIGURDSON, L.W. (1995) The structure and control of a turbulent reattaching flow. *Journal of Fluid Mechanics* **298**, pp. 139 – 165. doi:10.1017/S0022112095003259. 153
- SINGER, J., WANG, Y.Z. & BAU, H.H. (1991) Controlling a chaotic system. *Physical Review Letters* **66** (9), pp. 1123–1125. doi:10.1103/PhysRevLett.66.1123. 145
- TIAN, Y.P. & YU, X. (2000) Adaptive control of chaotic dynamical systems using invariant manifold approach. *IEEE Transactions on Circuits and Systems I: Fundamental Theory and Applications* **47** (10), pp. 1537–1542. doi:10.1109/81.886986. 144
- YASSEN, M. (2005) Controlling chaos and synchronization for new chaotic system using linear feedback control. *Chaos Solitons & Fractals* **26** (3), pp. 913 – 920. doi:10.1016/j.chaos.2005.01.047. 144

Conclusions and perspectives

8.1 Concluding remarks

In [chapter 2](#), a new velocimetry method based on an optical flow algorithm has been successfully implemented on different GPUs using CUDA language. This method allows rapid calculation of dense and accurate velocity fields from 4MP images. It is embedded in a homemade LabVIEW program which handles the devices involved in the PIV as well as in different flow control experiments. Other fields characteristic to the flow are also very fast derived from the velocity as detailed in [chapter 3](#). A new method to capture rapid dynamics like the Kelvin-Helmholtz instability is now available and gives expected results for various geometries. The program is completely operational for a hydrodynamic channel as well as for a large wind tunnel. Regarding the material requirement, most of the set up already installed for 2D-2C FFT-PIV in wind tunnel may be directly used with the program if the camera and the frame-grabber device are compliant with the LabVIEW environment.

The spatial resolution of the resulting velocity fields is tied to the size of the interrogation window (IW) such as for advanced PIV algorithms. Nevertheless, the output fields are dense (one vector per pixel), giving not only better results in the vicinity of edges and obstacles but also smoother fields and better calculations for values based on velocity gradients. To achieve such results, the algorithm parameters have to be properly set regarding the optical devices and the experimental conditions. The IW radius depends thereby both on the tracers density and on the free stream velocity which is mainly fixed via the inter-frames time the camera can reach. To enable correct initialization of the algorithm, snapshots are reduced via a Gaussian pyramid. The free stream velocity determines the pyramid level, being cautious regarding the obstacles position with respect to the sensor size. Finally the number of iterations can be estimated via trial and error, making a compromise between accuracy and computation speed.

In [chapter 4](#), a system identification method based on the N4SID algorithm has been successfully implemented for the forced boundary layer flow developing Tollmien-Schlichting (T-S) waves. The input data have been obtained from the optical flow PIV measurements, retaining a double visual sensor of the streamwise and the vertical fluctuating velocity in a small area of the velocity fields. The output data have been defined from a proper orthogonal decomposition of the data set composed of 1500 recorded velocity fields at 60 Hz. The TKE increase induced by the T-S waves propagating along the flat plate has been identified with acceptable agreement between the estimated and the real decomposed flow. Choosing the good state order remains an open question.

The square-back configuration of the Ahmed body is investigated in [chapter 5](#). The barycenters of the pressure distribution over the rear part of this model and of the intensity recirculation are found highly correlated. Both described the most energetic large-scale structures dynamics, confirming the relation between the large-scale recirculation bubble and its wall-pressure footprint. The switching process and the vortex shedding from the top shear layer seem to dominate the depression dynamics. A third state, transient symmetric, is highlighted when analysing the bimodality. The influence of the central pod seems to stabilize the vertical bimodality.

In [chapter 6](#), a stochastic behavior is first observed when analysing the trajectory of the pressure barycenter through some tools of the dynamic systems framework. But applying the same process to the low-frequency signal reveals a chaotic aspect: the instantaneous pressure barycenter circles around two stable areas acting like strange attractors and randomly switches from one attractor to the other. The nonlinear dynamics of the pressure center are thus investigated by reconstructing its phase space from the spanwise component. The largest Lyapunov exponent is first estimated, leading to a low positive value, characteristic of strange attractors and weak chaotic systems. The weak aspect is then confirmed by the correlation dimension found close to one. Afterwards, the low-frequency signal is transformed and studied as a telegraph signal, showing that its dynamics correspond to a quasirandom telegraph signal. All of these elements tend therefore to describe the dynamics of a complex 3D turbulent wake as a weak chaotic system, which can be qualified as “stochastic chaos”, due to the physical noise.

Different open-loop controls with micro jets have been applied to the turbulent wake behind the square-back body in [chapter 7](#). A simple opposition control has been then based on the real-time computations of the location of the recirculation area barycenter. To our knowledge, this is the first implementation of a closed-loop flow control experiment based on the dense velocity fields computations at such Reynolds numbers (up to 5.1×10^5). The chaotic spanwise oscillations of the location of the recirculation (and pressure) barycenter is then forced into a well-controlled periodic oscillation at the time scale imposed by the PIV setup and the control algorithm.

The chaotic spanwise oscillations of the location of the recirculation (and pressure) barycenter is then forced into a well-controlled periodic oscillation at the time scale imposed by the PIV setup and the control algorithm. Moreover, a much larger reduction of the recirculation area is obtained when a pulsed actuation is used in the closed-loop control experiments, instead of a continuous blowing. When the frequency of the pulsed actuation used in the closed-loop experiments corresponds to the natural shedding frequency the fluctuations in the phase space are strongly increased. Moreover, if the PDF of trajectories exhibits well-defined stable foci points for most of the configurations, the low-frequency actuation case leads to a new four attractors configuration, suggesting multi-modality behavior with a right-left oscillation together with a top-bottom oscillation of the wake. These results are also confirmed by a POD analysis.

8.2 Perspectives

Here come the unrealized experiments and the unanswered questions. We planned to control every flows encountered during these three years and the transient boundary layer flow requires still

some adjustments due to the difficulty to properly trigger and follow T-S waves. The previously summarized results pave the way for further work from which, I hope, the society at large will benefit.

8.2.1 Real-time PIV anywhere

The most interesting change into the optical flow algorithm is the adapting IW radius to deal with the different constraints imposed by the investigated flow. The upgrade of the 32-bit LabVIEW program to a 64-bit version (especially for the *cuFFT* library) will be completed with the new camera. The protocol to transfer the images (CoaXPress) is rather new and requires some stratagems to enable fully operating communication. It shall be mentioned that the first frame-grabber device supporting LabVIEW has been just announced in August 2017.

The new camera will be FPGA compliant, making the implementation of the optical flow code directly in the camera conceivable. Even if it may save time when only closed-loop applications are considered, writing a version of the algorithm for a FPGA configuration will be a weighty task due to the hardware compilation. As the current CUDA code can still be improved thanks to the new library, it could be interesting to evaluate a possible combination of both devices.

8.2.2 The transition from laminar to turbulent has been delayed

The region investigated in [chapter 4](#) contains a slotted jet designed like the one forcing the T-S waves. A second external tank has been built and a second air controller has been calibrated. The closed-loop control of the boundary layer flow via the dynamic observer will therefore be soon tested at the PMMH laboratory. Control attempts during the first steps of this work showed promising results¹. This may require a larger PIV window to capture a longer T-S waves evolution, giving more distributed POD modes along the flat plate. The reduction of the TKE may be finally a good objective to fix to the built system since it can also be tracked in real-time.

8.2.3 The stochastic chaos

The results obtained in the [chapter 6](#) are the most surprising. Even more when another research team finds similar conclusions for a different turbulent flow. Is the applied low filter too strong? Is there another mathematical equation than the Langevin equation which could properly model such dynamics? Those results still need further confirmations, knowing the two opposing representations of the turbulence recalled above. Recent improvements in the dynamic system framework via the recurrent neural network approach for short times series and the evaluation of multi-variables should help.

1. Before some parts of the water channel decided to give away.

8.2.4 Control of a personal car wake

The real-time PIV setup will be used to investigate the flow over a reduced modular SUV designed by Plastic Omnium. This model has been conceived by designing various rear and front profiles, as well as different configurations for the nature of the embedded actuators (discontinuous jets, Coanda effect). Rear pressure and aerodynamic forces are planned to be synchronously measured with the velocity fields.

In fact, these experiments have already started through the characterization of the natural turbulent wake for some configurations of the SUV model. A few open-loop controls have also been applied. Instantaneous measurements of the Q -criterion in a XY -plane revealed high swirling activities in the shear layers. Even if the third velocity component is missing and the wake is 3D, simulations done by S. Edwige (PO-CNAM) showed that 2D (in the concerned plane) and 3D computations of the Q -criterion are very close. A machine learning control has even been rapidly tested to reduce the swirling activity. This finally requires last adjustments of the actuators management via the LabVIEW program. The possibility to select ROIs directly on the sensor of the new camera is well suited for this kind of application.

Résumé

Les écoulements décollés sont omniprésents dans la nature comme dans les écoulements industriels (aérodynamique externe des véhicules, des bâtiments, écoulements autour d'aubes de turbines, aérodynamique interne dans des tuyaux...) où ils sont en général sources de nuisances (vibrations, bruit aéroacoustique, forces de traînée ou de portance). Les enjeux associés à la compréhension et à la maîtrise de tels écoulements, caractérisés par une bulle de recirculation, sont donc considérables.

Un capteur *visuel* non invasif développé au laboratoire PMMH est d'abord amélioré afin d'accéder en temps réel aux champs de vitesses - et à leurs grandeurs dérivées - des écoulements rencontrés en soufflerie industrielle. Basée sur un algorithme de flot optique issu de la vision par ordinateur, cette approche expérimentale novatrice permet de faciliter les études paramétriques et peut être implémentée dans des boucles de contrôle réactif. Ensuite, les mesures obtenues pour un écoulement sur une plaque plane sont analysées dans le cadre de l'identification de système. Un modèle d'ordre réduit est alors construit par apprentissage, permettant de prédire la dynamique de la transition de la couche limite laminaire vers la turbulence.

Enfin, le sillage pleinement turbulent derrière une géométrie modélisant une voiture simplifiée est caractérisé, de façon classique et en tant que système dynamique. Différentes modifications de l'écoulement à l'aide de micro-jets sont testées. Une loi de contrôle réactif consistant à suivre et forcer la recirculation est mise en œuvre avec succès.

Mots Clés

Contrôle d'écoulements - Flot optique - Sillage - Système dynamique.

Abstract

Separated flows are ubiquitous in nature and industrial systems, such as diffusers, airfoils, air conditioning plants, moving vehicles... As the separation can strongly influence the performances of such devices, investigating their dynamics and their control is of great interest.

A visual sensor developed at PMMH laboratory is first improved to measure in real time the velocity fields and its derived values for flows available in wind tunnels. Based on an optical flow algorithm from the computer vision domain, this new experimental approach makes easier parametric studies and may be used in closed-loop controls.

The dynamics of the flow over a flat plate are then investigated. A system identification method - the dynamic observer - is successfully implemented to build a reduced-order model of the transient flow, which captures and predicts well the instabilities generated.

Finally, the fully turbulent wake of the square-back Ahmed body is described. Dynamical system tools are applied to characterize it. Using continuous and pulsed micro-jets, different forcing strategies are analyzed. An opposition closed-loop control is implemented, tracking and driving the recirculation.

Keywords

Flow control - Optical flow - Wake - Dynamical system.